

Modelling and Simulation of Hybrid Electric Vehicles

A thesis presented

in partial fulfilment of the requirements for the degree of
Doctor of Philosophy

by
Amit Shukla

**Imperial College
London**

to the

Department of Mechanical Engineering,
Imperial College London, London
United Kingdom
May 2012

Dedication

An offering unto the lotus feet of Supreme Personality of Godhead Lord Sri Krishna

तव कथामृतं तप्तजीवनं कविभिरीडितं कल्मषापहम्।
श्रवणमङ्गलं श्रीमदाततं भुवि गृणन्ति ये भूरिदा जनाः॥

tava kathamrtam tapta-jivanam, kavibhir iditam kalmasapaham
sravana-mangalam srimad atatam, bhuvi grnanti ye bhuri-da janah

The nectar of Your words and the descriptions of Your activities are the life and soul of those suffering in this material world. These narrations, transmitted by learned sages, eradicate one's sinful reactions and bestow good fortune upon whoever hears them. These narrations are broadcast all over the world and are filled with spiritual power. Certainly those who spread the message of Godhead are most munificent.
(SB10.31.9)

वंशी विभूषित करान्नवनीरदाभात् पीताम्बरादरूण बिम्बाफलाधरोष्ठात्।
पूर्णन्दु सुन्दरमुखादरविन्दनेत्रात् कृष्णात्परम किमपि तत्वमहं न जाने॥

vamshi-vibhushita-karan nava-niradabhat, pitambarad aruna-bimba-phaladharausthat
purnendu-sundara-mukhad aravinda-netrat, krishnat param kimapi tattvam aham najane

With a flute adorning his hand, the color of a new cloud, dressed in a yellow cloth as bright sun and with lips as red as the bimba fruit, with a face as beautiful as the full moon and eyes like lotuses, I know of no truth higher than Lord Krishna.
(Madhushudan Saraswati)

ABSTRACT

Inclusion of real physics based dynamics instead of conventional charts and maps, while capturing the transient behavior of the overall powertrain is the primary objective of this research effort. The multi-body model of the longitudinal car is described in detail, including mathematical models of tyres, suspensions, aerodynamic behaviour and continuous variable transmission (CVT). The PMSM and PMSG along with DC/AC, AC/DC are modeled in the $d - q$ frame. A novel frictional torque function, predicting all mechanical and electrical losses except resistance loss, is proposed. The results of the proposed frictional torque function compare well with the results obtained from empirical sources. Average models for AC/DC, DC/AC and DC/DC converters are used to ensure the simplicity and feasibility of the simulation in acceptable time scale. Bidirectional converters fed-back the recaptured mechanical energy during regeneration to the battery. A switching-frequency dependent average model for soft-switching isolated DC/DC converter is used in this research. A generic dynamic Li-ion battery model has been chosen which expresses the electrochemical parameters of the battery directly in terms of electrical parameters of the circuit.

A control oriented, fast and simple 0D model of the turbocharged diesel engine, combining mean value model and filling and emptying models has been presented in this work. Inlet manifold and exhaust manifolds are modeled as filling and emptying model, engine cylinder dynamics with mean value model, engine torque as a three dimensional map of indicated torque ($T_{eng} = f(\omega_{eng}, \lambda)$), engine speed ω_{eng} and air-fuel ratio λ , and flow characteristics of the compressor and turbine are modelled with mean value model. A novel control mechanism is proposed to control the fuel mass flow rate and relative air-fuel ratio. Simulation results of the present engine model are validated against a high-fidelity commercial Ricardo-wave model of the same engine.

A novel DC-link control mechanism is proposed to simulate the transient operation of the series HEV powertrain during different modes of operation. The supervisory control is implemented to meet the driver's demand for the traction power, at the same time avoiding over-discharging of the battery below certain threshold level, and optimizing the drive train efficiency, fuel consumption and emissions. On the basis of thermostat control and power follower, a novel "load follower" supervisory control strategy is proposed in the present work. A PI controller based driver model is developed and performance seems satisfactory while tracking the standard NEDC cycle. Simulation results are validated by energy balance computations and available transient and steady state data points for individual components as well as the overall powertrain. The research has successfully achieved the goal of developing a complete model for a series hybrid powertrain while capturing the transient performance of the all the components involved in the powertrain with module based, control oriented and forward facing modelling approach.

The work presented in this thesis has been conducted by the author,
all other work has been appropriately referenced.

ACKNOWLEDGEMENTS

From the core of my heart, I am very much thankful to Lord Sri Krishna, by whose mercy only, I have got this opportunity to write this doctoral thesis. By his grace, I have got extraordinary support, help and motivation from people around me, to only some of whom it is possible to give particular mention here.

First of all, I am sincerely grateful to my principle supervisor Dr. Simos Evangelou for providing me the required guidance and motivation to accomplish this work. Success of all my efforts is the result of his careful attention and help on each stage of my work.

I would like to mention my deep appreciation for Dr Ricardo Martinez-Botas for giving me guidance on some of the crucial issues during my research work. He was one of the person who always boosted-up my moral and motivated me to perform up to my best capacity.

Above all, I am very much indebted to my teacher Dr. Laxmidhar Behera, whose inspiration brought me here to do PhD in first place. He taught me that real freedom from matter can be brought only by performing all the duty of oneself in right consciousness. Since proper actions lead to internal purification of self, there is no reason to abandon the natural duties coming across in the path of life. By his mercy only today I am on the path of Krishna Consciousness.

I am most grateful to my spiritual ideal H.H. Bhakti Rasamrita Swami, his instructions made me capable to understand the very essence of all the actions and purpose of life is to attain the lotus feet of Supreme Personality of Godhead, Sri Krishna. I will always beg for his instructions, association and mercy.

I would like to thank all my colleagues in the lab who gave me company during my research work. I would also like to thank Dr Alessandro, who has helped in this work by generating various data required for completing the engine model.

I would like to acknowledge the financial, academic and technical support of the Imperial College London and its staff, particularly in the award of a research scholarship that provided the necessary financial support for this complete research work.

Finally, I would like to thanks my parents and friends for their good wishes and support in various ways, especially Ratnesh, Prashant and Rajesh. I would like to mention special thanks to Pawan Prabhu, who has tirelessly helped me in various ways.

I am thankful to each individual to whom I met ever, because in every interaction with them I have got addition of some valuable experiences to my personality. Myself and my work is summation of those experiences.

CONTENTS

Abstract	5
Acknowledgements	7
List of Publications	30
1 Introduction	31
1.1 Objectives	34
1.2 Achievements	37
1.3 The thesis is organized as follows:	39
2 Literature Review	42
2.1 Background	42
2.2 Types of Hybrid Powertrain	48
2.2.1 Series hybrid powertrain	48
2.2.2 Parallel hybrid powertrain	49
2.2.3 Series-parallel hybrid powertrain	50
2.3 Advantages and disadvantages of using series hybrid powertrain . . .	51
2.4 Components of the HEV Powertrain	52
2.4.1 Car model	54
2.4.2 Motor / Generator & power converters	55
2.4.3 Turbocharged diesel engine	57

2.4.4	Battery & DC/DC converter	60
2.4.5	Regenerative Braking	63
2.4.6	Driver	64
2.4.7	Supervisory Control	65
2.4.8	Integration of the components	68
3	Car Modelling	70
3.1	Introduction	70
3.2	Car	70
3.2.1	Vehicle dynamics	71
3.2.2	Tyre model	74
3.3	Aerodynamic Behavior	76
3.3.1	Aerodynamic drag	77
3.3.2	Aerodynamic lift	78
3.4	Powertrain Transmission	79
3.4.1	Implementation of the CVT	82
3.5	Summary	83
4	Permanent Magnet Synchronous Motor Modelling	85
4.1	Introduction	85
4.2	Permanent Magnet Synchronous Motor	88
4.2.1	PMSM drive	92
4.2.2	Permanent magnet synchronous motor model in the D-Q frame	93
4.3	Power Processing Unit	98
4.3.1	Average model of the three phase DC/AC converter (Inverter)	100
4.4	Speed Control of the Permanent Magnet Synchronous Motor	105
4.4.1	Voltage and current control loop design	107
4.4.2	Simulink implementation of the PMSM drive	109
4.5	Power Loss Model of the PMSM	111
4.6	Driver Model	114

4.7	PMSM Simulation Results	116
4.8	Summary	120
5	Permanent Magnet Synchronous Generator Modelling	121
5.1	Introduction	121
5.2	Permanent Magnet Synchronous Generator	122
5.2.1	Permanent magnet synchronous generator model in the D-Q frame	123
5.3	Average model of the three phase AC/DC converter (Rectifier)	127
5.4	Control Mechanism	129
5.4.1	Speed control loop design	130
5.4.2	Voltage and current control loop design	130
5.4.3	Simulink implementation of the PMSM drive	132
5.5	Power Loss Model of the PMSG	135
5.6	Simulation Results	136
5.7	Summary	140
6	Modelling of the Diesel Engine	141
6.1	Introduction	141
6.2	Modelling	145
6.2.1	Thermodynamic modelling	147
6.2.2	Fluid dynamic modelling	148
6.2.3	Black box modelling	149
6.2.4	Quasi stationary modelling	150
6.3	Mean Value Diesel Engine Model	150
6.3.1	Manifold modelling	152
6.3.2	Exhaust gas recirculation (EGR)	156
6.3.3	Engine cylinder	158
6.3.4	Turbocharger	167
6.4	Calibration Factors	180

6.5	Control of the Turbocharged Diesel Engine	184
6.5.1	Fuel amount control unit	187
6.5.2	Control of the relative air-fuel ratio (λ)	188
6.6	Simulation and Results	190
6.6.1	Simulink model of engine	190
6.6.2	Discussion of simulation results	195
6.7	Summary	200
7	Battery Modelling	202
7.1	Introduction	202
7.2	Battery	203
7.2.1	Battery modelling	205
7.2.2	Description of the battery model	207
7.3	DC/DC Converter	210
7.4	Control Mechanism	213
7.5	Simulink Implementation of Battery Model with DC/DC Converter .	215
7.6	Simulation Results	216
7.7	Summary	221
8	Integration of Component Models and Supervisory Control	222
8.1	Introduction	222
8.2	Heuristic Supervisory Control	225
8.3	Optimization Based Supervisory Control	227
8.4	Integration of Component Models	230
8.4.1	Power flow from the IC engine to the wheels	232
8.4.2	Power flow from the battery to the wheels	234
8.4.3	Hybrid mode operation	236
8.5	A novel DC-link control strategy	238
8.6	Inclusion of the Various Efficiency Factors	241
8.6.1	Power balance for the various components of the powertrain	241

8.6.2	Dynamic DC-link equations for various modes of operation	244
8.7	Supervisory Control Rule	246
8.8	Thermostat supervisory control strategy	247
8.9	Power follower supervisory control strategy	248
8.10	Load follower supervisory control strategy	250
8.11	Simulink block diagram of the series HEV powertrain	252
8.12	Summary	252
9	Simulation Results and Discussions	255
9.1	Introduction	255
9.2	Simulation results	256
9.2.1	Thermostat supervisory control strategy	257
9.2.2	Load follower supervisory control strategy	266
9.3	Summary of the results	295
10	Conclusions and Future work	298
10.1	Conclusions	298
10.2	Novel Contributions	301
10.3	Future Scope of the work	303
10.3.1	Vehicle Dynamics	304
10.3.2	Electric Machines	305
10.3.3	Electronic Converters	305
10.3.4	Battery Model	306
10.3.5	Engine	307
10.3.6	Supervisory Control Strategy	308
Appendix		309
A	Longitudinal vehicle dynamics	309
A.1	VehicleSim® code for the longitudinal vehicle	309

LIST OF FIGURES

2.1	Schematic diagram of the Series Hybrid Electric Vehicle [21]	49
2.2	Schematic diagram of the Parallel Hybrid Electric Vehicle [21]	50
2.3	Schematic diagram of the Series-Parallel Hybrid Electric Vehicle [21]	51
2.4	Complete structure of series hybrid vehicle powertrain	54
2.5	Interconnection concept among different mechanical and electrical subsystems	68
3.1	Tree structure of the bodies and contact points included in the mo- delling of the longitudinal vehicle in VehicleSim®	71
3.2	Vehicle rigid body diagram showing forces except gravity [174] . .	73
3.3	Longitudinal force as a function of longitudinal slip and load [32] .	75
3.4	Higher and lower pressure zones created around the car due to streamlined air flow	77
3.5	Overall aerodynamic drag and lift forces applied on the car due to streamlined air flow	77
3.6	CVT implementation	83
4.1	Current and voltage in the brushless DC and AC motors [25]	87
4.2	Cross sectional view of a surface mounted PMSM [188]	88
4.3	Axial PMSM (a) one stator and rotor; (b) two stator and one rotor [49]	89
4.4	Different types of PMSM	90

4.5	Cross-section of slotted and slottless PMSM	91
4.6	High level design of the PMSM motor drive	93
4.7	Three phase (<i>abc</i>) and two phase (<i>d</i> – <i>q</i>) representation of the PMSM	94
4.8	Transformation of the PMSM equations from three phase (<i>abc</i>) to two phase <i>d</i> – <i>q</i> rotating axes	95
4.9	Three Phase DC to AC Inverter-fed PMSM	98
4.10	Detailed and average models of the PWM switch	103
4.11	Schematic diagram of the control loops of the PMSM with the longitudinal car.	106
4.12	Simulink block diagram of the PMSM drive	109
4.13	Simulink block diagram of the PMSM model level I	110
4.14	Simulink block diagram of the PMSM model level II	110
4.15	PMSM steady-state power efficiency map for the variations in load torque	113
4.16	Variation of the PMSM frictional torque, T_f , with rotor speed, ω_r . .	114
4.17	Schematic diagram of the driver model	115
4.18	Simulink implementation of the driver model	116
4.19	Standard NEDC drive cycle for testing of the PMSM drive	117
4.20	Error between the supplied NEDC speed profile and the actual for- ward speed	117
4.21	Electromagnetic torque T_e generation in the PMSM	118
4.22	Load torque T_L applied at the transmission shaft of the longitudinal car	118
4.23	Quadrature axis current of the PMSM i_q	119
4.24	Direct axis current of the PMSM i_d	119
4.25	Quadrature axis voltage of the PMSM v_q	119
4.26	Direct axis voltage of the PMSM v_d	120
5.1	Circuit diagram showing electrical connection of the generator (PMSG), AC/DC rectifier, DC/AC inverter and motor (PMSM). .	122

5.2	Permanent magnet synchronous generator with three phase AC/DC rectifier with constant DC-link voltage	123
5.3	Equations of PMSG in rotating d-q axis reference frame	125
5.4	Schematic diagram of the control loops of the PMSG.	129
5.5	Overall PMSG drive control model in simulink	133
5.6	Average modelling of the rectifier in simulink	133
5.7	DC-link model in simulink	133
5.8	Level I of the PMSG model in simulink	134
5.9	Level II of the PMSG model in simulink	134
5.10	Variation of the PMSG frictional torque, T_f , with rotor speed, ω_r . .	137
5.11	PMSG steady-state power efficiency map for variations in output power	137
5.12	Voltage produced by the PMSG Generator at DC-link	138
5.13	Direct axis current of the PMSG i_d	138
5.14	Quadrature axis current of the PMSG i_q	138
5.15	Direct axis voltage of the PMSG v_d	139
5.16	Quadrature axis voltage of the PMSG v_q	139
5.17	Rotational speed of the PMSG rotor shaft	139
5.18	Comparative magnitudes of all three torques	140
6.1	Diesel cycle	141
6.2	Schematic diagram of the diesel engine with turbocharger and EGR	144
6.3	Inside view of the diesel engine cylinder [209]	145
6.4	Cubic Interpolation of torque, λ and speed ω_{eng}	162
6.5	Turbocharger shaft	167
6.6	Compressor map supplied by the manufacturer.	174
6.7	Coefficient a_1 map fitting	174
6.8	Coefficient a_2 map fitting	175
6.9	Coefficient a_3 map fitting	175

6.10	Compressor map fitting where the measurement data	176
6.11	Turbine map fitting where the measurement data are plotted	179
6.12	Calibration factor for exhaust gas K_x	183
6.13	Control loops of the turbocharged diesel engine.	185
6.14	Fuel amount control unit with antiwind-up control	188
6.15	Implementation of the feedback control for the relative air-fuel ratio λ	189
6.16	Simulink block diagram of the diesel engine with components . . .	191
6.17	Simulink block diagram of the Inlet Manifold	192
6.18	Simulink block diagram of the Exhaust Manifold	192
6.19	Simulink block diagram of the Engine Cylinder	194
6.20	Simulink block diagram of the Compressor (level I)	196
6.21	Simulink block diagram of the Compressor (level II)	196
6.22	Simulink block diagram of the Turbine	196
6.23	Verification of the fuel consumption between the Ricardo-Wave (EXP) model versus the Simulation (SIM) model.	198
6.24	Exhaust temperature (T_x) at 1500 rpm.	199
6.25	Exhaust temperature (T_x) at 2000 rpm.	199
6.26	Exhaust temperature (T_x) at 2500 rpm.	199
7.1	Electrochemical cell of a battery	203
7.2	Primary referenced equivalent circuit for the DC-DC converter . .	212
7.3	Matlab/Simulink block diagram for control of the DC-DC converter, level-I	214
7.4	Matlab/Simulink block diagram for control of the DC-DC converter, level-II	215
7.5	Matlab/Simulink block diagram of the battery model along with DC-DC converter and DC-link	215
7.6	Matlab/Simulink block diagram of the battery model	217
7.7	Matlab/Simulink block diagram of the DC-link	218

7.8	Load current i_{load} and dc current i_{ob}	218
7.9	Reference DC-link voltage $V_{dc,ref}$ and actual DC-link voltage $V_{dc} = v_{34}$	218
7.10	Battery current i_{bat}	218
7.11	Variation of the terminal battery voltage v_{bat} during the charge and discharge cycle of the battery	219
7.12	State of charge profile of the battery during discharging and charging SOC	219
7.13	v_{12} average voltage	220
7.14	Flow of power from the battery	220
7.15	Variation of the phase shift angle	220
8.1	Categorization of different supervisory control strategies	223
8.2	Interconnection concept among different kinds of mechanical and electrical subsystems	231
8.3	Circuit diagram showing the electrical connection of the generator (PMSG), AC/DC rectifier, DC/AC inverter and motor (PMSM). . .	232
8.4	Block diagram showing the interconnection of the engine, PMSG, rectifier, inverter, PMSM and car and the related control loops. . .	233
8.5	Circuit diagram showing the electrical interconnection of the battery, DC/DC converter, inverter, and PMSM.	235
8.6	Block diagram showing the interconnection of the battery, DC/DC converter, inverter, PMSM and car and the related control loops. . .	235
8.7	Circuit diagram showing the electrical connection of the interconnection of the engine, generator, AC/DC converter, battery, DC/DC converter, DC-link, inverter, PMSM and car in one powertrain. . .	237
8.8	Block diagram showing the interconnection of the engine, PMSG, AC/DC converter, battery, DC/DC converter, DC-link, inverter, PMSM, and, car and related control loops.	237

8.9	Simulink block diagram showing the implementation of DC-link voltage with various efficiency factors for the converters.	246
8.10	Simulink block diagram of the HEV powertrain containing longitudinal car, PMSM, DC/AC converter, DC/DC converter, battery, AC/DC converter, PMSG and turbocharged diesel engine	253
9.1	NEDC drive cycle for testing the supervisory controller of the HEV powertrain	257
9.2	Stateflow chart for the thermostat supervisory control	257
9.3	Error between desired speed profile and actual forward speed of the CVT installed longitudinal vehicle	258
9.4	Time history of the <i>SOC</i> of the battery while tracking the NEDC .	260
9.5	Energy provided by the engine, battery, battery recharging, SOC equivalent and total energy spent	260
9.6	Time history of the total fuel consumption during NEDC	261
9.7	Energy dissipated by the engine, battery, DC/DC converter	261
9.8	Time history of the energy generated in the engine for the powertrains	261
9.9	Time history of the engine friction loss in the powertrains	262
9.10	Quantification of all the losses except the copper loss in the PMSG	263
9.11	Quantification of the copper loss in the PMSG	263
9.12	Quantification of copper loss in the PMSM	264
9.13	Quantification of all losses except copper loss in the PMSM	265
9.14	Time profile of total energy loss in the PMSM	265
9.15	Quantification of the total energy supplied from DC-link onwards .	266
9.16	Stateflow chart for the proposed load follower supervisory control strategy.	267
9.17	Error between desired speed profile and actual forward speed . . .	269
9.18	Energy provided by the engine, battery, battery recharging	269
9.19	Energy dissipated by the engine, battery, DC/DC converter	270

9.20	Time history of the total fuel consumption during NEDC	270
9.21	Time history of the energy generated in the engine	272
9.22	Time history of the energy lost due to engine friction	272
9.23	Quantification of all the losses except the copper loss in the PMSG	273
9.24	Quantification of the copper loss in the PMSG	273
9.25	Quantification of copper loss in the PMSM	274
9.26	Quantification of all losses except the copper loss in the PMSM . .	274
9.27	Time profile of total energy loss in the PMSM	275
9.28	Quantification of the total energy supplied from DC-link	275
9.29	Time history of PMSM efficiencies in the cases of $f_{drat} = 2, 3, 4, 5, 6$ and CVT for urban (ECE-15)	276
9.30	Time history of PMSM efficiencies in the cases of $f_{drat} = 2, 3, 4, 5, 6$ and CVT form extra urban (EUDC)	276
9.31	Variation of the f_{drat} in the case of CVT for the urban (ECE-15) . .	277
9.32	Variation of the f_{drat} in the case of CVT for the extra urban (EUDC)	277
9.33	DC-link voltage profile during the tracking of the complete NEDC	278
9.34	DC-link current time history for urban (ECE-15)	278
9.35	DC-link current time history for extra urban (EUDC)	279
9.36	Current generated by the PMSG-rectifier, and battery and DC-link load current	280
9.37	Quadrature axis current profile in the PMSM	281
9.38	Quadrature axis current profile in the PMSM	281
9.39	Load torque profile of the PMSM	282
9.40	Load torque profile of the PMSM	282
9.41	Rotational speed profile of the PMSM	282
9.42	Rotational speed profile of the PMSM	283
9.43	Quadrature axis voltage profile of the PMSM	283
9.44	Quadrature axis voltage profile of the PMSM	283
9.45	Direct axis currents profile in the PMSM	284

9.46	Phase shift angle of the DC/DC converter	285
9.47	Time history of battery voltage during the complete NEDC cycle . .	285
9.48	Time history of battery current during the complete NEDC cycle . .	285
9.49	Time history of the energy discharged by the battery	286
9.50	Time history of the energy recharged to the battery	286
9.51	Time history of the energy loss due to internal resistance of the battery	286
9.52	Time history of the total battery energy level	287
9.53	Time history of the <i>SOC</i> of the battery	287
9.54	Time history of quadrature axis current i_q in the PMSG	288
9.55	Time history of direct axis current i_d in the PMSG	288
9.56	Time history of quadrature axis voltage v_q in the PMSG	288
9.57	Time history of direct axis voltage v_d in the PMSG	289
9.58	Time history of the various torques such as the indicative torque T_{eng}	290
9.59	A closer look at the first part of the transient dynamics	290
9.60	A closer look at the second part of the transient dynamics	291
9.61	Time history of the rotational speed of the PMSG (ω_{rg})	291
9.62	Transient time history of the calculated fuel-mass flow rate ($w_{fuel,cal}$)	292
9.63	Transient time history of the air mass flow rate ($w_{ie,air}$)	292
9.64	A closer look at the first part of the transient dynamics of the air mass flow rate ($w_{ie,air}$)	293
9.65	A closer look at the second part of the transient dynamics of the air mass flow rate ($w_{ie,air}$)	293
9.66	Time history of the relative air-fuel ratio (λ) during the EUDC cycle	293
9.67	A closer look at the first part of the transient dynamics	294
9.68	A closer look at the second part of the transient dynamics	294
9.69	Transient time history of the rotational speed of the turbo-shaft (ω_{tc}) during the EUDC cycle	294
9.70	A closer look at the first part of the transient dynamics of	295
9.71	A closer look at the second part of the transient dynamics	295

LIST OF TABLES

3.1	Parameter values of the longitudinal car	73
4.1	Parameter values of the PMSM.	111
5.1	Parameter values of the PMSG.	135
6.1	Measurements of λ , fuel consumed w_{fuel} , exhaust temperature T_x with different engine speed	161
6.2	Compressor map fitting coefficients k_{i1} and k_{i2}	173
6.3	Turbine map fitting coefficients b_{ij}	178
6.4	Parameters of the turbocharged diesel engine	190
6.5	Comparison of the experimental and simulated results for various parameters of the engine	197
7.1	Parameter values of the Li-Ion cell	210
9.1	Quantification of all the energy generation and losses involved in different components of the HEV powertrain	271

NOMENCLATURE

PM machines and converters

λ_d, λ_q Stator flux linkages of PM machines in the $d - q$ frame

λ_f Flux linkage due to rotor magnet

ω_e Speed of the rotating electromagnetic field in PM machines [rad/s]

ω_r Speed of the rotor in PM machines [rad/s]

$d - q$ frame Direct and quadrature axis reference frame

d_a, d_b, d_c Bipolar switching functions in the three phase

d_d, d_q Switching period of the power converters in the $d - q$ frame

f_{drat} Final drive ratio

i_a, i_b, i_c Three phase stator currents in the PM machines [V]

i_d, i_q Stator currents of PM machines in the $d - q$ frame [A]

i_{dc} DC current drawn by the inverter

J_m, J_g Rotor inertia of the PMSM and PMSG

L_d, L_q Stator inductances of PM machines in the $d - q$ frame [H]

p	Number of poles in the PM machine
P_{in}	Input power to the system
$P_{l,b}$	Bearing loss in the PM machines
$P_{l,c}$	Copper loss in the PM machines
$P_{l,e}$	Eddy current loss in the PM machines
$P_{l,h}$	Hysteresis loss in the PM machines
$P_{l,w}$	Windage loss in the PM machines
P_{out}	Output power of the system
R	Stator resistance of PM machines [Ω]
T_e	Electromagnetic torque in PM machine
T_L	Load torque torque in the PM machine
T_f	Frictional torque in PM machines
v_a, v_b, v_c	Three phase stator voltages in the PM machines [V]
v_d, v_q	Stator voltages of PM machines in the $d - q$ frame [V]
v_{dc}	DC-link voltage [V]
CSI	Current source inverter
CVT	Continuous Variable Transmission
FTP-75	Federal Test Procedure
HWFET	EPA Highway Fuel Economy Cycle
KCL	kirchhoff's current law
KVL	kirchhoff's voltage law

LFSCS Load Follower Supervisory Control Strategy

LTI Linear time invariant

NEDC New European Driving Cycle

NYCC New York City Cycle

PI controller Proportional integral controller

PID controller Proportional integral derivative controller

PM machine Permanent magnet synchronous machine

PMSG Permanent Magnet Synchronous Generator

PMSM Permanent Magnet Synchronous Motor

PWM Pulse width modulation

TSCS Thermostat Supervisory Control Strategy

VSI Voltage source inverter

Battery

ϕ Phase angle shift between the LVS and HVS voltages

i_{bat} Current drawn from the battery [A]

K Polarisation constant [$\frac{V}{(Ah)}$]

Q Battery capacity [Ah]

v_{12} Average voltage at LVS

v_{34} Average voltage at HVS

V_{bat} Terminal voltage of the battery [V]

HVS Higher voltage side of the DC/DC converter

LVS Lower voltage side of the DC/DC converter

SOC State of charge of the battery

Engine

η_v, η_e volumetric (1) and fuel efficiency

η_{ic} Inter-cooler efficiency (1)

λ Relative Air-Fuel ratio

ω_{eng} Engine rotational speed [RPM]

ω_{tc} Rotational of the turbocharger shaft [rad/s]

ρ_i Density of the injected air inside the inlet manifold

σ Number of revolutions per cycle

J_e Inertia of the engine shaft ($0.2[kgm^2]$)

J_{tc} Inertia of the turbocharger shaft ($0.00012[kgm^2]$)

m_i, m_x Air mass in inlet and exhaust manifold [kg/s]

p_i, p_x Pressure of Inlet and exhaust manifold [kPa]

p_{atm} Atmospheric pressure 100[kPa]

Q_{HV} Low heating value of fuel ($42[MJ/kg]$)

r_c Compressor wheel radii ($24.45[mm]$)

T_i, T_x Air temperature in the inlet and exhaust manifold [K]

T_{atm} Atmospheric temperature 293.15[K]

T_b, T_{load} Brake and load torque on the engine shaft [Nm]

T_{ci} Compressor outlet temperature [K]

$T_{coolant}$ Coolant temperature (303.5[K])

T_{cor} Correction term for the air temperature in the exhaust manifold [K]

T_{eng}, T_{fric} Indicative and friction torque on the engine shaft [Nm]

T_{ex} Exhaust temperature [K]

u_{vgt} VGT vane position

V_d Engine displacement (0.0004496[m^3])

V_i Inlet manifold volume (0.00151655[m^3])

V_x Exhaust manifold Volume (0.000448[m^3])

w_{ci} Air mass flow rate through the compressor [kg/s]

w_{fuel} Fuel mass flow rate [kg/s]

w_{ie} Air mass flow rate into the engine cylinder [kg/s]

w_{xi} EGR mass flow rate [kg/s]

w_{xt} Turbine mass flow rate [kg/s]

A/F Air-Fuel mixture

PM Particulate matter

LIST OF PUBLICATIONS

Papers

1. S. A. Evangelou, A. Shukla, “Advances in the modelling and control of hybrid electric vehicles” American Control conference, Montréal, Canada 2012. (Accepted)
2. A. Shukla, R. Martinez-Botas, and S. A. Evangelou, “Dynamic modelling of turbocharged diesel engines,” ASME Journal of Dynamic Systems, Measurement, and Control. (In preparation)
3. S. A. Evangelou, A. Shukla, S. Wassif, “Dynamic model development for the evaluation of powertrain, transmission and control of hybrid electric vehicles” IEEE Transactions on Vehicular Technology. (In preparation)

CHAPTER

ONE

INTRODUCTION

After the post industrial era, demand for energy is growing at an ever increasing rate because of increasing use of electrical and mechanical machines. One of the largest energy consuming sectors is transportation. After the invention of petroleum engines, motorized vehicles have become an essential part of modern daily life. In modern times, a large part of the world population use motorized vehicles for personal transportation. Today, rail transportation is increasingly run on electricity while commercial heavy duty vehicles and personal vehicles still use IC engines. The stark reality of modern times is the serious threat posed by environmental pollution which, to a large extent is produced by CO_2 emissions from IC engine based vehicles [1]. In addition to pollution related disadvantages, fossil based resources are running out. Therefore, new technologies have to be identified optimizing the use of petroleum products. Researchers are striving to come up with novel greener energy technologies in the field of transportation. Despite obvious disadvantages of scarcity and pollution, petroleum products have many advantages in comparison to non-traditional energy sources. For example, petroleum products have very high energy density in comparison to batteries, fuel cells, etc. Also, refueling the fuel tank is very quick, whereas recharging batteries can takes a few hours. In contrast to a chemical battery, fuel cell generates electric energy than storing it, and production of energy continues in the fuel cell as long as supply of the fuel is there. This main difference gives longer driving range for fuel cell based

vehicle. But to get higher energy density for fuel cells generally highly compressed hydrogen is used which is costly and dangerous as well [2]. On consideration of the pros and cons of petroleum and non-petroleum energy sources, researchers have slowly moved towards hybrid technologies for near term viable solutions. With hybrid technologies, the main strategy is to optimize the use of petroleum and simultaneously enhance use of green energy technologies in powering the vehicle.

Engineers have invented and considered completely electrical vehicles running on chemical batteries, fuel cells and solar cells but these power sources have their own limitations. At least with the present state of technology, significant limitations include charging time, durability, performance, supporting infrastructure, etc. [3]. A middle ground approach has been opted for, where engines downsize with higher power-output using modern control techniques and powertrains become increasingly electrified. Generally, the concept of the Hybrid Vehicles suggests presence of multiple sources of energy to drive the vehicle. Most commonly in Hybrid Vehicles, an internal combustion engine is used in association with batteries. It has been found by simulation and experimentally that batteries and internal combustion engines have individually higher efficiencies when the power demand is lower and higher respectively. Therefore, this complementary nature of efficiency characteristics of the power sources, lends itself to the hybridization of the powertrain (for e.g., with IC engine and battery). When the vehicle is running at low speeds in the city, the battery can provide the required power, and when the vehicle is running at high speeds on freeways, the IC engine can supply the power. This is an example of one of many possible combinations resulting from energy management systems. Regenerative braking is also a very useful feature, which can provide additional energy savings.

The history of Electric Vehicles dates back to mid 19th century. Until the early 20th century, they performed well, however better inventions in the field of internal combustion engines revolutionized the market of IC engine based vehicles resulting in phasing out of EVs. In modern times, with increasing oil prices and environmental

concerns, research related to EVs and HEVs is becoming quite relevant. In the past, the biggest drawback of electric vehicles was poor control of electric machines (especially, the motor) due to lack of sophisticated power electronics. Since slip rings and brushes used in brushed DC machines were subjected to mechanical wear and sparking so maintenance was very costly and dangerous as well from the safety point of view. Modern inventions in the field of power electronics, especially transistors, avoided above mentioned problems and gave an essential boost to the performance of electric vehicles.

From 1984 to date, there have been significant improvements in various technological aspects of electrical propulsion systems such as batteries, electrical machines and electronic controllers [4]. However, EVs are not yet able to replace IC engine based vehicles because EVs utilize batteries having very low energy density as the power source in comparison to IC engines using gasoline having very high energy density. This energy density limitation poses a very strong challenge on the driving range of EVs. There are other concerns with the batteries relating to their charging and discharging capabilities, thermal characteristics and safety. Batteries decay very fast at high load current and take long time to recharge back to the same level. Recharging also causes the battery to heat up due to the internal dissipation of power. In comparison, petroleum fuel is very convenient because refueling is very easy due to existing infrastructure. In one sense, when refueling petroleum fuel, “recharging” takes place instantaneously. Therefore, there exists a need for all these critical issues to be addressed before electric vehicles become a popular market reality. As research and development of electric vehicles is heavily limited by existing battery technologies, engineers realized that a middle-ground approach in the form of the hybrid electric vehicle is practical. Success has already been demonstrated by the commercial HEVs produced by Toyota and Honda in recent years. New research related to the powertrain structure, energy management and supervisory control are resulting in improved commercial HEVs and paving the pathways for complete EVs in the coming decades [2].

1.1 Objectives

In contrast to already available modelling and simulation approaches, the present work is unique in its precise dynamic mathematical modelling and simulation capability for every component of the vehicle. Efficiency maps are replaced by modelling loss mechanisms. For example, rather than using efficiency maps to represent the behavior of generators and motors, novel mathematical models for frictional losses in these machines are combined with existing electro-mechanical models to predict both dynamic and steady-state behavior more accurately. The dynamics of the system are captured not only by empirical relationships but by modelling components based on fundamental physics. Definitely, there are limitations to what extent everything can be modeled completely from fundamental physics. Therefore, with the intent of avoiding extreme mathematical complexity and lengthy simulations, at times a trade-off has been applied without compromising the capacity to capture important transient behaviors.

Most of the available research tools, described in Section 2.1, are still heavily dependent on steady-state performance based charts and maps. Analysis based on the steady-state performance may be appropriate in some cases for overall high level modelling but lacks the required accuracy for component level modelling and control. With progressive research in the field of EVs and HEVs, more capable modelling and simulation tools are required. In the literature, many dynamic models for different components of the powertrain seem available. However, they all are separately available for the purpose of analysis and control of the respective standalone components. The present work combines these discretely available dynamic models from the respective research areas to a common platform with the purpose of integrating them as one powertrain. Some system level changes are done in the form of input and output definitions to adjust compatibility of components with each other. There are many physical events involved in the processes of an HEV operation, such as the combustion of fuel in an IC engine, which are extremely complex to be included in fast modelling processes. Hence, the integration of completely transient models from basic fundamentals of physics for

every component in detail is a nearly impossible task from a modelling standpoint. Not only will this kind of modelling be complex and computationally expensive, this kind of cumbersome complexity will not be useful for the very purpose of modelling. So, the present research tries to fill gaps between steady state modelling and complete dynamic modelling.

In order to achieve the goal of building generic dynamic models, a mixed level modelling approach has been adopted. There are mainly three levels of modelling approaches, namely, the detailed level, average level and linearized or small signal level modelling. The goal is to simulate the complete powertrain in one model where all the different kinds of components such as mechanical, electrical and chemical are integrated together. Since different components involved in the powertrain have different levels of complexity and dynamics with time scales of different orders of magnitude, the mixed level modelling approach has been adopted. In the mixed level modelling approach some components are described in detail with basic fundamental physics, such as the dynamics of the PMSM and PMSG, whereas some other components are modeled with average modelling techniques such as the dynamics of the converters and yet some other components are modeled with linearized models or small signal models such as the field oriented control (vector control) of electric machines. There are also some components which are modeled with the inclusion of empirical relationships in combination with the earlier three approaches already mentioned.

The main objective of the work is to present a module based fast and dynamic model of the powertrain of series HEVs. The basic platform of the modelling involves all the components of the HEV drivetrain as separate modules with appropriate independent controllers. All components are modeled to capture the best possible, mathematically accurate and required dynamic behavior. Some components are modeled completely mathematically from first principles rather than using any behavioral charts because this increases accuracy for wider range of operating conditions and flexibility for parameterizations later on to conduct design optimization studies. Some components

involve very fast dynamics such as combustion in IC engines and switchings of IGBT and MOSFET devices in the converters. These fast dynamics have been ignored but this does not affect the generality and accuracy of predictions for the intended studies. This kind of fast dynamics not only increases the complexity of the model but also slows down the simulation speed without adding any significant information to the purpose at hand. Such components are modeled with state space averaging techniques or with relevant empirical relations. Direct use of charts and maps in the form of tabular data are avoided due to overall control oriented nature of our modelling. Discontinuity and non-differentiability of charts and maps creates serious problems in interpolated and extrapolated regions of powertrain operations which are very frequent in transient simulations. Instead continuous functions fitted to the data are used.

There are mainly two kinds of modelling approaches firstly backward facing modelling approach and secondly forward facing modelling approach. In backward facing approach a drive profile is taken as input and then the required power to track that particular drive profile is calculated. Now this power calculation is carried backward, component after component, from the wheels to the power sources (IC engine or battery) in contrast to the tractive power flow direction in the actual vehicle. In forward facing modelling approach power flow calculation is done from the power sources to the wheels very similar to the actual vehicle. The forward facing modelling approach gives a designer lot of flexibility in designing the components due to access of internal variables of the system. For the development and implementation of control strategies a forward facing modelling approach is more appropriate than backward facing approach [5]. Most of the simulators available in the literature and software market are backward facing or at best backward facing with seriously limited forward facing capabilities. Chapter 2 will give detailed description about these two modelling approaches. Thus this work contributes to development of a platform for forward facing simulations with dynamic response analysis capabilities.

Since a hybrid powertrain uses multiple power sources there is need for a

supervisory controller to optimally split the power contribution between different power sources. There are many supervisory controllers proposed in the literature with various levels of complexities. Most of the advanced optimization based supervisory controllers proposed in the literature are implemented on steady state approximated models of HEVs powertrains. It will be highly interesting to implement various supervisory controllers on more accurate models which have real time component controllers and transient dynamics. These implementations will give more realistic and accurate predictions on the role of supervisory controllers in affecting performance parameters of the vehicle.

A driving cycle consists of speed versus time curve which needs to be tracked by the vehicle to allow an emission and fuel consumption test under reproducible conditions. There are mainly two categories of drive cycles firstly transient driving cycle and secondly modal driving cycle. The transient driving cycle involves many frequent acceleration and deceleration periods which are very typical to most of the city drive. Whereas modal drive cycle involves gentle accelerations and decelerations periods along with many constant speed sections [6]. Since present work is making a case for complex dynamic modelling of the HEV powertrain so at first a modal drive cycle (e.g. New European Driving Cycle (NEDC)) has been chosen for simulation and transient drive cycles (e.g. New York City Cycle (NYCC), EPA Highway Fuel Economy Cycle (HWFET) and Federal Test Procedure(FTP-75)) with present model will be tested in the future.

1.2 Achievements

The main achievement of the present work lies in the dynamic modelling of all the components involved in the HEV powertrain. This research work presents a general methodology for modelling and simulation of various dynamic components in one powertrain. Although, in this work modelling and simulation of series hybrid

electric powertrain is presented but this model can be extended to other configurations as well such as parallel and series-parallel. Since, all the components are modelled as separate modules so, they can be arranged in any configuration as required with little changes in the component integration methods and supervisory control architecture. There are some novel achievements in the present research work which is summarized below:

- This work focuses on the fast, accurate and dynamic analysis of the complete HEV along with its components. Inclusion of real physics based dynamics instead of conventional charts and maps for the components of the HEV is one of the most novel feature of this work.
- A novel frictional torque function is proposed in this work to model all the losses except copper loss (which is already known) in the PMSM and PMSG. The results of the proposed frictional torque function compare well with the empirical data provided by the manufacturer [7].
- A novel power split control mechanism is proposed in this work to deliver the required power to the traction motor and simultaneously regulating the DC-link voltage as well. This control mechanism incorporates dynamic DC-link equation which is generally ignored by maps and charts based models of the HEV powertrain [8].
- A control oriented dynamic 0D model for the turbocharged diesel engine is developed based on the physics of the system. A novel control mechanism for controlling the fuel amount and relative air-fuel ratio (λ) with an anti-windup controller is proposed in this work. Two calibration factors are included in the engine model to account for all the major possible uncertainties involved in modelling [9].
- The modelling methodology presented in this work provides the access to the internal variables of the different components, which precisely lacked by steady-state

and map based models, and it is required for any component level optimization. At present only by optimizing the PMSM for its operations significant reduction in the total energy consumption for the complete powertrain is achieved. Similar component level optimization can be done for all other different components to further reduce the total energy consumption.

- A novel “load follower” supervisory control strategy has been proposed in this work to efficiently operate the series hybrid powertrain. Present work provides the potential for testing more advance and sophisticated supervisory control schemes on dynamic model of the powertrain.

1.3 The thesis is organized as follows:

Chapter 2 presents literature review regarding current state of the art about tools and techniques used for modelling and simulation of the Hybrid Electric Vehicle (HEV). In this chapter, a comparative study regarding individual components of the powertrain from already published literature is also presented.

Chapter 3 discusses the longitudinal vehicle dynamics model with realistic description of tyres, aerodynamic resistance, suspension and tyre slip. The level of detail available in this model allows various kinds of losses from tyre slip, tyre damping, aerodynamic drag & lift, and suspension to be quantified. The model is validated by observing its good transient performance and energy balance between energy given and energy dissipated by the vehicle. The benefits and implementation details of a continuously variable transmission (CVT) are also described.

Chapter 4 focusses on behavior description of the Permanent Magnet Synchronous Motor (PMSM) and its Drive. Modelling is done in the $d - q$ frame (Direct and quadrature axis reference frame) along with a novel friction model to calculate equivalent losses in the motor [7]. A PID controller based driver model is also described

which takes an NEDC drive cycle as input and generates torque references for the PMSM to track the drive cycle accurately. A vector control method is employed to design the speed control strategy of the PMSM. This vector control method generates $d - q$ phase currents and voltages in the PMSM stator in such a way that the required torque can be generated in the PMSM. The DC/AC converter (inverter), which drives the PMSM, is described by the standard average modelling technique in the continuous conduction mode. An average efficiency factor is used to quantify the losses in the DC/AC converter. Simulation results are generated for the PMSM driving a longitudinal car while tracking the standard NEDC cycle.

Chapter 5 describes the modelling of the Permanent Magnet Synchronous Generator (PMSG) in $d - q$ frame along with a similar loss model as described for the PMSM. A simple PI controller based engine model is used in this stage to test the standalone PMSG model. This PI controller applies the required mechanical torque to the PMSG to maintain the speed of the rotor. The PMSG output voltage is common to a DC-link which is desired to be maintained at a constant voltage throughout the operation. A control strategy via the PMSG drive based on vector control method is designed for maintaining the constant DC-link voltage. Once again, average modelling is used for modelling the three phase AC/DC converter (Rectifier) with inclusion of average efficiency factor. Simulation results are presented for standalone operation of the PMSG with AC/DC converter maintaining constant DC-link voltage while constant current is drawn from the PMSG drive.

Chapter 6 presents the control oriented dynamic 0D model for a turbocharged diesel engine, which is based on the fundamental physics and processes of the system. Inlet manifold and exhaust manifolds are described according to filling and emptying model, engine cylinder dynamics with a mean value model, engine torque as a three dimensional map of indicated torque, rotational speed of engine shaft and relative air-fuel ratio and flow characteristics of the compressor and turbine according to a mean value model. A Ricardo-Wave model of the same engine is used to validate the steady

state results of this engine.

Chapter 7 presents a generic model of the Li-ion battery which expresses the relationship between chemical parameters and electrical parameters of the equivalent circuit. This generic model is also included in the simulink library. A frequency dependent state space averaged model of the bi-directional DC/DC converter, which connects the battery to the DC-link, is also described in this chapter.

Chapter 8 contains discussions on the integration of discrete components of the powertrain with implementation of supervisory control. The main function of the supervisory controller is to facilitate optimal utilization of available resources in the powertrain, thereby minimizing fuel consumption over a given driving schedule. On the basis of thermostat control and power follower, a “load follower” supervisory control strategy is proposed in the present work.

Chapter 9 elaborates on the simulation results obtained for the complete Hybrid Electric Vehicle. Two supervisory control strategies, namely, “thermostat” and “load follower” are implemented successfully to test the efficacy of the HEV powertrain. Various kinds of comparative analysis are also performed to understand facts behind better performance of the HEV powertrain installed with the CVT.

Chapter 10 summarizes the achievements of the present work. This chapter also gives concluding remarks about novel ideas which helped this work to evolve as contribution in the field of HEV research. Finally, directions and possibilities of future research are discussed.

CHAPTER

TWO

LITERATURE REVIEW

2.1 Background

There are various software tools available in the market and academic area for the simulation and analysis of HEVs. One of the most widely used software tools is ADVISOR [10], developed by NREL (National Renewable Energy Laboratory) in USA in 1992. ADVISOR uses MATLAB/SIMULINK as the operating platform. ADVISOR's simulations are mainly backward facing with very limited capacity for forward facing designing. Moreover, ADVISOR is mainly an analysis tool, not a design tool. Backward facing implies that the speed profile that a vehicle desires to follow is provided as input and the required torque, speed and power for the various components are obtained as outputs. The biggest drawback of this tool is its inability to capture transients behavior of the powertrain because all components of the powertrain are either modeled by empirical relationships or quasi-static data, collected during steady-state operations [11].

The backward facing modelling works on the assumption that required demands for torques, voltages and currents are supplied by the respective components, so there is no need to describe the dynamics of the component. Since, most of components are modelled by steady state maps and charts in backward facing modelling approach, therefore energy consumption and performance of different components (engine) during

transient periods of the drive are not calculated correctly. Further more backward facing modelling approach also lack access to the internal variables of the system, so ideally no component level controller can be designed in this approach [10].

Backward facing approaches have two serious limitations:

1. The output (required power or load profile) is known and the input (available power) has to be calculated. This approach works on the principle determination of “how each component in the drive train must perform” with an assumption that the requested power has been delivered by the power source. This approach leads to calculation from load (requested power) to source (available power) and sometimes the requested power does not match up with power supplied resulting in a non-convergent solution. One more drawback of this approach is that sometimes the feasible solution includes a component size beyond physical possibility.
2. It uses quasi-static models of all the components, therefore, it lacks the capability for analyzing the dynamic behavior of components locally and of the complete vehicle in general. It is therefore unable to predict phenomena inherent in the components such as mechanical vibrations, oscillating currents and voltages, and other similar crucial dynamic behavior.

The current work uses forward facing modelling, which is free from the above mentioned limitations. In forward facing models, energy flows from source to sink and it is known beforehand as an input. It is tracked downstream through various stages with known parameters starting from the battery or the engine to the electronic switches and finally to the wheels. In the forward facing approach, required demands for torque, voltages and currents are compared with actual variables of the system and with the help of controllers, these errors between them are minimized to achieve desirable performance [10]. The forward facing approach, having access to the internal variables of the system, is very much suitable for hardware development and detailed

simulation. Forward facing approach allows more accurate representation of the system dynamics and control strategy, which is an important consideration in complex power system and energy storage system interactions [10].

Argonne National Laboratory - USA has developed the Powertrain System Analysis Toolkit (PSAT) under the direction of Ford, General Motors and Daimler Chrysler [12]. This forward-looking model simulates vehicle fuel economy, emissions and performance. PSAT can simulate an unrivalled number of predefined configurations (conventional, electric, fuel cell, series hybrid, parallel hybrid and power split hybrid) [13]. Like most other HEV simulation tools, PSAT also uses MATLAB/SIMULINK as a fundamental platform for conducting module based development of the powertrain. PSAT is very user friendly and very good for performing fast and simple simulations useful in comparing many powertrain structures. The best advantage of PSAT is that it offers multiple models for single components depending on the level of sophistication desired. With continuous development by dedicated developers, this tool is now integrated with high fidelity models for certain components such as coupled thermal-electrochemical battery models and crank-angle resolved diesel engine models [13]. This tool is ranked among the 100 best newly available technological products for the industry.

Software SimPowerSystems and Simscape (Simulink toolbox for Physical Modeling) work together with Simulink to model electrical, mechanical, and control systems. SimPowerSystems has good models of electric machines. PMSM motor, three-phase inverter, and three-phase diode rectifier models are provided with the SimPowerSystems library. The speed controller, braking chopper, and vector controller models are specifically designed to operate different motor drives [14].

Simscape extends the Simulink product line with tools for modelling and simulating multi-domain physical systems, such as those with mechanical, hydraulic, and electrical components. Unlike other Simulink blocks, which represent mathematical operations or operate on signals, Simscape blocks represent physical components or

relationships directly. With Simscape blocks, one builds a system model just as one would assemble a physical system. This approach lets one describe the physical structure of a system rather than the underlying mathematics. From a model which closely resembles a schematic, Simscape technology automatically constructs equations that characterize the behavior of the system. These equations are integrated with the rest of the Simulink model [14]. Simscape serves as the platform for the following vertical products of the Physical Modelling family:

1. SimHydraulics, for modelling and simulating hydraulic systems
2. SimDriveline, for modelling and simulating powertrain systems
3. SimMechanics, for modelling and simulating general mechanical systems
4. SimElectronics, for modelling and simulating electromechanical and electronic systems

Components available in SimDriveline provide engine models that use programmed relationships between torque and speed, modulated by the throttle signal. At best these models represent steady-state relations of parameters.

Modelica is an object oriented language for physical system modelling, freely available and developed by Modelica Association. It is used for modelling complex dynamic behaviour of mechanical, electrical, fluid, hydraulic and thermal systems. Standard differential, algebraic and discrete equations are used to describe the system dynamics under modelling. Different components used for modelling are presented in the form of objects (icons) and connections between different objects represent actual physical coupling such as flow of fluid, heat and electricity. Modelica contains library of vast number of components for analog electric and electronics, digital electronics, electrical machines, vehicle dynamics, and control blocks etc. Modelica is designed such that specialized algorithms can be utilized to enable efficient handling of large models having more than one hundred thousand equations. Modelica is suited and used

for hardware-in-the-loop simulations and for embedded control systems [15]. This tool also have some limitations such as there are no provisions for solving partial differential equations (such as no FEM (finite element method) and no CFD (computational fluid dynamics)). There is a very limited support for external functions, only external C functions with scalar inputs and outputs are supported [16]. Inspite of some limitations this tool is very good to be used in industry due to its flexibility, dynamic simulation capability and free availability. There are many commercially available tools which include Modelica as base language such as CATIA Systems, Dymola, LMS Imagine and Lab AMESim, MapleSim, MathModelica and SimulationX. Dymola is perhaps the most representative Modelica-based language at this moment, which utilizes all the above mentioned capabilities of Modelica and simultaneously integrates its unique features and powerful graphical user interface to it [17, 18].

AVL's CRUISE [19] is a forward facing commercial powertrain simulation software developed by company named AVL in association with BMW, VW, and Daimler. An object oriented modelling approach has been adopted for CRUISE, as evidenced by the use of Simscape, to reflect physical counterparts of a vehicle in a powertrain model. It has advanced features for engine modelling and data management. The combustion engine is modeled by means of characteristic curves and maps. CRUISE can be easily linked to other simulation tools such as AVL BOOST (engine thermodynamics, exhaust aftertreatment), AVL DRIVE (drivability assessment), MATLAB/SIMULINK (control systems), FLOWMASTER (fluid cycle simulation), KULI (fluid cycle simulation), AVL InMotion (HiL system, testbed integration, vehicle dynamics, handling) and IPG CarMaker (HiL system, vehicle dynamics, handling). Out of many described above, one of the most important tools is AVL BOOST. AVL BOOST is an advanced and fully integrated “Virtual Engine Simulation Tool” with advanced models for accurately predicting engine performance, acoustics, and the effectiveness of exhaust gas after treatment devices. Most of the electrical and mechanical components such as the motor, generator, battery and engine are modeled by using characteristic maps and charts.

There are separate characteristic maps for each mode of operations. The basic model of a battery in CRUISE consists of a voltage source and an ohmic resistance. Internal resistance is defined either as a constant value or as a temperature dependent function. The interface of MATLAB/SIMULINK is used for the integration of controllers and/or mechanical elements into the computational model of CRUISE which can call models created and parameterized under SIMULINK. However, although AVL-CRUISE has advanced features for engine modelling, it lacks the capability of transient response and accurate dynamics for the overall system.

Most of the simulators summarized above are based on the MATLAB/SIMULINK platform in their implementation. The main aim for these simulators is to help identify design parameters for a vehicle which can satisfy certain standards of performance in terms of emission limits set by the government, fuel economy and so on. Simulations are made user friendly and computationally fast due to the use of charts and maps. Interpolation and extrapolation of charts are very common throughout the simulations. At many places, simple empirical relationships are used to further simplify the modelling and simulation. For design optimization, efficiency maps are used very heavily. Design parameters for every component are based on the power balance in quasi-static operation. With increasing demands for simulators by the automotive industry, some of the above mentioned tools are now evolving and becoming more sophisticated, transient and realistic. The research work presented in this thesis is an attempt to further extend this trend in the same positive direction with some novel contributions.

The powertrain is an important part of any motorized vehicle. It is a group of different components which together generate and deliver power to the wheels to move the vehicle at the desired speed. Mainly there are two categories of powertrain structures, namely, series hybrid and parallel hybrid powertrain configurations [20]. To get the benefit of both series and parallel hybrid powertrains, a third category of powertrain, namely, series-parallel or split hybrid powertrain has been devised. The

next section describes the details of all three powertrain structures.

2.2 Types of Hybrid Powertrain

IC engine based vehicles have a very high energy density power source, which can be refueled with liquid fuel in a short time. However, in these vehicles, the engine often operates very inefficiently (especially during low torque and low speed) wasting significant amount of energy in the form of different kinds of unavoidable losses and dangerous emissions. EVs have very little loss while operating in any range of speed and torque (except during hard acceleration when current drawn from the battery is very high) but use a low energy density power source, the battery, which further takes a long time to recharge. Therefore both types of vehicle have some advantages and disadvantages. In an HEV, by inclusion of both an IC engine and battery in the same powertrain, the advantages are integrated and the disadvantages are compensated with mutual help.

The three categories of powertrain structures in the HEVs are described next.

2.2.1 Series hybrid powertrain

In the series hybrid powertrain, power flowing from power sources (i.e., IC-engine and battery) to the wheels follows a series path. Figure 2.1 presents a schematic diagram of the series hybrid powertrain architecture. There is a powerful traction motor which is directly connected to the transmission and it receives power from the DC-link, which is fed by one of the two power sources, generator or battery. The generator is powered by a relatively small IC-engine. The components of the powertrain have their own individual controllers to operate in the desired ways. PWM based AC/DC, DC/AC and DC/DC converters are typically used to control the motor supply. When required, the engine-generator set can also recharge the battery. When the vehicle is

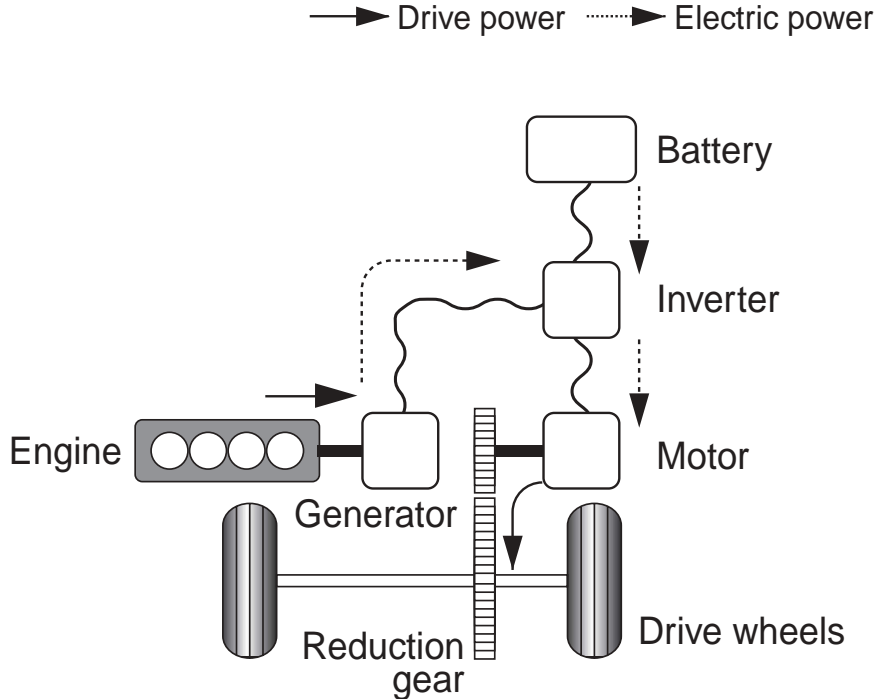


Figure 2.1: Schematic diagram of the Series Hybrid Electric Vehicle [21]

idle or moving at low speeds, the traction motor is powered by the battery and at higher speeds, it is powered by the generator. This can decrease the overall fuel consumption. In series powertrain, a clutch is not needed because the motor shaft can be attached to the wheels via fixed ratio gears or CVT transmission.

2.2.2 Parallel hybrid powertrain

In the parallel hybrid powertrain, both the IC-engine and the motor are attached to the transmission. In this architecture, the wheels can be powered by the motor and the IC-engine simultaneously [22]. The overall power flow, from the power sources (IC-engine and battery) to the wheels, follows a parallel path. The benefit of this architecture is that the size of the motor can be reduced [23] and there is no need to use a generator to run the vehicle. However, the main drawback of this architecture is that the battery can only be charged by regenerative braking with motor operating as the generator. Potentially, this structure can be very economical in terms of powertrain weight and size. However, in this structure, clutches and gears are needed to engage

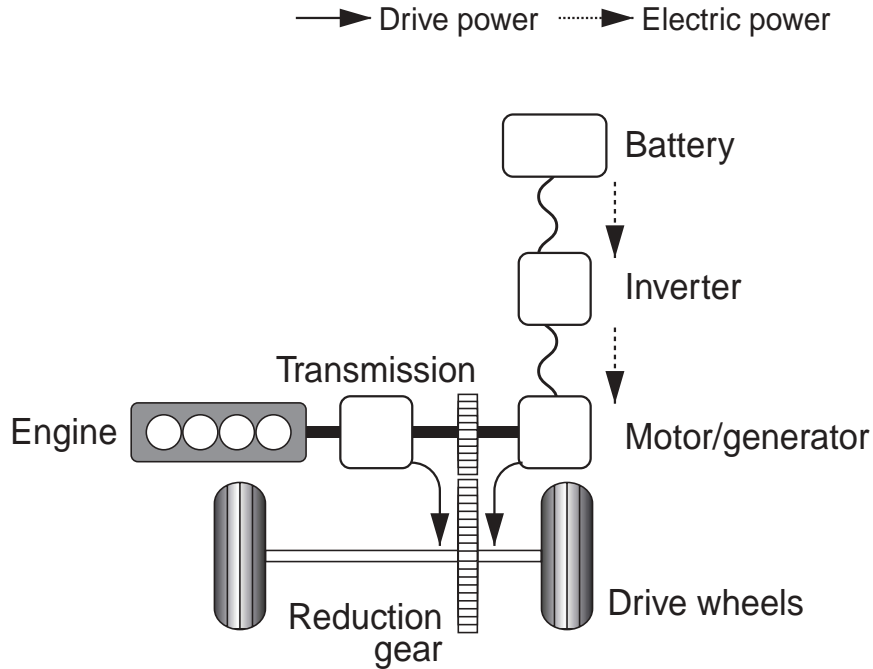


Figure 2.2: Schematic diagram of the Parallel Hybrid Electric Vehicle [21]

and disengage the engine from the wheels. Figure 2.2 presents a schematic architecture of the parallel hybrid powertrain.

2.2.3 Series-parallel hybrid powertrain

Series and parallel hybrid powertrains have advantages and disadvantages as described above, the series-parallel hybrid powertrain combines the benefits of both these architectures. In the series-parallel architecture, powertrain has two electric machines, where one acts as a motor to drive the wheels and the other acts as a generator to charge the battery and start the engine. There is a power splitting device which decides the optimal power distribution for all the power sources so that the efficiency is highest at all times. Figure 2.3 presents a schematic architecture of the series-parallel hybrid powertrain also known as power-split hybrid powertrain.

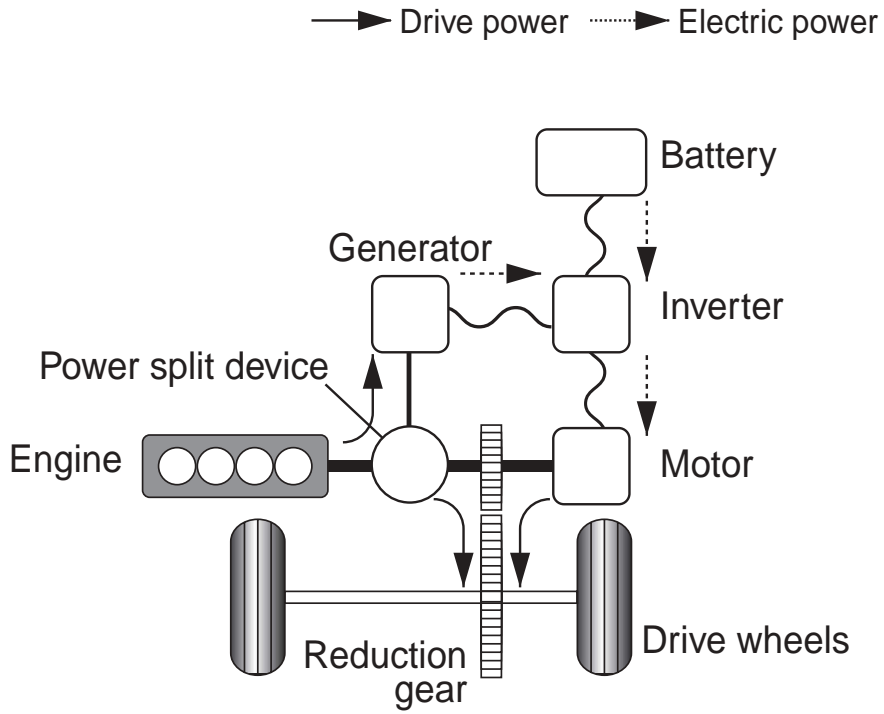


Figure 2.3: Schematic diagram of the Series-Parallel Hybrid Electric Vehicle [21]

2.3 Advantages and disadvantages of using series hybrid powertrain

In a series hybrid vehicle, the following advantages are apparent. The engine is not mechanically connected to the wheels, but instead it is connected to the PMSG. Therefore, the engine is not directly facing the heavy transients during driving. Emissions and fuel consumption during transient driving conditions are very high in comparison to normal steady state conditions [24]. In a series hybrid powertrain, the engine can safely run in the most optimal operating region all the time according to the need of the driving conditions and demands. Emissions can further be reduced by designing suitable control architecture for engine operation in a very narrow zone due to decoupling from the transmission. Since the traction motor is driving the wheels, the transmission is greatly simplified given the absence of clutches and complicated multi-gear systems. As the motor can start both, itself and the vehicle, from zero speed due to the ideal torque-speed curve, driving is very efficient at lower speeds with the

help of traction motor [2].

The series configuration has disadvantages during highway driving (long range driving at high speeds on freeways) because of multiple energy conversion stages (i.e., from chemical to mechanical to electrical and then again to mechanical). However, it is effective for city driving because most of the time the vehicle can run in pure electric mode and can be powered by the engine only during cruising and higher power demands. The series architecture can be further advantageous if the efficiencies of the components are improved such that the conversion losses are minimized [25].

The series hybrid architecture can be further divided in two categories depending on the capacity of the energy storage elements involved in the powertrain. If the energy storage element is of lower energy capacity such as the ultra-capacitor, then the IC-engine will be the prime mover and energy storage elements will only supply deficit energy during transient operation. Such architecture results in mild hybridization. If the energy storage element has high energy capacity like a battery, then most of the low-speed driving can be done in electric mode and the IC engine will work only as a range extender [25]. The main aim of the present work is to capture the dynamic response of all the components involved in the powertrain of the HEV. The modelling methodology presented in this work is general enough to be applied on any kind of powertrain structure and series hybrid structure is chosen just to demonstrate its modelling and simulating capabilities.

2.4 Components of the HEV Powertrain

The present work is mainly concerned with dynamic modelling of the overall powertrain by integrating dynamic models of all the components. Analysis of energy losses, fuel consumption, efficiency and performance with steady state models has already been published in the literature, so the present work will present similar kinds of analysis using dynamic modelling in coming chapters. The aim is to model the transient

response of the system while preserving the simplicity and feasibility of simulation in an acceptable time domain. Figure 2.4 illustrates the high level architecture of a typical series hybrid powertrain.

A series hybrid powertrain presented in this work has the following components:

1. Car model
 - (a) Vehicle dynamics
 - (b) Aerodynamic behavior
 - (c) Tyres
 - (d) Suspension
 - (e) Powertrain transmission
2. Motor
3. Generator
4. Engine
5. Battery
6. Regenerative braking
7. Supervisory control
8. Driver model

Thin lines in Figure 2.4 represent electrical coupling or electrical energy or electrical data flow, whereas thick lines represent mechanical coupling or mechanical energy flow. Details of each and every component with their respective control mechanisms in this powertrain will be given in the following chapters of this thesis.

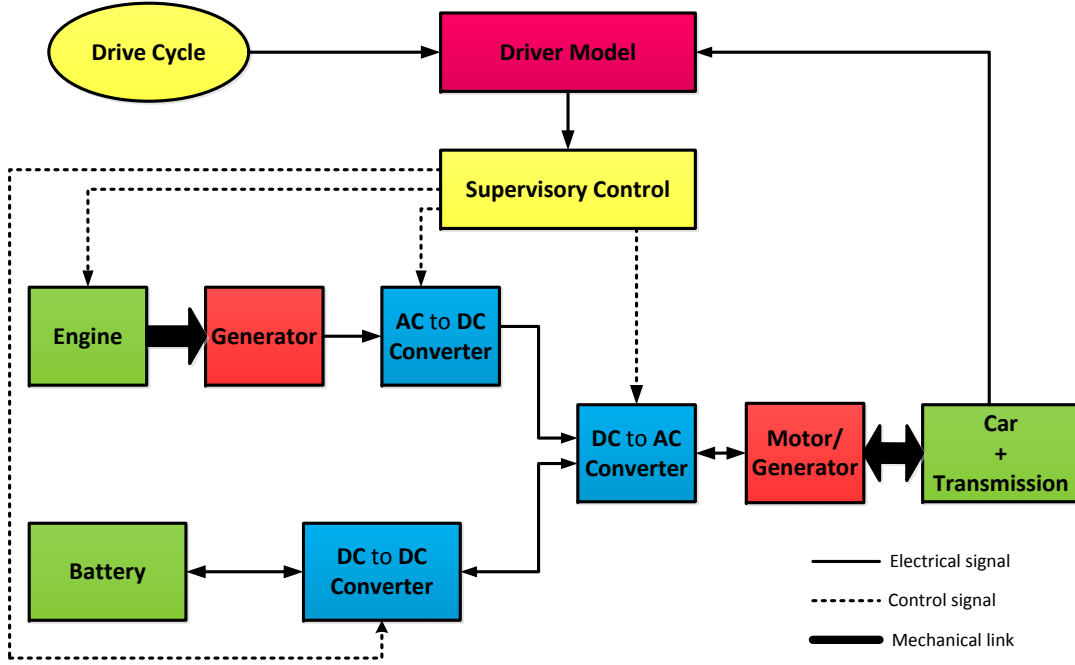


Figure 2.4: Complete structure of series hybrid vehicle powertrain

2.4.1 Car model

Vehicle dynamics plays an important role in determining the performance of the vehicle. Most of the time, vehicle dynamics is modeled using simple estimation of tractive power against predefined conditions [26]. This tractive power is calculated as the sum of power, required to overcome rolling resistance, aerodynamic drag, compensating weight component while climbing slopes and vehicular acceleration. These kind of vehicular dynamic based models are single body and mostly without involvement of components such as tyres and suspension. Tractive force (can be calculated in the form of torque as well) works as load for the traction motor, so essentially there is no real model of the vehicle [25, 27, 28].

A detailed multibody model of the longitudinal car can be used to capture all kinds of losses such as lift, drag, tyre damping, tyre slip, etc. A detailed description of longitudinal car dynamics has been given in [29, 30] by using multibody modelling software called VehicleSim®, formerly called AutoSim [31]. The main body of the car is included as the parent body and all other constituent bodies such as the front hub

career and rear hub career are directly attached to it at respective common points with one degree of freedom in the vertical direction. Spinning wheels are attached to their hub careers with equivalent inertias. The model described in [29, 30, 32] is built for general purpose motion, but this general model can be simplified for only longitudinal motion as desired by the standard drive cycles such as the NEDC. Traction forces are friction forces between the tyre and ground and they are described by standard magic formulae [33] in this work. The magic formulae used in this work is not a solution to any kind of dynamic equation of motion rather its just a convenient fitting of mathematical functions to empirical data. It allows one to compute forces involved in interaction of a tyre and rough surface at a higher precision. Aerodynamic lift and drag forces are further calculated to describe vehicle dynamics and respective losses in driving.

2.4.2 Motor / Generator & power converters

In the series hybrid electric vehicle, wheels are directly driven by the powerful traction motor and power is supplied by the IC engine or battery. There are many kinds of motors available in the industry designed specifically for different purposes. Motors required for EVs and HEVs face different kind of challenges than the ones used in other industries (for example, to run heavy rolling machines in the manufacturing industries which mostly operate in steady state). Motors used in the HEV powertrain have to go through sudden start on-off, heavy acceleration and deceleration, very wide operating speed, and torque range. DC motors are simple in construction and easy to control but suffer from high maintenance costs due to existence of mechanical commutators. With advancing technology, commutator-less motors are becoming more and more accepted in the industry.

The induction motor is one such electrical machine with cheaper production cost coupled with robust and maintenance free operation [34]. There are several serious suggestions where an induction motor can be used in the powertrain of HEVs [35–39]. However, the biggest problem with the induction motors comes from the requirement

of complicated control techniques due to their non-linear time variable system response. Control techniques such as variable-voltage variable-frequency dependent on slip speed does not provide the desired performance. Although field oriented control (FOC) [40–42] and direct torque control [43–45] techniques are proposed, they also suffer from poor transient response and sensitivity to the system parameter variations and insensitivity to the variations in the reference values respectively [34, 46]. There are several commercial automobiles in the market with induction motors such as the Renault/Kangoo, Chevrolet/Silverado and DaimlerChrysler/Durango etc. However, now industry has largely adopted permanent magnet synchronous motors having all the benefits of DC machines and induction machines but no drawbacks of either of these in terms of dynamics and control. PMSM machines require expensive sensors for direct rotor position detection (or some indirect way to estimate rotor position). But, there are many other high performance drives which utilize position feedback, so this can not be necessarily considered as a disadvantage [47]. High speed operation creates problems to both induction machines and PMSMs because the control of induction machines becomes very difficult at higher speeds and the generation of large eddy currents in the PMSM is a serious problem. Continuous operation of PMSM machines in the field weakening region can demagnetize the permanent magnets. Another problem for PMSMs is cogging torque, which is produced due to the interaction of rotor magnets and stator slots and it is undesirable for PMSMs. Cogging torque become seriously problematic at low speed, but can be minimized either by appropriate design of the machine or by electronic mitigations [47]. The availability of newer and cheaper material for making magnets and emergence for betters electronic controllers enhancing the possibilities for using PMSM machines in HEVs. Growing numbers of commercially available automobiles using permanent magnet synchronous motors such as Nissan/Tino, Honda/Insight and Toyota/Prius etc. are boosting the research on PMSM machines [48].

Permanent magnet synchronous machines are the most adequate to be used in the HEV powertrain due to good dynamic performance, high energy density, low weight

and low cost of maintenance [23, 49, 50]. Mathematical models for the PMSM and the PMSG can be described by using the standard $d - q$ frame equations as in [51–54] and [55, 56] respectively. Direct torque control (DTC) [57–59] and field oriented control (FOC) [60–63] are two most prominent methods used in designing speed control drives for the PMSM [64]. Field oriented control method (i.e. vector control method) has been described as the most effective technique for the adjustable speed PMSM drive [65, 66]; the same strategy can be used for the PMSG drive as well.

Electronic controllers play a very important role in the operation of the HEV powertrain. Basically there are three stages or segments of electronic controller - sensor, interface circuitry and processor. Sensors are used to measure the physical state variables of the machine. With the help of interface circuitry, these variables are amplified and sent to the processor (at this stage signals are conditioned and processed such pulse-width modulation) so that they can be fed further to the power converters of the overall drives. The power converters are semiconductor devices which are responsible for feeding the required voltage and currents to the electrical machines, so that desired performance can be achieved [2]. According to the series hybrid architecture, there is a DC-link, which supplies the power to the motor from the inverter and this DC-link is directly connected to the PMSG through the rectifier and to the battery through the bidirectional DC/DC converter. Average models for the AC/DC converter (rectifier) [67, 68] and the bi-directional DC/AC converter (inverter) are described in the $d - q$ frame for integration with the PMSM and PMSG models, respectively [69, 70].

2.4.3 Turbocharged diesel engine

In the series hybrid electric vehicle, the internal combustion engine can be used as a range extender or prime power source. Compression ignition engines have many advantages over spark ignition engines in terms of overall efficiency and control [24, 71, 72]. Therefore, a diesel engine is chosen in this work and its modelling as

appearing in the literature is reviewed in this section.

Most of the hybrid vehicle modelling tools, such as ADVISOR, present the engine just as an efficiency map without any internal dynamics [73]. Such kind of efficiency map based engine model cannot give accurate results in transient operating conditions. For instance, during acceleration of the vehicle, the demanded DC-link current has heavy transients which get translated into demanded engine torque. If the engine is not modeled accurately to respond to such transients in torque demand, the overall prediction of the behavior will not be correct. Also the steady-state models can not predict many of the internal variables of the engine [74]. Some neural network based modelling and control techniques are also presented in the literature but they lack any information of the internal dynamics of the system [75–77]. Moreover, these models require huge data and time for training the neurons and experimental calibrations for different engine operating environments. These repeated calibrations are very expensive, so physics based models are preferable. There are other kind of models such as combined model of diesel engine in association with generator [78] and polynomial based non-linear models of the diesel engine [79]. However, these models suffer from the same limitations described earlier.

Increasingly stringent laws are forcing newer and better control and design of the engine, such that the fuel consumption and emissions can be reduced. Contrary to the heavy machinery industry, an engine used in automobiles faces heavy and sudden transients, where both the emissions and fuel consumptions are critical to comply with the defined limits. Nowadays, different drive cycles are designed to test the engine performance, not only for the steady state but transient performance as well [80]. When the engine is operated in transient conditions, the turbocharger does not respond adequately to meet the air demand while fuel is injected rapidly to meet the transient torque demands. Since there is insufficient air to burn all the fuel, such transient operations come with emissions of soot (also known as PM - Particulate Matters) [81,82]. Access to internal variables of the engine is mandatory to understand

the real behavior of the engine and implement suitable controls for reducing emissions. Accurate modelling of the fuel path and air-flow path gives detailed dynamics of the engine.

There are mainly two approaches towards engine modelling, thermodynamics analysis based modelling [83] and fluid dynamics analysis based modelling [82, 84, 85]. These modelling approaches are categorized based on the equations and relations used to develop the complete model. For instance, thermodynamic models and fluid dynamic models depend on mass and energy conservation, and fluid flow analysis, respectively [80, 86]. But there are also some other modelling techniques which use combination of these two methods in different degrees according to specific usage of the model.

The level of model complexity is an important factor in deciding the approach to be chosen for modelling. Black box models and map based models are the simplest ones because output variables are associated with the input using some empirical relationship [81]. Due to such simple relationships, models are very fast in simulation environments but these models can not be used for any kind of useful control design. Models based on fluid dynamics and thermodynamics are divided in several control volumes based sub-models which leads to distributed modelling. These types of models are very detailed in nature and computationally expensive. So a mixed modelling approach has been adopted where some of the components are modeled from basic physics and some are modeled with empirical equations. These empirical equations are derived from quasi-stationary or mean-value data of the process such as air-flow inside the turbochargers.

It has been already established that mixed modelling approach is best for a system which involves many complex processes; a turbocharged diesel engine is an example of such a system. Map based models lack overall system dynamics, therefore accounting for transient response is the motivation. While building a detailed control oriented dynamic model of the turbocharged diesel engine, simplicity and accuracy

of the predictions must be preserved. A Turbocharged diesel engine involves inlet manifold, exhaust manifold, engine cylinder, intercooler, EGR and turbocharger as the main components. Inlet and exhaust manifolds can be modeled with the filling and emptying method [87], engine cylinder dynamics with the pump model [87], and flow characteristics of the compressor and turbine with a mean value model [88–91]. Thermodynamics and fluid flow equations are used to describe state variables of the system, such as pressure, temperature and mass flow inside the control volumes [84]. Inclusion of inertia of the engine and turbo-shaft along with other differential equations in the model helps to capture realistic transient performance of the turbocharged diesel engine. Usually, calibration factors are necessary to compensate all the uncertainties involved in the experimental measurement of system parameters such as engine inertia, manifold volumes and EGR data [87].

There are various kinds of control objectives depending on the modes of operation and types of engine. SI engines operate with almost fixed air-fuel ratio (λ), whereas, in a diesel engine torque and speed vary with the amount of fuel burned. To design the control for a diesel engine, there are two control variables, the amount of fuel to be burned and the timings of fuel injections [92]. Generally in a mean value model, the fuel injection (amount of fuel to be burned) control strategy is employed to control the speed and torque generation of the diesel engine. General theories for different components of the turbocharged diesel engine model are already well established in the existing literature [72, 88, 89, 93–98]. These theories can be utilized to design an overall control oriented diesel engine model which can be directly used in the Matlab/Simulink based HEV powertrain simulation.

2.4.4 Battery & DC/DC converter

Limitations of battery power is one of the most critical factors for the complete electric vehicle. Due to the very low power density of the battery, an IC engine or some other power sources are used in conjunction for on-board driving as a range extender or

prime power source in HEVs. The invention of the rechargeable lead-acid battery goes back to 1859 [99] and from that time, many different materials have been tried but no significant breakthrough achieved. Among many materials, the Li-ion based batteries have the highest energy density, and therefore research is underway to make batteries of this technology more competitive with the IC engine in terms of energy density.

In the literature reviewed, numerous battery models are proposed with different degrees of complexity and details to capture real-time behavior of the battery. Often these models do not represent the complete dynamics of the battery which is very common in mathematical modelling of electrochemical systems. In general terms, battery models can be categorized as electrochemical [100, 101], equivalent circuit [102, 103], fractional discharge [104], dynamic lumped parameter [105, 106], hydrodynamic and finite element [107] models, etc. Most of the models either exclusively follow one of the above mentioned categories or a combination of more than two of these modelling approaches.

All the proposed battery models to be used in HEVs are broadly categorized in three categories namely, electrochemical dynamics based models, experimental data based models and electrical circuits based models [108]. The electrochemical model proposed by Smith in [106] solves six coupled partial differential equations related to concentration of charge and species, overpotential and terminal potential. These differential equations are formed by using the Butler-Volmer kinetic equation, which is the basis of many electrochemical models. The objective of this model is to analyze the internal dynamics of the Li-ion based batteries when they are used in HEVs, where short bursts of current pulses are either drawn from the battery while accelerating or sent back to the battery while regenerating. Such models are also known as 1d electrochemical lumped thermal models [109]. In [109] C++ code has been developed which is general enough to simulate any other lithium battery cell by solely changing electrochemical parameters used in the battery model. However, this model was found to be extremely computationally expensive for the Simulink platform

based simulation in conjunction with other components. Experimental charts (data) based models are very specific to particular battery types and are seriously limited in their functional adaptability to general operating conditions other than ones for which they are experimentally calibrated. Electrical model based circuits have one attractive characteristic in comparison to all other models - the battery states are presented in terms of electrical quantities such as terminal voltage, state of charge (SOC) and internal impedance. Given the above mentioned considerations, the electrical circuit based battery model was chosen for this research work.

There are mainly four types of electrical circuit based battery models, which are included in the ADVISOR library as well. All these models are Matlab/Simulink dependent programs as summarized in [110]. These models are based on the different arrangement of resistive and parasitic elements in series or in parallel with a constant DC voltage source such as the RC model and internal resistance model [111]. There are two more models - the fundamental lead acid and neural network models. Most of these models work fine as long as the operation of the battery lies in the steady state. But when the current is subjected to dynamic changes, the results are not very accurate and sometime unacceptable. The generic dynamic Li-ion model described in [112] has been chosen and experimented with in this research. This model is included in the Simulink library as well [113].

Powering the vehicle with batteries has the benefits of recapturing the braking energy loss along with zero emissions. Recapturing the braking energy requires bidirectional DC/DC converters. Availability of high energy MOSFET and IGBT at higher frequencies have improved the speed and efficiency of electronic switches. Due to the involvement of isolation ac current and voltage in the working of isolated DC-DC converters, simple state space based averaging techniques are difficult to apply. Therefore, a switching frequency dependent average model is developed for soft switch DC-DC converters [114,115]. This model is simulated in Simulink and it's experimental validation is presented in [116].

2.4.5 Regenerative Braking

There are three kinds of braking for any rotating electrical machine, namely, mechanical, dynamic and regenerative. Regenerative braking is a mechanism used in modern hybrid and electric vehicles to save and store that energy, which will otherwise get wasted in the form of heat by mechanical braking. In traditional vehicles, when brakes are applied to stop the vehicle brake pads rub against the rotating wheels. Due to friction between brake pads and wheels, a counter torque is generated, which eventually stops the vehicle with significant heat generation [117].

In regenerative brakes, the traction motor reverses its function which acts as a generator by applying negative torque on the motor shaft. This negative torque slows down the rotating motor shaft which is connected to the wheels of the vehicle and recaptures the available kinetic energy of the load by recharging the battery with regenerated current [117]. Eventually, the vehicle will stop with no or very little generation of heat along with a recharged battery level.

In the case of dynamic braking, the torque angle is adjusted in such a way that the direction of electromagnetic torque is reversed but the direction of current is not reversed. In this case, the PMSM works as a generator by converting the kinetic energy of the rotating load into electrical energy and simultaneously taking energy from the DC link to generate negative electromagnetic torque to decelerate the rotating rotor. Eventually energy flows from both the DC-link and the rotating load to the windings of the PMSM and there, it is wasted in the form of heat. Sometimes a special and extra circuit is designed to waste the excess energy in the form of heat. Due to the involvement of huge energy, the rate of declaration is very high in the case of dynamic braking. However, due to the generation of a lot of heat in the PMSM windings, this way of braking is not very safe and it is avoided most of the times. This kind of braking is used only in the machines where the necessary brake circuit is designed for this purpose.

2.4.6 Driver

A Driver Model in forward facing modelling approach simulates the behavior of a human driver or automatic driving controller. A driver decides whether to brake or accelerate the vehicle in order to follow the desired drive cycle closely. It is essentially a tracking controller which takes the drive cycle or speed profile as input and generates the output in terms of throttle and brake commands to track the trajectory. In the literature, many types of driver models are investigated, starting from simple PI controllers to advanced optimal control based models. Different models are motivated by different objectives such as analyzing interactions of the human driver with the vehicle in different operating conditions like cornering and rollover [118]. With an increasing understanding of human psychology, mimicking the human response under different emotional conditions is also considered [119]. Minimizing chances of accidents and ensuring good safety measures by assisting the human driver in the decision making process are some of the prime concerns in such modelling techniques. Such models can also investigate driver performance under the condition of intoxication and tiredness. Most of these driver models simulate steering actions in the vehicle with lateral motion capabilities along with the use of preview information [29].

Since driver models are approximated as an optimal solution for performance based cost functions [118], it becomes difficult and complex to use them in online driving conditions where preview of the drive cycle is not available. Moreover, in the present work, only longitudinal motion of the vehicle is investigated, so a simple PID controller based model will suffice for the simulation. It has been found during simulations that tracking results are very good and acceptable in the standard domain of performance. A standard NEDC cycle [6] is used in this work for validating the tracking capability of the driver model.

2.4.7 Supervisory Control

A hybrid powertrain is a complex combination of electrical, mechanical and electrochemical components in the same drivetrain. Proper operation of all the components in a coordinated way requires an overall controller named as supervisory controller. There are basically two kinds of controllers involved in the operation of HEVs. Every component in the drivetrain requires an individual controller to function properly and to get integrated with the rest of the drivetrain. These component controllers receive control inputs from the supervisory controller to decide their operating regions.

Improvement in the fuel economy and emissions of HEVs strongly depends on energy management strategies. The supervisory controller regulates the power flow in the complete drive train from energy sources to energy sinks. Generally, the supervisory controller takes the input in the form of vehicle operating conditions such as required speed, present state of charge of the battery (SOC), and required torque to track the speed profile provided by the driver model. These inputs are processed to generate instructions in the form of switching the specific components OFF and ON or to modify their operating regions by commanding the local component controllers. For example, the IC engine can be commanded to recharge the battery also, while powering the traction motor for the drive. The main tasks of the control strategies are meeting the driver's demand for traction power, avoiding the charging and discharging of the battery above or below certain threshold levels and optimizing the drive train efficiency, fuel consumption, emissions, etc.

Supervisory control strategies can be classified in various ways depending on the parameters chosen. Guzzella [120] has given two different ways on which basis controllers can be divided. Firstly, based on the their knowledge of future driving conditions, and secondly based on heuristic, optimal and suboptimal controllers. Any supervisory controller which requires knowledge of future driving conditions in any form can be classified further as causal and non-causal. All the heuristic supervisory

controllers fall in the category of causal controllers whereas optimal supervisory controllers fall in the category of non-causal controllers. Suboptimal controllers are mainly causal but sometimes fall in the non-causal category as well.

Supervisory control strategies aim to solve the problem of power distribution between different power sources. There are many supervisory control techniques proposed in the literature and experimented for online implementations. Supervisory control strategies can be classified in two main categories, rule based supervisory control and optimization based supervisory control [5, 111, 121–136]. Rule based supervisory control strategy is further divided into several subcategories such as powertrain state variable based supervisory control [10, 137–142], power follower supervisory control [137, 143–148] and fuzzy rule based supervisory control [149].

Rule based supervisory control strategy is also known as thermostat control strategy. In most of the cases, rule based strategies are used as online supervisory controllers because they mainly consider the power ratings and higher efficiency regions for operation of the power components. These heuristics or rule based control strategies are found to be more robust and computationally efficient than optimization based power split control strategies [150]. Most of the state of the art supervisory controllers used in mass production vehicles are heuristic in nature [120]. However, the main drawback is that these strategies may lead to suboptimal solutions [125].

To get an optimal solution, many optimization based control strategies are proposed in the literature. Optimization based strategies can be categorized in two ways - on the basis of the nature of optimization and on the basis of the methods used in solving the optimization problem. The nature of optimization can be of two types - instantaneous power split optimization and global power split optimization. Instantaneous optimization based strategies focus on minimizing an objective based cost function which optimizes the power split at every instant of time finally giving a solution closer to global optimum [5, 125, 126, 151–153]. Global optimization based strategies require “a priori” information of the drive cycle leading to global optimal

solutions [128, 134–136, 154–158]. Some controllers are combination of optimization based control and neural network techniques [159]. In essence, in an optimization based control strategy, an objective function is framed and then that objective function is solved for optimal solutions. There are many solution strategies proposed in the literature to solve this objective function [160, 161]. Lorenzo Serrao [150] has proposed four classifications on the basis of the solution approach of an objective function, described below:

- Numerical methods for global optimization: These methods require “a priori” knowledge of complete drive cycle and dynamic programming [154, 162, 163], and genetic algorithms [128, 134–136, 155, 164] are used as numerical methods.
- Numerical methods for local optimization: The previous category of numerical optimization can only be applied to offline analysis. But in the present category of optimization, complete knowledge of the future driving cycle is not required. Rather, a rough estimation of the future driving cycle in the near future will suffice. This optimization technique can be applied for online analysis. Some of these methods are known as model predictive control [165–167] and stochastic dynamic programming [168–170].
- Analytical methods for optimization: In this approach, rather than using numerical methods to solve the objective function, a closed analytical solution is achieved which simplifies the overall computation [171, 172].
- Instantaneous minimization methods: As already described, in this technique, the objective function is solved for minimization at every instant of time rather than searching for a global optimum [5, 151, 152, 173].

Optimization based control strategies require complicated optimization techniques such as dynamic programming and genetic algorithms. Therefore, they cannot be used for online implementation but only for offline analysis. Moreover, resulting

solutions are very particular to a drive cycle, being unrobust and unsuitable for unknown speed profiles. A novel load follower supervisory control strategy (LFSCS) based on the power follower supervisory control strategy (PFSCS), with some important changes, is proposed in the present work. Development of optimization based supervisory control strategy for dynamic model presented in this work is under preparation [8].

2.4.8 Integration of the components

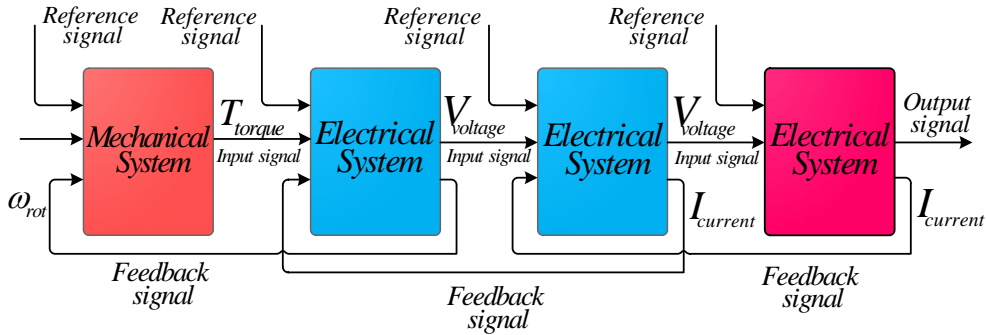


Figure 2.5: Interconnection concept among different mechanical and electrical subsystems

Figure 2.5 presents the interconnection rule followed unexceptionally in the present work for integrating different components of the powertrain. All the components are modeled in the multiport input and output format. Electrical components have input-output in the form of voltage and current. Similarly, mechanical components have input-output in the form of torque and speed (rotational or translational). Components are integrated together on the basis of exchange of compatible input and output. Electrical components are modeled on the concept of accepting voltage as input and generating current output. This current output becomes feedback input for the preceding electrical component. Voltage is a potential variable and current is a kinetic variable for the electrical system. Similarly, torque is a kinetic variable and rotational speed is a potential variable for the mechanical system. As already mentioned, the potential variable is used as input signal and the kinetic variable is used as feedback signal. However, in some cases these variables are interchangeable with one other or a combination of

both. Every component has two more variables, reference signal and control signal. Reference signals can be the reference driver speed profile, DC-Link voltage for PMSG, desired rotational speed for the IC engine, etc., as illustrated in Figure 2.5. Every component has few control signals as well, but they are part of the internal system dynamics and are not shown in Figure 2.5. Component-wise details of all signals and their integration will be presented in the following chapters of this thesis.

CHAPTER
THREE

CAR MODELLING

3.1 Introduction

Early vehicles were designed as a single box supported at the ends, much like horse driven carriages. Increasing load of the car had adverse effects on the performance of the vehicle such as beaming (vertical vibration). To get rid of such adverse effects, there was a need for improved structural designs. With further development of vehicle technologies, vehicle structure, transmission and powertrain components gradually evolved and improved. Now a normal car has distributed load between front and rear axles to compensate the beaming and similar affects [25]. There are many components involved in the overall design of the vehicle. Some components have translational motion, some have rotational motion and some have combination of both with respect to each other and the road. Therefore, to model vehicle response accurately especially during longitudinal motion, consideration of multibody dynamics is necessary.

3.2 Car

Accurate car response for our purpose requires accurate representation of longitudinal car behavior. The model employed, capable of general motions, describes the longitudinal car dynamics and is based on the multibody model presented in [29, 32]. The model of a passenger car is presented including sprung mass (its weight and dimen-

sions), unsprung mass hub-carriers, wheels and transmission. Models for suspension, tyre slip, aerodynamic drag and lift behavior are included for the purpose of analyzing transient behavior and various losses. The transmission system model includes the differential with fixed gear ratios or CVT between the motor and transmission shaft for different cases. The standard NEDC cycle is chosen for testing vehicle performance and quantification of different kinds of losses involved.

3.2.1 Vehicle dynamics

The longitudinal vehicle model used in the present work is described in Figure 3.1. Firstly, an inertial reference frame ‘n’ is chosen and a child body ‘S’ is attached to it with three degrees of freedom. The body ‘S’, shown in Figure 3.1, is the sprung mass which is the chassis of the longitudinal car with total mass M_s and rotational inertia I_{sy} around its center of mass.

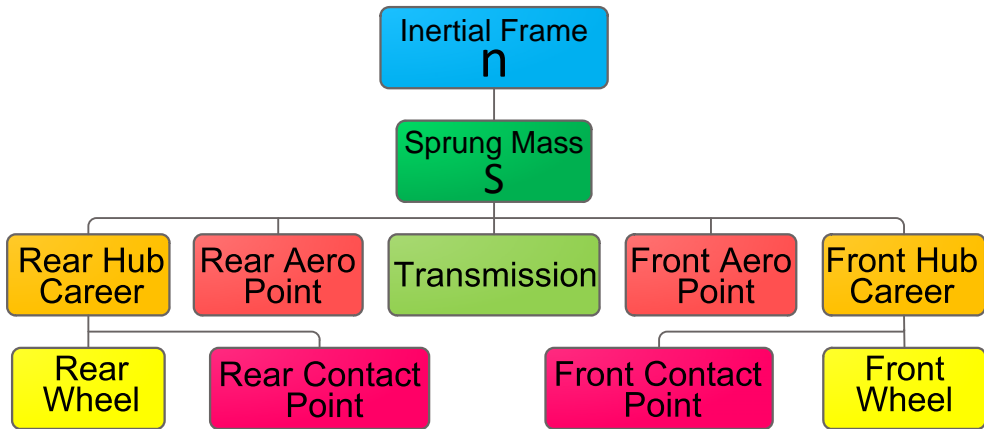


Figure 3.1: Tree structure of the bodies and contact points included in the modelling of the longitudinal vehicle in VehicleSim®

All other bodies in the vehicle are considered children bodies of the parent body ‘S’. The constituent masses are introduced in a tree structure with the help of common points. Masses and inertias, degrees of freedom, and forces between the constituent bodies and parent bodies are specified. Thus, the main body of the vehicle is allowed to have forward translation, vertical translation, and pitch rotation. Front and rear

hub carriers are attached to the sprung mass of the vehicle body with only vertical translational motion relative to it. Wheels are attached to the hub carriers with freedom to rotate around their rotational axis, with the vertical compliance of tyres governed by spring and damper systems. Only rotational inertias of the wheels are mentioned because the masses of the wheels are already included in the masses of hub careers.

The rear wheel is connected via a crown wheel and pinion, and a transmission to the motor shaft. In the present work only single motor is used to supply all the power to the transmission shaft. The wheel tyres interact with the ground through longitudinal friction forces and these are directly applied on the front and rear wheels. The tyre longitudinal force is generated from normal load and longitudinal slip using standard “magic formulae” [33]. The model employed also includes aerodynamic lift and drag forces, both proportional to the square of the car speed. In the present vehicle model rolling resistance is not considered. This is a strong assumption, because during urban drive cycle losses due to rolling resistance will be higher than drag resistance, but rolling resistance will be definitely included in this model in the future while upgrading this work to a more complete level.

A schematic free-body diagram of the car, Figure 3.2, represents different external forces and braking moments applied on the car. Drag force is applied at the center of mass of the mass of the car. L is the length between the center of the front and rear wheels. h is the height of the center of gravity of the car from the ground.

The parameter values used in the model are representative of a contemporary European family saloon and are taken from [29] and presented here in the form of Table (3.1).

The car model is written in LISP making use of the multibody modelling code VehicleSim®, formerly called AutoSim [31]. Already defined bodies with names, joint coordinates with parent, rotation axes, coordinates of center of mass, mass and inertia of bodies, line of action for torques and point of action for forces are included in the code enabling VehicleSim® to derive equations for relationships between the bodies.

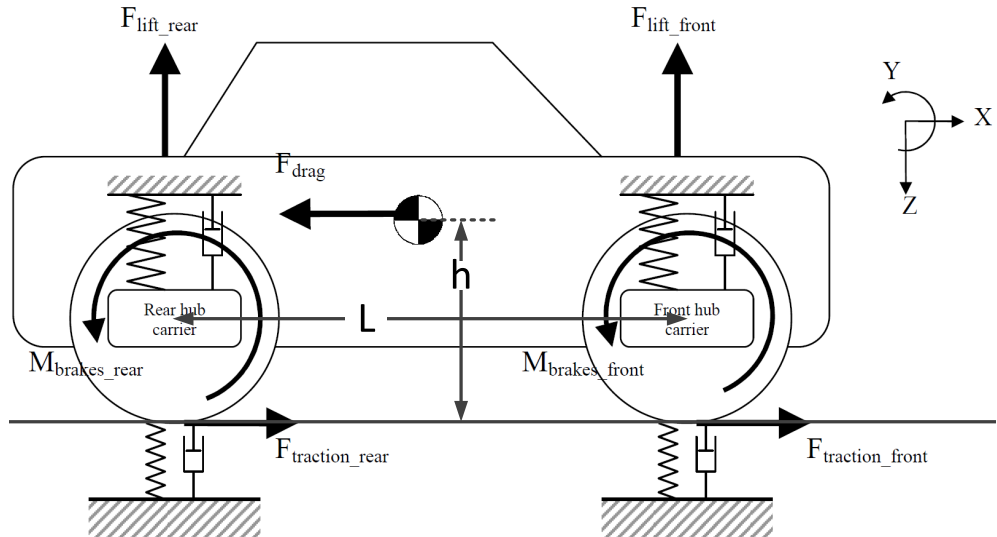


Figure 3.2: Vehicle rigid body diagram showing forces except gravity [174]

Parameter	Symbols	Value
Chassis		
Mass	M_s	1355.6Kg
Mass center	$(x_g = L, y_g, z_g = h)$	$(0.291, 0, -0.576)m$
Inertia	I_{sy}	$2152.1Kgm^2$
Hub carrier		
Mass	m_{hc}	60Kg
Inertia	I_{hy}	$0.1Kgm^2$
Road wheel (each)		
Radius	r_w	0.3m
Spin inertia	I_{wheel}	$0.653Kgm^2$
Aerodynamics		
Drag coefficient	C_d	$0.35Nkgms^2$
Lift coefficient	C_{lf}	$0.1Nkgms^2$
Lift coefficient	C_{lr}	$0.16Nkgms^2$
Cross-section	A	$2.0m^2$
Air density	ρ	$1.227kgm^3$
Stiffness		
Front suspension	k_{fsus}	$19480Nm$
Rear suspension	k_{rsus}	$16800Nm$
Tyre (each)	k_{tyr}	$180000Nm$
Damper coefficients		
Front suspension	c_{fsus}	$1500Nms$
Rear suspension	c_{rsus}	$1500Nms$
Tyre (each)	c_{tyr}	$800Nms$

Table 3.1: Parameter values of the longitudinal car

The equations of the motion for connected bodies derived by VehicleSim® are based on the Kane's equations [175]. The VehicleSim® model can be configured to generate C/C++ MEX code that numerically integrates the nonlinear equations of motion. This code can be compiled into an S-Function for integration with the Simulink model of the remaining powertrain.

3.2.2 Tyre model

Frictional interactions of the tyre and road generate the forces required for the longitudinal motion of the vehicle. This longitudinal force is compensated by traction force supplied by the PMSM installed in the powertrain. When the vehicle moves forward and the tyre touches the rough ground at the bottom most point, a normal force is generated between the tyre and ground as a result of this reaction. The generated normal force is proportional to the total weight of the vehicle. With forward moving tyres, there are continuous deformations in the contact patch of the tyres. Due to these deformations, reaction forces provided by the ground get shifted forward and generate a moment in association with normal forces on the center of the wheel. Calculation of frictional force (shear force) in the tyre in such a situation by fundamental physics is very cumbersome and therefore cannot be included in fast vehicle simulations. This difficulty has encouraged researchers to use empirical formulae for calculating frictional forces and torques. The well known empirical tyre model, “Magic Formula” [33], features tyre shear forces and moments represented by a combined-slip model. General form of “Magic Formula” for longitudinal slip model can be described as follows:

$$F = D \sin[C \arctan B\kappa - E(B\kappa - \arctan(B\kappa))] \quad (3.1)$$

Where F is the force in the longitudinal direction. κ is the tyre longitudinal slip ratio. D , C , B are E are the tyre-force-shaping factors calculated by empirical data provided by the manufacturer. This “Magic Formula” is further normalized and redefined by Sharp and

Bettella in [176–178] which has been adopted in this work. In steady state, longitudinal forces and moments can be expressed as a function of longitudinal slip, lateral slip conditions, vertical load and camber angle. Prediction of forces and respective torques are quite accurate in the steady state, representing general running conditions of the vehicle. The coefficients of the basic formula represent tyre characteristics and are taken from [32]. Since present work is only considering longitudinal motion of the car the effects of lateral slip and camber angle are relatively negligible in the tyre model. Figure 3.3 presents general variation trend in the longitudinal force against longitudinal slip and applied load in the absence of lateral slip.

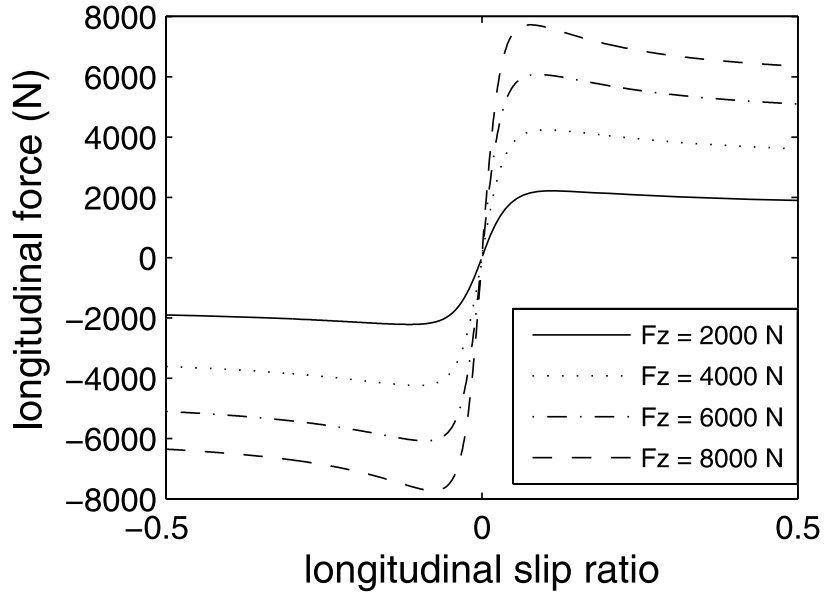


Figure 3.3: Longitudinal force as a function of longitudinal slip and load [32]

As already mentioned the general formula also contains lateral behavior of the tyres which is unnecessary and only complicates the computation for longitudinal motion of the vehicle. Therefore, a streamlined magic formula is presented in [174] and used in the present work. This simpler tyre model is validated with a complex model used in [32]. Details of the Magic Formula are presented in the Appendix. The

fundamentals of longitudinal force calculations are presented here:

$$u_{slip} = u_{ground} - r_{wheel} \cdot \omega_{wheel} \quad (3.2)$$

$$\kappa = \frac{u_{slip}}{u_{ground}} \quad (3.3)$$

where u_{slip} is the longitudinal slip speed, u_{ground} is the translational speed of the vehicle, ω_{wheel} is the rotational speed of the wheel, r_{wheel} is the radius of the wheel and κ is the tyre longitudinal slip ratio.

Knowing the normal load of the vehicle and tyre slip ratio, the longitudinal driving force can be calculated with the help of magic formula. In this model this force can be applied at the wheel contact point or it can be represented as a force acting at the center of the hub carrier plus a moment acting on the wheel. This moment is given by

$$T_{friction} = r_{wheel} \cdot F_{longitudinal} \quad (3.4)$$

As the longitudinal force for forward motion is provided by friction, $T_{friction}$ will be compensated by the driving torque provided by the transmission with the help of the PMSM.

3.3 Aerodynamic Behavior

As the speed of the vehicle increases, the aerodynamic analysis starts becomes more and more critical from a vehicular stability point of view. Any object moving through air flow is subjected to aerodynamic forces proportional to the square of speed and the projected area normal to the flow direction. These aerodynamic forces have two components - one in the direction of flow known as aerodynamic drag and the second in the perpendicular direction of the flow known as aerodynamic lift. In the present HEV case, the car model built in VehicleSim®, includes aerodynamic behavior.

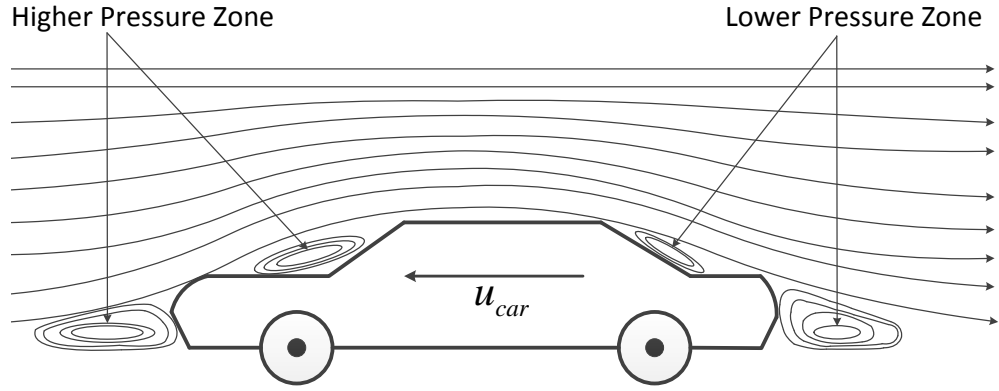


Figure 3.4: Higher and lower pressure zones created around the car due to streamlined air flow

3.3.1 Aerodynamic drag

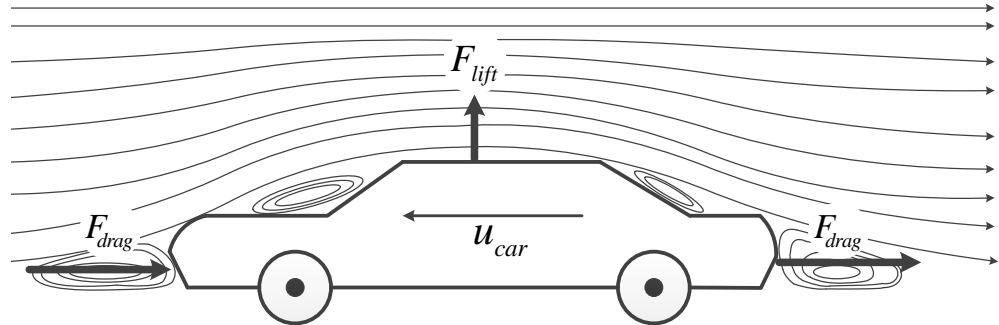


Figure 3.5: Overall aerodynamic drag and lift forces applied on the car due to streamlined air flow

Aerodynamic drag is generated as a result of air-flow passing through the surface of a vehicle. Aerodynamic drag gets maximum contribution from its two important components, the shape drag and the skin friction. Due to forward motion of the vehicle, air at the front of the vehicle is compressed and air at rear of the vehicle expands. This compression and expansion creates higher and lower pressure zones at the front and rear regions of the vehicle, respectively. Due to this pressure difference, there is an overall backward force on the vehicle called shape drag. The layer of air closer to the vehicle surface has the same speed as that of the vehicle but air farther from the vehicle surface remains at a different speed. This difference of speed between different layers of air generates net force called the skin friction. Both these forces together are known

as F_{drag} and can be calculated as follows:

$$F_{drag} = C_d \cdot A_u \cdot (u_{car} + v_w)^2 \quad (3.5)$$

where F_{drag} is the total aerodynamic drag, C_d is the drag coefficient, A_u is the projected area normal to the direction of air flow, u_{car} is the speed of the car and v_w is the speed of the wind parallel to the motion of the vehicle. v_w has a negative or positive sign depending on whether wind flows in the same or in the opposite direction of vehicle motion. In the present work, v_w has been taken to be zero. When the object moves through a laminar flow and the flow gets divided at the front stagnation point, the flow remains attached to the vehicle surface and the value of C_d will be very low even after the stagnation point. But if the air flow gets separated from the vehicle surface after the stagnation point, it becomes turbulent and C_d increases. The value of C_d depends on the smoothness and curvature of the surface with respect to the flow. Therefore, the design of the vehicle and material used for the car body strongly affect the overall drag force. A reasonable value of C_d is tabulated in Table (3.1). Almost 40% of the total energy supplied to the vehicle is expended in overcoming the drag force. The total energy lost in overcoming the drag force depends on the drive cycles (i.e. NEDC) and remains almost constant for the powertrains having fixed gear ratios ($f_{drag} = 2, 3, 4, 5, 6$) and CVT, as long as the vehicle aerodynamic design is fixed (means having same C_d and A_u in all the cases). In Chapter 8, this fact will be demonstrated clearly.

3.3.2 Aerodynamic lift

When the air passes through the surface of the vehicle, it creates lower or higher pressure zones. This pressure difference creates an overall force on the vehicle whose vertical component generates lift force. When the flow of air passes through the front of the car, it creates very high pressure at front stagnation point and when it passes through the roof of the car at high speed, it creates a low pressure zone according to Bernoulli's

law. The large surface area of the roof of the car generates significant lift force which can be dangerous at higher speed. Due to this reason, sport cars are designed with slanted wings so that the generated lift forces push the car in the downward direction to get balanced and better traction force at higher speed. This lift force can be quantified as follows:

$$F_{f,lift} = C_{lf} \cdot A_u \cdot u_{car}^2 \quad (3.6)$$

$$F_{r,lift} = C_{lr} \cdot A_u \cdot u_{car}^2 \quad (3.7)$$

where $F_{f,lift}$, $F_{r,lift}$, C_{lf} and C_{lr} are the front lift force, rear lift force, front lift coefficient and rear lift coefficient respectively. In simulations it has been found that total energy lost due to lift forces are very small in comparison to energy lost due to drag forces.

3.4 Powertrain Transmission

Transmissions are a collection of many mechanical subsystems, which as a unit, transfer mechanical power from the power source units, such as engine or motor, to the wheels of the vehicle. Normally, the HEV transmission contains three important components, namely, gears, differential and driveshaft. There are two kinds of drive configurations, front-wheel drive and rear-wheel drive. Front wheel-drive is more compact in design, efficient in assembly due to the absence of driveshaft and has improved fuel efficiency due to lower weight but suffers from unevenness of weight and lesser traction force. Rear-wheel drive has even weight distribution, efficient steering and higher traction force but suffers from a cost point of view because of the involvement of extra components such as driveshaft, etc. [179]. Manufacturers of the powerful cars have chosen to go for rear wheel drive mainly because of potential threat of excessive understeering in front wheel drive. Understeer is the situation when car turns less than what is expected by the driver. Which drive is better; this debate has gone

for decades without any conclusive answer. So just for the purpose of demonstrating modelling methodology, rear-wheel drive is considered in the present work.

Traditional IC engine based vehicles have drivetrain consisting of clutches, gearbox and differential [180]. Clutches are required to engage and disengage the engine shaft from the output shaft. Since the engine cannot start itself and the car simultaneously in motion from initial zero speed, the engine has to shutdown completely or the engine shaft has to be disengaged from the wheel shaft when the vehicle has to stop even for a moment. Shutting down the engine immediately is not possible, so disengaging the engine shaft is the only feasible option. Considering these situations, the clutch is inevitable in traditional IC engine based vehicles. Clutches are exposed to very hard friction, so continuous maintenance is required. Since electric motors can propel both itself and the car from zero speed and can be shutdown in very short time with faster dynamics, the clutch is not required in an electric motor based drivetrain [26].

Gear boxes are generally used between the driving shaft (engine shaft in the traditional IC engine based drivetrain and motor shaft in electric or hybrid powertrain) and the differential. Gears are used in the HEV as a torque multiplier $f_{drat} \cdot T_L$ (where f_{drat} is the final drive ratio and T_L is the supplied load torque to the transmission from the prime mover such as engine or traction motor) at the cost of reducing speed [23]. Since the driving motor has higher efficiency at higher speed relative to the speed of the driven wheels, single ratio gear can be used to achieve this task. A differential is required to control the applied torque and rotational speed of the wheels. Differential is a device which enables a pair of the wheels to rotate at different speeds without slipping while turning around a corner. The differential is supplied with power from the engine or the motor through the driveshaft and then this power is distributed to both wheels in different amounts according to the rotational speeds [181]. In the present work, the standard differential gear ratio of 3.42 : 1 is used similar to the one in Chevrolet Corvette Z06.

There are many kinds of transmissions such as manual transmission (MT),

automatic transmission (AMT) and continuous variable transmission (CVT). Manual transmission is already in its mature state with the highest possible efficiency of 96% [182–184]. Automatic transmission is still in a developing state with the highest possible efficiency of 85.3% [183]. Instead of gear box with discrete number of gears, a CVT can be used in the vehicle and an infinite number of gear ratios can be attained in a certain range. The main benefit of using a CVT is that it provides flexibility for drive sources such as engine or motor to operate in their optimum operating zone independent of the driven wheels by providing stepless change in gear ratios. Smoother drive experience, higher drive source efficiency, faster adaptability to varying road conditions and improved acceleration are a few other advantages of the CVT. The biggest disadvantages of the CVT are manufacturing cost and frictional losses. With ongoing research in the field of improved CVT design, better and efficient CVTs are being produced in the industry with overall average efficiency ranging from 88.4% to 91%, as described in [182, 183] and 89% to 94%, as described in [25]. There are many different kinds of CVTs such as rubber belt, metallic belt, toroidal, magnetic, hydrostatic, ratcheting, cone, and radial roller CVT, etc. These CVTs have different operating ranges, conditions and efficiencies. The efficiency of the belt CVT is around 88% and for the toroidal CVT, it is 93% [184]. Although the efficiencies of fixed gears and CVTs change with the applied load torque, in the present work, the average efficiency of both of these types of transmission has been used in the interest of simplicity. The advanced XTRONIC CVT produced by NISSAN has significantly improved the gear ratio range from 6.0 : 1 to 7.3 : 1 and this ratio will be used in the current work [185]. If the higher gear ratio is taken as 0.427 : 1 and the total gear ratio range is taken as 7.3 : 1, the lower gear ratio will be 3.117 : 1 [185, 186].

In the present work, the series hybrid powertrain is implemented where a PMSM is driving the wheels of the car with the help of the transmission. In the overall transmission, two stages of reduction are involved, from motor shaft to differential and from differential to wheels. The overall reduction from motor shaft to wheels can vary

continuously between $10.66 : 1 - 1.42 : 1$ when a CVT is used in the transmission. The transmission in the present longitudinal vehicle is implemented inside the VehicleSim® code of the vehicle. The model of the vehicle with the transmission takes as input the load torque T_L provided by the motor (PMSM) and outputs the rotational wheel speeds ω_{wheel} . The translational speed of the vehicle u_{car} can be easily calculated.

3.4.1 Implementation of the CVT

The advantage of stepless gear ratios offered by the CVT is that the PMSM can rotate at its optimum speed while driving the wheels of the car at any speed. This is achieved by controlling the final drive ratio, f_{drat} , achieving motor operation in its most efficient operating region. The power loss model of the PMSM will be described in Section 4.5 in detail. Here, the knowledge of the PMSM efficiency contours is used to describe the implementation of the CVT. The power loss model has enabled defining a relationship between load torque T_L and motor speed ω_r for which PMSM efficiency is high. Temperature has significant effect on the overall performance of the CVT (especially as lower temperature in rubber belt CVT), but in current modelling of the CVT and PMSM temperature effects are neglected. The following simple relationship has been chosen given the possibility of practical implementation:

$$T_L = 0.38862 \omega_r. \quad (3.8)$$

This will be recognized as a straight line on the load-torque vs PMSM-speed map in Figure 4.15 on page 113, that passes through the middle of the contour of maximum achievable efficiency of 96%. Since $\omega_r = f_{drat} \omega_{wheel}$, the effective final gear reduction ratio will be:

$$f_{drat} = \frac{T_L}{0.38862 \omega_{wheel}}. \quad (3.9)$$

Here f_{drat} is the total gear reduction from motor shaft to the rear wheel of the car. This includes two stages of reduction, one stage from the CVT, typically in the range $3.117 : 1 - 0.427 : 1$ [185], and another stage from the differential gear with a typical value of $3.42 : 1$. Consequently, f_{drat} is allowed to take values anywhere in the range $10.66 : 1 - 1.42 : 1$.

The dynamic response of the CVT is assumed to be characterized by a first order lag with a corresponding time constant, τ , and generally, this time constant lies in the range of a few hundred milliseconds [187]. This time constant includes the overall average delay of the complete transmission rather than the CVT alone. The value $\tau = 200ms$ is used in the present work. The implementation of the CVT in the overall model is shown in Figure 3.6.

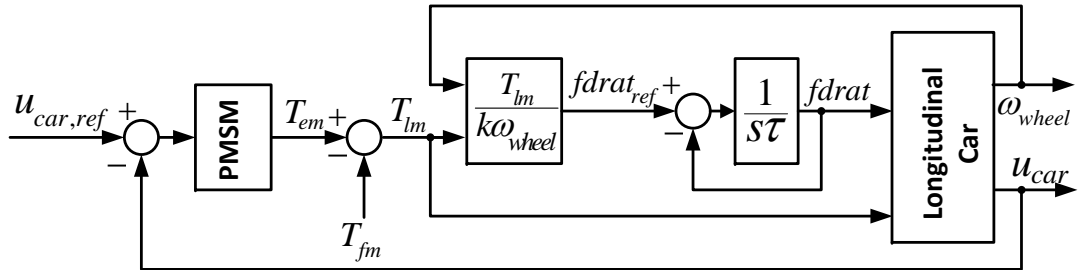


Figure 3.6: CVT implementation, $k = 0.38862$. The subscript ‘m’ corresponds to ‘motor’. T_{em} is the electromagnetic torque provided by the PMSM and T_{fm} is the friction torque inside the PMSM

3.5 Summary

- Detailed multibody dynamic model of the longitudinal vehicle with realistic description of tyres, aerodynamics resistance, suspension and tyre slip is described in this chapter. Magic Formula, featuring tyre shear forces and moments represented by a combined-slip model has been used to describe the tyre model.
- Theory behind the calculations of aerodynamic losses is understood and included in the loss modelling of the longitudinal vehicle model.

- Various types of transmission suitable for the HEV powertrain are explored and implementation of the fix gear ratio and CVT transmission are described in detail.

The VehicleSim® implementation of the longitudinal car dynamics with CVT implementation is provided in the Appendix.

CHAPTER
FOUR

PERMANENT MAGNET SYNCHRONOUS MOTOR MODELLING

4.1 Introduction

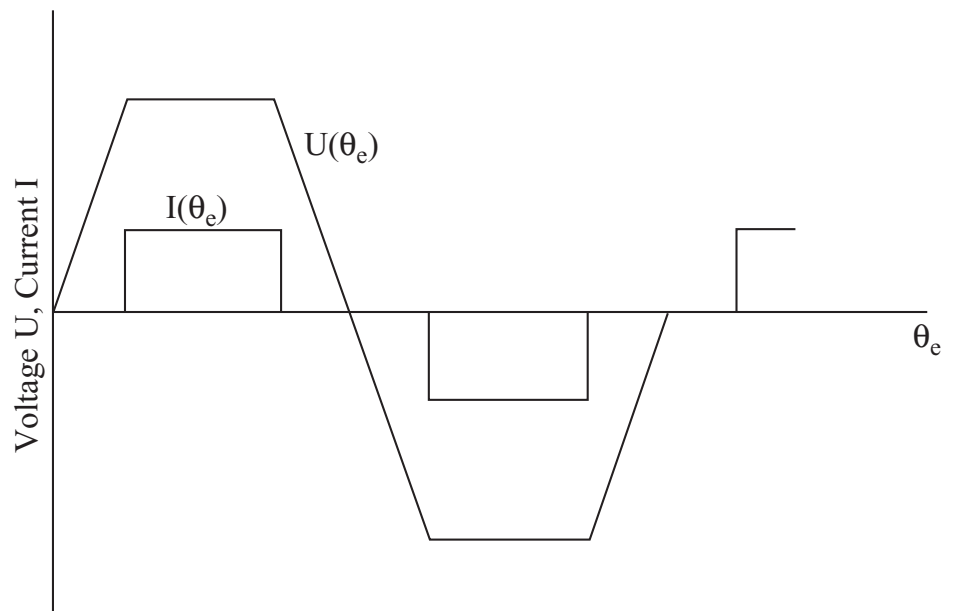
The hybrid powertrain along with the IC engine contains electrical components such as generator, motor and converters to regulate energy flow. In electrical machines, a rotating magnetic field transfers energy from the mechanical domain to the electrical domain and vice versa. A machine which converts electrical energy at the input port to magnetic energy at the intermediate stage and finally into mechanical energy at the output port is called a motor. When energy flow is exactly in the reverse direction, the machine is called a generator. Depending on the direction of the energy flow, the same machine can be used as both motor and generator. Electrical machines can be categorized on the basis of their operation and types of input-output energy. The two main categories are Direct Current (DC) Machines and Alternating Current (AC) Machines.

DC machines are further categorized as brushed and brushless. DC machines internally produce only AC signals but with the help of external commutation, produce DC voltage and current at the output port. In the brushless DC machine back *emf* produced due to permanent magnets have trapezoidal shape and stator currents have conduction of 120° duration as shown in Figure 4.1. However, in the brushless AC

machine rotor magnets are designed in such a way that they produce sinusoidal back *emf* with stator currents having conduction duration of 180° as shown in Figure 4.1 [25]. AC machines can accept or supply AC currents and voltages directly without any commutation. AC machines are also divided into two categories, synchronous and asynchronous. In the synchronous machine, the rotor rotates synchronously with the oscillating field or current. In the asynchronous machine, the rotor turns slightly slower than the current frequency such as in the induction machine.

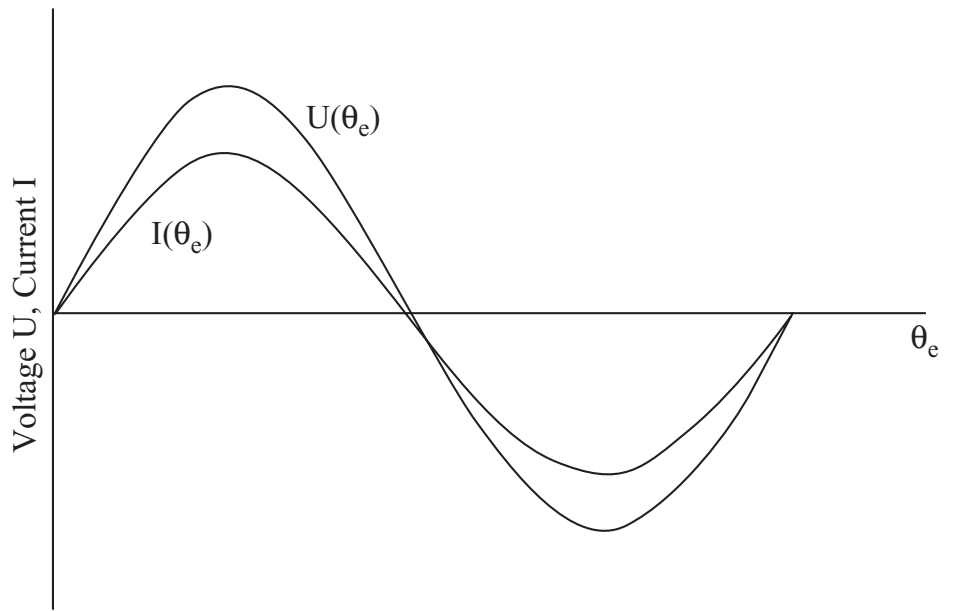
DC machines have very good transient response and therefore implementation of control is easy. However, use of slip rings and commutators cause severe maintenance problems, and, the sparking at the brushes presents safety issues. In spite of these difficulties, the dynamic performance and simple control aspects of the separately excited DC machine are very attractive. Synchronous machines exhibit all the good qualities of the separately excited machines such as easy control and good dynamic response but do not have any of the shortcomings of DC machines such as commutators and brushes. Asynchronous machines such as induction machines are also free from the shortcomings of DC machines but the implementation of the control is very difficult due to slip calculations.

When in the synchronous machine rotor windings are replaced with permanent magnets it is called as a permanent magnet synchronous machine (PMSM). The PMSM like AC synchronous machines has multiphase stator and speed of the rotor is directly proportional to the electrical frequency of the stator current. By implementing appropriate control it can be made to have the input/output characteristics much like a separately excited brush-type DC machine [47]. The present research work focuses only on the permanent magnet synchronous motor and generator.



(a)

Brushless dc or trapezoidal flux



(b)

Brushless ac or sinusoidal flux

Figure 4.1: Current and voltage in the brushless DC and AC motors [25]

4.2 Permanent Magnet Synchronous Motor

Permanent magnet synchronous motors (PMSM) and generators are used in the present work. In surface mounted permanent magnet synchronous machines, the permanent magnets are placed on the outer surface of the rotor. These magnets are used to generate field excitation, so rotor windings are dropped out making the machine very compact in design. Windings are placed over the stator thereby obviating slip rings and brushes and making synchronous machines maintenance free. Due to the use of switch converters to supply the required voltage and current, commutators are also obviated. The use of magnet reduces the weight and complexity of the whole machine, and the maintenance cost. PMSMs are easy to build and permanent magnets are easily magnetized. Permanent magnet synchronous machines are more reliable, efficient and have longer service life in comparison to DC machines. A cross-sectional structure of surface mounted PMSM is shown in Figure 4.2 [188].

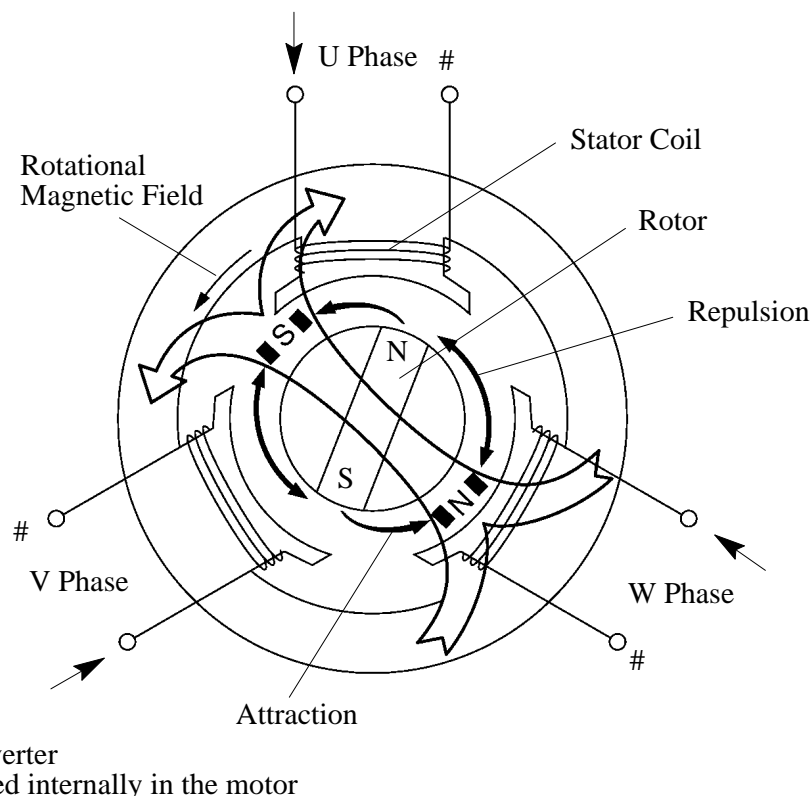


Figure 4.2: Cross sectional view of a surface mounted PMSM [188]

Depending on the field flux direction, PMSMs can be broadly categorized in two categories [49] as shown in Figures 4.3 and 4.4 :

- Axial Flux PMSM: When the direction of the produced flux is parallel to the axis of the rotor shaft it is called as Axial Flux PMSM.
- Radial Flux PMSM: When the direction of the produced flux is along the radius of the rotor shaft it is called as Radius Flux PMSM.

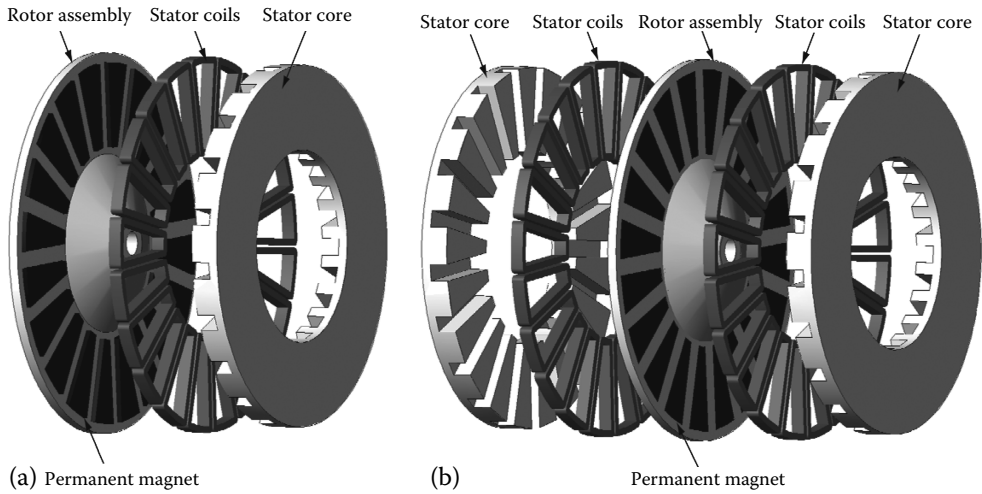


Figure 4.3: Axial PMSM (a) one stator and rotor; (b) two stator and one rotor [49]

Different ways of arranging magnets on the surface of the machine rotor creates further categories of the radial flux PMSM [49] as shown in Figure 4.4:

- Surface-Mounted PMSM: In this arrangement, magnets are directly mounted on the surface of the machine rotor facing air-gap. This kind of arrangement provides highest air-gap flux density but this arrangement is less robust at higher speed due to centrifugal force on magnets.
- Surface-Inset PMSM: In this arrangement, magnets are placed in the grooves on the outer surface of the machine rotor providing more mechanical strength to the magnets to stay on the machine rotor during high speed operations.
- Interior PMSM with radial and circumferential orientation: In this arrangement magnets are buried inside the rotor, rather than on the surface, with radial and

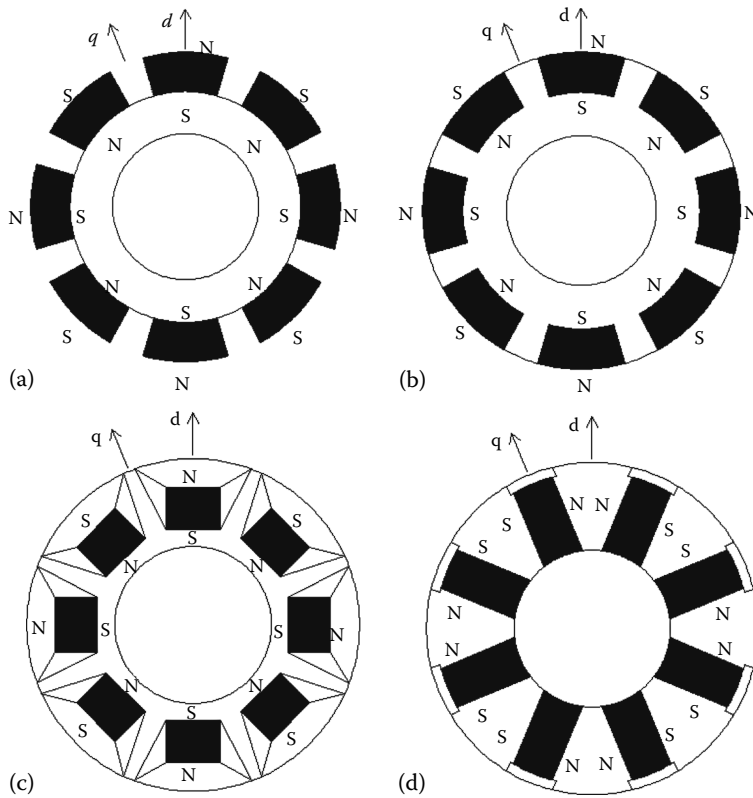


Figure 4.4: Different types of PMSM (a) Surface-Mounted PMSM. (b) Surface-Inset PMSM. (c) Interior PMSM with radial orientation. (d) Interior PMSM with circumferential orientation [49]

circumferential orientation respectively. These PMSMs have highest mechanical robustness during high speed operation and high ratio between the quadrature and direct axis inductances. Complex manufacturing process is the biggest drawback of these kinds of PMSMs.

Due to presence of the permanent magnet on the rotor of the PMSM there is a interaction between rotor magnets and stator teeth. This interaction causes change in the magnetic energy around the stator teeth which further generates the cogging torque. This torque is undesirable for the PMSM (sometimes due to improper design they goes up to 25% of the electromagnetic torque). Cogging torque is mainly affected by machine design variables such as magnet strength, stator slot width and irregularities in the manufacturing of the PMSM. The best way to eliminate the cogging torque is to completely eliminate the stator teeth which practically makes the cogging torque equal

to zero [189]. Such PMSMs are called as slottless PMSM as shown in Figure 4.5. But after the elimination of the stator teeth retention of the stator windings on the stator is far greater manufacturing challenge. Therefore, such slottless PMSMs are generally used for lower power and speed range operations [49]. There are several other methods to minimize cogging torque especially for the slotted PMSMs, as proposed in [49], such as skewing (phase shifting of the stator laminations along the axial direction in radial flux machines), varying the width of rotor magnets and stator slots, shifting alternate pair of poles, and notching of teeth etc.

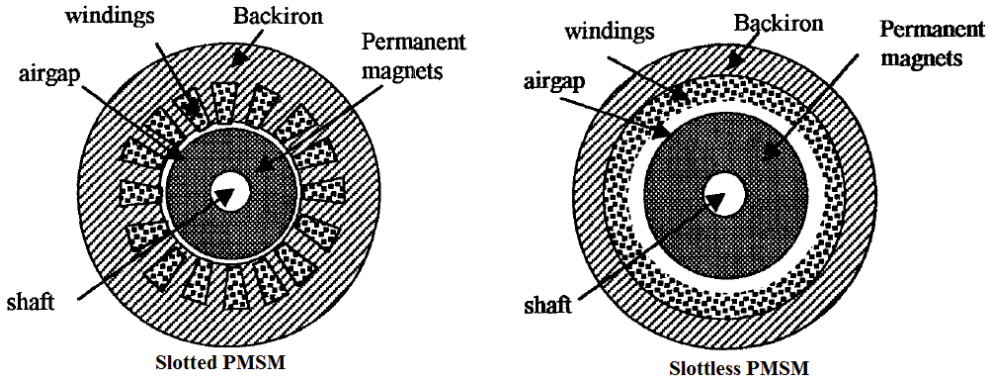


Figure 4.5: Cross-section of slotted and slottless PMSM [189]

The PMSM has many other advantages in the HEV over other machines. For instance, the use of permanent magnets in the rotor causes constant air-gap flux to be controlled by magnet strength alone. Although air-gap flux can be further increased or decreased by manipulating direct-axis current i_d (air-gap flux increases when $i_d > 0$ and decrease when $i_d < 0$). Furthermore, the electromagnetic torque can be controlled separately by controlling the stator current. Both of these characteristics are special features of separately excited DC machines. For the same output, the PMSM will operate at a higher power factor with no losses in slip rings and brushes, making it more efficient overall. The PMSM also has higher torque-to-inertia ratio and power density when compared to the induction machine or the wound-rotor synchronous machine, making it most suitable in the weight constrained HEVs. Due to the compact design, cooling is very easy and efficient in the PMSM as compared to the induction

machine. Operation of the PMSM in field weakening zone or heavy eddy currents can demagnetize the permanent magnets [23]. For this reason PMSMs are built and used for small and medium power application.

4.2.1 PMSM drive

In general, two kinds of PMSM drives are available, with sinusoidal flux distribution and trapezoidal flux distribution. In trapezoidal-flux-distribution machines (also known as PM brushless DC machines) power density is 15% higher than sinusoidal-flux-distribution machines. This difference can be attributed to the fact that the ratio of the rms value to peak value of the flux density in the trapezoidal-flux-distribution machine is higher than that of the sinusoidal PM machine. In trapezoidal-flux-distribution machines, the produced torque has ripples due to the high rate of change in currents, which is unacceptable for dynamic-performance applications [49]. Therefore, trapezoidal-flux-distribution is inadequate for providing smooth and precise motor control specifically at lower speeds whereas sinusoidal-flux-distribution machines have smooth dynamic responses in every operating region. In the present context, PMSM refers to the sine wave-wound PMSM following the convention used in most of the literature. These motors are also called non-salient pole synchronous machines because they have equal inductance in the quadrature and direct axis. In the HEV, the motor drive is used to enable the motor to track the given speed profile with performance constraints (good tracking even in the low torque and low speed regions).

To drive the PMSM, the vector control (also known as the field oriented control) technique [190] is employed to obtain the best performance in the speed tracking. This technique requires expensive rotor-speed and current sensors. There are also several sensorless vector techniques proposed in the literature to overcome this problem as well [69]. However, considering the smooth and dynamic response of the system in return, this is acceptable. Figure 4.12 gives a high level structure of the PMSM drive used in the present work. The controller receives the feedback from the car, which is

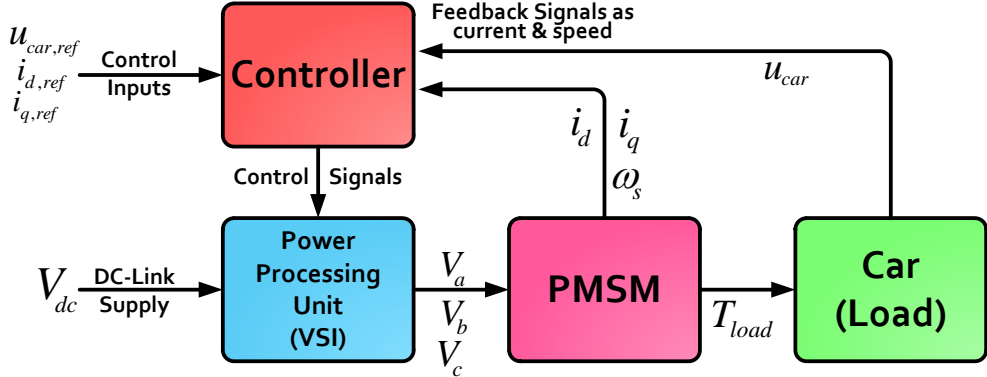


Figure 4.6: High level design of the PMSM motor drive

driven by the PMSM, and then triggers the power processing unit in such a way that it generates required voltage and current input for tracking the speed profile. Electrical power to the overall drive is provided by the DC-Link, which is maintained at constant voltage by the permanent magnet synchronous generator (PMSG) or the battery as will be shown in Chapter 8.

4.2.2 Permanent magnet synchronous motor model in the D-Q frame

With improvements in the production of permanent magnets and high resistivity rare-earth metals, PMSMs became favourable for usage in HEVs. Since the materials used for magnets such as NdFeB (Neodymium-iron-boron) have high resistivity, the induced current in the rotor is negligible at normal operation speeds. Permanent magnets replace all functionalities of rotor coils with no difference in terms of performance.

In a PMSM, a voltage source inverter supplies sinusoidal voltage to the stator windings causing the flow of sinusoidal currents. These sinusoidal currents generate a rotating MMF (magnetomotive force) at current frequency. This rotating MMF interacts with the overall magnetic field of the permanent magnets. The interaction forces the rotor to rotate with the same synchronous speed as of the sinusoidal current frequency [23, 190]. Voltage and current with variable frequency and magnitude

are supplied to the stator windings to control rotor speed. When the motor model is presented in the reference frame fixed to the rotating rotor, the equations for the motor control become independent of the rotor position. This transformation makes the implementation of control for the PMSM very similar to separately excited DC machines. Such a rotating reference frame in the literature is known as the $d - q$ reference frame [51].

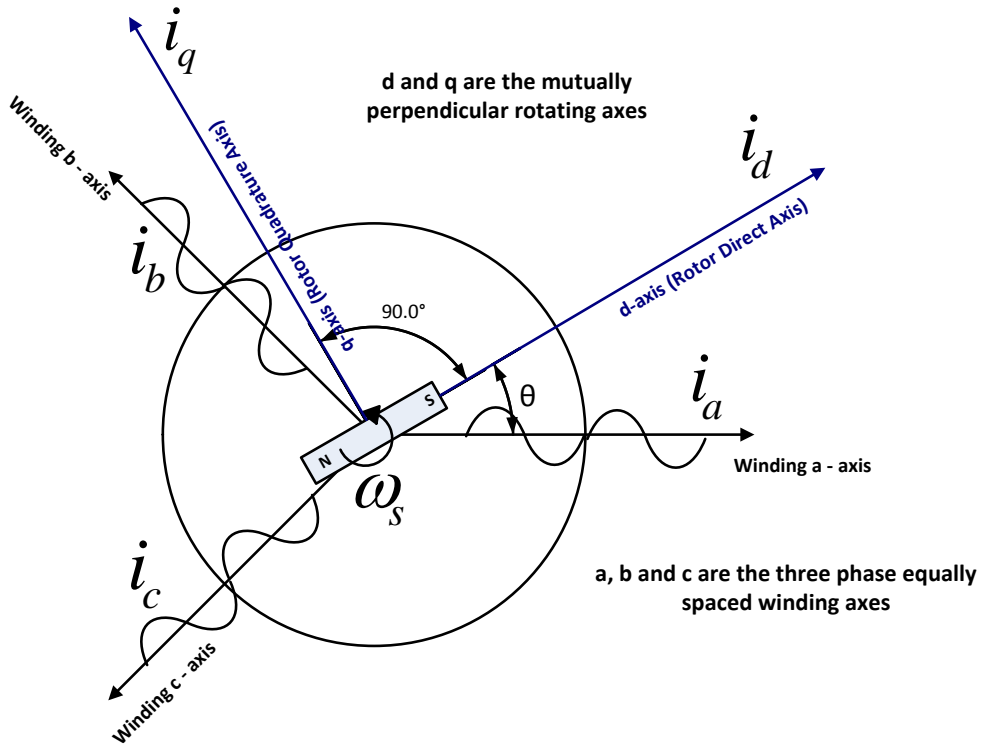


Figure 4.7: Three phase (abc) and two phase ($d - q$) representation of the PMSM

The mathematical model of the PMSM can be derived in the same manner as for the wound-rotor synchronous motor. Pillay and Krishnan [51] made the following assumptions in order to derive a mathematical model of the PMSM:

1. Saturation is neglected although it can be taken in account by parameter changes.
2. The induced EMF is sinusoidal.
3. Eddy currents and hysteresis losses are negligible.
4. There are no field current dynamics.

5. There is no cage on the rotor.

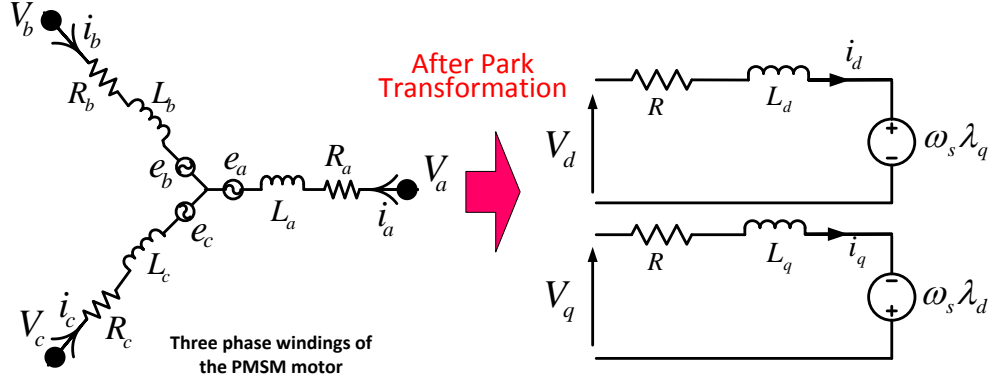


Figure 4.8: Transformation of the PMSM equations from three phase (abc) to two phase $d - q$ rotating axes

With these assumptions, equations for the PMSM in the rotating rotor reference frame $d - q$ can be described as [51, 191]:

$$v_q = Ri_q + \frac{d\lambda_q}{dt} + \omega_e \lambda_d \quad (4.1)$$

$$v_d = Ri_d + \frac{d\lambda_d}{dt} - \omega_e \lambda_q \quad (4.2)$$

where

$$\lambda_q = L_q i_q \quad (4.3)$$

and

$$\lambda_d = L_d i_d + \lambda_f \quad (4.4)$$

v_d , v_q , i_d , i_q , L_d , L_q , λ_d and λ_q are the stator voltages, stator currents, stator inductances and stator flux linkages in the direction of d and q axes respectively. R and ω_e are the stator resistance and inverter frequency (speed of the rotating electromagnetic field) respectively. λ_f is the flux linkage due to the other rotor magnets linking the stator.

The electromagnetic torque is given by the following equation [191]:

$$T_e = 3p[\lambda_f i_q + (L_d - L_q)i_d i_q]/2 \quad (4.5)$$

and the rotor dynamics equation is

$$T_e = T_L + B\omega_r + J_m \frac{d\omega_r}{dt} \quad (4.6)$$

where p is the number of pole pairs, T_L is the load torque, B is the damping constant, ω_r is the rotor speed and J_m is the moment of inertia of the rotor. The various motor losses in the motor such as damping, windage, hysteresis, eddy and frictional are included in the PMSM loss model by introducing a novel frictional torque T_f . Details about the modelling of this novel frictional torque are presented in Section 4.5.

The rotor speed and the inverter frequency are related as:

$$\omega_e = p\omega_r \quad (4.7)$$

It can be seen that the model given here is a non-linear coupled system as shown in Figure 4.8. The state space form of the equations is as follows:

$$\frac{di_d}{dt} = (v_d - Ri_d + \omega_e L_q i_q) / L_d \quad (4.8)$$

$$\frac{di_q}{dt} = (v_q - Ri_q - \omega_e (L_d i_d + \lambda_f)) / L_q \quad (4.9)$$

$$\frac{d\omega_r}{dt} = (T_e - T_l - B\omega_r) / J \quad (4.10)$$

The d, q voltages are related to the stator windings voltages, v_a, v_b, v_c according to the Park transformation [191]:

$$\begin{pmatrix} v_q \\ v_d \\ v_o \end{pmatrix} = \frac{2}{3} \begin{pmatrix} \cos(\theta) & \cos(\theta - 2\pi/3) & \cos(\theta + 2\pi/3) \\ \sin(\theta) & \sin(\theta - 2\pi/3) & \sin(\theta + 2\pi/3) \\ 1/2 & 1/2 & 1/2 \end{pmatrix} \begin{pmatrix} v_a \\ v_b \\ v_c \end{pmatrix}$$

Here v_a, v_b, v_c are the voltages produced in the windings a, b and c respectively. θ is the instantaneous position of the rotor with respect to the fixed winding phase a . v_o is

the sum of all the three phase winding voltages and for balanced three phase supply, generally this value is taken as zero.

The reverse transformation is also possible, i.e., a, b, c variables can be obtained from $d - q$ variables using the inverse park transform, as follows:

$$\begin{pmatrix} v_a \\ v_b \\ v_c \end{pmatrix} = \begin{pmatrix} \cos(\theta) & \sin(\theta) & 1 \\ \cos(\theta - 2\pi/3) & \sin(\theta - 2\pi/3) & 1 \\ \cos(\theta + 2\pi/3) & \sin(\theta + 2\pi/3) & 1 \end{pmatrix} \begin{pmatrix} v_q \\ v_d \\ v_o \end{pmatrix}$$

Figure (4.8) represents the transformation of equations of the PMSM from three phase ($a - b - c$) reference frame to the two phase rotating reference frame ($d - q$).

The total power input in the PMSM can be presented as follows [191]:

$$P_{in} = v_a \cdot i_a + v_b \cdot i_b + v_c \cdot i_c \quad (4.11)$$

Total output power is

$$P_{out} = T_L \omega_r \quad (4.12)$$

Similarly, the power can be calculated in the $d - q$ frame [191]:

$$P_{in} = \frac{3}{2}(v_q i_q + v_d i_d) \quad (4.13)$$

When the overall losses are considered:

$$P_{in} = P_{out} + P_{loss} \quad (4.14)$$

$$P_{loss} = P_{l,c} + P_{l,e} + P_{l,h} + P_{l,b} + P_{l,w} \quad (4.15)$$

$$P_{l,c} = \frac{3}{2}R(i_q^2 + i_d^2) \quad (4.16)$$

where $P_{l,c}$ is the copper loss, $P_{l,e}$ is the eddy current loss, $P_{l,h}$ is the hysteresis loss, $P_{l,b}$ is the bearing loss and $P_{l,w}$ is the windage loss. Only the expression for copper

loss evaluation is given here. A novel model accommodating all other losses will be described in detail in Section 4.5.

4.3 Power Processing Unit

The task of the drive unit is to deliver the required electrical power to the machine by controlling its voltage or current. When it supplies voltage, it is known as a voltage source inverter (VSI) and when it supplies current, it is known as a current source inverter (CSI) [192, 193]. The current source inverter works as an ideal current source which supplies constant current irrespective of the load. It is designed by adding a very high impedance (an inductor of high value) in series with a DC voltage source. The voltage source inverter works as an ideal voltage source applying constant voltage across the load irrespective of any variation in the load. It is designed by adding a capacitor in parallel to a constant DC voltage source. The topology of a VSI is more efficient in comparison to a CSI because it offers higher bandwidth in operation and eliminates current harmonics [194]. Figure 4.9 shows the circuit of the PMSM, fed by three phase DC to AC converter.

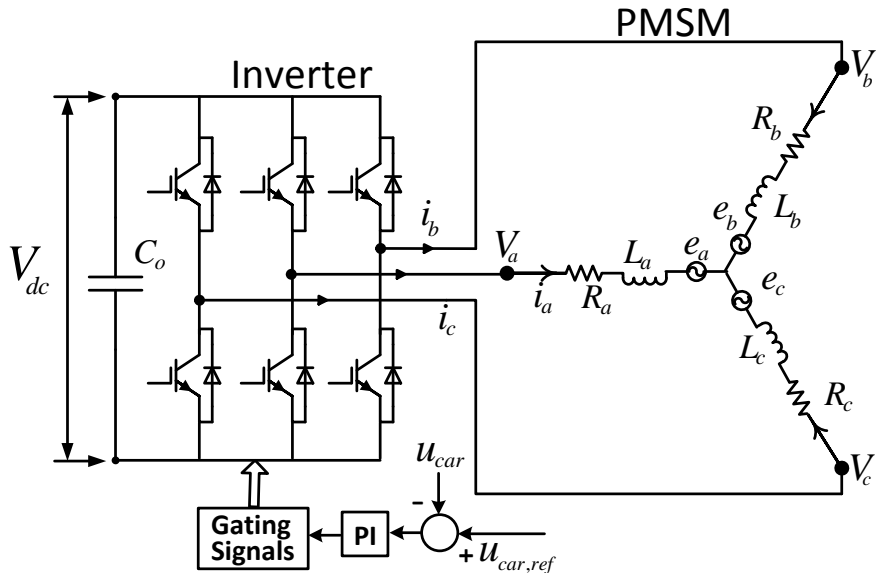


Figure 4.9: Three Phase DC to AC Inverter-fed PMSM

The main objective of the voltage source inverter is to invert the input DC voltage to three phase AC voltage. There are many ways in which the inverter can be designed - line commutated inverter, force commutated inverter and switch mode converter. Line commutated converters have thyristor based topology and are controlled by the firing angle of the thyristor. These inverters are fully controlled and can be used for very high power ratings as well. However, these are bulky in design and work well only with line frequencies in the range of 50 – 60 Hz. Therefore, line commutated inverters are used for high power applications only [194]. Switch mode converters are designed by gate controlled switches such as BJT, MOSFET, IGBT, etc. These switches can be turned on and off at very high frequencies. Therefore, these converters are suitable for speed control drives where the speed of the motor is directly proportional to the current frequency. The most popular and efficient methods of voltage control in these converters involve the use of pulse width modulation techniques [195].

There are many modulation techniques available in the literature but the sinusoidal pulse width modulation technique is considered the best one. IGBTs can turn DC voltage on and off with specific duty cycles and these duty cycles are proportional to the magnitude of the sinusoidal wave. A reference sine wave with desired frequency is compared to a high frequency triangular wave generating the pattern for the pulse width. This pulse width pattern controls the switching duration of IGBTs. Due to this pulse width modulation, an AC voltage of variable frequency and variable amplitude is produced at the output of the inverter [195].

In general, there are three levels of modelling approach for converters, detailed model, small signal model and average model. Detailed modelling of VSI includes the detailed switching frequency dependent model of IGBT switches. These detailed switching models are useful in the analysis of switching frequency current ripple, current harmonics, high frequency spectrum, oscillations of switching currents and effects of various PWM modulation schemes. The small signal model of any system can be derived by linearizing the nonlinear model around a stable solution of system

dynamics. This model is only valid for small perturbations of the system around its stable operating point (for switches this stable point is around its DC bias) but not very useful in the cases of large signal dynamics. In average modelling, higher frequency effects are not considered and variables changing at high frequency are averaged out over switching periods. These kinds of average models still allow the analysis of large signal transients while the computational burden of high frequency details is eliminated [196]. The inverter dynamics is of the order of kHz but in the context of the present work, the prime interest lies in modelling and investigating the system behavior in the range of 0.1 to 10 Hz. Therefore, for the present research purposes, an average switching model can be used without any loss in accuracy.

The simulation results have shown that the average modelling approach is justified because it allows the simulation speed to be increased substantially without compromising the accuracy of the results. In AC converters, even at the steady-state, the system variables have sinusoidal values and therefore, the model cannot be linearized. However, by transforming the variables into the rotating $d - q$ frame, a linear average model of the converter can be achieved. Average model of the switches and VSI in the $d - q$ frame is explained in the next section.

4.3.1 Average model of the three phase DC/AC converter (Inverter)

Three Phase converters are mainly known as inverter and rectifier depending on the inversion or rectification of the input signals. Three phase rectifiers and inverters are used in the present work for delivering the required power from power source to power sink. With the help of switchings, the inverter supplies variable voltage and variable current to the PMSM for adjusting the speed drive. In modelling of the physical system, it is important to recognize the most important and dominant factors of system behavior. For this purpose, some dynamics are modeled in a detailed way and some dynamics

are simplified and linearized. Fast and complicated system dynamics are generally ignored or averaged out to focus more on the important dynamics. While modelling the three phase converters, knowledge of the relationship between the output variables (voltage and current) and the input variables (voltage and current) are more important, so high frequency ripples in these variables can be neglected. Principles of inductor volt-balance and capacitor charge-balance are used to develop relationships between the average values of input and output variables of the converter during steady state operation. By averaging a variable over one time switching period, high frequency ripples are eliminated and low frequency contents illustrate the behavior trend of that variable [70]. Since the average value of that variable varies from one switching period to another, the overall average behavior is preserved and only higher frequency details are neglected. This averaging technique is called “moving average” and is described in the form of Equation 4.17.

$$\langle x(t) \rangle_{T(s)} = \frac{1}{T_s} \int_t^{t+T_s} x(\tau) d\tau \quad (4.17)$$

Suppose $x(t)$ is a pulsating signal to the input terminal of the switch giving pulsating signal $y(t)$ at the output terminal of the switch.

$$x(t) = \begin{cases} Y_{on}, & 0 < t < dT_s \quad \text{Switch is ON} \\ Y_{off}, & dT_s < t < T_s \quad \text{Switch is OFF} \end{cases} \quad (4.18)$$

This output signal takes average values Y_{on} during ON period of the switch and Y_{off} during OFF period of the switch with duty period d . The relationship between the average values of the input and output variables during one switching period T_s will be

given by:

$$\langle x(t) \rangle_{T(s)} = \frac{1}{T_s} \left(\int_0^{T_s} dT_s x(\tau) d\tau + \int_{dT_s} T_s x(\tau) d\tau \right) \quad (4.19)$$

$$= \frac{1}{T_s} (d \cdot T_s \cdot Y_{on} + T_s \cdot (1 - d) \cdot Y_{off}) \quad (4.20)$$

$$= d \cdot Y_{on} + (1 - d) \cdot Y_{off} \quad (4.21)$$

Duty period for a signal denotes the ratio of the time duration when the switch is ON to the total switching period. The longer the time period the switch is ON, the higher the duty cycle and correspondingly higher the average value of the output signal. The value of the duty period varies from a maximum of 1 (when the switch is ON over the complete switching period) to a minimum of 0 (when the switch is OFF over the complete switching period). If this averaging is done over each switching period of the input signal, the discrete duty periods become a continuous duty cycle function $d(t)$ eliminating high frequency ripples but preserving the relationship between the average values of input and output variables at the terminals [197, 198]. When the duty period d is represented by a continuous duty cycle function $d(t)$, then the relationship between the average value of $x(t)$ and $y(t)$ can be described as:

$$\langle x(t) \rangle = d(t) \cdot \langle y(t) \rangle \quad (4.22)$$

The averaging action is similar to applying a low pass filter to input signals having high frequency ripple content. This filtering action is naturally brought about by the parasitic elements used in the input and output network circuitry, and it becomes the physical basis for average models of PWM switches in a particular switch and in the converter as a whole. By turning on and off at high frequency switches with variable duty cycle $d(t)$, the PWM converter regulates voltage and current at the output terminal. Figure 4.10 presents the canonical switching cell, where the behavior of an ideal switch is presented. This canonical switch has three terminals namely active (\hat{a}), passive (\hat{p}) and common (\hat{c}). In an ideal switch, switching variable s can instantaneously take

either of the two values, 0 (ON) or 1 (OFF). The terminal behavior of an ideal switch in a detailed model can be described by following equations [198]:

$$i_{\hat{a}} = s \cdot i_{\hat{c}} \quad (4.23)$$

$$v_{\hat{c}\hat{p}} = s \cdot v_{\hat{a}\hat{p}} \quad (4.24)$$

where s can take values either 0 and 1 according to following conditions:

$$s = \begin{cases} 1, & 0 < t < dT_s \quad \text{Terminals } \hat{c} \text{ and } \hat{a} \text{ are connected} \\ 0, & dT_s < t < T_s \quad \text{Terminals } \hat{c} \text{ and } \hat{p} \text{ are connected} \end{cases} \quad (4.25)$$

By taking the average over a switching period, the discrete switching variable s can be replaced with duty period d [198].

$$\begin{aligned} \langle i_{\hat{a}} \rangle &= d \cdot \langle i_{\hat{c}} \rangle \\ \langle v_{\hat{c}\hat{p}} \rangle &= d \cdot \langle v_{\hat{a}\hat{p}} \rangle \end{aligned} \quad (4.26)$$

The most important step in averaging the switching network is to replace the

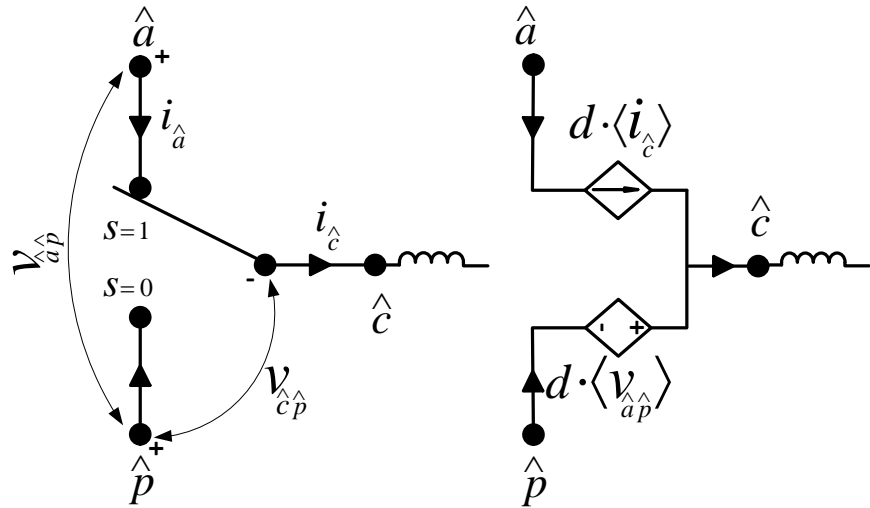


Figure 4.10: Detailed and average models of the PWM switch

converter switches with voltage and current sources as shown in Figure 4.10 [70]. This averaged switch model can be placed in any of the PWM based converter topologies by

just replacing all the switching networks with the averaged switch model. It has been found that all the circuit analysis laws such as KCL and KVL, which are applicable for the instantaneous values of the voltage and current are also very well applicable to their average value counterpart in the same circuit. So, averaging all the switches in a network leads to averaging the whole circuit network, without doing any topological changes. This average switch model is applied to get the average behavior of the DC/AC converter in the present work.

An optimal DC to AC converter should output pure AC voltage and current and should draw pure DC current at unity power factor from the DC-Link. All the elements involved in the circuit given in Figure 4.9 are linear time invariant (LTI) and all the switches are bi-directional. The switches operate in continuous conduction mode and are turned on and off in such a way that the input DC voltage is never shorted. By using the concept of average modelling of the PWM switching, as given in Equation (4.26) and described in Figure 4.10, the DC/AC converter can be modeled as [69]:

$$i_{dc} = d_a \cdot i_a + d_b \cdot i_b + d_c \cdot i_c \quad (4.27)$$

i_{dc} is the DC current drawn through the DC-Link by the inverter to supply three phase AC currents (i_a, i_b, i_c) and three phase AC voltages (V_a, V_b, V_c) to the motor.

$$v_a = v_{dc} \left(d_a - \frac{d_a + d_b + d_c}{3} \right) \quad (4.28)$$

$$v_b = v_{dc} \left(d_b - \frac{d_a + d_b + d_c}{3} \right) \quad (4.29)$$

$$v_c = v_{dc} \left(d_c - \frac{d_a + d_b + d_c}{3} \right) \quad (4.30)$$

where d_a, d_b and d_c are the bipolar switching functions. Each converter leg has two

switches and the switching is defined as follows:

$$d_j = \begin{cases} 1, & S_j \text{ closed} \\ 0, & S'_j \text{ open} \end{cases} \quad j = a, b, c. \quad (4.31)$$

Equations (4.27)-(4.30) express the relationship between the DC and AC sides under certain switching pattern. After the transformation from abc to $dq0$ frame, Equations (4.27)-(4.30) can be expressed as follows [69, 199]:

$$i_{dc} = \frac{3}{2}(d_q \cdot i_q + d_d \cdot i_d) \quad (4.32)$$

$$v_d = d_d \cdot v_{dc} \quad (4.33)$$

$$v_q = d_q \cdot v_{dc} \quad (4.34)$$

where d_d, d_q stand for the switching patterns or duty cycles in the $d - q$ frame.

4.4 Speed Control of the Permanent Magnet Synchronous Motor

The wheels of the car are connected to the motor shaft with the help of the transmission. The nature of the transmission has already been described in Chapter 3. At every instant of time, there is a fixed ratio between the rotational speed of the wheels and motor speed, decided by the transmission. Therefore, the speed of the wheels is directly proportional to the speed of the motor. To control the speed of the car, a speed controller for the motor has to be designed. In order to design a speed controller, a linear model of the motor is required. The vector control technique is commonly used to linearize the motor model. In order to derive the maximum torque out of the power

supplied, the direct axis current i_d needs to be kept parallel to the rotor flux direction. Since the quadrature axis is perpendicular to the direct axis, only the quadrature axis current i_q will play a role in determining the torque. i_d contributes only in the increase and decrease of the net air-gap flux. If i_d has non-zero positive value (i_d has the same direction as the rotor flux), then the net air-gap flux will increase and if i_d has non-zero negative value (i_d has opposite direction to the rotor flux), then the net air-gap flux will decrease [200]. By forcing $i_d = 0$, the following equations can be derived [51,60,62,65]:

$$\lambda_d = \lambda_f \quad (4.35)$$

$$T_e = 3P\lambda_f i_q / 2 \quad (4.36)$$

From Equation (4.36), it is clear that torque is a linear function of the quadrature current and by controlling i_q alone, the electromagnetic torque produced in the motor can be controlled. This is the way by which vector control technique linearizes the PMSM model. Although this control scheme is derived for the linear model of the PMSM, it is required that it operates over the entire speed range of the PMSM.

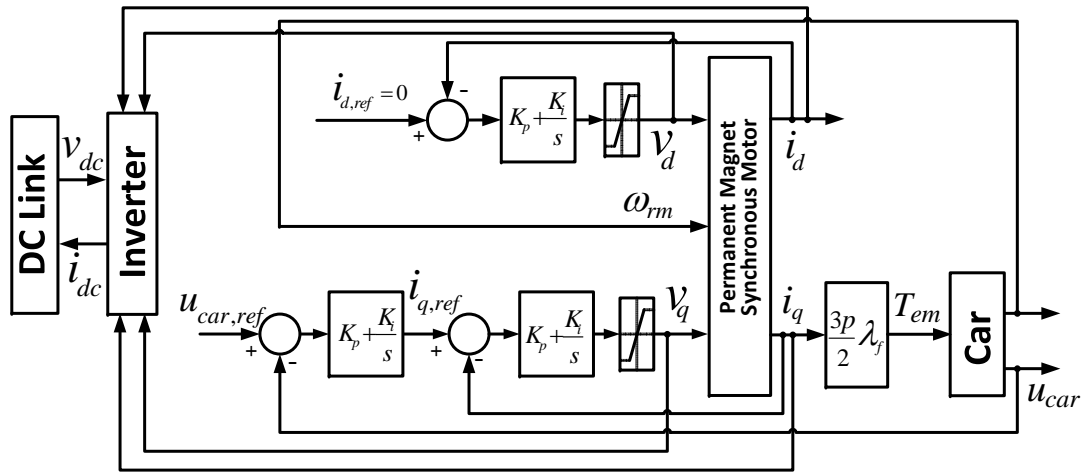


Figure 4.11: Schematic diagram of the control loops of the PMSM with the longitudinal car. Symbols used in diagram represent conventional variables as described in different equations of PMSM drive.

The complete strategy for speed control of the PMSM is presented in Figure 4.11 and the simulink implementation block diagram is given in Figures 4.12- 4.14.

Once the dynamic equations of the PMSM and controllers are obtained in the rotating $d - q$ reference frame, speed control is a straightforward job. Two PI controllers are used, one for the quadrature current i_q and another for the direct current i_d . Since current space vectors in the $d - q$ frame are static, the PI controllers operate on DC quantities rather than sinusoidal signals. This isolates the controllers from the time variant winding currents and voltages eliminating the limitation of controller frequency response and phase shift on the motor torque and speed [190]. Using this vector control technique, the quality of current control largely remains unaffected by the rotation of the motor. In Figure 4.11, two control loops are presented and their details are presented in the next section.

4.4.1 Voltage and current control loop design

First the speed difference is calculated by setting the reference speed $u_{car,ref}$ and taking feedback of the actual speed of the car u_{car} . From this speed difference, the reference torque T_{ref} is calculated by using the driver model. The outer speed controller gives current reference (current reference $i_{dq,ref} = \frac{T_{ref}}{K_t}$, where K_t is just a constant factor) [191], which gets multiplied with the required power factor and corresponds to the amplitude of the reference phase currents.

$$i_{dq,ref} = \frac{T_{ref}}{K_t} = (K_p + K_i \int dt) \{u_{car,ref} - u_{car}\} \quad (4.37)$$

Optimal performance of the DC/AC converter in terms of power can be achieved when the converter draws perfect DC current at unity power factor from the DC-link. So, in order to achieve the unity power factor, $\sin \phi = 0$ and $\cos \phi = 1$ are taken. The reference signals should satisfy $i_{d,ref} = 0$. Since $\sin \phi = 0$, the converter outputs no

reactive power. The required terminal voltages are given as follows:

$$\begin{aligned} v_d^* &= k_{11} + k_{12} \int (i_{d,ref} - i_{d-actual}) \\ v_q^* &= k_{21} + k_{22} \int (i_{q,ref} - i_{q-actual}) \end{aligned} \quad (4.38)$$

k_{11} , k_{12} , k_{21} and k_{22} are proportional and integral gains for the PI controllers for the control loops.

v_d^* and v_q^* in Equation (4.38) are required voltages to be applied at the coil terminals. Although in reality, the PWM converters are used to generate these voltage signals, it has been assumed here that these voltages are generated instantaneously by the average PWM switch model, ignoring the detail dynamics of the PWM switchings. Since the PWM switching dynamics is very fast in comparison to the longitudinal dynamics of the powertrain and has insignificant energy loss, it can be neglected. It can therefore be safely assumed that the required voltages v_d^* and v_q^* are provided to the motor by the average model without using PWM in the simulation model [192]. Since magnitudes of the $d - q$ axes voltages v_d and v_q depend on the DC-link voltage and can not be more than that, therefore dynamic saturations are used to limit the desired v_d^* and v_q^* as shown in Figure 4.13.

$$\begin{aligned} v_d &= v_d^* \\ v_q &= v_q^* \end{aligned} \quad (4.39)$$

In Equation (4.38), the command signals $i_{d,ref}$ and $i_{q,ref}$ are determined in such a way that the maximum electrical torque can be generated in the PMSM to track the desired speed profile. In the meantime, v_d and v_q ensure the actual currents be equal to $i_{d,ref}$ and $i_{q,ref}$ respectively, therefore, both the amplitude and phase can be controlled. Figure 4.13 represents the Simulink model of both control loops. v_d and v_q are supplied to the motor as mentioned in Equations (4.8)-(4.9) generating i_d and i_q , used as feedback to the current control loop. Since the constant DC-link voltage is

known beforehand, the duty cycles d_d and d_q can be determined by Equation (4.34)

$$d_d = \frac{v_d}{v_{dc}} \quad (4.40)$$

$$d_q = \frac{v_q}{v_{dc}} \quad (4.41)$$

The DC current desired by the motor can be determined by Equation (4.27) as follows:

$$i_{dc} = \frac{3}{2}(d_q \cdot i_q + d_d \cdot i_d) \quad (4.42)$$

4.4.2 Simulink implementation of the PMSM drive

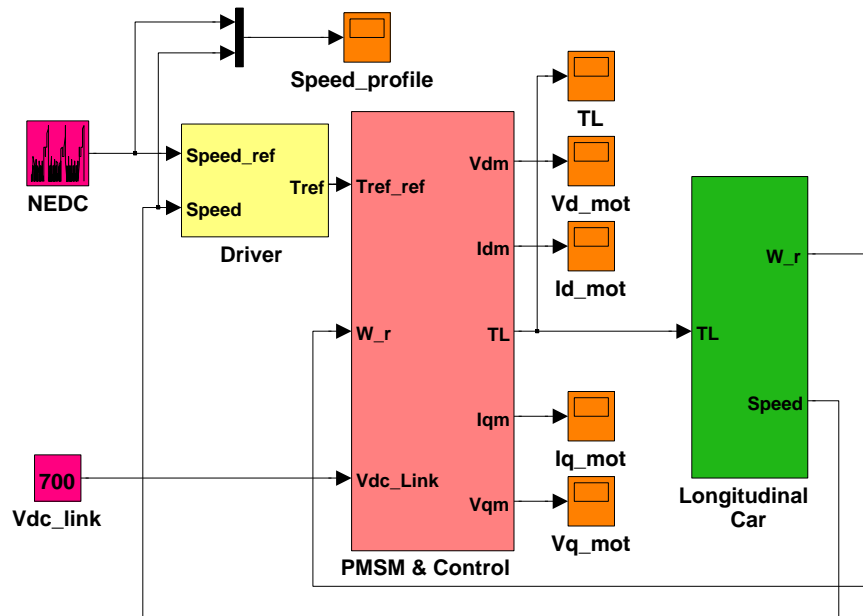


Figure 4.12: Simulink block diagram of the PMSM drive

In this section, the simulink block diagram of the PMSM drive is presented. Figure 4.12 presents the high level view of the PMSM drive, which is driving a longitudinal car. Since all the components in the hybrid powertrain are first tested standalone, here also the PMSM, which is a prime mover, is tested standalone with the longitudinal car alongwith its transmission as the driven load. In the complete powertrain, there will be a PMSG and a battery with their respective converters to feed the DC-link.

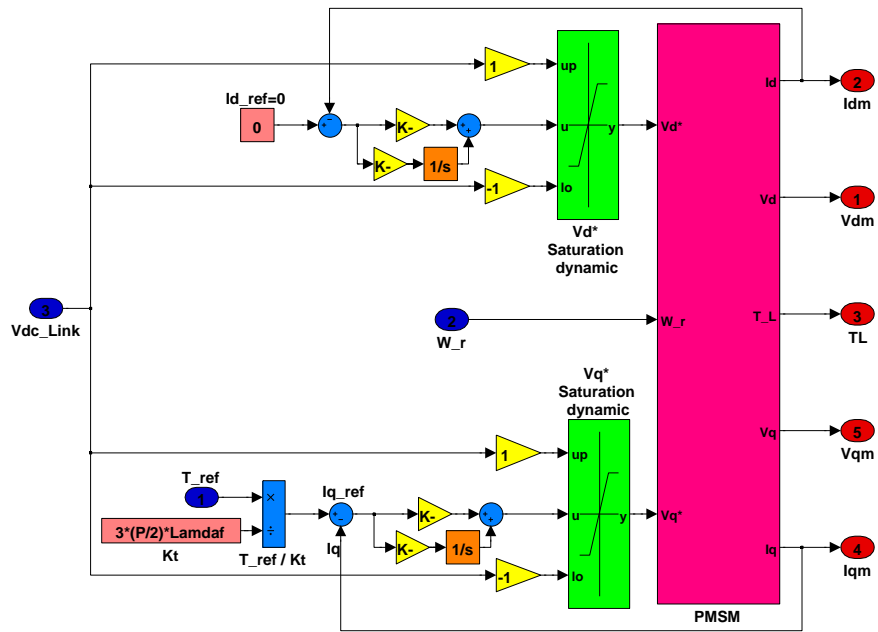


Figure 4.13: Simulink block diagram of the PMSM model level I

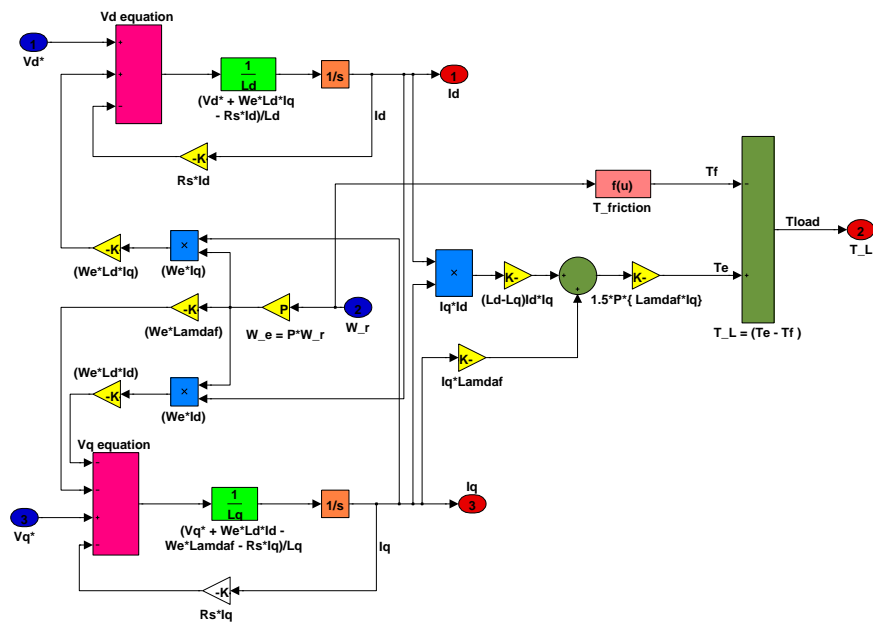


Figure 4.14: Simulink block diagram of the PMSM model level II

Furthermore the DC-link feeds the inverter to supply the power to the PMSM drive. For the standalone testing of PMSM, the inverter is supplied with the constant voltage of $v_{dc} = 700V$. Figure 4.14 describes the calculation of the load torque $T_L = T_e - T_f$ which is applied on the transmission shaft of the longitudinal car, which in turn rotates the wheels of the car. The rotational speed of the motor shaft and forward speed of the car are taken as feedbacks for the speed controller of the PMSM and driver model respectively. The longitudinal car model developed in VehicleSim®, and exported to simulink as an *s*-function. This *s*-function takes the load torque as input and outputs the motor shaft and vehicle speed. Since load torque T_L is applied on the coupled inertia of the motor and transmission, therefore the inertia J_m of the motor shaft is included in the transmission of the longitudinal car inside the *s*-function itself. In this way, the car model serves as a mechanical load of the PMSM model.

4.5 Power Loss Model of the PMSM

The PMSM parameter values used correspond to the AFM-140 axial flux, PMSM developed and manufactured by EVO Electric [201] and are shown in Table 4.1.

Table 4.1: Parameter values of the PMSM.

PMSM Parameter	Symbols	Values
Nominal rated power	P_n	75 KW
Maximum speed	ω_n	5000 RPM
Stator resistance	R	0.04 Ω
D axis stator inductance	L_d	0.002 mH
Q axis stator inductance	L_q	0.002 mH
Rotor magnetic flux	λ_f	0.1252 Wb
Moment of inertia	J	0.05 Kgm ²
Number of pole pairs	p	6

The dynamic model of the PMSM given by Equations (4.5) to (4.9) involves only losses due to the resistance of the copper windings. However, there are several other mechanisms of energy dissipation in the PMSM such as eddy current losses ($P_{l,e} \propto \omega_r^2$), hysteresis losses ($P_{l,h} \propto \omega_r^2$), mechanical losses comprising bearing losses

$(P_{l,b} \propto \omega_r)$ and windage losses $(P_{l,w} \propto \omega_r^5)$ [202]. In order to obtain a more accurate prediction of the motor efficiency in comparison to the steady-state experimental measurements provided by the manufacturer [201], a rotor-speed-dependent friction torque is included in the model. This friction moment is acting on the rotor and under equilibrium conditions, it is related to T_e and the load torque, T_L , according to

$$T_e = T_L + T_f. \quad (4.43)$$

In order to quantify T_f , expressions for P_{in} , the total power-in (electrical) and P_{out} , the total power-out (mechanical), of the PMSM in steady state, are derived. Hence,

$$\begin{aligned} P_{in} &= \frac{3}{2}(v_q i_q + v_d i_d) = \frac{3}{2} i_q^2 R + T_e \omega_r \\ &= \frac{3}{2} \left(\frac{T_e}{\frac{3}{2} \lambda_f p} \right)^2 R + T_e \omega_r, \end{aligned} \quad (4.44)$$

in which it was assumed that $i_d = 0$ and Equation (4.36) was used to substitute i_q . Similarly,

$$P_{out} = T_L \omega_r. \quad (4.45)$$

Power efficiency is defined as

$$\eta = \frac{P_{out}}{P_{in}}. \quad (4.46)$$

By substituting Equations (4.43), (4.44) and (4.45) in (4.46) and rearranging, yields

$$\frac{2R}{3\lambda_f^2 p^2} T_L^2 + \left(\frac{4RT_f}{3\lambda_f^2 p^2} + \omega_r - \frac{\omega_r}{\eta} \right) T_L + \frac{2RT_f^2}{3\lambda_f^2 p^2} + \omega_r T_f = 0. \quad (4.47)$$

This equation can be written as a simple quadratic equation in T_L as follows:

$$aT_L^2 + bT_L + c = 0, \quad (4.48)$$

where $a = \frac{2R}{3\lambda_f^2 p^2}$, $b = \frac{4RT_f}{3\lambda_f^2 p^2} + \omega_r - \frac{\omega_r}{\eta}$, and $c = \frac{2RT_f^2}{3\lambda_f^2 p^2} + \omega_r T_f$.

T_L is therefore given by

$$T_L(\eta, \omega_r) = \frac{-b \pm \sqrt{b^2 - 4ac}}{2a}, \quad (4.49)$$

which is a function of efficiency and rotor speed. The friction torque is chosen so that the constant efficiency contours on T_L - ω_r axes fit the experimental results in [201] at different efficiencies, as shown in Figure 4.15.

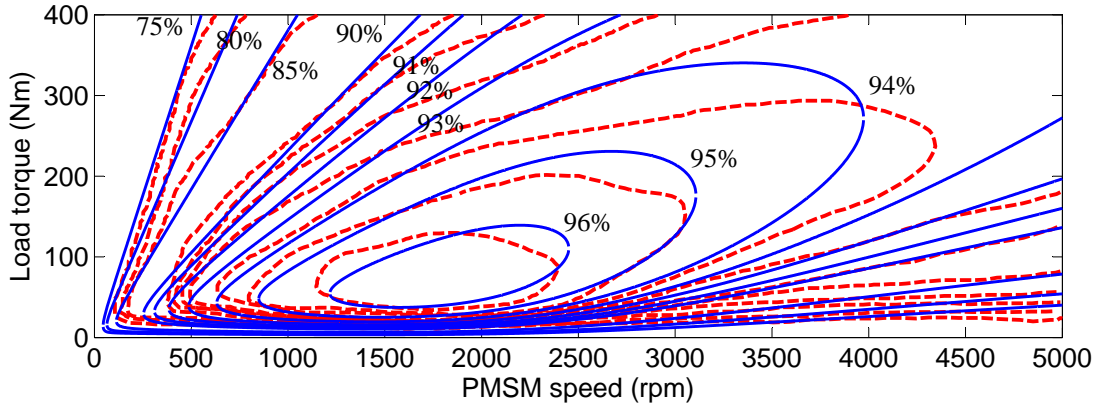


Figure 4.15: PMSM steady-state power efficiency map for the variations in load torque, T_L , and rotor speed, ω_r , for the experimental results in [201] (red dashed line) and for the PMSM model in Equation (4.49) (blue solid line). The contours correspond to constant efficiencies in the range 75%-96%.

At first constant torque functions was used but there was no formation of contours of efficiencies. At next stage a cubic function of ω_r was chosen for T_f . Although this time contours of constant efficiencies were formed but predicted and experimentally generated contours were not giving good match. Finally after a lot of tuning a novel function for friction torque is proposed, which gives best matching of efficiency contours [7] as described in Equation (4.50)

$$T_f = \frac{2}{\pi} \arctan(a_1 \omega_r) \left[a_2 e^{-a_3 |\omega_r|} + (a_4 (|\omega_r| - a_5) + a_6 (|\omega_r| - a_5)^2) \cdot \left(\frac{2}{\pi} \arctan(a_7 (|\omega_r| - a_5)) + a_8 \right) + a_9 \right] \quad (4.50)$$

and its parameter values are found by trial and error to be $a_1 = 10$, $a_2 = 6.0$, $a_3 = 0.6$, $a_4 = 0.03$, $a_5 = 250$, $a_6 = -1.0 \times 10^{-5}$, $a_7 = 0.008$, $a_8 = 0.75$ and $a_9 = 2.1$.

The variation of T_f with positive rotor speed is illustrated in Figure 4.16. It can

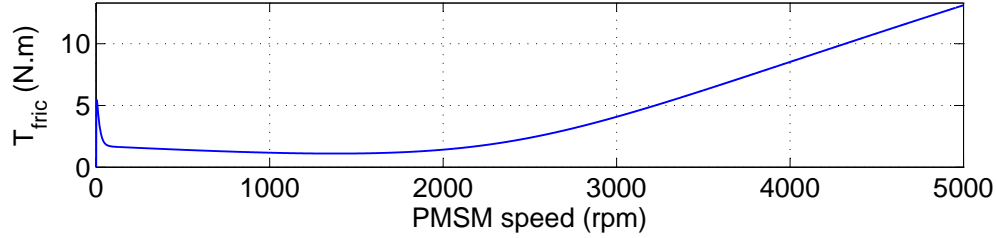


Figure 4.16: Variation of the PMSM frictional torque, T_f , with rotor speed, ω_r .

be seen that at low speed (very near to $\omega_r = 0$), the variation involves some familiar characteristics of mechanical friction, such as static and coulomb friction type behaviors. Here, it is important to remember that T_f is not a friction force in real sense rather it is just a conceptual force used in this model to calculate both electrical (eddy and hysteresis current losses) and mechanical losses (bearing and windage loses), so following a pattern of real mechanical friction is not necessary for T_f . Finally, this particular shape of the friction force T_f is achieved by tuning its parameters to get best fit on the experimentally provided efficiency map as shown in Figure 4.15. The first arctan term in Equation (4.50) is used to provide correct representation of the torque at negative speeds and also to smoothen discontinuity of the torque at zero speeds preventing numerical instability in the simulation. Due to friction and eddy currents temperature of the PMSM increases and this affect the internal resistance and overall losses in the PMSM but there is no model included in this work to account for such thermal effects. Inclusion of thermal model in the PMSM will be a interesting part of the future work.

4.6 Driver Model

A driver model is required in the powertrain to assist the PMSM in tracking any standard drive cycles. The driver model is essentially a tracking controller designed to simulate the actions of a human driver. In simple words, the job of a driver is to accelerate or brake the vehicle while tracking a speed profile. A simple PID controller based driver model was implemented to simulate the actions of acceleration and braking.

Actually, the driving action is already involved in the control of the PMSM drive and that is seen in Equation (4.37). Therefore, the only new thing is that this control action is defined separately as a driver model in Figure 4.12 for better understanding of the PMSM drive. In Figure 4.12 driver model is defined as a black box and in this section its internal dynamics is explained. Figures 4.17 and 4.18 present the schematic diagram of the driver model and its simulink implementation, respectively.

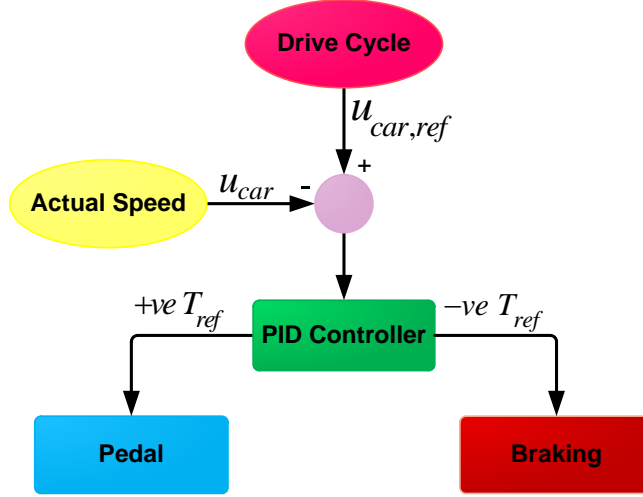


Figure 4.17: Schematic diagram of the driver model

At first, the difference between the reference car speed $u_{car,ref}$ and the actual car speed u_{car} is calculated and is fed to the PID controller, which calculates the torque reference T_{ref} to be generated for tracking the drive cycle. A positive torque reference $T_{ref} > 0$ signifies acceleration of the vehicle and the action involved is the pushing down of pedal according to the magnitude T_{ref} . Similarly, negative torque reference $T_{ref} < 0$ signifies braking of the vehicle and the action involved is to push down the brake. However, in the present case, no mechanical braking is involved, rather dynamic braking and regenerative braking techniques are used to brake the vehicle. As already explained, in the process of regeneration, all the recaptured mechanical energy is sent back to recharge the battery and in the case of dynamic braking, recaptured mechanical energy and supplied electrical energy are dissipated as heat in the winding resistance of the PMSM. Since regeneration is not feasible at very low speeds, dynamic braking is

used to brake the vehicle. The dynamic braking stops the vehicle in a very short time in comparison to regenerative braking. The threshold value of speed, when PMSM goes from regeneration to dynamic braking, depends on the values of parasitic elements of the PMSM drive and demanded level of deceleration.

The mathematical form of the driver model can be presented as follows:

$$T_{ref} = (K_p + K_i \int dt + K_d \frac{d}{dt}) \{u_{car,ref} - u_{car}\} \quad (4.51)$$

Values for the gain of PID controller (K_p , K_i and K_d) are assigned by trial and error

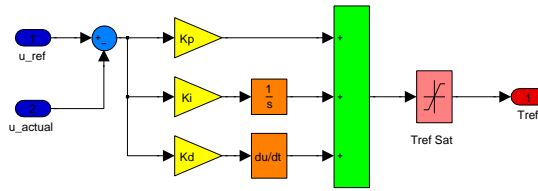


Figure 4.18: Simulink implementation of the driver model

and they are tuned in such a way that tracking error is minimized. Since PID controller tries to generate very high value of the reference torque T_{ref} so that it can track give speed profile immediately but there is always a realistic physical limit for any motor to support desired torque (T_{ref}). Therefore to limit the value desired torque a saturation has been used as shown in Figure 4.18.

4.7 PMSM Simulation Results

The component models built thus far will be used as part of a final integrated HEV model but before the integration, each component will be simulated individually to ensure that they exhibit accurate performance.

The presented PMSM model integrated with the longitudinal car has been used for tracking the standard NEDC cycle [6]. Different simulation cases can be run for powertrains having fixed gear ratios and CVT. In present simulation only CVT led

transmission case has been chosen just to demonstrate the efficacy of the PMSM control mechanism. At this stage, the powertrain does not have any power source such as battery or engine-genset. The DC-link voltage is assumed to be constant 700V, which in the complete model will be supplied by the combined efforts of the engine-generator and the battery with help of suitable converters. At first, the speed difference of the NEDC speed profile and the current forward speed of the longitudinal car is calculated. This speed difference goes to a driver model (PID controller), which calculates the electrical torque reference which in turn decides the magnitudes of quadrature current and direct current as described in Section 4.4. Initial values of all the variables of the PMSM is set to zero ($v_q(0) = 0$, $i_q(0) = 0$, $v_d(0) = 0$, $i_d(0) = 0$ and $u_{car} = 0$). Figure 4.19 presents the standard NEDC drive cycle supplied to the PMSM drive for the testing the PMSM model along with the driver model and the longitudinal vehicle model.

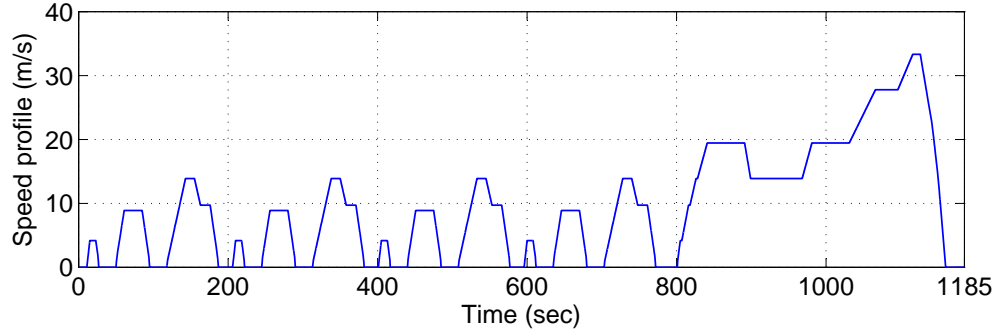


Figure 4.19: Standard NEDC drive cycle for testing of the PMSM drive, along with the driver model and the longitudinal vehicle

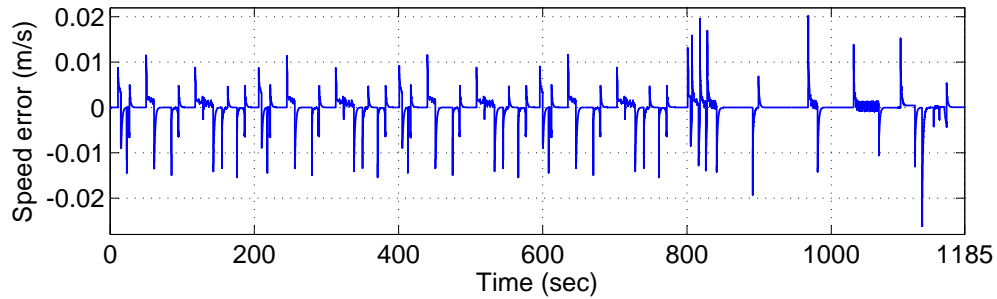


Figure 4.20: Error between the supplied NEDC speed profile and the actual forward speed of the longitudinal vehicle

Figure 4.20 presents the tracking error in the NEDC speed profile of the longitu-

dinal car powered by the PMSM. The electromagnetic torque (caused by the currents in the stator windings of the PMSM) produced by the motor is shown in Figure 4.21. The transient response of the PMSM can be clearly observed in the figure. The load torque supplied to the longitudinal car is calculated by the expression $T_L = T_e - T_f$ and is presented in Figure 4.22. As a result of transients, high frequency components can clearly be seen in all variables of the PMSM.

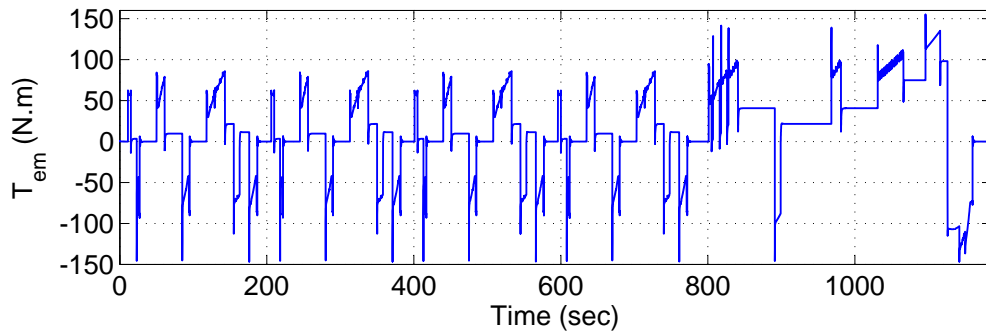


Figure 4.21: Electromagnetic torque T_e generation in the PMSM

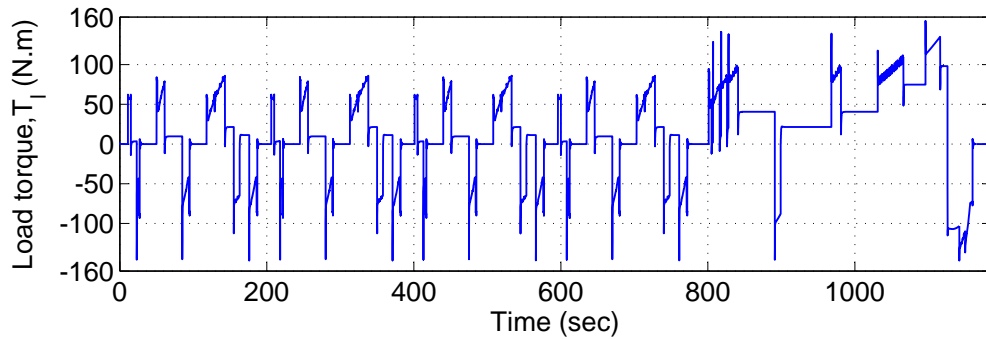


Figure 4.22: Load torque T_L applied at the transmission shaft of the longitudinal car

Figures 4.23 and 4.24 present the $d - q$ axes currents of the motor. Vector control method linearizes the non-linear model of the PMSM due to which the electromagnetic torque is directly proportional to the quadrature current i_q . Since there are high frequency transients in the load torque getting further translated into electromagnetic torque and subsequently $d - q$ axes currents, according to the control law, the quadrature current i_q during acceleration of the car will have high transient values but constant non-zero value during steady state. This can be observed in Figure 4.23. Ideally, direct current i_d should be zero all the time but i_d deviates from zero value during transients

of the car and immediately attains very nominal value such as 0.2A during steady state conditions. Moreover, even during transients, the maximum deviation of $i_d = 12\text{A}$ is very small in comparison to i_q having values as high as 140A. Therefore, the overall control mechanism is working significantly in the accepted domain.

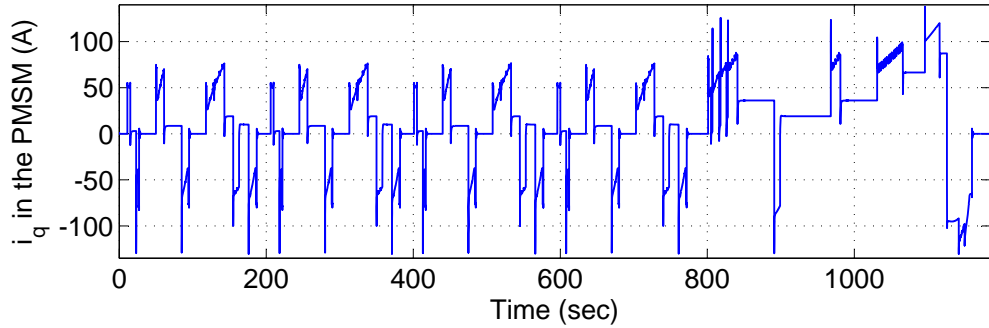


Figure 4.23: Quadrature axis current of the PMSM i_q

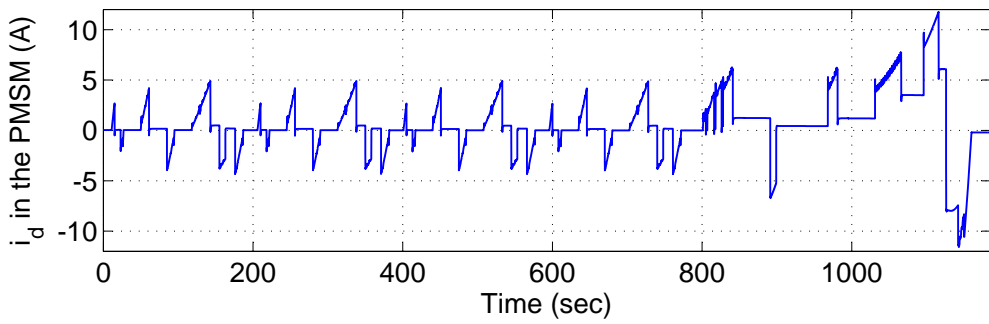


Figure 4.24: Direct axis current of the PMSM i_d

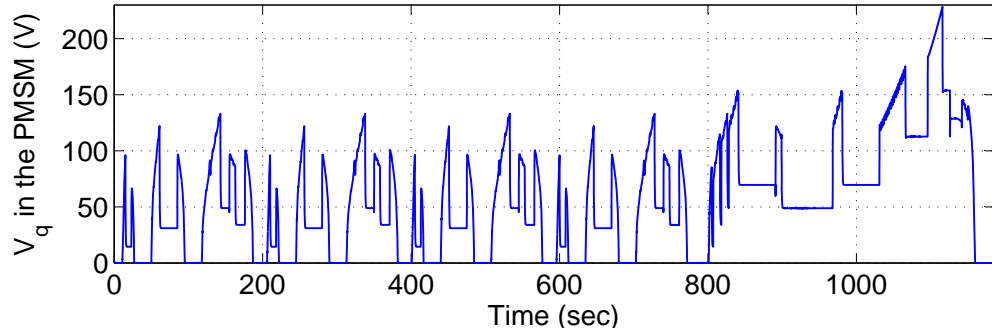


Figure 4.25: Quadrature axis voltage of the PMSM v_q

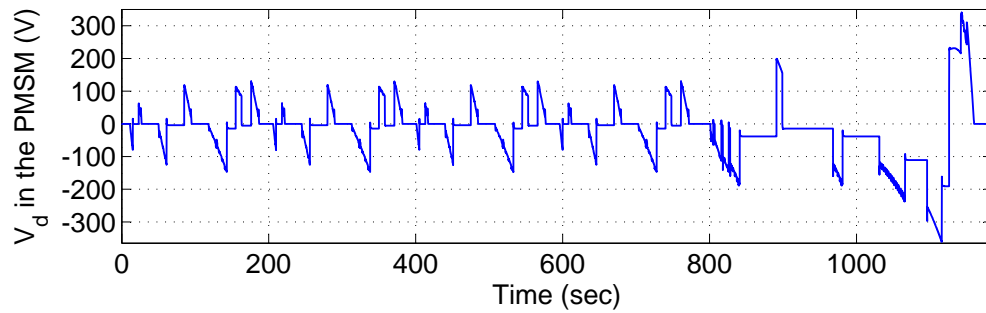


Figure 4.26: Direct axis voltage of the PMSM v_d

4.8 Summary

- The benefits of using the PMSM for the HEV powertrain, and its modelling are presented in this chapter. Standard and detailed $d - q$ frame equations based mathematical model is used to capture the dynamics of the PMSM drive.
- Average modelling technique in the $d - q$ frame is used to describe the dynamics of the pulse-width modulation (PWM) based DC/AC converter. Vector control method (field oriented control) is used to linearize the PMSM model. Simple PI controllers based control strategy is implemented for the speed control of the PMSM drive.
- A novel friction torque model to calculate the various losses in the PMSM is presented and validated against experimental data provided by the manufacturer.
- A PID controller based driver model is presented to track the standard NEDC cycle.
- The longitudinal car, presented in the previous chapter, driven by the PMSM successfully tracks the NEDC cycle with maximum error in the order of 10^{-4} m/s.
- The ability to capture the transient dynamics of the PMSM and energy balance across its input and output ports mark the success of the standalone modelling of the PMSM drive.

CHAPTER**FIVE**

PERMANENT MAGNET SYNCHRONOUS GENERATOR MODELLING

5.1 Introduction

The Permanent Magnet Synchronous Generator (PMSG) has the exact reverse function of the PMSM. In this work, a series-architecture powertrain has been used. The engine applies torque to the generator and the generator produces electrical power, supplied at a constant voltage to motor electronics (including inverter). Finally, the motor drives the wheels of the vehicle through the transmission. Supervisory control governs the power splitting mechanism, which decides usage of the generator and the battery, to manage the power splitting in an optimal way. It is a commonly observed fact that at higher load, the engine gives higher efficiency and at lower load, the battery gives higher efficiency, and the supervisory control considers these aspects along with other principles and constraints. Figure 5.1 gives detailed circuitry diagram of the PMSG driven AC/DC converter (rectifier), DC/AC converter (inverter) and the PMSM. Details of the PMSG modelling are given in further sections. Here again, the PWM switching has been simplified to an average model for faster simulation.

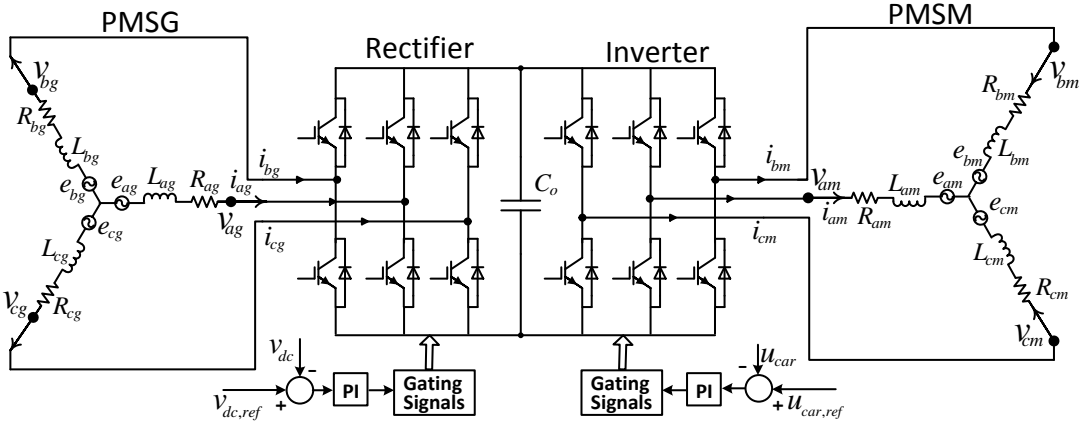


Figure 5.1: Circuit diagram showing electrical connection of the generator (PMSG), AC/DC rectifier, DC/AC inverter and motor (PMSM). Symbols v , i , R , L and e represent phase voltages, currents, resistances, inductances and induced e.m.f.'s respectively. Subscripts a , b and c correspond to the individual phases, and subscripts g and m correspond to 'generator' and 'motor' respectively. C_0 is the DC-link capacitor, v_{dc} is the DC-link voltage and u_{car} is the forward speed of the car. The signals related to the control of v_{dc} and u_{car} are also shown.

5.2 Permanent Magnet Synchronous Generator

The PMSG is used in hybrid electric vehicles to transform mechanical energy produced by the engine into electrical energy. This electrical energy may be accounted as voltage and current supplied to the motor or to charge the battery. The mechanical structure of the PMSG is the same as the PMSM. In the PMSG, when the rotor holding magnets are rotated, back *emf* is generated in the stator coils. This back *emf* causes current to flow in the stator coils. Once this motion and flow of current has started, the mathematical equations for the generator are the same as for the motor. The only difference between the PMSG and the PMSM is the direction of current flow and generated torque. In the case of the motor, current and voltage are applied as inputs and torque is produced as the output. In case of the generator, torque is applied to the generator shaft as an input and current and voltage flow-out and appear at the stator coils as outputs.

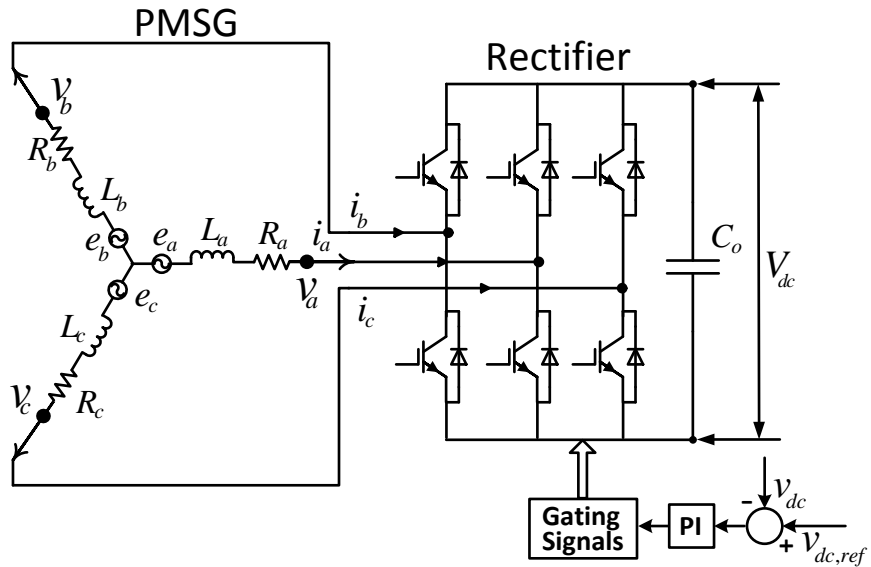


Figure 5.2: Permanent magnet synchronous generator with three phase AC/DC rectifier with constant DC-link voltage

5.2.1 Permanent magnet synchronous generator model in the D-Q frame

All electrical and mechanical dynamic equations of the PMSG are the same as the PMSM. The only difference is that the flow of current and torque are reversed in the case of the generator as compared to the motor. Some authors present equations with a few sign changes in order to include flow reversal of current and torque. Any of the sign conventions can be followed but that should be consistent from beginning to end.

Figure 5.2 presents the circuit diagram of the PMSG with three phase AC/DC rectifier while maintaining constant DC-link voltage. Three phase terminal voltages v_a , v_b , v_c can be expressed as [68]:

$$v_a = E \sin \theta - R i_a - L \frac{di_a}{dt} \quad (5.1)$$

$$v_b = E \sin(\theta - \frac{2\pi}{3}) - R i_b - L \frac{di_b}{dt} \quad (5.2)$$

$$v_c = E \sin(\theta + \frac{2\pi}{3}) - R i_c - L \frac{di_c}{dt} \quad (5.3)$$

where E is the amplitude of the back *emf* directly proportional to the rotational speed

of the PMSG ($E \propto \omega_r$). i_a , i_b and i_c are instantaneous three phase stator currents. R and L are the resistance and inductance of the stator coils. $\theta = \omega t + \theta_0$ is the instantaneous position of the rotating q phase with respect to the fixed winding phase a .

The three phase equations of the PMSG are transformed into two phase rotating $d - q$ frame as in the case of the PMSM. By this transformation, three phase AC variables are transformed into DC variables, where the control design becomes easy. The transformation of three phase equations to two phase helps eliminate cross coupling terms between the real and reactive power. Park transformation was illustrated in Figure 4.7, and the transformation can be described by:

$$\begin{pmatrix} f_q \\ f_d \\ f_o \end{pmatrix} = \frac{2}{3} \begin{pmatrix} \cos(\theta) & \cos(\theta - 2\pi/3) & \cos(\theta + 2\pi/3) \\ \sin(\theta) & \sin(\theta - 2\pi/3) & \sin(\theta + 2\pi/3) \\ 1/2 & 1/2 & 1/2 \end{pmatrix} \begin{pmatrix} f_a \\ f_b \\ f_c \end{pmatrix}$$

Here f_a , f_b , f_c are variables (currents i_a , i_b , i_c or voltage v_a , v_b , v_c) in three phase a, b and c respectively.

The reverse is also possible. That is, a , b , c variables can be obtained from the $d - q$ variables using the inverse Park transform, as follows:

$$\begin{pmatrix} f_a \\ f_b \\ f_c \end{pmatrix} = \begin{pmatrix} \cos(\theta) & \sin(\theta) & 1 \\ \cos(\theta - 2\pi/3) & \sin(\theta - 2\pi/3) & 1 \\ \cos(\theta + 2\pi/3) & \sin(\theta + 2\pi/3) & 1 \end{pmatrix} \begin{pmatrix} f_q \\ f_d \\ f_o \end{pmatrix}$$

Boldea [56] describes the PMSG $d - q$ frame equations in motor format, i.e, the machine will be working as a generator only when both i_q and i_d have negative signs. In the present work, the generator format is employed, according to which the machine will be working as a generator when both i_q and i_d have positive values. According to the sign conventions followed in the present work, in the case of the PMSM, positive i_q and i_d means that the current is flowing-in to the stator coils from the DC-link whereas in the case of PMSG, positive i_q and i_d means that the current is flowing-out of the

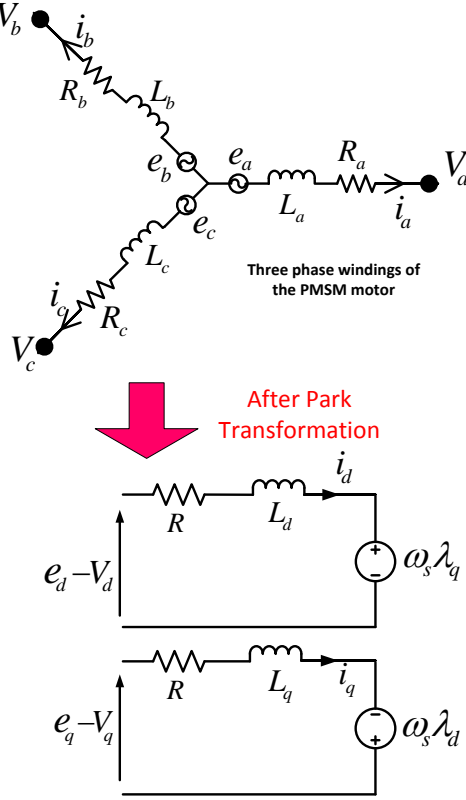


Figure 5.3: Equations of PMSG in rotating d-q axis reference frame

stator coils. This scheme is followed consistently in the present work.

$$\frac{di_q}{dt} = (-R \cdot i_q - \omega_e L_d i_d + e_q - v_q) / L_q \quad (5.4)$$

$$\frac{di_d}{dt} = (-R \cdot i_d + \omega_e L_q i_q + e_d - v_d) / L_d \quad (5.5)$$

e_d , e_q are the d and q components of the back emf ; v_d , v_q are the d and q axis terminal voltages; i_d , i_q are the d and q axis stator currents; L_d , L_q are the d and q axis inductances. R and ω_e are the stator resistance and rectifier frequencies (speed of the rotating electromagnetic field), respectively.

Since the q -axis counter electric potential $e_q = \omega_e \lambda_f$ and the d -axis counter electric potential $e_d = 0$, the above equation can be presented as [55, 203]:

$$\frac{di_q}{dt} = (-R \cdot i_q - \omega_e (L_d i_d + \lambda_f) - v_q) / L_q \quad (5.6)$$

λ_f is the flux linkage due to other rotor magnets linking the stator.

$$\frac{di_d}{dt} = (-R \cdot i_d + \omega_e L_q i_q - v_d) / L_d \quad (5.7)$$

The electromagnetic torque is calculated by the following equation:

$$T_e = 3p[\lambda_f i_q + (L_d - L_q)i_d i_q] / 2 \quad (5.8)$$

and the generator mechanical dynamics equation is

$$T_L - T_e = B\omega_r + J_g d(\omega_r) / dt \quad (5.9)$$

where p is the number of pole pairs, T_L is the mechanical torque supplied by the IC engine, B is the damping coefficient, ω_r is the rotor speed, and J_g is the moment of inertia. In addition, the rotor speed and rectifier frequency are related as:

$$\omega_e = p\omega_r \quad (5.10)$$

Total power input into the generator is

$$P_{in} = T_L \omega_r \quad (5.11)$$

Total power output from the generator is

$$P_{out} = (v_a \cdot i_a + v_b \cdot i_b + v_c \cdot i_c) \quad (5.12)$$

Similarly, power can be calculated in the $d - q$ frame as

$$P_{out} = \frac{3}{2}(v_q \cdot i_q + v_d \cdot i_d) \quad (5.13)$$

$$P_{loss} = P_{l,c} + P_{l,e} + P_{l,h} + P_{l,b} + P_{l,w} \quad (5.14)$$

$$P_{l,c} = \frac{3}{2}R(i_q^2 + i_d^2) \quad (5.15)$$

Once again, $P_{l,c}$ denotes copper losses, $P_{l,e}$ denotes eddy current losses, $P_{l,h}$ denotes hysteresis losses, $P_{l,b}$ denotes bearing losses and $P_{l,w}$ denotes windage losses. Only the expression for copper loss evaluation is given here. However, in Section 5.5, a novel model accommodating all other losses will be described in detail.

5.3 Average model of the three phase AC/DC converter (Rectifier)

The time averaged model for the three phase converter has already been discussed in the previous chapter on the motor. The same modelling technique will be used here for the three phase AC to DC converter or rectifier. Details for average switching will not be discussed again, rather the average model of the AC/DC converter will be presented directly. The reasons to use an average model have been established in the previous sections.

Optimal AC/DC converter should output pure DC voltage and current and draw a pure sinusoidal current at unity power factor from the AC lines. It has been assumed that all the circuit elements given in Figure 5.2 are linear time invariant (LTI) and all the switches are bi-directional. The switches operate in continuous conduction mode and are turned on and off, such that the output DC voltage is never shorted. Using the concept of average modelling of the PWM switching given in Equation (4.26), the AC/DC converter can be modelled as [69]:

$$i_{dc} = d_a i_a + d_b i_b + d_c i_c \quad (5.16)$$

where i_{dc} is DC current drawn from the DC-link by the motor and i_a , i_b and i_c are respective three phase AC currents flowing from the generator. The DC-link voltage v_{dc}

can be related to the three phase AC voltages (v_a , v_b , v_c) in the following manner [68]:

$$v_a = v_{dc} \left(d_a - \frac{d_a + d_b + d_c}{3} \right) \quad (5.17)$$

$$v_b = v_{dc} \left(d_b - \frac{d_a + d_b + d_c}{3} \right) \quad (5.18)$$

$$v_c = v_{dc} \left(d_c - \frac{d_a + d_b + d_c}{3} \right) \quad (5.19)$$

where d_a , d_b and d_c are bipolar switching functions. Each converter leg has two switches and the switching is defined as follows:

$$d_j = \begin{cases} 1, & S_j \text{ closed} \\ 0, & S'_j \text{ open} \end{cases} \quad j = a, b, c. \quad (5.20)$$

Equations (5.16)-(5.19) show the relationship between the DC and AC sides of the converter under certain switching patterns. After the transformation from abc to $d-q$ frame, equations (5.16)-(5.19) can be expressed as follows [68, 69, 204]:

$$i_{dc} = \frac{3}{2}(d_q \cdot i_q + d_d \cdot i_d) \quad (5.21)$$

The rectifier input terminal voltages are related to the DC voltage through switching functions d_d and d_q , as follows [69, 204]:

$$v_d = d_d \cdot v_{dc} \quad (5.22)$$

$$v_q = d_q \cdot v_{dc} \quad (5.23)$$

where d_d , d_q stand for switching patterns in the $d-q$ frame.

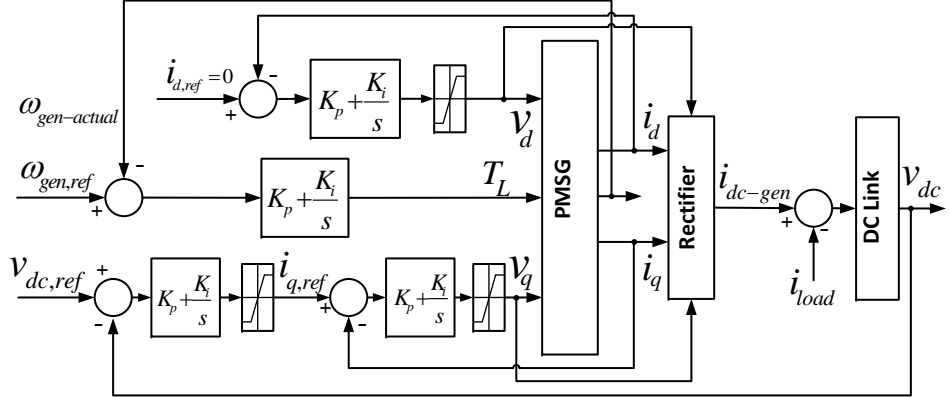


Figure 5.4: Schematic diagram of the control loops of the PMSG. Symbols used in diagram represent conventional variables as described in different equations of PMSG drive.

5.4 Control Mechanism

It is known that while the rotor is rotating at a constant speed, it is possible to generate fixed peak voltage at the terminals. The shaft of the generator is mechanically coupled with the shaft of the IC engine driving the generator at constant angular speed and providing required torque T_L to overcome opposing electrical torque T_e . Once the PMSG is driven at a fixed angular speed, the DC-link voltage regulation will be achieved by controlling the AC/DC converter. Figure 5.4 illustrates the complete strategy of the control in a schematic diagram.

The overall DC voltage regulator has three control loops, a speed control loop and other two loops nested successively to control the DC-link voltage. The speed control loop controls the speed of the PMSG shaft to ensure sufficient back *emf* generation supplying the power demand from the load and also ensure that engine and generator are operating at an efficient operating condition. In the present chapter, standalone simulation of the PMSG is presented. Since there is no IC engine to supply the required torque to the PMSG, a simple PI controller is used instead of the complete IC engine. The other two control loops are the voltage and current control loops, described in the next section.

The DC-link equation can be written as follows:

$$C_o \frac{dv_{dc}}{dt} = i_{gen-dc} - i_{load} \quad (5.24)$$

where v_{dc} is the DC-link voltage, $i_{gen-dc} = i_{dc}$ is the DC current fed to the DC-link by the rectifier and i_{load} is the DC-load current drawn by the load on other side of the DC link. C_o is the capacitance of the DC-link capacitor.

5.4.1 Speed control loop design

To implement the speed control loop, the difference between the reference rotor speed ($\omega_{gen-ref}$) and the actual rotor speed ($\omega_{gen-actual}$) of the PMSG is calculated first. Subsequently, this speed difference is passed through a PI controller to generate the load torque T_L . Later in the integrated powertrain, this PI controller will be replaced by the IC engine along with its fuel controller. Before integrating the engine to the generator, the PMSG is tested standalone with the help of the PI controller.

$$T_L = (k_1 + k_2 \int dt) \{ \omega_{gen,ref} - \omega_{gen-actual} \} \quad (5.25)$$

5.4.2 Voltage and current control loop design

In the nested control loops, the outer loop is a slower voltage control loop and the inner loop is a faster current control loop. First of all, a reference voltage will be given and since the motor needs supply of constant voltage, the DC-link reference voltage is already known. The difference between the actual DC-link voltage $v_{dc-actual}$ and the reference DC-link voltage $v_{dc,ref}$ is passed through a PI controller and this output will be multiplied by $\sin\phi$ and $\cos\phi$ to generate the references $i_{d,ref}$ and $i_{q,ref}$, respectively. These reference currents in d and q axis will determine the real and reactive power respectively supplied by the generator. The reference currents $i_{d,ref}$

and $i_{q,ref}$ are compared with the actual phase currents i_d and i_q . The error is again passed through a PI controller and the output is the required v_d^* and v_q^* , respectively. Since switching is very fast in comparison to longitudinal dynamics of the complete powertrain, the switching can easily be ignored without any significant loss of accuracy due to fast simulation and modelling simplicity. Hence, these required terminal voltages v_d^* and v_q^* are directly fed to the PMSG as v_d and v_q after passing through the saturation blocks.

The outer voltage controller gives the current reference, which gets multiplied with the required power factor and corresponds to the amplitude of the phase current.

$$i_{dq,ref} = (k_1 + k_2 \int dt) \{v_{dc,ref} - v_{dc-actual}\} \quad (5.26)$$

Optimal performance of AC to DC converter in terms of power can be achieved when the converter draws perfect sinusoidal current at unity power factor from the PMSG. In order to achieve unity power factor, $\sin \phi = 0$ and $\cos \phi = 1$ are taken and the reference signals should satisfy $i_{d,ref} = 0$. Since $\sin \phi = 0$, the converter outputs no reactive power.

In order to design a voltage controller, a linear model of the generator is required similar to the PMSM. The vector control technique, as in the case of the PMSM, can be applied here as well to linearize the PMSG model. To draw maximum power at unity power factor from the generator, $i_{d,ref} = 0$ has already been chosen. In the case of the PMSM, $i_{d,ref} = 0$ generates maximum torque whereas in the case of the PMSG, $i_{d,ref} = 0$ generates maximum power. Hence, the direct axis current i_d needs to be kept parallel to the direction of rotor flux. Since the quadrature axis is perpendicular to the direct axis, only the quadrature axis current i_q will play a role in determining the resultant electromagnetic torque. i_d contributes only to the increase and decrease of the net air-gap flux similar to the PMSM. By forcing $i_d = 0$, the following equations can be

derived for the PMSG:

$$\lambda_d = \lambda_f \quad (5.27)$$

$$T_e = 3p\lambda_f i_q / 2 \quad (5.28)$$

From Equation (5.28), it is clear that torque is a linear function of the quadrature current and by controlling the i_q alone, the electromagnetic torque produced in the generator can be controlled. In the summary, the PMSG model is now linearized by the application of the vector control technique. Although this control scheme is derived for the linear model of the PMSG, it is required for operation over the entire operating range of the PMSG. The required terminal voltages are as follows [68]:

$$\begin{aligned} v_d^* &= k_{11} + k_{12} \int (i_{d,ref} - i_{d-actual}) \\ v_q^* &= k_{21} + k_{22} \int (i_{q,ref} - i_{q-actual}) \end{aligned} \quad (5.29)$$

k_{11}, k_{12}, k_{21} and k_{22} are proportional and integral gains for the control loops.

v_d^* and v_q^* in Equation (5.29) are the required instantaneous voltages provided by the average model of the PWM converter. In Equation (5.29), the command signals $i_{d,ref}$ and $i_{q,ref}$ are determined by the desirable power factor finally determining the active power (P) and the reactive power (Q) of the rectifier terminals. In the meantime, v_d and v_q ensure that the actual currents are equal to $i_{d,ref}$ and $i_{q,ref}$, respectively, so both amplitude and phase can be controlled. Figure 5.8 represents both control loops and Figure 5.9 describes the internal dynamics of the PMSG.

5.4.3 Simulink implementation of the PMSM drive

Figure 5.5 presents simulink block diagram of the high level view of the PMSG drive. The PMSG in association of the AC/DC converter (rectifier) regulates the DC-link voltage. Figure 5.6 describes the simulink implementation of the AC/DC converter as described in Equations (5.21)-(5.23). Simulink implementation of the DC-link Equation

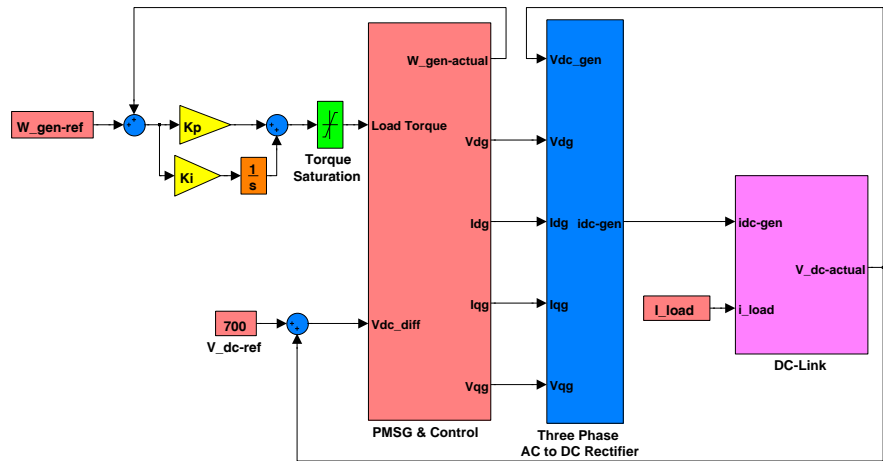


Figure 5.5: Overall PMSG drive control model in simulink

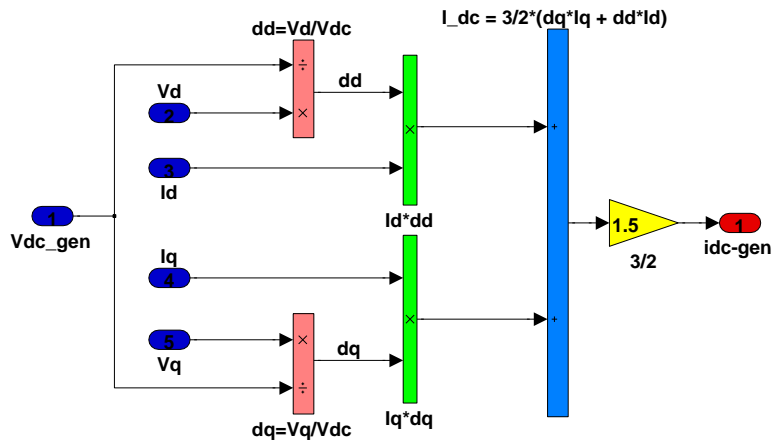


Figure 5.6: Average modelling of the rectifier in simulink

5.24 is presented in Figure 5.7. Figure 5.8 presents the simulink implementation of PMSG control. Internal dynamics of the PMSG, as described by Equations (5.6)-(5.9), is presented in 5.9.

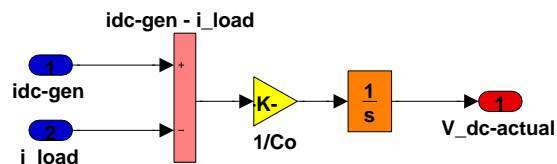


Figure 5.7: DC-link model in simulink

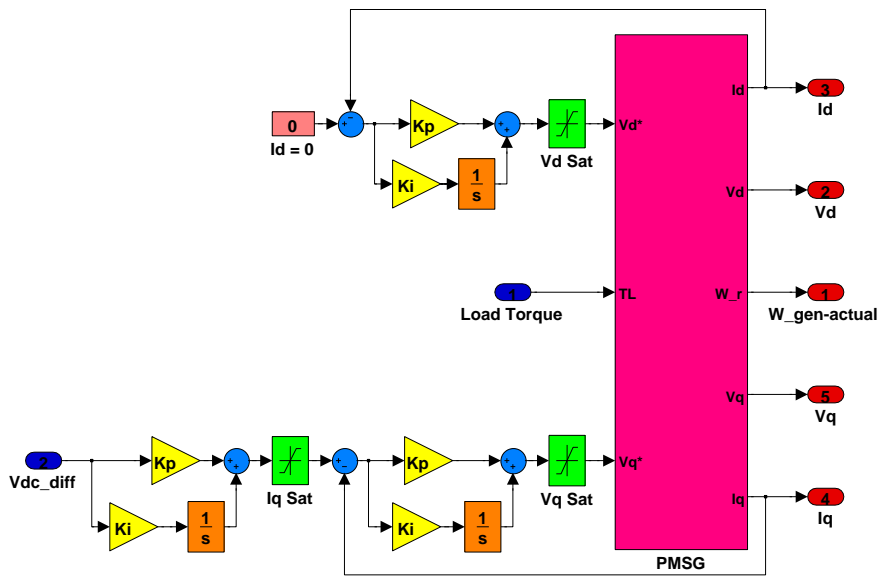


Figure 5.8: Level I of the PMSG model in simulink

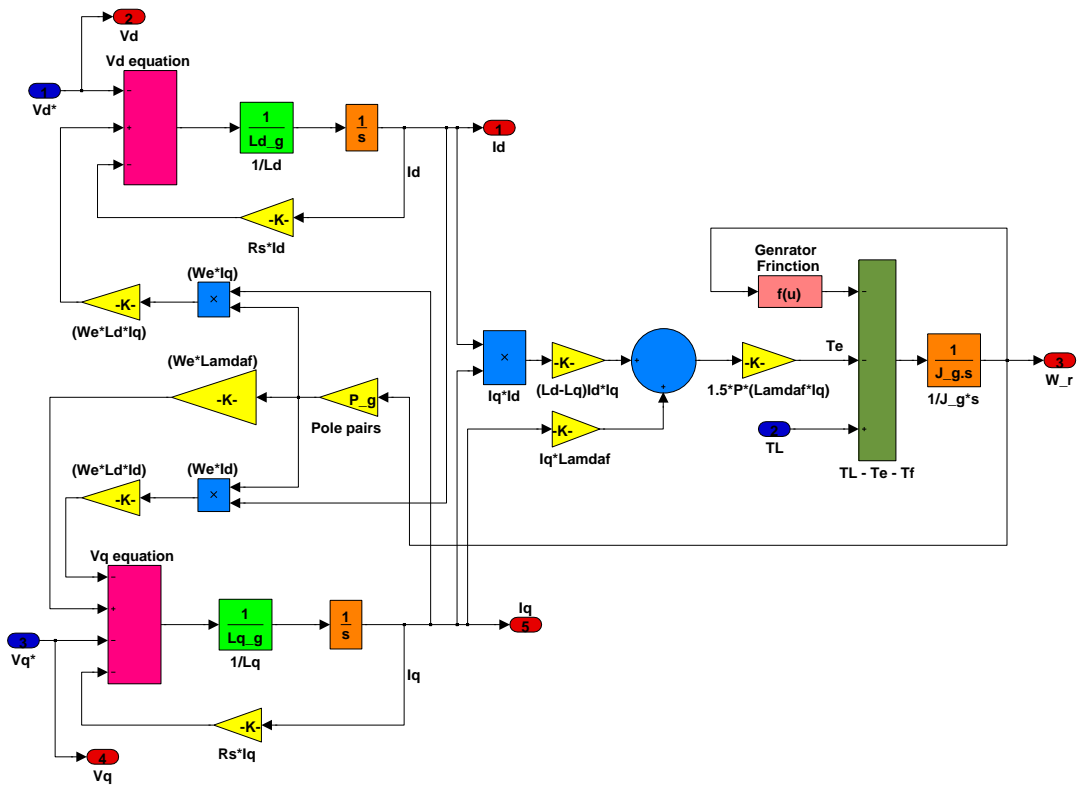


Figure 5.9: Level II of the PMSG model in simulink

Table 5.1: Parameter values of the PMSG.

PMSG Parameter	Symbols	Values
Nominal rated power	P_n	92 KVA
Maximum speed	ω_n	5000 RPM
Stator resistance	R	0.09 Ω
D axis stator inductance	L_d	0.0045 mH
Q axis stator inductance	L_q	0.0045 mH
Rotor magnetic flux	λ_f	0.2125 Wb
Moment of inertia	J	0.05 Kgm^2
Number of pole pairs	p	6

5.5 Power Loss Model of the PMSG

The PMSG parameter values used in our model are from the AFG-140 axial flux PMSG, developed and manufactured by EVO Electric [205], and shown in Table (5.1).

Under steady-state conditions, T_e , the driving torque T_L , and T_f are related as follows:

$$T_e = T_L - T_f. \quad (5.30)$$

$$P_{in} = T_L \omega_r \quad (5.31)$$

$$P_{out} = \frac{3}{2}(v_q i_q + v_d i_d) = -\frac{3}{2} i_q^2 R + T_e \omega_r \quad (5.32)$$

$$= -\frac{3}{2} \left(\frac{T_e}{\frac{3}{2} \lambda_f p} \right)^2 R + T_e \omega_r \quad (5.33)$$

$$\eta = \frac{P_{out}}{P_{in}} \quad (5.34)$$

$$\eta = \frac{-\frac{3}{2} \left(\frac{T_e}{\frac{3}{2} \lambda_f p} \right)^2 R + T_e \omega_r}{T_L \omega_r} \quad (5.35)$$

Here $\omega_r = \omega_{gen}$ is the rotational speed of the PMSG.

Using a similar analysis to the one conducted for the PMSM in Section 4.5, it can be shown that in the case of the PMSG, the following relationship holds true under

steady-state conditions:

$$\frac{2R}{3\lambda_0^2 p^2} T_L^2 + \left(-\frac{4RT_f}{3\lambda_0^2 p^2} - \omega_r + \eta \omega_r \right) T_L + \frac{2RT_f^2}{3\lambda_0^2 p^2} + \omega_r T_f = 0. \quad (5.36)$$

The efficiency is given by $\eta = \frac{P_{out}}{P_{in}} = \frac{P_{out}}{T_L \omega_r}$, and by rearranging we following relationship will be obtained

$$T_L = \frac{P_{out}}{\eta \omega_r}. \quad (5.37)$$

On substituting Equation (5.37) in Equation (5.36), a quadratic equation for P_{out} is obtained which can be solved to obtain $P_{out}(\eta, \omega_r)$. The friction torque is chosen so that the predicted P_{out} fits well the experimental data provided by the manufacturer [205] as η and ω_r vary. The proposed friction torque is given in Equation (5.38) very similar to the PMSM one:

$$T_f = \frac{2}{\pi} \arctan(a_1 \omega_r) \left[a_2 e^{-a_3 |\omega_r|} + (a_4 (|\omega_r| - a_5) + a_6 (|\omega_r| - a_5)^2) \cdot \left(\frac{2}{\pi} \arctan(a_7 (|\omega_r| - a_5)) + a_8 \right) + a_9 \right] \quad (5.38)$$

The optimal parameter values for the friction expression for the PMSG are found to be $a_1 = 10$, $a_2 = 1$, $a_3 = 0.1$, $a_4 = -0.0019$, $a_5 = 0$, $a_6 = 1.38 \times 10^{-5}$, $a_7 = 0.02$, $a_8 = 1$ and $a_9 = 1.2$. The variation of friction torque with rotational speed is shown in Figure 5.10 and the accuracy of the power loss model is demonstrated in Figure 5.11. Once again very similar to PMSM, this particular shape of the friction force T_f in the PMSG is result of tuning its parameters to get best fit on the experimentally provided efficiency map as shown in Figure 5.11.

5.6 Simulation Results

Simulation results of the standalone PMSG drive are presented in this section. The PMSG drive contains the PMSG along with the AC/DC converter and the DC-link.

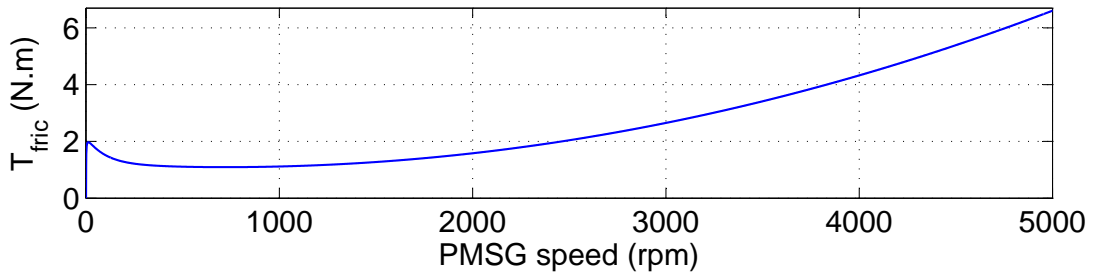


Figure 5.10: Variation of the PMSG frictional torque, T_f , with rotor speed, ω_r .

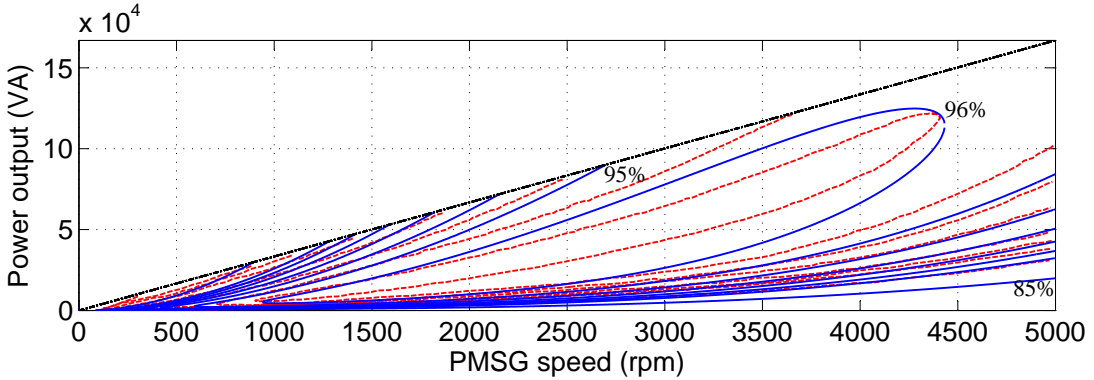


Figure 5.11: PMSG steady-state power efficiency map for variations in output power, P_{out} , and rotor speed, ω_r , for experimental results in [205] (red dashed line) and for the PMSG model in Equations (5.36) and (5.37) (blue solid line). The contours correspond to constant efficiencies in the range 85% – 96%.

The aim of this drive is to maintain the 700V at the DC-link, which is connected to the other end of the AC/DC converter. The AC/DC converter is connected to the PMSG to transform the input AC power to DC power at the output of the converter. In the present standalone PMSG drive simulation, a PI controller is used to supply the mechanical load torque T_L at constant PMSG rotor speed to meet the power required at the DC-link. In the integrated powertrain, this required load torque T_L will be supplied by an IC engine rather than a PI controller and inertias of the engine and the PMSG will be coupled by a constant gear ratio G . Initial DC-link voltage is taken as $v_{dc}(0) = 700V$ (capacitor is fully charged) else all other variables have zero as initial value ($v_q(0) = 0$, $i_q(0) = 0$, $v_d(0) = 0$, $i_d(0) = 0$ and $\omega_r = 0$). A constant DC current $i_{load} = 40A$ is drawn from the DC-link as load on the PMSG drive. Figure 5.12 presents the DC-link voltage which is kept constant at 700V by controlling the stator voltages and currents and constant rotational speed of the generator. Since, initial winding currents and voltages (i_q , i_d ,

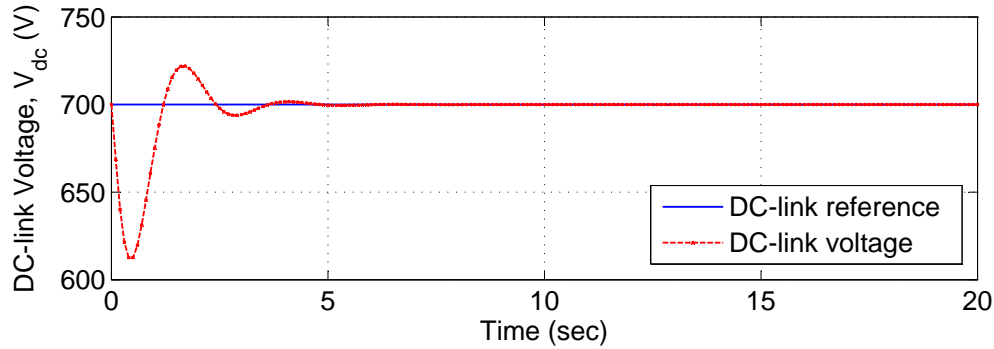


Figure 5.12: Voltage produced by the PMSG Generator at DC-link

v_d and v_q) have zero value but load current have nonzero value ($i_{load} = 40A$) so there is a deviation in the DC-link voltage at the beginning of the simulation. But once the PMSG rotor set in to the rotation, voltages and currents in the windings start taking non-zero values, after passing through the initial transient phase DC-link voltage soon get regulated at 700V.

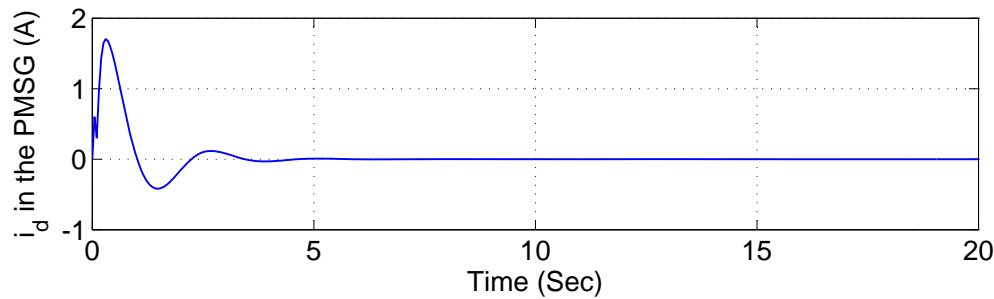


Figure 5.13: Direct axis current of the PMSG i_d

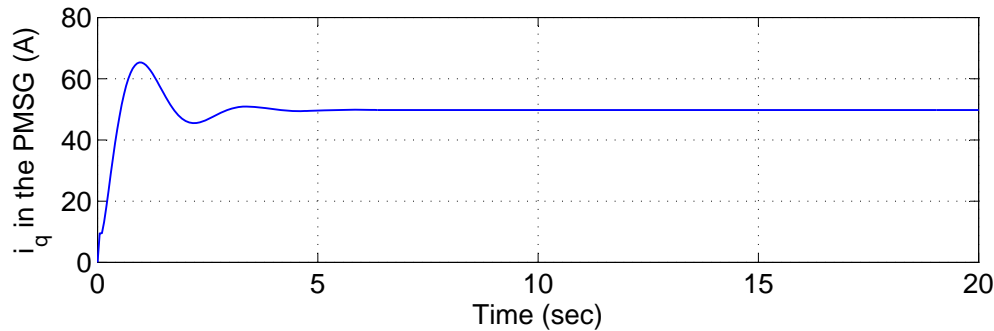


Figure 5.14: Quadrature axis current of the PMSG i_q

According to the control laws for the currents, the direct axis current i_d and the quadrature axis current i_q should be zero and non-zero (positive value) respectively.

It can be observed in Figures 5.13 and 5.14 that the direct axis current ($i_d = -1.93 \times 10^{-6}$ A) is approximately zero in the steady state and the quadrature current ($i_q = 49.75$ A) is non zero at steady state. Figures 5.15 and 5.16 present the direct axis voltage and quadrature axis voltage of the PMSG.

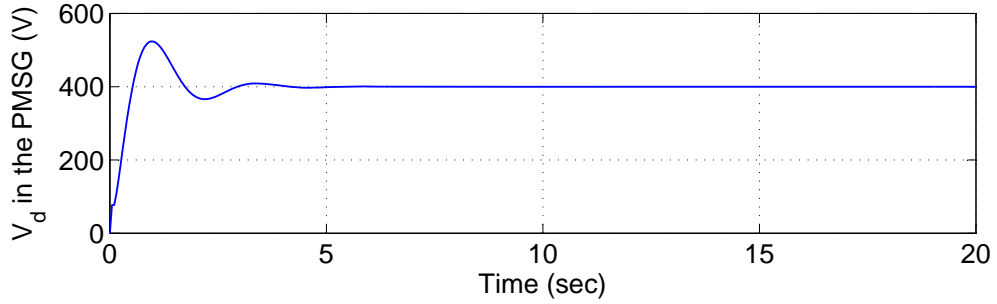


Figure 5.15: Direct axis voltage of the PMSG v_d

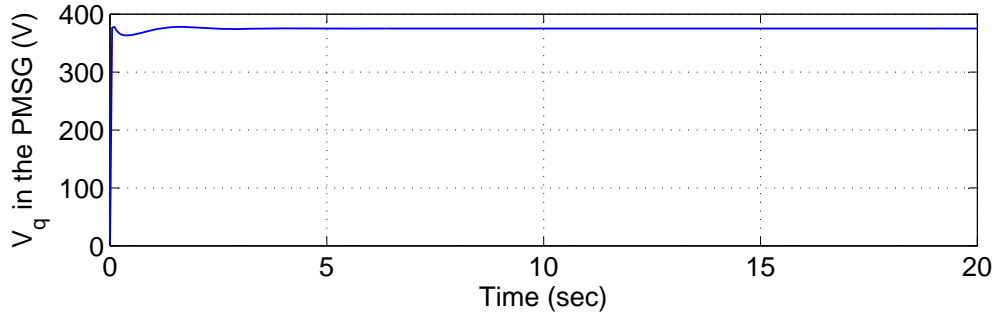


Figure 5.16: Quadrature axis voltage of the PMSG v_q

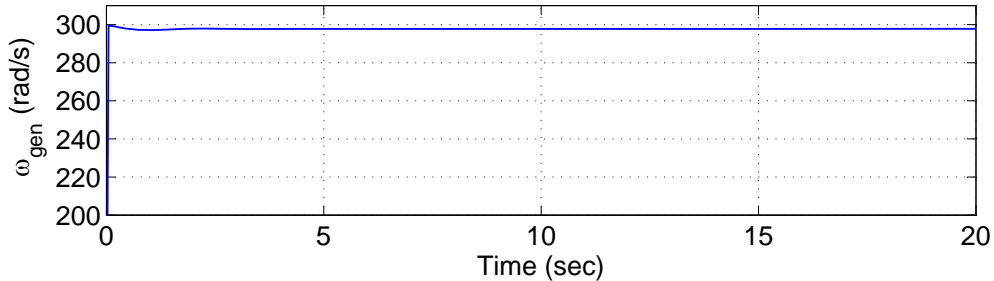


Figure 5.17: Rotational speed of the PMSG rotor shaft

Figure 5.17 shows that the rotational speed is successfully kept constant at 300 rpm as desired. The power input to the PMSG is $P_{in} = T_L \cdot \omega_r$ and the power output from the PMSG drive at the DC-link is $P_{out} = i_{load} \cdot v_{dc-link}$. At the input port, rotor speed ω_r is kept constant and at the output port, the DC-link voltage $v_{dc-link}$ is kept constant. Therefore, the load torque T_L varies in response to the variation of demanded

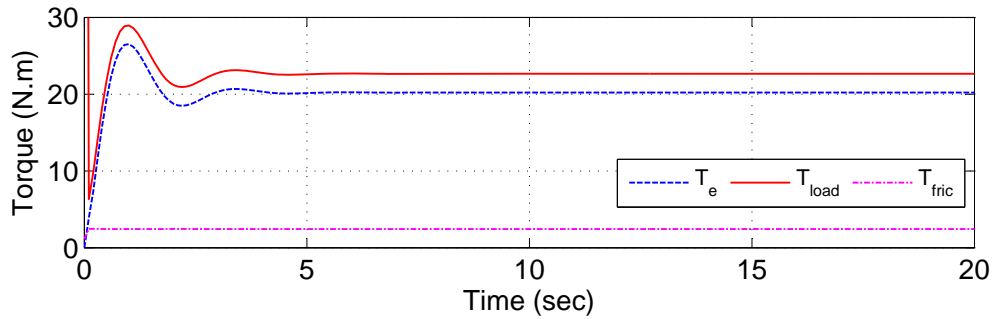


Figure 5.18: Comparative magnitudes of all three torques, namely, load torque $T_L = T_{load}$, electromagnetic torque T_e , and frictional torque T_f involved in the PMSG drive

i_{load} . In the present case, since the load current $i_{load} = 40A$ has constant value, the load torque T_L is also constant. Figure 5.18 presents comparative magnitudes of all the three torques, namely, the load torque T_L , the electromagnetic torque T_e , and the frictional torque T_f involved in the PMSG drive. Since the load current $i_{load} = 40A$ has constant value, the load torque T_L and T_e are also constant in steady state. Due to constant rotational speed of the PMSG ω_r , the frictional torque T_f is also constant in steady state. On observing all the simulation results, it can be concluded that all the control objectives are achieved with reasonable accuracy.

5.7 Summary

- A mathematical model for the PMSG drive is presented in this chapter. Standard and detailed $d - q$ frame equations are used to capture the dynamics of the PMSG.
- Average modelling technique in the $d - q$ frame is used to describe the dynamics of the AC/DC converter. Vector control method is used to linearize the PMSG model and simple PI controllers are used to regulate the DC-link voltage.
- A novel friction torque model to calculate the various losses in the PMSG is presented and validated against experimental data provided by the manufacturer.
- Achievement of good regulation of the DC-link voltage and ability to capture the dynamics of the PMSG mark the success of the modelling of the PMSG drive.

CHAPTER
SIX

MODELLING OF THE DIESEL ENGINE

6.1 Introduction

An engine is a mechanical device which converts chemical energy stored in the fuel to mechanical energy, generally received at the output end of the rotating shaft. There are two kinds of engines depending on the place of combustion - external combustion engine and internal combustion engine [206].

The term “Internal Combustion”

itself tells the story that in this case, the fuel is burned inside the engine cylinder to generate the required power. Internal combustion engines are also of two types, Spark Ignition engine (SI engine, petrol engine or gasoline engine) and Compression Ignition engine (CI engine or diesel engine). The present work is mainly concerned with the compression ignition engine modelling.

Diesel Engine is named after its inventor Rudolf Diesel. It is a compression ignition engine where the air/fuel mixture is compressed to such an extent where

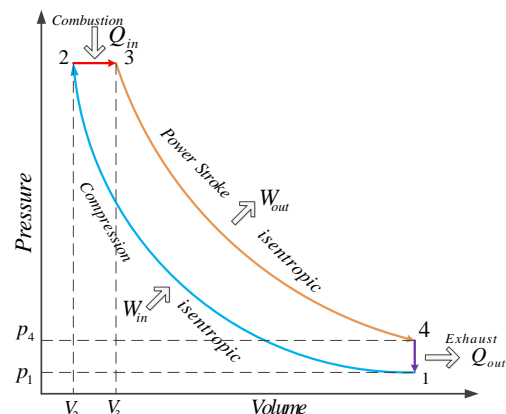


Figure 6.1: Diesel cycle

self ignition takes place at certain temperature and pressure. Figure 6.1 describes the idealized diesel cycle for a four stroke CI engine. Excellent fuel efficiency along with lower emission of CO_2 by diesel engines in comparison to similar rated SI engines over the entire operating range are very attractive features for researchers [24].

There are a few other good reasons to prefer CI engines over SI engines such as:

1. In SI engines, the air-fuel ratio is kept closer to its stoichiometric ratio to achieve optimum power and less pollution. Therefore, the amount of air and fuel is varied with the help of the throttle, while operating at different loads. So, the performance of the SI engine is very sensitive to the air-fuel ratio, whereas CI engines are less sensitive to air-fuel ratio variations. Having a better operational capacity at higher torque, temperature and pressure, makes CI engines more favorable than SI engines [24].
2. The higher compression ratio generally leads to higher thermal efficiency in the IC engine. But, sometimes due to higher compression ratios SI engines suffer through problem of knocking because when a fluid is compressed, its temperature increases and the air/fuel mixture can be compressed only up to a certain limit before knocking. However in the case of CI engines only by compressing the air in its cylinder, chances for self ignition is successfully avoided. The diesel engine thus attains higher thermal efficiency by compressing air only at higher compression ratio [72, 84]. Now even in a modern SI engine, the problem with knock has been overcome to a major extent by means of carefully controlled direct injection.
3. The torque produced by the CI engine depends on the air/fuel mixture burnt. Due to the capability of operating at a very lean mixture, the throttling of intake air can be completely avoided. However, in SI engines, throttling taking power from the engine is necessary even at low loads. Consequently, part-load efficiencies of CI engines are better than the similar rated SI engines [72].

4. Most of the CI engines are turbocharged to attain higher power to weight ratio, having good potential to be downsized while maintaining the same output power level with the help of higher boost [84]; whereas initially turbocharging in SI engines were rare [207] but nowadays turbocharging of SI engines, while downsizing, are becoming very attractive option for improving the fuel economy [208].
5. Due to less dependence on fuel quality, more flexibility of the fuel type is possible in CI engines than in SI engines. SI engines are highly sensitive to fuel quality due to their operation close to stoichiometric ratio and requirement of fuel with high antiknock quality [84].

In the diesel engine, air is first drawn into the cylinder and then compressed leading to higher temperature and pressure at the end of the compression cycle. Now by the appropriate fuel injection mechanism, a jet of cold fuel enters the cylinder where compressed air is already present. Hot air causes liquid fuel to heat-up and vaporize, and vaporization of the fuel causes temperature of the air to decrease. But, new hot air is entrained which again increases the temperature of the air inside the cylinder and this process continues further. Once the process of ignition starts it generates additional heat which helps further to vaporize the new fuel entering into the cylinder [87]. Ignition of the fuel increases the temperature and pressure inside the cylinder which, forces the piston downward for the power stroke as shown in Figure 6.1. Combustion in the diesel engine is very complex, transient, non-uniform, unsteady and heterogeneous in nature [84].

In a diesel engine, the overall torque produced by combustion completely depends on the fuel burned. If somehow more air can be compressed in the engine cylinder increasing the density of the injected air, more fuel can be burned and more power can be extracted from the same cylinder volume. Superchargers and turbochargers are the mechanisms used for compressing the air before the inlet manifold and engine cylinder. A supercharger takes power from the engine shaft itself to compress the inlet

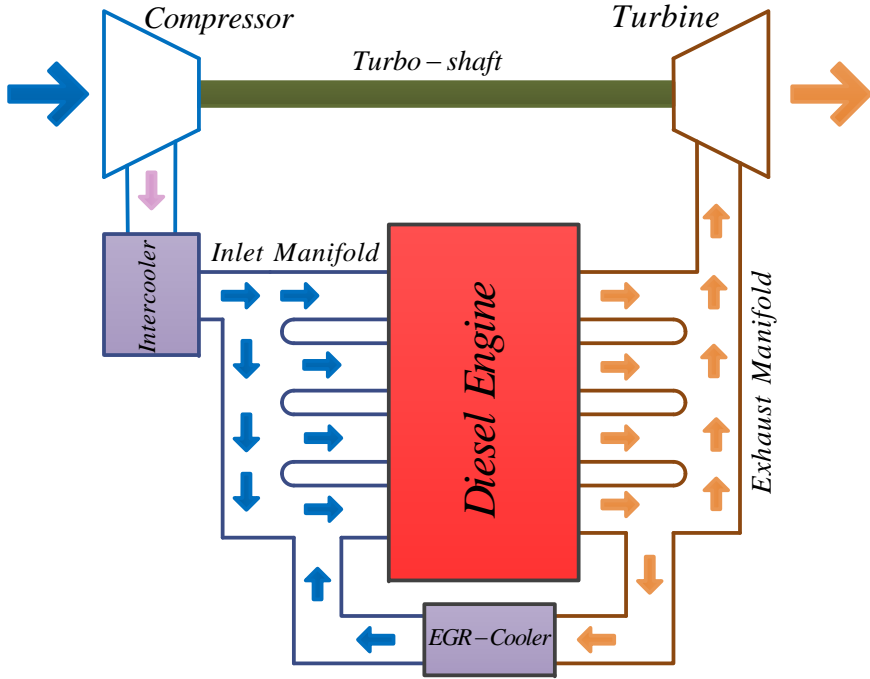


Figure 6.2: Schematic diagram of the diesel engine with turbocharger and EGR

air, and acts only on the inlet air, independent of the exhaust port. A turbocharger is a dynamic device and is driven by power extracted from the exhaust gases. The operation of the turbocharger is dependent on the inlet and exhaust port air flow. Thus, compressing more air and varying the amount of injected fuel can control the output torque on driver request. The introduction of a turbocharger improves the efficiency of the engine significantly but complicates the overall system dynamics due to the introduction of additional feedback path and operational instability around the surge line. Figure 6.2 shows the overview of a typical turbocharged diesel engine. Figure 6.3 depicts the combustion cylinder of a diesel engine [209].

Most of the engine modelling techniques and approaches are limited to prediction of steady state engine behavior. However, most of the times in real life, engines are driven at unsteady and nonuniform patterns (i.e., at transient conditions) rather than at steady state [24]. The engine performance at unsteady transient state is significantly different from the engine performance at steady state. Emissions of NO_x , PM and turbo-lag further complicate the diesel engine performance. A decrease in the emissions of NO_x increases emissions of the PM (particulate matters) and conversely a decrease

in the *PM* emissions increases *NO_x* emissions. Therefore, a trade-off exists requiring sophisticated control techniques. Application of control techniques necessitates availability of control oriented models which can capture the transient dynamics as well.

Diesel engines have two main drawbacks. The first one is that due to a lean A/F mixture, less fuel can be burned at normal atmospheric conditions leading to low power density. The second one is emission related which is very serious limitation for the diesel engines (as gasoline engines have very good exhaust emission control mechanism namely three-way catalytic converter). Use of turbochargers or superchargers can eliminate the first drawback and application of EGR (Exhaust Gas Recirculation) and electronic controls can improve the emission conditions. So, all these benefits along with future hopes for improved turbochargers and electronic controllers make diesel engines good choice for HEVs.

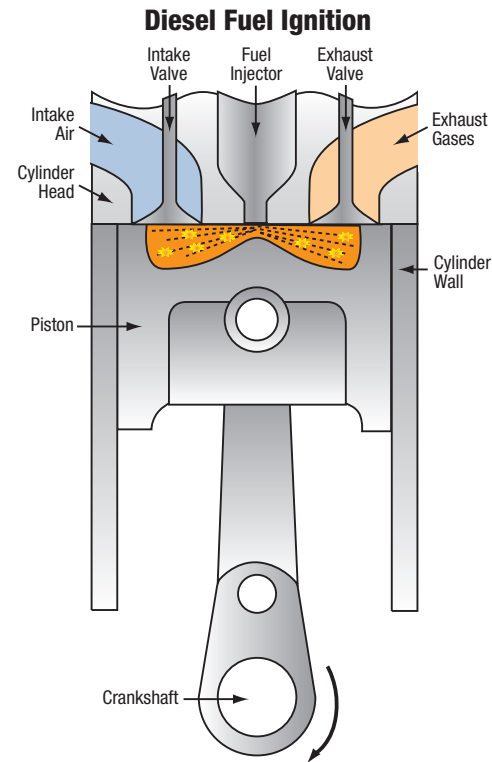


Figure 6.3: Inside view of the diesel engine cylinder [209]

6.2 Modelling

Modelling of a physical system serves many purposes for the manufacturing industry, especially in analysis and reducing time required in testing of products before actually manufacturing it. Mathematical modelling also offers better understanding of the functioning of different components and their mutual interactions. Proper knowledge

of the system behavior in reality helps predict and understand the system behavior in different situations beforehand, which is needed in the control design purposes. Increasing constraints on emissions and cost of fuel is forcing engineers to understand engine fundamentals and optimize it for all round performance using available modern control techniques. Control oriented modelling of diesel engines is now a popular topic because of the increasing trend of using cheaper and complex control techniques in hybrid electric vehicles. Therefore at this stage, modelling the engine becomes an important requirement for control development. However, the model must be chosen according to the goal aimed for. The processes governing the overall engine performance such as combustion and flow of fluid mixtures through geometries follow very complex dynamics and are not yet well understood. So practically, it is not possible to build a model for the engine purely from fundamental physics, without making any assumptions.

Ideally, a real transient model for the diesel engine should analytically model all the systems and sub-systems of the engine. The real requirements for such a model are mentioned in [24]. But as it has already been discussed, it is impossible to build such a fully transient model due to the lack of fundamental understanding of many physical events and the need for intense computational ability. So, there is a trade-off between analytical understanding and establishing empirical relations. The gap between fundamental understanding and its modelling with real functioning of the engine is filled by establishing empirical relationships among the variables. So in reality, all models available in the literature are mixtures of these analytical relations and empirical relations with certain reasonable approximation of operating conditions and phenomena under consideration. There are many types of modelling approaches for diesel engines but present work choose the modelling approach that is simple in computation and detailed enough to capture the transient performance of important engine parts. Finally, the most important point is that the chosen model should be suitable for control purposes.

There are mainly two kinds of approaches towards engine modelling, thermodynamics based analysis [83] and fluid dynamics based analysis [82, 84]. Depending on the equations and relations used to develop the consistent model, the modelling approaches are categorized. For instance, thermodynamic models and fluid dynamic models depend on the energy conservation and fluid flow analysis respectively [80, 86]. But, there are some other modelling techniques that are combinations of these two methods at different degrees according to the specific model usage.

6.2.1 Thermodynamic modelling

Energy and mass conservation is the basis of this kind of modelling approach and details of engine geometry and its subsystems are more or less irrelevant. This approach may be applied to open thermodynamic systems as intake/exhaust manifold and engine cylinder. This kind of modelling approach has some strong assumptions. For example, the gas inside the open system boundaries is uniform in composition and state at each point in time. The gas composition and state can only vary when heat transfer, mass flow or work transfer across the system boundaries takes place. Thermodynamic models of the engine and its manifolds have three main classifications [84, 87]:

1. **Quasi-Steady Model** - In this model, inlet and exhaust valves are modelled as series of restrictions in the path of fluid flow from the inlet port to the exhaust port. Steady state values are taken for air-fuel mixture pressure, temperature and mass-flow rate. The inlet port and exhaust port are connected by a simple map of the in-cylinder dynamics in terms of quantities such as output torque, exhaust temperature and exhaust mass flow rate.
2. **Gas Dynamics Model** - This model is characterized by one-dimensional unsteady compressible flow with mass, momentum and energy conservation equations having geometrical variations throughout the air-path from inlet manifold to exhaust manifold. This model is able to predict variations of pressure and temperature

in the flow field direction with respect to time. Method of characteristics or finite difference methods are used to solve partial difference equations of the model [83].

3. Filling and Emptying Model - In this model, the engine components are modelled as a series of connected finite number of control volumes, where the mass of gas inside the component can vary with time. Work and heat are exchanged with each other and with the surrounding environment, but there is no spatial variation with any of the state variables. Each control volume is connected with the other by input and output of mass flow. Next, mass and energy conservation equations are applied and differentiated with respect to time to calculate the rate of change of mass flow and other variables. Gases are assumed to be perfect and ideal gas laws are used to develop the relationship between various state variables such as pressure, temperature and mass flow. Since there is no directional consideration for the flow field variables, it is a kind of zero dimensional modelling. Mainly, exhaust and inlet manifolds are modelled by this technique [24].

6.2.2 Fluid dynamic modelling

In reality, gases inside the engine and its subsystems are not fixed in composition and are compressible with variable heat capacities. The thermodynamic processes are not exactly adiabatic or isothermal as assumed in the modelling. Combustion, heat and work transfer processes are not steady processes, rather they are highly turbulent, complex and unsteady in nature. State variables such as pressure and temperature, assumed as average and uniform throughout the manifolds and cylinder to calculate mass flow, torque and other variables, are locally non-uniform and significantly deviant from the average values. Variable geometries of the inlet-exhaust ports of the manifolds and cylinder and fuel injections timings have significant effects on the torque generation and pollutant emissions. Therefore, to capture more details of the fluid flow of the

engine, a more detailed model is required and the fluid dynamic model aims at that.

Fluid dynamic models are used to get the detailed analysis of flow fields and combustion processes in the engine completely missed or ignored by the thermodynamic modelling approach. This model involves volume and time level discretization to solve partial differential equations for conservation of mass, momentum, energy and species concentrations at the local level. The discretized mesh has to be fine enough to accurately describe the phenomena under consideration. These kind of models are highly computationally intensive. However, since computers are developing to perform faster and complex calculations, this challenge is concerning from an analysis point of view. But definitely, these models are not fit to be used for any real time control processes. Sometimes, these models lead to numerical instability due to different possible combinations of time and volume scales. Generally, these models are exclusively used in describing the in-cylinder behavior and are too computational intensive to be used for control oriented modelling.

6.2.3 Black box modelling

Black box modelling is a kind of mapping between relevant inputs and outputs without involving any physics or chemistry of the system under consideration. Overall modelling is based on huge amount of data fitting dependent on the environment from which the data has been taken. There are some fuzzy neural network based controllers trained with transient simulation data to develop an observer for predicting fresh air mass entering the cylinders [75–77]. These models are linear in nature and the states are physical. However, the model parameters are determined purely through system identification [210]. One mapped model cannot be freely used for another environment without recalibration and identification of the complete data set. This data intensive training and calibration for different possible environments makes this model unfavorable for even simple control purposes.

6.2.4 Quasi stationary modelling

Multiple performance charts are used to model the overall behavior of the engine. The actual values of interest are taken directly from the tables as per requirements. This method does not consider whether the engine is at a stationary point or just passes through a fast transient. The performance is computed taking it as steady state condition.

6.3 Mean Value Diesel Engine Model

The mean value modelling approach is a balanced trade-off between the analytical approach and the empirical approach, where the model is quasi-linear with physics based system modelling, rather than being collections of empirically calibrated relationships. The characteristics of mean-value modelling approach are described in [24] in the following words:

1. The working medium is assumed to be pure air or combustion products, both treated as perfect gases with constant specific heat capacities. Since gas velocities are relatively low, dynamic pressures and temperatures are considered equal to the corresponding static ones.
2. Accumulation volumes in the system have negligible effect.
3. Mean values are used for engine and manifold pressures and temperatures.
4. The engine output is related to the fuel input via empirical equations or tabulated steady-state data.
5. An empirical relation is applied for estimating the exhaust gas temperature at the turbine inlet. This is defined from the inlet manifold temperature by adding a temperature rise factor to it to account for combustion effects.
6. A pulse factor is used for correction of the turbine expansion ratio in order to account for pulse turbocharging.

Some of the modelling approaches already described are not suitable for control purposes. A control oriented model is an attempt to model the input-output behavior of a system with reasonable accuracy but low computational demands [90]. Different modelling techniques have different goals to achieve. Our goal is to develop a simple, fast and accurate enough control oriented model. Present work is not very concerned with detailed analysis and simulation of the physical processes inside the engine. Thermodynamic and kinetic processes of combustion of the A/F mixture are fast enough and cannot participate in speed, external load and fuel injection based control techniques of the engine. Control techniques are effective only with slower dynamic processes such as mass transfer, temperature and pressure change. Fast processes such as combustion can be taken as static without any loss of accuracy and generality. In the present modelling approach, a control oriented mean-value model has been developed. It takes a few assumptions for the simplification of the model such as “all the processes and effects are evenly spread out over the engine cycles” [90].

A combination of the mean-value model and filling and emptying model has been chosen, in the present work, for the purpose of modelling of different systems and sub-systems of the turbocharged diesel engine having components such as inlet manifold, exhaust manifold, EGR valves, intercooler, turbocharger and engine cylinder. The inlet manifold and exhaust manifold are modelled with the filling and emptying model, engine cylinder dynamics are modelled with the mean-value model, engine torque is modelled as a three-dimensional map of the indicated torque ($T_{eng} = f(\omega_{eng}, \lambda)$), rotational speed (ω_{eng}) of the engine shaft, and relative air-fuel ratio λ . The mean-value model is used for flow characteristics of the compressor and turbine ($W_c = f(\frac{p_{out}}{p_{in}}, \omega_{tc})$, where W_c is the mass flow rate, $\frac{p_{out}}{p_{in}}$ is the compression ratio and ω_{tc} is the rotational speed of the turbo-shaft). Inertia of the engine and turbo-shaft are included in the model to capture realistic transient performance of the turbocharged diesel engine. A fuel injection control scheme is devised to control the speed and torque generation in the model.

The parameters of this model were derived by utilizing simulation results generated by the Ricardo-WAVE model for Puma 2.0L engine. WAVE is a 1D engine and gas dynamics simulation software from Ricardo Software. It is used worldwide in many industry sectors including passenger car, motorcycle, truck, locomotive, motor sport, marine and power generation. WAVE enables performance simulations to be carried out based on virtually any intake, combustion and exhaust system configuration, and includes a drivetrain model to allow the complete vehicle simulation. It is a computer-aided engineering code developed by Ricardo Software to analyze the dynamics of pressure waves, mass flows and energy losses in ducts, plenums and the manifolds of various systems and machines. WAVE provides a fully integrated treatment of time-dependent fluid dynamics and thermodynamics by means of a one-dimensional formulation. This incorporates the general treatment of working fluids including air, air-hydrocarbon mixtures, combustion products, liquid fuels, and Freon gases. WAVE also includes a library of special machinery elements such as engine cylinders, piston compressors, turbochargers/supercharger compressors, turbines and pumps. These elements can be attached to pipe networks to serve as sources or absorbers of pulsating flows. These features make WAVE an excellent tool for simulating the internal combustion engine [211]. A Ricardo-WAVE based model of the Puma 2.0L has already been developed elsewhere. This Wave-based model is already calibrated with experimental results of the Puma 2.0L engine having a maximum error of 2%. Therefore, the results generated by this Ricardo-Wave model can be safely taken as the experimental results in normal operating region.

6.3.1 Manifold modelling

The filling and emptying modelling approach is used for describing the inlet and exhaust manifold. Manifolds are considered as the reservoirs of single control volume with changing gas mass with time inside them. Although the state variables such as pressure and temperature change with time, these remain uniform throughout

the manifolds at any particular point in time.

Conservation of the mass flow input and output for the inlet manifold leads to the following equation:

$$\frac{dm_i}{dt} = w_{ci} + w_{xi} - w_{ie} \quad (6.1)$$

where the rate of change of mass in the inlet manifold (m_i) is equal to the mass flow in and out of the system. w_{ci} is the gas mass flow rate through the compressor and intercooler, w_{xi} is the exhaust gas mass flow rate fed-back to the inlet manifold through the EGR valve, and w_{ie} is the gas mass flow rate from the inlet manifold to the engine cylinder. The gas mass flow rate is measured in units of kg/sec and the first letter of the subscript represents the system from which the gas flow starts and the second letter represents the system to which the gas finally reaches. Fluids involved in the process are assumed to be perfect gases with constant heat capacities, so the ideal gas law can be used to describe the state variables in the manifolds. The relationship between the mass of gas m_i inside the manifold with the average inlet manifold pressure p_i , inlet manifold temperature T_i and inlet manifold volume V_i can be described as follows:

$$p_i V_i = m_i R T_i \quad (6.2)$$

where R is gas constant (for air, R is 0.287 KJ/kg/K).

Differentiating Equation (6.2) with respect to time (t) to get the rate of change of inlet mass flow

$$\frac{dp_i}{dt} = \frac{R}{V_i} \left(\frac{dm_i}{dt} T_i + \frac{dT_i}{dt} m_i \right) \quad (6.3)$$

and rearranging Equation (6.3) following relationship is obtained,

$$\frac{dm_i}{dt} T_i = \frac{V_i}{R} \frac{dp_i}{dt} - \frac{dT_i}{dt} m_i \quad (6.4)$$

If the term $\frac{dT_i}{dt} m_i$ in Equation (6.4) is neglected because the rate of change of inlet manifold temperature with time is very small and by substituting Equation (6.1)

into Equation (6.4), following expression is obtained [87]

$$\frac{V_i}{RT_i} \frac{dp_i}{dt} = w_{ci} + w_{xi} - w_{ie} \quad (6.5)$$

Above model is referred as an isothermal model of the inlet manifold.

The thermodynamic equations of the inlet manifold can also be derived by using enthalpy flow and change in internal energy of the manifold [90]. A differential equation of the heat exchange is given below.

$$\frac{dU_i}{dt} = \dot{H}_{ci} + \dot{H}_{xi} - \dot{H}_{ie} - \dot{Q}_i \quad (6.6)$$

where U_i is the internal energy in the inlet manifold. \dot{H}_{ci} , \dot{H}_{xi} and \dot{H}_{ie} are thermodynamic enthalpy changes of the compressor to the inlet manifold, of the EGR valve to the inlet manifold and of the inlet manifold to the engine cylinder, respectively. Finally, \dot{Q}_i is the heat loss from the inlet manifold. Enthalpy changes are related to mass flow rates by the following equations,

$$U_i = c_v \cdot T_i \cdot m_i \quad (6.7)$$

$$\frac{dU_i}{dt} = c_v \left(\frac{dm_i}{dt} T_i + \frac{dT_i}{dt} m_i \right) \quad (6.8)$$

$$\dot{H}_{ci} = c_p \cdot T_{ci} \cdot w_{ci} \quad (6.9)$$

$$\dot{H}_{xi} = c_p \cdot T_{egr} \cdot w_{xi} \quad (6.10)$$

$$\dot{H}_{ie} = c_p \cdot T_i \cdot w_{ie} \quad (6.11)$$

c_v and c_p are the specific heat capacities at constant volume and constant pressure respectively. T_{ci} is the temperature of the gas after passing through the compressor and T_{egr} is the temperature of the gas flowing through the EGR valve.

Substituting Equation (6.8) into Equation (6.6) with other equations from (6.9) -

(6.11), the following relationship can be obtained:

$$\frac{dm_i}{dt}T_i + \frac{dT_i}{dt}m_i = \frac{c_p}{c_v}(T_{ci}w_{ci} + T_{egr}w_{xi} - T_iw_{ie}) - \dot{Q}_i \quad (6.12)$$

By substituting Equation (6.3) into Equation (6.17) and neglecting heat loss to the walls \dot{Q}_i based on the assumption of adiabatic process,

$$\frac{dp_i}{dt} = \frac{R\kappa}{V_i}(T_{ci}w_{ci} + T_{egr}w_{xi} - T_iw_{ie}) \quad (6.13)$$

where $\kappa = \frac{c_p}{c_v} = 1.4$ is the ratio of specific heat constants. This model is referred as adiabatic model of the inlet manifold. It is assumed that no heat loss occurs in the manifold as opposed to the isothermal model which assumes a large heat transfer such that the temperature in the manifold is the same as the inlet gases. It has already been discussed that a real thermodynamic process is neither purely adiabatic nor purely isothermal in nature. It has been found during simulations that the adiabatic model becomes unstable in certain operating conditions whereas the isothermal model was stable for all conditions. Therefore, the isothermal model of manifolds has been accepted for inclusion in the overall model.

Once again, the ideal gas law can be used to describe the relationship between the exhaust manifold pressure (p_x), exhaust manifold temperature (T_x), total control volume of the exhaust manifold (V_x) and exhaust gas mass (m_x).

$$p_x V_x = m_x R T_x \quad (6.14)$$

$$\frac{dm_x}{dt} = w_{ex} - w_{xt} - w_{xi} \quad (6.15)$$

where w_{ex} is the exhaust gas mass flow rate from the engine cylinder and w_{xt} is the exhaust gas mass flow rate through the turbine to the environment. The isothermal model of the exhaust manifold can be derived by Equations (6.14)-(6.15) in a similar

way as the inlet manifold

$$\frac{V_x}{RT_x} \frac{dp_x}{dt} = w_{ex} - w_{xt} - w_{xi} \quad (6.16)$$

Similarly, the adiabatic model is

$$\frac{dp_x}{dt} = \frac{R\kappa}{V_x} (T_{ex}w_{ex} - T_xw_{xt} - T_{egr}w_{xi}) \quad (6.17)$$

where T_{ex} is the temperature of gas exiting the cylinder.

6.3.2 Exhaust gas recirculation (EGR)

Nowadays, EGR is an important part of modern engines and is used to reduce NO_x emissions by recirculating the same volume of exhaust gases in the inlet manifold. Models for EGR are available in the literature. In the present work, the EGR model has not been included directly into the engine model due to the lack of experimental data. However, the effects of EGR are realized by introducing calibration factors.

EGR is either direct or cooled recirculation of cylinder exhaust gases into the inlet manifold. The inlet manifold can be modelled isothermally if the cooled EGR is used. Two important assumptions are made [90] for the EGR modelling:

1. There is no mixing or any exhaust delay in the collection of exhaust gases after combustion in the engine cylinder.
2. Specific heat capacities for the inlet air and exhaust gases are taken to be the same and both are treated as perfect gases.

EGR flow is modelled as the flow of a compressible fluid through an orifice with variable effective area A_{egr} . The pressure difference between exhaust manifold and inlet manifold is a natural driving force for EGR gases. Standard orifice equations can be used to describe the relationship among EGR mass flow rate through the EGR valve

(w_{xi}) , valve downstream pressure (p_i), upstream pressure (p_x) and upstream temperature of the valve (T_{egr}). If p_i/p_x is greater than or equal to the critical pressure ratio 0.528, the flow equation will be as follows:

$$w_{xi} = \frac{A_{egr} p_x}{\sqrt{RT_{egr}}} \left(\frac{p_i}{p_x} \right)^{1/\kappa} \sqrt{\frac{2\kappa}{k-1} \left[1 - \left(\frac{p_i}{p_x} \right)^{\kappa-1/\kappa} \right]} \quad (6.18)$$

The flow reaches sonic conditions while passing through the valve when the pressure ratio is less than 0.528 and the orifice equation can be written as:

$$w_{xi} = \frac{A_{egr} p_x}{\sqrt{RT_{egr}}} (0.528)^{1/\kappa} \sqrt{\frac{2\kappa}{k-1} \left[1 - (0.528)^{\kappa-1/\kappa} \right]} \quad (6.19)$$

The effective area of the EGR valve A_{egr} can be modelled in terms of the throttle plate angle and the input control signal for the throttle plate $u_{egr}(0 - 1)$ [90].

$$\theta_{th} = \theta_{th,0} + \left(\frac{\pi}{2} - \theta_{th,0} \right) \cdot u_{egr} \quad (6.20)$$

$$A_{egr}(\theta_{th}) = \pi \cdot r_{th}^2 \cdot \left(1 - \frac{\cos \theta_{th}}{\cos \theta_{th,0}} \right) + A_{egr,leak} \quad (6.21)$$

When the valve is fully closed, $u_{egr} = 0$, and when it fully open, $u_{egr} = 1$. $\theta_{th,0}$ is the throttle plate angle at fully closed position, r_{th} is the radius of the throttle plate and $A_{egr,leak}$ is the leakage opening area when the throttle is fully closed. These parameters need to be determined experimentally, but unfortunately in this research work, there is no separate experimental data available for the EGR phenomena. Therefore, EGR model has not been included in the overall engine model. While the Ricardo-Wave model of the PUMA 2.0L engine used in this project is equipped with the cooled EGR, the EGR effect is satisfactorily compensated with the inclusion of two calibration factors K_{in} and K_x , which will be described in Section 6.4.

6.3.3 Engine cylinder

6.3.3.1 Mass flow rate in-to the engine cylinder

To increase the efficiency of the engine, compressed air is fed to the inlet manifold. The compressor compresses the inlet increasing the temperature of the injected air and reducing air density which have adverse effect on the engine efficiency. Therefore, the injected air is cooled by the intercooler. This cooling action can be expressed by the following equation:

$$T_i = T_{ci} - \eta_{ic}(T_{ci} - T_{coolant}) \quad (6.22)$$

Where T_i is the uniform temperature of the inlet manifold. For simplicity effectiveness of the intercooler is assumed to be $\eta_{ic} = 1$. This cooling action increases the density of the inlet air.

The mass flow rate of the intercooled injected compressed air (w_{ie}) can be calculated by assuming the engine as a volumetric pump. This action is included in the inlet manifold block. Volume flow from this engine pump is approximately proportional to its speed [90]. The model can be described as

$$w_{ie} = \eta_v \frac{\rho_i V_d \omega_{eng}}{\sigma \cdot 60} \quad (6.23)$$

Where, η_v is the volumetric efficiency, ρ_i is the density of inlet air inside the inlet manifold, V_d is the maximum volume swept by the piston inside the engine cylinder, ω_{eng} is the rotational speed of the engine shaft and σ is the number of revolutions per cycle (for four-stroke engines, $\sigma = 2$ and for two-stroke engines, $\sigma = 1$).

η_v is defined as the volume air flow rate into the cylinder divided by the rate at which the volume is displaced by the piston [84]. In the present modelling, the air is assumed to be incompressible but real gases are compressible, so essentially η_v is a measure of the ratio of the actual injected-mass-flow to mass-flow achieved when the

fluid is inviscid and incompressible [212]. Boundary layers, separation, Mach number and valve timings also affect volumetric efficiency. It can be modelled as a function of engine speed and inlet manifold pressure, i.e. $\eta_v = f(\omega_{eng}, p_i)$, in future this model can be included in the overall engine model. Since at present no model is employed to calculate this efficiency, for the purposes of simplicity, the efficiency in this model is assumed to be constant at 1.0. In future research work ,such as in [9], volumetric efficiency will be modelled with a suitable function such as $\eta_v = f(\omega_{eng}, p_i)$.

6.3.3.2 Torque calculations

An engine is a mechanical device which transforms the chemical energy available in the fuel into usable mechanical energy. In internal combustion engines, torque is produced by burning the right amount of the fuel. This torque is called the indicative torque T_{eng} . After all frictional losses, the available torque is known as brake torque (T_b). In a four stroke diesel engine power is produced only in one stroke known as power stroke, after combustion of the air-fuel mixture. However in the mean-value modelling approach employed in this work, power is assumed to be distributed uniformly over all thermodynamic cycles of the engine. Although by solving the fluid and thermal equations (for e.g., in the case of Ricardo-Wave software), the exact power and produced torque can be calculated, such simulation models are not feasible for real time control purposes. The calculations involved are only computationally expensive but also the dynamics described are extremely fast, and therefore do not participate in external control actions. Thus the combustion process and can be safely treated as a static effect as discussed in the earlier section.

Transient operation of the engine poses a further challenge to modelling and prediction of the engine torque. Historically, this transient problem was first faced by manufacturers around 1960, when a medium sized diesel engine was operated against sudden change from 0 to 100Nm in the operating load and several problems were encountered [24]. A similar problem is encountered in the transient modelling as

well when the engine changes load and its turbocharger is not in steady state, which represents a case of operation where the engine is operating outside the domain of stationary data. The challenge is how to predict torque generation in transient conditions when data for modelling comes from only steady state operations.

To calculate the torque produced by the engine, three dimensional mapping of the indicated torque T_{eng} , λ (relative air-fuel ratio) and current engine speed ω_{eng} is used. Data for this map is generated by Ricardo-Wave model of the Puma 2.0L diesel engine. λ is a relative air/fuel ratio, which is calculated as the ratio of actual air/fuel mass flow ratio to the stoichiometric air/fuel mass flow ratio $(Air/fuel)_{stoichiometric} = 14.22$ [84].

$$\lambda = \frac{(Air/Fuel)_{actual}}{(Air/Fuel)_{stoichiometric}} \quad (6.24)$$

Once the mapping is ready, the produced indicative torque T_{eng} can be calculated from this map by getting the relevant inputs λ and engine speed ω_{eng} .

The stationary measurements obtained from simulation of the Ricardo-Wave Puma 2.0L diesel engine model are shown in Table 6.1. However, it cannot be used directly in the control oriented simulation. To implement it as a smooth continuous function of the form $T_{eng} = g(\lambda, \omega_{eng})$, an interpolated surface between λ and engine speed from 1000 rpm to 3500 rpm is created. Since the available data points are limited, a Matlab program was written to fit a surface plot of torque values on a grid defined by the engine speed and air-fuel ratio vectors. Cubic interpolation yields a smooth and continuously differentiable surface over the grid data. However under transient operations, sometimes the engine goes beyond the mapped range of the data where extrapolation is the only solution which is not reliable due to discontinuity and non-differentiability of the data over that range. One more point of the concern is that calculating the value of torque at non grid points involves interpolation and extrapolation of the 3D torque surface, which is a very cumbersome and time consuming process. To permanently avoid this difficulty, a continuously differentiable polynomial function is

Table 6.1: and indicative torque T_{eng} , obtained by simulating the Ricardo-Wave Puma 2.0L engine model

Speed rpm	Ind. torque Nm	Brake torque Nm	Fric. torque Nm	Vol. Effi.	Ex. temp. K	A/F ratio	λ	Air $\times 10^{-2}$ kg/sec	Fuel $\times 10^{-3}$ kg/sec
1000	73.69	61.39	12.3	0.62	645.1	26.61	1.87	1.19	0.45
1000	97.25	84.95	12.3	0.63	791.3	19.56	1.38	1.20	0.62
1000	136.8	124.5	12.3	0.83	899	18.32	1.29	1.59	0.87
1500	57.94	44.24	13.69	0.59	582.7	33.43	2.35	1.69	0.51
1500	77.73	64.04	13.69	0.67	690.8	27.77	1.95	1.94	0.70
1500	90.06	76.37	13.69	0.69	704.9	25.76	1.81	2.00	0.78
1500	100.2	86.5	13.69	0.78	757.8	24.88	1.75	2.24	0.90
1500	121.6	107.9	13.69	0.94	805	24.69	1.74	2.72	1.10
1500	143.5	129.8	13.69	1.02	863.2	22.63	1.59	2.94	1.30
1500	165.3	151.6	13.69	1.12	919.4	21.54	1.51	3.23	1.50
1500	199.2	185.5	13.69	1.07	1188	16.27	1.14	3.09	1.90
2000	45.55	29.90	15.65	0.89	572.7	56.51	3.97	3.44	0.61
2000	57.88	42.23	15.65	0.56	636.7	31.45	2.21	2.14	0.68
2000	90.68	75.03	15.65	0.66	769.2	24.05	1.69	2.54	1.06
2000	124.30	108.7	15.65	0.88	836.8	23.91	1.68	3.40	1.42
2000	137.30	121.7	15.65	0.95	890	22.71	1.60	3.63	1.60
2000	160.00	144.3	15.65	1.05	951.2	21.61	1.52	4.03	1.87
2000	182.70	167	15.65	1.18	1010	21.21	1.49	4.53	2.13
2000	204.10	188.4	15.65	1.27	1054	20.39	1.43	4.89	2.40
2000	230.20	214.5	15.65	1.34	1071	19.35	1.36	5.16	2.67
2500	55.09	36.93	18.16	0.9	587.7	53.30	3.75	4.30	0.81
2500	61	42.84	18.16	0.65	655.2	34.86	2.45	3.13	0.90
2500	94.77	76.60	18.16	0.77	776.2	27.00	1.90	3.70	1.37
2500	128.9	110.8	18.16	0.93	876.4	24.14	1.7	4.48	1.86
2500	160.5	142.3	18.16	1.09	979.4	22.38	1.57	5.22	2.33
2500	181.4	163.3	18.16	1.18	1043	21.30	1.50	5.68	2.67
2500	200.3	182.2	18.16	1.25	1109	19.96	1.40	5.99	3.00
2500	210.9	192.8	18.16	1.32	1190	19.06	1.34	6.35	3.33
3000	57.88	36.65	21.23	1.05	610.6	57.72	4.06	6.06	1.05
3000	88.15	66.91	21.23	1.04	706.6	39.30	2.76	6.02	1.53
3000	122.30	101.10	21.23	1.11	817.5	30.32	2.13	6.38	2.10
3000	196.00	174.70	21.23	1.19	1218	18.33	1.29	6.84	3.73
3500	87.48	62.62	24.86	1.07	743	39.11	2.75	7.17	1.83
3500	122.20	97.36	24.86	1.14	855.7	30.25	2.13	7.65	2.53
3500	201.50	176.60	24.86	1.15	1399	15.65	1.10	7.73	4.94

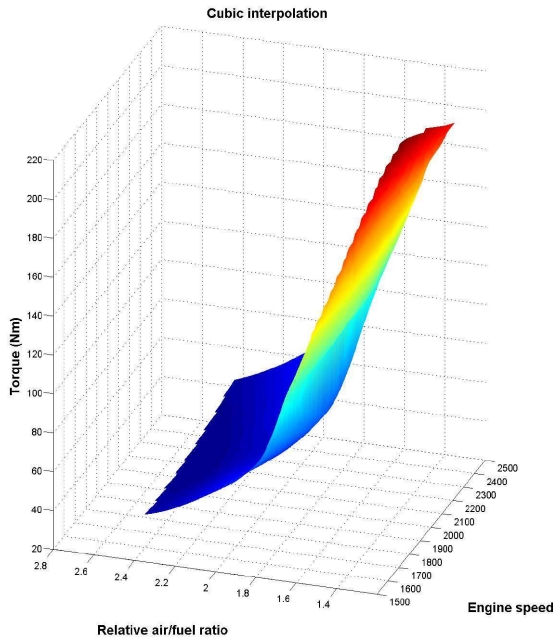


Figure 6.4: Cubic Interpolation of torque, λ and speed ω_{eng}

obtained for this interpolated 3D torque surface giving good trend of approximation inside the interpolated grid area of λ and ω_{eng} as well as for the extrapolated range.

This polynomial in the form of $T_{eng} = g(\lambda, \omega_{eng})$ makes calculations very fast and easy. The polynomial equation is of the following form:

$$T_{eng} = a + bx + cy + dx^2 + ey^2 + fxy + gx^3 + hy^3 + ixy^2 + jx^2y \quad (6.25)$$

where $x = \lambda$ is the relative air-fuel ratio and $y = \omega_{eng}$ is the rotational speed of the engine in rpm. For this particular surface, coefficients of the polynomial equation are $a = 592.53$, $b = -728.38$, $c = 0.21$, $d = 287.38$, $e = -4.2 \times 10^{-5}$, $f = -0.068$, $g = -31.18$, $h = -2.26 \times 10^{-9}$, $i = 2.63 \times 10^{-5}$ and $j = -0.014$.

It can be observed that the torque is unrealistically large at very high engine speeds and low lambda values. These inaccuracies are taken care of by placing a variable saturation torque limit, which is a function of the rotational speed of the engine. A maximum load torque versus engine speed curve at full throttle is supplied by the manufacturer. In this curve, the maximum possible torque, T_{sat} , is expressed

as a function of the rotational speed ω_{eng} . A rational function is fitted in the form of $T_{sat} = f(\omega_{eng})$ such that it should behave well even in the extrapolated regions where experimental data is not available. The following function has been chosen:

$$T_{sat} = (a_s + c_s x^{0.5} + e_s x + g_s x^{1.5}) / (1 + b_s x^{0.5} + d_s x + f_s x^{1.5} + h_s x^2) \quad (6.26)$$

where $x = \omega_{eng}$ is the rotational speed of the engine shaft in rpm and $a_s = 19.17$, $b_s = -7.75 \times 10^{-2}$, $c_s = -0.63$, $d_s = 2.29 \times 10^{-3}$, $e_s = 4 \times 10^{-3}$, $f_s = -3 \times 10^{-5}$, $g_s = 3.23 \times 10^{-5}$ and $h_s = 1.5 \times 10^{-7}$

6.3.3.3 Fuel injection model

The speed and torque of the diesel engine is controlled by varying the air-fuel ratio. Air-mass flow rate is governed by the dynamics of the turbocharger, while the fuel amount is controlled by an independent fuel injection control unit. In the present engine model, there is a PID controller which decides the amount of fuel to be injected inside the engine cylinder, so that the required torque can be generated to track the desired speed profile. In reality the fuel is not injected into the engine cylinder instantaneously. Rather, there is some finite duration of time, so a low pass filter has been used to model this effect.

$$\frac{dw_{fuel,out}}{dt} = \tau(w_{fuel,in} - w_{fuel,out}) \quad (6.27)$$

$w_{fuel,in}$ is the fuel mass flow rate demand and $w_{fuel,out}$ is the actual fuel mass flow rate. The fuel mass flow rate injected in to engine cylinder for combustion will be denoted in general as w_{fuel} unless stated otherwise. $\tau = 5ms$ is the time constant for actual fuel mass flow rate.

6.3.3.4 Exhaust temperature

The temperature of exhaust gases increases substantially due to the combustion of the in-cylinder gases. The temperature of cylinder-out gases and exhaust manifold are different; however, the temperature of the exhaust manifold is generally available. Darlington has proposed in [87] that the temperature rise of the cylinder-out gases due to combustion can be mapped as a function of λ and rotational speed of the engine shaft ω_{eng} .

Chen [213] has proposed a linear function between λ and cylinder-out temperature T_{ex} in the form of $T_{ex} = f(\lambda, \omega_{eng})$:

$$T_{ex} = m_1\lambda + m_2 \quad (6.28)$$

$$m_1 = a_x\omega_{eng}^2 + b_x\omega_{eng} + c_x \quad (6.29)$$

$$m_2 = d_x\omega_{eng} + e_x \quad (6.30)$$

Due to unavailability of any data for the cylinder-out temperature (T_{ex}) therefore experimental data for the exhaust temperature (T_x) (assuming that $T_{ex} \approx T_x$) given in Table 6.1 are used to calculate the coefficients of above temperature polynomial as $a_x = 6.23 \times 10^{-5}$, $b_x = -0.34$, $c_x = -35.03$, $d_x = 0.26$ and $e_x = 998.86$.

During the transient operation of the engine, sometimes the fuel flow becomes zero making $\lambda = \infty$ which leads to unexpected values for the temperature such as $T_x = \infty$ or $T_x = -\infty$. Therefore, a saturation is used to limit the value of cylinder-out temperature from normal atmospheric $T_{ex}^{min} = 293K$ to the maximum $T_{ex}^{max} = 1500K$.

During the simulation, it has been observed that the fit proposed by Equations (6.29)-(6.30) is not good for all ranges of speed and torque. Therefore, a correction factor or correction temperature is introduced to get better fit for the exhaust temperature (T_x) map. Finally, temperature of the isothermal exhaust manifold of the engine, T_x , is

described as:

$$T_x = T_{ex} + T_{cor} \quad (6.31)$$

The expression for the correction temperature T_{cor} is assumed dependent on the rotational speed of the engine ω_{eng} :

$$T_{cor} = (a_c + c_c x^2 + e_c x^4) / (1 + b_c x^2 + d_c x^4) \quad (6.32)$$

where $x = \omega_{eng}$, $a_c = 18.5$, $b_c = -1.48 \times 10^{-7}$, $c_c = 1.73 \times 10^{-5}$, $d_c = 8.39 \times 10^{-15}$ and $e_c = -1.82 \times 10^{-12}$. Inclusion of the the correction temperature T_{cor} has improved the fit for the exhaust temperature map.

6.3.3.5 Mass Flow Rate out of the Cylinder

The mass flow out of the engine cylinder w_{ex} is the sum of the inlet air flow and injected fuel flow,

$$w_{ex} = w_{ie} + w_{fuel} \quad (6.33)$$

where w_{fuel} is fuel mass flow into the cylinder.

6.3.3.6 Engine dynamics

The engine generates power by combustion of fuel in the power stroke of the engine cycle. This power stroke sets the crank shaft of the engine into motion. The crankshaft, due to inertia, carries this motion to all other three remaining phases of the thermodynamic cycle such as exhaust, intake and compression. In the mean-value model, it is assumed that torque generation is a uniform and continuous process like others such as injection of air and fuel over the complete cycle of the engine. For the calculation of the brake torque T_b and the rotational speed of the engine ω_{eng} , the inertia

is assumed to be constant and the following differential equation of torques is used [89].

$$\frac{d\omega_{eng}}{dt} = \frac{60}{2\pi} \cdot \frac{T_{eng} - T_{fric} - T_{load}}{J_e} \quad (6.34)$$

where ω_{eng} is the engine speed in rpm and J_e is the inertia of the engine shaft. The load torque T_{load} is assumed to be known and changes according to the external demands. T_{fric} is the resistance torque due to the mechanical friction in the engine and is modelled as a polynomial function of the engine speed ω_{eng} [84].

$$T_{fric} = f_1 + f_2 \omega_{eng} + f_3 \omega_{eng}^2 + f_4 \omega_{eng}^3 \quad (6.35)$$

where $f_1 = 11.18$, $f_2 = -5.42 \times 10^{-6}$, $f_3 = 1.12 \times 10^{-6}$ and $f_4 = -4.04 \times 10^{-13}$. The coefficients f_i are calibrated according to the data generated for the frictional torque T_{fric} at different engine speeds from the Ricardo-Wave model of the Puma engine under consideration. This data is tabulated in Table 6.1.

6.3.3.7 Engine efficiency

The engine efficiency is used to measure how efficiently an engine uses the supplied fuel to produce mechanical energy [84]. The efficiency used is also known as the fuel conversion efficiency and can be defined as follows:

$$\eta_e = \frac{T_{eng} \times \omega_{eng}}{w_{fuel} \times Q_{HV}} \quad (6.36)$$

where η_e is the engine efficiency, T_{eng} is the indicated torque of the engine, ω_{eng} is the speed in rad/s and Q_{HV} is the lower heating value of commercial hydrocarbon fuels. The efficiency is provided as an output in our model.

6.3.4 Turbocharger

In the intake cycle of a naturally aspirated diesel engine, lowering of the piston creates a lower pressure region inside the engine-cylinder and inlet-manifold to draw the air from the ambient. Since there is a limit to the net pressure difference between the engine cylinder and ambient, power is also limited. Turbochargers are used to increase this pressure difference by increasing the speed of the inlet air. This compressing action of the compressor forces more air into the inlet manifold causing more fuel to burn producing more power. Turbochargers are mainly used with diesel engines to attain a higher compression ratio.

A turbocharger is a mechanical device containing a compressor and turbine on the same shared shaft as shown in Figure 6.5. Exhaust gases are passed through the turbine blades, forcing them to rotate at very high speeds. This results in the compressor on other side being able to draw more air from the ambient pressure and to deliver it to the intercooler at high speeds. However, cooling of the inlet air inside the intercooler increases the density of the air in the inlet manifold. Exhaust gases have very high temperatures and speeds at significantly higher pressure. Some part of this energy present in the exhaust gas is utilized by the turbine. Since the turbocharger is driven by the exhaust gases and is not dependent on the engine shaft like superchargers, it not only increases the power output but also increases the engine efficiency. Use of the turbine at the exhaust side in one sense puts obstacle in the path of exhaust gas flow which raises the back pressure of the engine. So, in the process of capturing some excess energy from the exhaust gas, sometimes turbocharger can also adversely affect the performance of the engine especially by excessively increasing

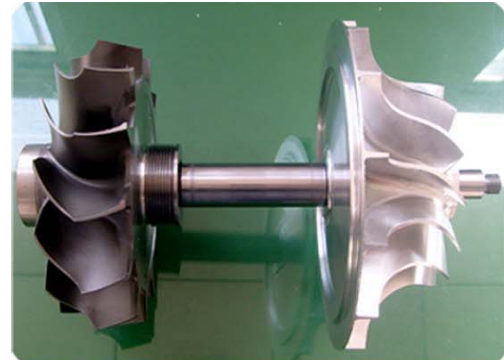


Figure 6.5: Turbocharger shaft

the exhaust back pressure. So there is always a price to pay for any gain; there is no completely free energy even in the exhaust gas. There are many types of designs available for the compressor and the turbine but single stage radial flow is the mostly used design in automotive turbochargers for the compressors and turbines.

Two main drawbacks of using turbochargers are its operation around the surge-line and turbo-lag. In the first situation, turbochargers become unstable in their operation at the left of the surge-line, which is a very serious limitation for any turbocharger. In the second situation, at lower engine speed, there is not enough exhaust gas flow through the turbine. Therefore, the speed of the turbo-shaft is relatively low and as a result, the boost is small. At this condition, if there is a sudden steep change in load, the turbocharger responds to this instantaneous demand in the boost with some time lag known as the turbo-lag. The transient response of the diesel engine depends on the ability of the turbocharger to provide sufficient boost so that λ will not be too low; otherwise the transient torque (engine torque T_{eng}) output will be unrealistically high. While there is a lot of fuel in the engine cylinder, there is not sufficient air to burn this fuel and this situation also leads to the formation of soot, which is very dangerous from emissions point of view. In the next section, a feedback control scheme is suggested for limiting the fuel injection to avoid very low value of λ in such a situation. The maximum load change of the engine mainly depends on the ability of the turbocharger to change its rotational speed within a short time [82].

Since the turbocharger is a dynamic system and is connected between the inlet air-port and the exhaust air-port, an understanding of the turbocharger dynamics is very important from the control point of view. Completely map based models lack the overall dynamics of the system and maps for turbochargers at low speed are difficult to generate and are generally avoided by manufacturers. Therefore, at low load conditions, the performance of such models is not very reliable. Maps for the turbochargers are supplied by manufacturers in the form of data tables which are not very compact to include in simulation models directly [88]. So some sort of continuous and differentiable

empirical relationships governing the function of turbochargers are indeed required, which can be used as a quasi-dynamic model of the turbocharger. The main assumption in the mean-value modelling of the turbocharger is that the fluid dynamic processes are much faster in dynamics in comparison to thermodynamic processes, so steady-state maps can be used to describe highly nonlinear behaviors of the turbochargers [90]. In the present modelling of the turbocharger surge phenomena has been ignored for simplicity.

6.3.4.1 Compressor modelling

The mean value modelling approach has been taken for the compressor and turbine modelling. Steady state data maps supplied by the manufacturers are used to extract the mathematical relationships between inputs and outputs. Pressure ratio ($\frac{p_i}{p_{atm}}$), inlet temperature (T_i) and rotational speed of the turbo-shaft (ω_{tc}) are input variables for the model and mass flow rate (w_{ci}) and torque generated at the compressor side (T_c) are the outputs. Isentropic efficiency (η_c) and actual compressor outlet temperature (T_{ci}) are the intermediate variables.

Compression and expansion in the compressor and turbine are assumed as isentropic processes. The inlet conditions for the compressor are considered to be atmospheric. The isentropic temperature ratio across the compressor can be expressed in terms of pressure ratio by the standard relation,

$$\frac{T_{ci,is}}{T_{atm}} = \left(\frac{p_i}{p_{atm}} \right)^{\frac{\kappa-1}{\kappa}} \quad (6.37)$$

where $\kappa = \frac{c_p}{c_v}$, $T_{ci,is}$ is the compressor outlet temperature when process is completely isentropic. p_{atm} and T_{atm} are the normal atmospheric pressure and temperature.

It is well known that the actual compressor requires more power than the isentropic compressor to compress the inlet gases, so the isentropic efficiency of the compressor $\eta_c (0 < \eta_c < 1)$ is introduced and defined as the ratio of work (power) in

the isentropic compression and actual compression. Work done is directly proportional to the temperature change in respective processes, so the compressor efficiency can be defined as follows:

$$\eta_c = \frac{T_{ci,is} - T_{atm}}{T_{ci} - T_{atm}} \quad (6.38)$$

Substituting Equation (6.37) into (6.38) gives,

$$T_{ci} = T_{atm} + \frac{T_{atm}}{\eta_c} \left(\left(\frac{p_i}{p_{atm}} \right)^{\frac{\kappa-1}{\kappa}} - 1 \right) \quad (6.39)$$

where T_{ci} and p_i are actual temperature and pressure at compressor outlet.

The first law of the thermodynamics can be used to describe the power absorbed by the compressor ((P_c)) as the rate of change of enthalpy across the compressor's inlet and outlet, and then the compressor torque (T_c) can be calculated as follows:

$$P_c = w_{ci} c_p (T_{ci} - T_{atm}) \quad (6.40)$$

$$T_c = \frac{P_c}{\omega_{tc}} \quad (6.41)$$

combining (6.39) - (6.41),

$$T_c = \frac{w_{ci} c_p T_{atm} \left(\left(\frac{p_i}{p_{atm}} \right)^{\frac{\kappa-1}{\kappa}} - 1 \right)}{\eta_c \omega_{tc}} \quad (6.42)$$

All the variables namely compression ratio $\frac{p_i}{p_{atm}}$, rotational speed ω_{tc} , compressor mass flow rate w_{ci} and compressor efficiency η_c used for describing the compressor model are described in Equations (6.37)-(6.42). As discussed previously, a compressor map is usually used to describe the relations between these variables. The compressor maps are generated in controlled test-bed conditions with temperature T_{ref} and pressure p_{ref} , but, real operating conditions may not be the same. Therefore, a correction scheme

is devised for it.

$$w_{ci}^* \frac{\sqrt{T_{ref}}}{p_{ref}} = w_{ci} \frac{\sqrt{T_{atm}}}{p_{atm}} \quad (6.43)$$

$$\omega_{tc}^* = \sqrt{\frac{T_{ref}}{T_{atm}}} \omega_{tc} \quad (6.44)$$

where w_{ci}^* and ω_{tc}^* are corrected compressor mass flow and rotational speed used to draw the compressor map. T_{atm} and p_{atm} have already been assumed as the actual inlet conditions of the compressor. Fortunately, the reference conditions are the same as the assumed inlet conditions. Hence, no correction will be made for the compressor maps, i.e. $w_{ci} = w_{ci}^*$, $\omega_{tc} = \omega_{tc}^*$. However, corrections must be made to the turbine maps and details are given in the turbine section.

6.3.4.2 Compressor map fitting

Maps for the turbine and the compressor are supplied by the manufacturer of the turbocharger. Normally, data below a certain speed of the turbo-shaft is not presented on the map because they represent a small area on the map; however, these areas are critical while operating the engine in automotive vehicles. The engine frequently operates at low load conditions and consequently the turbocharger goes through a very low speed range due to insufficient mass flow through the exhaust manifold. There can be two options to handle the situation, the first option is to have a very good physics based model in that region and the second one is to extrapolate the map in that region either directly using data or by using some empirical relationships. Unfortunately, the first option is not very well defined because in those areas; pressure ratios and mass flow rates are very small and lead to significant errors [90]. Therefore, extrapolation is the only solution. That said, linear extrapolation is difficult, so empirical relation based extrapolation is the best option. Fortunately, there are few available methods giving sufficient accuracy in the predictions [88]. One approach proposed in [89] is adopted in the current work giving sufficient accuracy as described in [88].

There are mainly two approaches to express the relationship between mass flow

rate, pressure ratio and rotational speed. One can be in the form of $W_c = f(\frac{p_{out}}{p_{in}}, \omega_{tc})$ and the second one can be in the form of $\frac{p_{out}}{p_{in}} = f(w_{ci}, \omega_{tc})$. It has been observed that the second model is more suitable for our fitting purpose because the first model is too sensitive to speed variations and also sometimes in the first model approach, the dynamic model exhibits surge behavior after integration. On the other hand, the second model is found to be more robust and efficient for the compressor map fitting.

Overall as a part of the mapping strategy, at first the compressor pressure ratio is expressed as a function of the mass flow rate and rotational speed, i.e. $\frac{p_{out}}{p_{in}} = f(w_{ci}, \omega_{tc})$ and then this relationship is inverted to give the compressor mass flow rate according to pressure ratio and rotational speed, i.e. $w_{ci} = g_1(\frac{p_{out}}{p_{in}}, \omega_{tc})$. The efficiency of the compressor can also be expressed as a function $\eta_c = g_2(\omega_{tc})$ [88].

Two dimensionless parameters are defined, the head parameter Ψ_c and the normalized compressor mass flow rate Φ_c .

$$\Psi_c = \frac{c_p \cdot T_{atm} \left(\left(\frac{p_i}{p_{atm}} \right)^{\frac{\kappa-1}{\kappa}} - 1 \right)}{\frac{1}{2} u_c^2} \quad (6.45)$$

$$\Phi_c = \frac{w_{ci}}{\rho_a \cdot \pi r_c^2 \cdot u_c} \quad (6.46)$$

where u_c is the compressor blade speed and r_c is the compressor wheel radius, $u_c = r_c \cdot \omega_{tc}$. The inlet Mach number is defined as,

$$M_a = \frac{u_c}{\sqrt{\kappa R T_{atm}}} \quad (6.47)$$

The head parameter Ψ_c and compressor efficiency η_c can be approximated by Φ_c and M_a in the following way [88],

$$\Psi_c = \frac{k_1 + k_2 \cdot \Phi_c}{k_3 - \Phi_c} \quad (6.48)$$

$$k_i = k_{i1} + k_{i2} \cdot M_a \quad (6.49)$$

k11	0.3529	k12	-0.1299
k21	-1.7782	k22	0.5432
k31	0.2686	k32	-0.071

Table 6.2: Compressor map fitting coefficients k_{i1} and k_{i2}

$$\eta_c = a_1 \cdot \Phi_c^2 + a_2 \cdot \Phi_c + a_3 \quad (6.50)$$

$$a_i = \frac{a_{i1} + a_{i2} \cdot M_a}{a_{i3} - M_a} \quad (6.51)$$

The coefficients k_i and a_i can be determined through a least square fit on the measurement data by using the interactive parametric fitting tool available in Matlab. Coefficients k_{i1} and k_{i2} are tabulated below,

Compressor maps are generally in the form of pressure ratios, expressed in terms of normalized mass flow rate and rotational speed of the turbo-shaft. Efficiency contours are plotted on top of that as shown in Figure 6.6. By these efficiency contours, coefficients a_i can be determined for different Mach numbers M_a . To determine the coefficients a_i by using Equation (6.51) is proposed in [88] but instead of that a new and more convenient approach has been adopted in present work. Once the data for a_i versus M_a is available, the coefficients a_i can be mapped as a function of M_a using the interactive parametric fitting tool.

$$a_i = f_i(M_a) \quad (6.52)$$

$$a_1 = p_{11} \cdot e^{q_{11} \cdot M_a} - p_{12} \cdot e^{q_{12} \cdot M_a} \quad (6.53)$$

$$a_2 = p_{21} \cdot e^{q_{21} \cdot M_a} + p_{22} \cdot e^{q_{22} \cdot M_a} \quad (6.54)$$

$$a_3 = p_{31} \cdot e^{q_{31} \cdot M_a} \quad (6.55)$$

Where $p_{11} = -3.979 \times 10^{-9}$, $q_{11} = 16.12$, $p_{12} = 61.32$, $q_{12} = -1.67 \times 10^{-2}$, $p_{21} = 11.75$, $q_{21} = 0.2$, $p_{22} = 2.62 \times 10^{-4}$, $q_{22} = 6.898$, $p_{31} = -1.0 \times 10^{-3}$ and $q_{31} = 4.47$.

Once mapping is done and all the unknown parameters such as k_i and a_i are calculated, the compressor model is ready to be used being integrated with rest of the model. Since pressure ratio $\frac{p_i}{p_{out}}$ and u_c are known inputs, head parameter Ψ_c can be

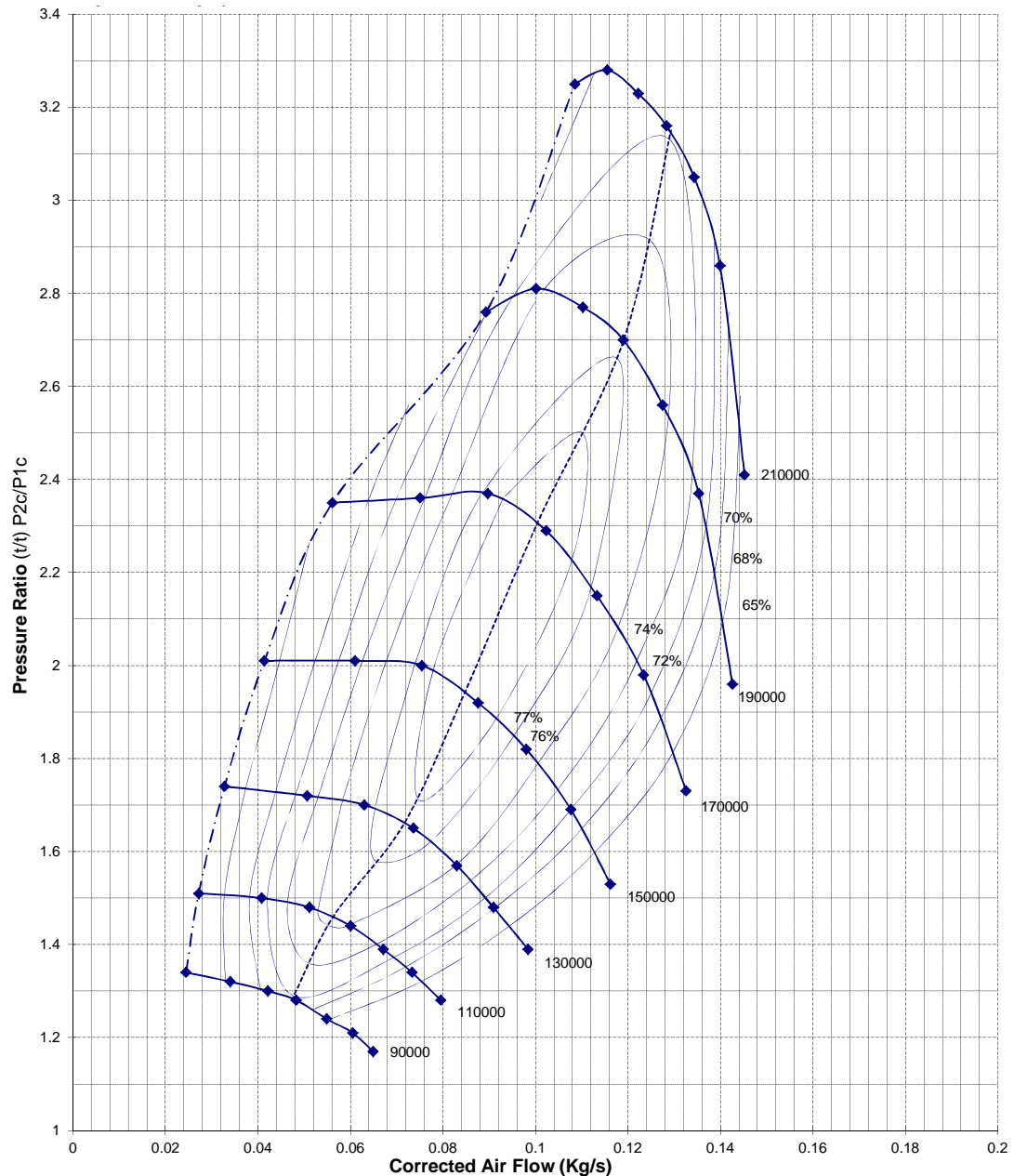


Figure 6.6: Compressor map supplied by the manufacturer. Experimental pressure ratios across the compressor are expressed in terms of normalized mass flow rate through it and at different rotational speed of the turbocharger. Efficiency contours are plotted on top of the map. Turbocharger speed is depicted in rpm.

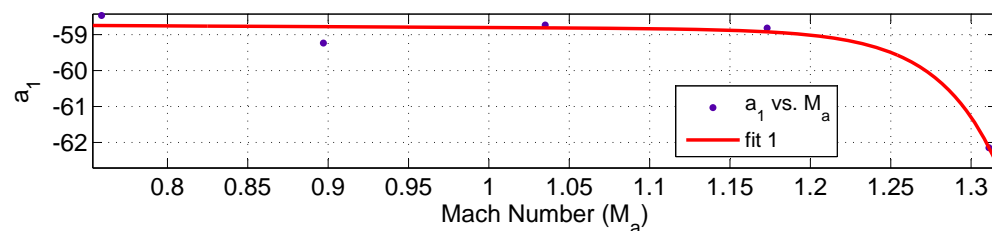


Figure 6.7: Coefficient a_1 map fitting

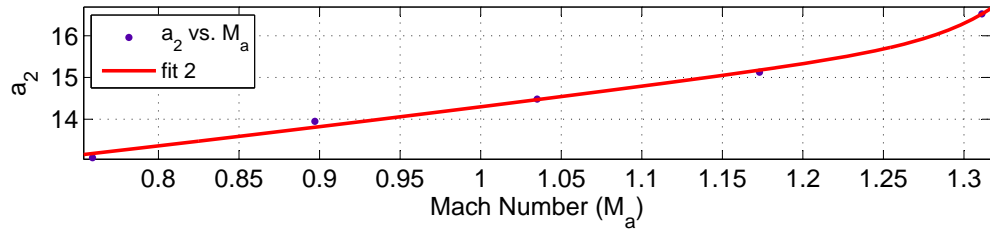


Figure 6.8: Coefficient a_2 map fitting

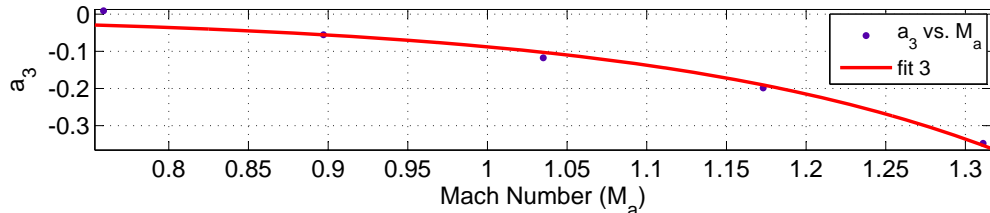


Figure 6.9: Coefficient a_3 map fitting

calculated by Equation (6.45). Then by inversion of Equation (6.48), compressor mass flow rate w_{ci} can be obtained by using Equation (6.46)

$$\Phi_c = \frac{k_3 \cdot \Psi_c - k_1}{k_2 + \Psi_c} \quad (6.56)$$

$$w_{ci} = \Phi_c \cdot \rho_a \cdot \pi \cdot r_c^2 \cdot u_c \quad (6.57)$$

Compressor map fitting results are presented in Figure 6.10. Extrapolations of the map are not shown in this figure. The measurement data are plotted as dashed lines with dots and the calculated data are represented by the continuous lines with dots in Figure 6.10. These two data are superimposed on each other to show the accuracy of data fitting and it can be observed that the fitting method yields quite satisfactory results. The numbers on this figure depict the speed of the turbocharger (ω_{tc} in rpm).

6.3.4.3 Variable geometry turbine (VGT)

The turbine of the turbocharger is driven by the energy of the exhaust gases leaving the engine cylinder. By using the first law of thermodynamics, the power

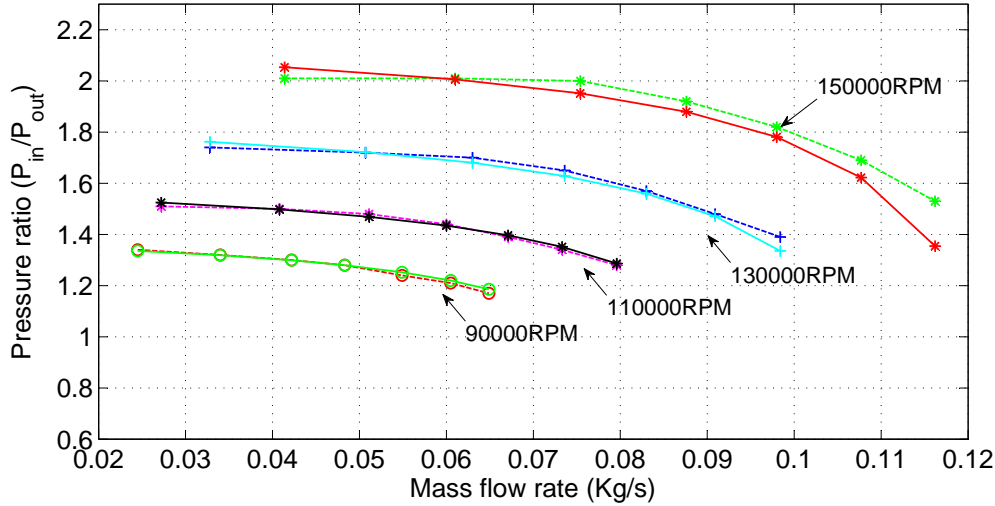


Figure 6.10: Compressor map fitting where the measurement data are plotted as dashed lines and the calculated data are represented by the continuous lines

transferred to the turbine by the exhaust gases can be calculated as follows:

$$P_t = w_{xt} c_p (T_x - T_{ref}) \quad (6.58)$$

$$T_t = \frac{P_t}{\omega_{tc}} \quad (6.59)$$

where P_t is the power input to the turbine, w_{xt} exhaust gas mass flow rate, c_p is the specific heat capacity of exhaust gas at constant pressure, T_x and T_{ref} is the temperature at the inlet and outlet of the turbine. T_t is the torque applied at the turbo-shaft due to exit of the exhaust gasses.

Expansion process of the exhaust gases is considered isentropic and the outlet temperature of the turbine is calculated as follows:

$$\frac{T_x}{T_{ref,is}} = \left(\frac{p_x}{p_{atm}} \right)^{\frac{\kappa-1}{\kappa}} \quad (6.60)$$

where $T_{ref,is}$ is the temperature of the exhaust gases at the output of the turbine if expansion were isentropic. p_x and p_{atm} (normal atmospheric pressure) is the pressure at the inlet and outlet of the turbine.

Since expansion is not isentropic as assumed for the purpose of calculation, the isentro-

pic efficiency is calculated to account for that [88],

$$\eta_t = \frac{T_x - T_{ref}}{T_x - T_{ref,is}} \quad (6.61)$$

Now, the torque produced by the turbine, T_t , can be derived using Equations (6.62)-(6.61)

$$T_t = \frac{w_{xt} c_p \eta_t T_x \left(1 - \left(\frac{p_{atm}}{p_x} \right)^{\frac{\kappa-1}{\kappa}} \right)}{\omega_{tc}} \quad (6.62)$$

Here it is assumed that the exhaust gases are expanded to atmospheric pressure by the turbine.

The correction terms play a more important role in the case of the turbine than the compressor because in the turbine, both inlet temperature T_x and pressure p_x vary substantially [90]. The turbine inlet gas temperature and pressure are assumed to be the same as that of the exhaust manifold. The measured data provided are corrected values, such that their relations to the actual values can be defined as

$$w_{xt}^* = w_{xt}^* \cdot \sqrt{\frac{T_{ref}}{T_x}} \cdot \frac{p_x}{p_{ref}} \quad (6.63)$$

$$\omega_{tc}^* = \sqrt{\frac{T_{ref}}{T_x}} \cdot \omega_{tc} \quad (6.64)$$

w_{xt}^* and ω_{tc}^* are corrected turbine mass flow rate and rotational speed. They are used to eliminate the dependence of the turbine map on inlet conditions. $T_{ref} = 288.33K$ and $p_{ref} = 101.32kPa$ are the reference temperature and pressure.

6.3.4.4 Turbine map fitting

Like the compressor, in the turbine also, pressure ratio $\frac{p_x}{p_{atm}}$, inlet temperature T_x and rotational speed of turbo-shaft ω_{tc} are taken as inputs and the exhaust mass flow rate w_{xt} is taken as output. The mass flow behavior of the turbine can be modelled using standard orifices with variable area (adiabatic nozzle flow), which is the same as for the

Table 6.3: Turbine map fitting coefficients b_{ij}

b_{11}	-0.0269	b_{21}	0.0798
b_{12}	0.038	b_{22}	0.0242
b_{13}	0.0043		

EGR valve. The effective flow area of the orifice is modelled as an explicit function of the pressure ratio and since the influence of the turbocharger speed on the mass flow rate and pressure ratio is very low, it is neglected in this model.

$$A_t = b_1 \frac{1}{\frac{p_{atm}}{p_x}} + b_2 \quad (6.65)$$

Since the turbine is of variable nozzle geometry, the vane angle has to be included in the model and for this purpose, coefficients b_1 and b_2 are extracted from the measured data as functions of the vane position u_{vgt} .

$$b_1 = b_{11} \cdot u_{vgt}^2 + b_{12} \cdot u_{vgt} + b_{13} \quad (6.66)$$

$$b_2 = b_{21} \cdot u_{vgt} + b_{22} \quad (6.67)$$

$u_{vgt}[0 - 1]$ takes the value 0 when the vane is fully closed and 1 when it is fully open. Since there is no model included in this work for the calculation of vane position, so a constant value $u_{vgt} = 0.5$ is taken in the present work.

Equations for the turbine expansion are derived assuming it to be an isentropic expansion although the actual expansion is not so. But the error introduced by the assumption of isentropic expansion is relatively low, therefore the corrected turbine mass flow can be defined by the standard adiabatic nozzle flow equation as [88],

$$w_{xt}^* = A_t \sqrt{\frac{2\kappa}{\kappa-1} \left(\left(\frac{p_{atm}}{p_x}\right)^{\frac{2}{\kappa}} - \left(\frac{p_{atm}}{p_x}\right)^{\frac{\kappa+1}{\kappa}} \right)} \quad \text{for } \frac{p_{atm}}{p_x} \geq p_{crit} \quad (6.68)$$

$$w_{xt}^* = A_t \sqrt{\frac{2\kappa}{\kappa-1} \left((p_{crit})^{\frac{2}{\kappa}} - (p_{crit})^{\frac{\kappa+1}{\kappa}} \right)} \quad \text{for } \frac{p_{atm}}{p_x} < p_{crit} \quad (6.69)$$

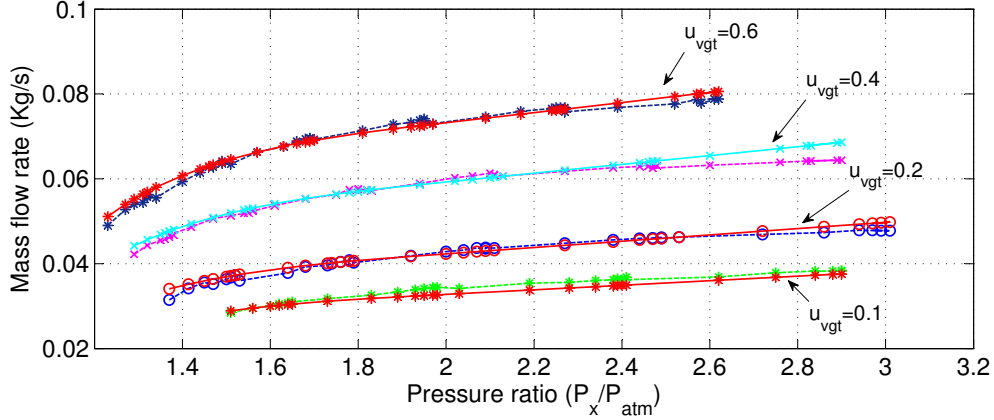


Figure 6.11: Turbine map fitting where the measurement data are plotted as dashed lines and the calculated data are represented by the continuous lines. The vertical and horizontal axis represent the ratio of pressures at the input and output port of the turbine $\frac{P_x}{P_{atm}}$ and the corrected mass flow rate w_{xt}^* , respectively.

where A_t is the effective flow area through the turbine and $p_{crit} = 0.528$ is the critical pressure ratio when the condition at the turbine inlet reaches sonic.

Turbine map fitting results are presented in Figure 6.11. Extrapolations of the map are not shown in this figure. The measurement data are plotted as dashed lines with dots and the calculated data are represented by the continuous lines with dots in Figure 6.11. These two data are superimposed on each other to show the accuracy of data fitting and it can be observed that the fitting method yields quite satisfactory results. The numbers on this figure depict the vane position u_{vgt} .

The turbine inlet stagnation temperatures are required for fitting the turbine efficiency map, but these data sets are not available at present. The efficiency of the turbine is simply assumed to be a constant value of $\eta_{t,avg} = 0.573$, which is the average value of all the efficiencies measured from the turbine. Although it is a strong assumption but seeing the overall complexity of the present model and time constraint for the current research work it has been used for simplifying the turbine modelling. Later on in the future a detail model for efficiency of the turbine η_t will be included in the overall engine model to capture the more realistic behaviour of the turbine. The calibration factor K_x introduced at the exhaust side is mainly to compensate for these kinds of uncertainties and assumptions in the modelling and the lack of operational data

at the experimental level.

6.3.4.5 Turbocharger dynamics

The mechanical dynamics of the turbocharger can be described as follows:

$$\frac{d\omega_{tc}}{dt} = \frac{1}{J_{tc}}(T_t - T_c) \quad (6.70)$$

where J_{tc} and ω_{tc} are the rotational inertia and the rotational speed of the turbocharger(rad/s) respectively. T_t and T_c are the torques generated in the turbine and compressor, respectively.

6.4 Calibration Factors

There are many assumptions and uncertainties in the model, either due to the lack of complex experimental verifications or unavailability of the required data. There are a few prominent sources of uncertainties, which are as follows:

1. Unknown volume of inlet and exhaust manifolds - Manifolds are made by the collection of pipes with different curved geometries, so the exact volume of the inlet and exhaust manifolds are unknown.
2. Unknown volumetric efficiency η_v - Volumetric efficiency of the engine cylinder is unknown beforehand because it depends on many geometrical and flow conditions, which are not considered in the present model. Being a 1D model, the Ricardo-Wave model of the engine has included these values. η_v changes substantially with change in engine/VGT vane angle conditions. Since no model has been employed to calculate η_v , therefor for simplicity in the present model η_v has been assumed a constant ($\eta_v = 1$). But from Table (6.1), it can be observed that η_v is not constant and is varying substantially.

3. Unknown efficiency of the intercooler η_{ic} - In the modelling of turbocharged diesel engine efficiency of the intercooler is assumed to be $\eta_{ic} = 1$, which is always not the case in reality.
4. Unavailability of EGR data - The data produced by the present Ricardo-Wave model of the Puma engine contains EGR components, but unfortunately, the present research lacking any information about the EGR radius, throttle angle and throttle control signal u_{egr} .
5. Unknown efficiency of the turbine - The efficiency of the turbine η_t over the different range of mass flow and turbine shaft speed depend on many complex factors and any relevant model for that is unknown to us, so a average value $\eta_t = 0.573$ has been assumed.
6. Unknown u_{vgt} - Variation of the VGT angle u_{vgt} for the turbine over the complete operating range is unknown, so a constant value of $u_{vgt} = 0.5$ has been assumed.
7. Unknown inertia - The inertia of the engine shaft is unknown to us, so an approximated value $J_e = 0.2 \text{kgm}^2$ proposed by Chen [213] for a similar engine is used in his work.
8. Unknown geometrical effects over fluid flow - Geometrical aspects of the engine and components are ignored while modelling the fluid flow inside and through the engine and its components.

The parameters mentioned above have minor and major impact on the overall accuracy of the results, generated by the simulation in terms of fuel consumption and torque generation. To compensate for these uncertainties, two calibration factors has been used, k_{in} (inlet calibration factor) and k_x (exhaust calibration factor), for the calculation of the inlet gas mass flow into the engine cylinder and the exhaust gas mass flow out through the turbine respectively.

Original equations for the inlet and exhaust gas mass flow rate without calibration factors is given by:

$$w_{ie} = \eta_v \frac{\rho_i V_d \omega_{eng}}{\sigma \cdot 60} \quad (6.71)$$

$$w_{xt} = w_{xt}^* \cdot \sqrt{\frac{T_{ref}}{T_x}} \cdot \frac{p_x}{p_{ref}} \quad (6.72)$$

Modified equations for the inlet and exhaust gas mass flow rate with calibration factors is defined by:

$$w_{ie} = k_{in} \cdot \eta_v \frac{\rho_i V_d \omega_{eng}}{\sigma \cdot 60} \quad (6.73)$$

$$w_{xt} = k_x \cdot w_{xt}^* \cdot \sqrt{\frac{T_{ref}}{T_x}} \cdot \frac{p_x}{p_{ref}} \quad (6.74)$$

In reality, these calibration factors are just mass flow correction factors for inlet air into the cylinder w_{ie} and exhaust air through the turbine w_{xt} . There is no scaling in the torque calculations and fuel consumption rate or in any other such critical variable. As described above, there are many factors affecting the air mass flow rate in and out of the turbocharged engine. Real predictions about the inlet and exhaust gases can be brought about only by including all the three dimensional geometrical aspects of the air-path in the model. But inclusion of such complex details about the air path will further increase the complexity of the model to such a substantial level that it will destroy the very purpose of the modelling. It has already been mentioned that our aim is to build a fast, simple and control-oriented engine model which can be used in the simulation of an HEV powertrain. The required accuracy of course retained in the model.

These calibration factors are tuned in such a way that error between experimental fuel consumption and calculated fuel consumption can be minimized. Trial and error method has been used to decide these values over different speed points. K_{in} and K_x are calculated for the given set of the parameters in this project such as the engine shaft

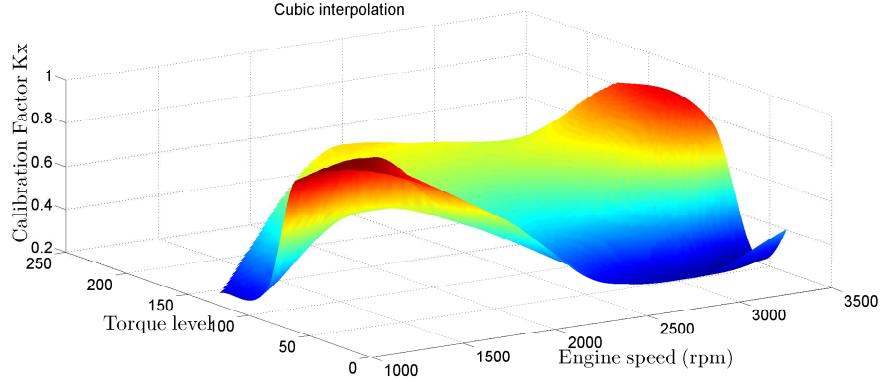


Figure 6.12: Calibration factor for exhaust gas K_x

inertia, inlet and exhaust manifold volumes. For different sets of parameters, these calibration factors have to be measured again on the given engine data. But still, this modelling approach is general enough to accommodate any kind of diesel engine having the previously mentioned source of uncertainties. The inlet calibration factor K_{in} is modelled as a function of rotational speed of the engine shaft ω_{eng} and an empirical relation is described as follows:

$$K_{in} = a_{cl} + b_{cl}\omega_{eng} + c_{cl}\omega_{eng}^{1.5} + d_{cl}\omega_{eng}^2 + e_{cl}\omega_{eng}^{0.5} \quad (6.75)$$

where $a_{cl} = -32.59$, $b_{cl} = -0.075$, $c_{cl} = 8.4 \times 10^{-4}$, $d_{cl} = -3.17 \times 10^{-6}$ and $e_{cl} = 2.74$.

The exhaust calibration factor K_x , which affects the exhaust gas mass flow rate w_{xt} , is modelled as a function of rotational speed of the engine shaft ω_{eng} and brake torque T_b . Figure 6.12 presents the three dimensional surface map for K_x at different speeds and torques in the form of $K_x = f(T_b, \omega_{eng})$.

With the inclusion of the EGR in the engine model, inlet air mass flow rate w_{ie} will increase and the exhaust gas mass flow rate w_{xt} will decrease, so it naturally points out that the correction factors multiplied to w_{ie} should be more than 1 ($K_{in} > 1$) and the correction factor multiplied to exhaust gas mass flow rate w_{xt} should be less than 1 ($K_x < 1$). During simulation, it has been found that this general trend of behavior as

suggested above is followed well by the calibration factors and Table (6.5) tabulates these values.

6.5 Control of the Turbocharged Diesel Engine

Control of the turbocharged diesel engine is the aim of this complete modelling task. There can be many control objectives and they require specific model architecture in terms of input and output to achieve the desired results. The most obvious and desired control objectives can be listed in the following ways [90]:

1. The torque demanded by the operating load should be instantaneously supplied along with good drivability conditions and minimum fuel consumption.
2. The engine must be chosen to run in such an operating region, where it gives safe and optimum performance in terms of no over smoke and no damage to the engine due to overheating.
3. The emission threshold conditions must be met safely by controlling the dynamic air-fuel ratio. The operating region is chosen in such a way that the poor performance conditions such as demanding transients, over smoke and cold start can be avoided.

Where in figure 6.13, $\omega_{desired}$ and ω_{eng} are the desired and actual speed of the engine. w_{fuel} and w_{ie} are the mass flow rate of the fuel and air injected into the engine cylinder for burning. λ is the relative air-fuel ratio. T_{ex} and w_{ex} are the temperature and mass flow rate of the cylinder-out gasses. w_{ci} and w_{xt} are the mass flow rate of the gasses into the inlet and exhaust manifolds after leaving compressor and turbine respectively. p_i , T_i , p_x and T_x are the pressure and temperature of the inlet and exhaust manifold respectively. T_{eng} , $T_{fric,eng}$, $T_{fric,gen}$, and $T_{elec,gen}$ is the indicative torque, engine friction torque, PMSG friction torque and electromagnetic torque of the PMSG, respectively. T_c and T_t are the torque on the turbo-shaft by the compressor and turbine, respectively.

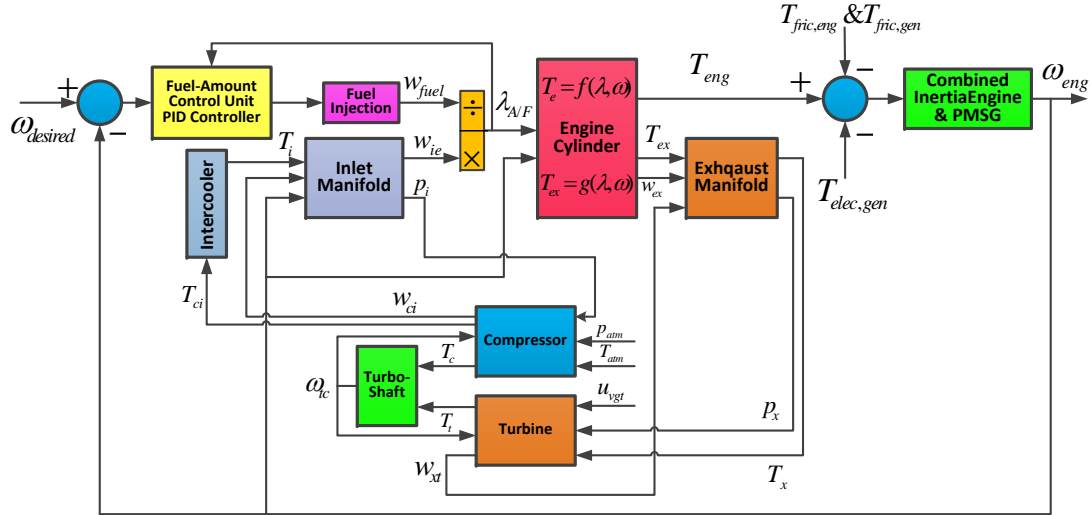


Figure 6.13: Control loops of the turbocharged diesel engine.

ω_{tc} is the rotational speed of the turboshaft. T_{ci} is the temperature of gasses at the output of the compressor. p_{atm} and T_{atm} are the atmospheric pressure and temperature. u_{vgt} is the vane angle for the turbine.

In the diesel engine, there are two parameters available to the designers for control of the generated torque and engine speed. One is the injected fuel amount and the other is the fuel injection timings. In the current mean-value modelling approach, all the in-cylinder effects are assumed to be evenly spread over all the thermodynamic cycles and the cylinders without any discontinuity. So, the discrete fuel-injections are not considered and the fuel injection timings are ignored. Rather, for the operation of the engine, a continuous fuel-mass flow rate is calculated. Speed and torque of the engine is controlled on the basis of fuel injection control. Figure 6.13 presents the overview of the control structure of the turbocharged diesel engine.

Overall the turbocharged diesel engine control scheme, where the engine is integrated with the drivetrain of the HEV, can be described in terms of one main control and two internal feedback loops. The control loop sets the desired speed $\omega_{desired}$ for the engine, such as idling speed $\omega_{idle} = 800$ rpm or operating speed $\omega_{operating} = 2000$ rpm, depending on the decision variables of the HEV. The command for the reference speed ($\omega_{desired}$) comes from the supervisory controller, which is external to the engine

model and therefore, will be described later. In Figure 6.13, it can be seen that there is one main outer control loop, which controls the speed of the engine and there are many internal loops due to the physics of the engine with complicated connections between engine inlet and exhaust side due to inclusion of the turbocharger. The objective of the outer control loop is to control the generated engine torque T_{eng} by controlling the air-fuel ratio λ to meet up the load torque demand. Here, the overall load torque is the summation of engine friction torque $T_{fric,eng}$, PMSG friction torque $T_{fric,gen}$ and electromagnetic torque of the PMSG $T_{elec,gen}$.

When the load torque is applied to the engine shaft, there is a sudden decrease in the actual engine speed (ω_{eng}) and this decrease in the engine speed creates positive speed difference between the actual speed and the desired engine speed reference ($\Delta\omega = \omega_{desired} - \omega_{eng}$). Further, this speed difference is fed to the fuel amount control unit, which decides the amount of the fuel to be burned so that the required engine torque T_{eng} can be generated and the actual engine speed (ω_{eng}) can be increased to the desired level ($\omega_{desired}$). The required engine torque T_{eng} which meets this demand of the load torque depends on the relative air-fuel ratio λ . The fuel injection rate w_{fuel} is already calculated by the fuel injection model and the turbocharger model calculates the injected air amount (w_{ie}). By knowing the air-fuel ratio ($\lambda = \frac{w_{ie}}{w_{fuel}} / 14.22$) and the current speed of the engine (ω_{eng}), the values of the generated engine torque (T_{eng}), exhaust temperature (T_x) and exhaust mass flow rate (w_{ex}) can be calculated by Equations (6.25), (6.31) and (6.33), respectively. The exhaust gases drive the turbine and compressor to compress the inlet air, so the turbocharger dynamics closes an internal physical feedback loop.

In the series hybrid vehicle, the engine is not directly connected to the wheels, rather it is driving the PMSG to maintain constant DC-link voltage. Below certain load current (i_{load}), the battery alone feeds the PMSM through the inverter to meet the driving power demand but over that current limit, the battery is disconnected from the DC-link power bus and the PMSG starts feeding the power demands of the PMSM

and the inverter. Though, there are some conditions for switching between the power sources other than the load current such as the SOC of the battery and speed of the car. The management of the power flow in association with multiple power sources is done by the supervisory controller and will be described in Chapter 8. During the complete operation of the HEV, the DC-link voltage is always maintained constant at 700V. When the engine is feeding the DC-link, it can be maintained at constant value only by running the PMSG above a certain threshold value of the rotational speed. PMSG and engine shafts are coupled with a constant gear ratio ($G = 2$). A speed level where the engine gives optimum performance is chosen as the desired speed of the engine.

6.5.1 Fuel amount control unit

Since the DC-link voltage is maintained at constant level, any increase in the power demand from the driver side leads to an increase in the load current (i_{load}) and this increase in the load current (i_{load}) is met by increasing the torque (T_{eng}) provided by the engine to the PMSG. The difference of the desired speed and the actual speed of the engine is fed to the fuel amount control unit, which is a PID controller with fixed saturation limits (only a fixed amount of fuel can be injected at any given instant of time and it has a maximum positive value of 0.0026 kg/s and a minimum value of 5×10^{-5} kg/s because 0 kg/s gives instability in torque calculation and negative values for the fuel input are not possible). This fuel amount control unit decides the amount of fuel to be burned for meeting the required torque demands of the driver end, while maintaining the desired speed of the engine.

At the time of deceleration or at the time of regeneration ($i_{load} = 0A$ on the PMSG), when the speed difference goes negative because suddenly engine is not required to provide any torque, the PID controller tries to put a negative amount of the fuel in the engine cylinder. The PID controller then hits the lower saturation limit of the fuel amount control unit, which does not go below zero, and as a result, the

integrator of the PID controller integrates continuously a persistent negative speed error and starts winding-up. To overcome this saturation problem (which is also known as the integrator-windup problem), a feedback loop is implemented by taking the difference of the calculated fuel amount ($w_{fuel,cal}$, before the saturation) and the actual fuel amount ($w_{fuel,in}$, after the saturation) and adding it to the integrator of the controller. Figure 6.14 describes the PID controller with the anti-windup scheme for controlling the fuel amount to be burned.

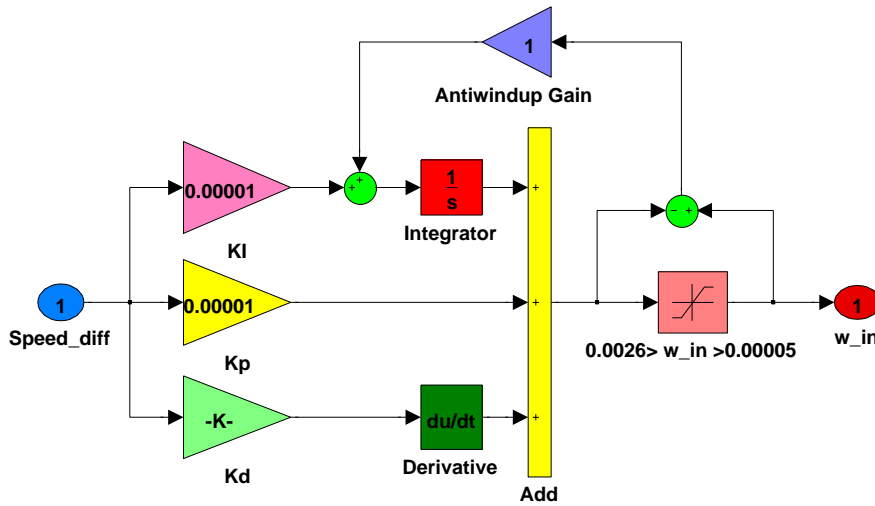


Figure 6.14: Fuel amount control unit with antiwindup control

This fuel amount is the total amount of the fuel to be burned instantaneously to meet the increase in the power demand by generating more torque T_{eng} . The total amount of the fuel is not injected inside the engine cylinder instantaneously, rather it takes some finite duration of time. Therefore, a low pass filter is used to model this effect with real time constant ($\tau = 5$ ms) as explained in previous Section 6.3.3.3. The engine torque is controlled by controlling the air-fuel ratio (λ), which depends on the injected fuel (w_{fuel}) and the inlet air amount (w_{ie}).

6.5.2 Control of the relative air-fuel ratio (λ)

At the time of acceleration, when the speed of the engine is switched from 800 rpm to 2000 rpm, the PID controller tries to burn a significant positive amount of fuel

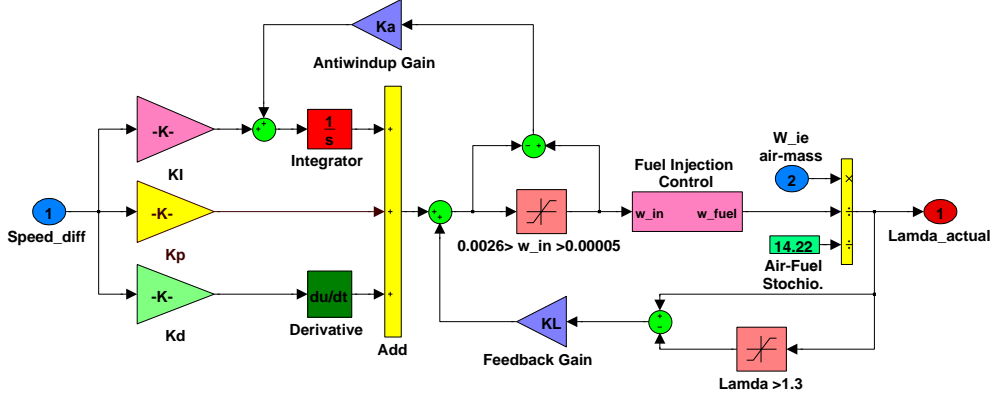


Figure 6.15: Implementation of the feedback control for the relative air-fuel ratio λ

instantaneously. The diesel engines are mostly operated at lean conditions, otherwise there can be excess emissions leading to the violation of emission constraints. When the temperature is high and the air-fuel mixture is too rich in fuel content, it leads to the formation of soot and visible smokes. To avoid such critical conditions, generally the fuel-air equivalence ratio is kept below a certain number ($\phi_{eq} < 0.8$) [206]. The fuel-equivalence (ϕ_{eq}) ratio is the inverse of the relative air-fuel ratio λ [84].

$$\lambda = \frac{1}{\phi_{eq}} \quad (6.76)$$

$$\text{Since } \phi_{eq} < 0.8 \quad \text{then } \lambda > 1.25 \quad (6.77)$$

To enforce this condition on λ , a feedback control loop is designed just like the anti-windup loop. This loop measures the current value of λ and compares it with the minimum allowed value (although $\lambda > 1.25$ is sufficient but more strict limit $\lambda_{min} = 1.3$ is chosen). If the current value of $\lambda > \lambda_{min}$, then there is nothing feedback but if $\lambda < \lambda_{min}$, a negative feedback is generated which is added to the calculated fuel amount ($w_{fuel,cal}$). Figure 6.15 describes the control of the relative air-fuel ratio λ . This control scheme successfully maintains the value of $\lambda > 1.3$ and has been demonstrated in Chapter 9.

In the case of stand-alone engine simulation, there is no PMSG coupled with the engine. The torque control loop is exactly the same but the load torque is now given

Table 6.4: Parameters of the turbocharged diesel engine

Symbols	Parameter	Values	Type
V_i	Inlet manifold volume	0.00044 m^3	Estimated
V_x	Exhaust manifold Volume	0.00044 m^3	Estimated
V_d	Engine displacement	0.002 m^3	Manufacturer
η_{ic}	intercooler efficiency	1	Estimated
$T_{coolant}$	Coolant temperature	$363K$	Manufacturer
r_c	Compressor wheel radius	22.62 mm	Experimental
J_e	Engine inertia	0.2 kgm^2	Estimated
J_{tc}	Turbocharger inertia	0.00012 kgm^2	Manufacturer
Q_{HV}	Low heating value of fuel	42 MJ/kg	Estimated

as an external input for the purpose of our simulation.

6.6 Simulation and Results

Models of the inlet manifold, engine cylinder, exhaust manifold, turbine, compressor and intercooler are already described in previous sections in terms of empirical relations, maps and dynamic equations. Now, in this section, the governing equations will be summarized and simulink implementations of these models will be described in detail. The important parameters of the turbocharged diesel engine used in our work are tabulated in Table 6.4. Some of these parameters are supplied by the manufacturer for the Puma 2.0L some of them are experimentally calculated and some of them are mathematically estimated for the purpose of modelling.

6.6.1 Simulink model of engine

This section presents the implementation of the mathematical equations described in the previous sections in the form of simulink block diagrams. Figure 6.16 presents the simulink block diagram of the engine alongwith its components. The EGR block diagram is not presented in Figure 6.16 because of non-availability of EGR data and the EGR model is not used for simulation.

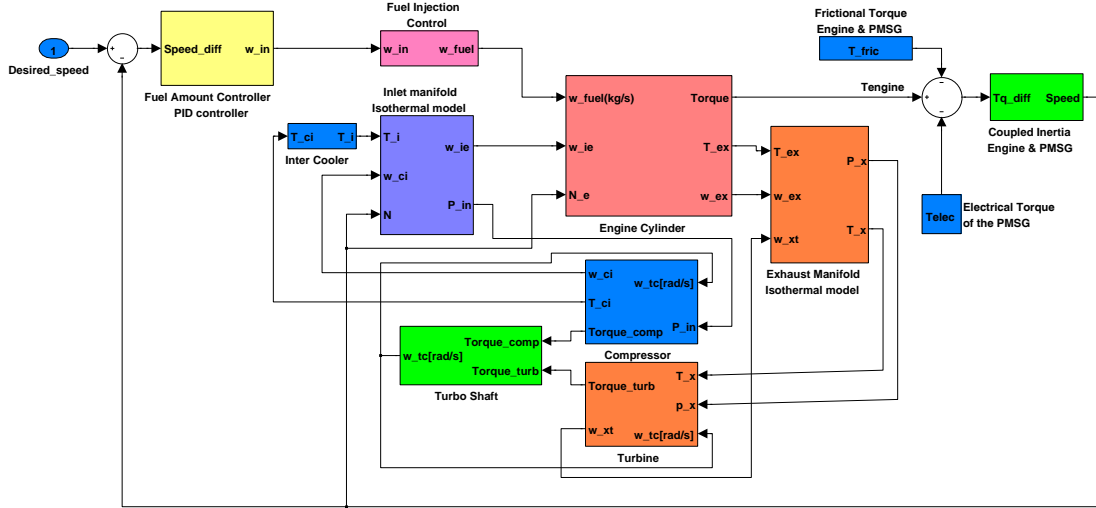


Figure 6.16: Simulink block diagram of the diesel engine with components

6.6.1.1 Inlet manifold block

Figure 6.17 presents the simulink block diagram of the inlet manifold. The filling and emptying modelling approach is used to describe the isothermal model of the inlet manifold as derived in Section 6.3.1. Calculation of the calibration factor K_{in} and the engine pumping action model is included in this block diagram to calculate the corrected air-mass flow rate inside the engine cylinder.

Inputs: Air temperature in the inlet manifold T_i [K]

Compressor air mass flow rate w_{ci} [kg/s]

EGR mass flow rate w_{xi} [kg/s]

Engine rotational speed [RPM]

Outputs: Air mass flow rate into engine cylinder w_{ie} [kg/s]

Inlet manifold pressure p_i [kPa]

Equations:

$$\frac{dm_i}{dt} = w_{ci} + w_{xi} - w_{ie} \quad (6.78)$$

$$p_i V_i = m_i R T_i \quad (6.79)$$

$$w_{ie} = K_{in} \eta_v \frac{\rho_i V_d N_e}{\sigma \cdot 60} \quad (6.80)$$

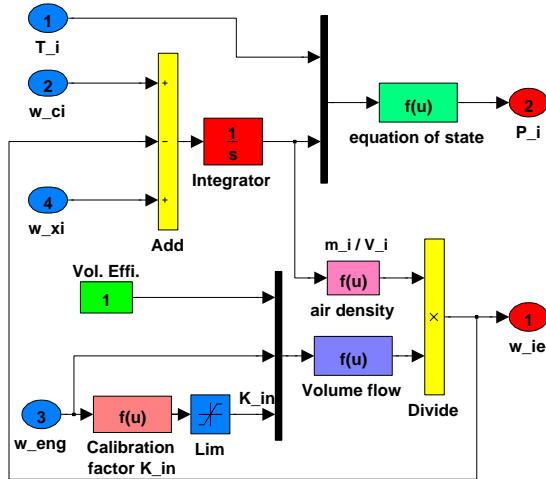


Figure 6.17: Simulink block diagram of the Inlet Manifold

6.6.1.2 Exhaust Manifold Block

The isothermal model of the exhaust manifold, as described in Section 6.3.1, is also derived with the help of filling and emptying modelling approach. Figure 6.18 presents the simulink implementation of the exhaust manifold.

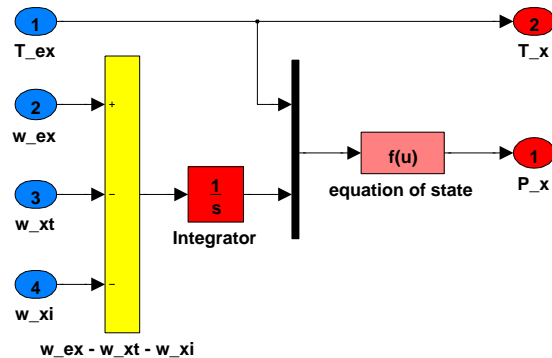


Figure 6.18: Simulink block diagram of the Exhaust Manifold

Inputs: Exhaust temperature T_{ex} [K]

Exhaust mass flow rate from cylinder w_{ex} [kg/s]

Turbine mass flow rate w_{xt} [kg/s]

EGR mass flow rate w_{xi} [kg/s]

Outputs: Exhaust manifold temperature turbine inlet [K]

Exhaust manifold pressure turbine inlet [kPa]

Equations:

$$p_x V_x = m_x R T_x \quad (6.81)$$

$$\frac{dm_x}{dt} = w_{cx} + w_{xt} - w_{xi} \quad (6.82)$$

6.6.1.3 Engine Cylinder

Torque generation and engine efficiency, as described in Section 6.3.3, are included in this block as shown in Figure 6.19.

Inputs: Air mass flow rate into engine cylinder w_{ie} [kg/s]

Engine rotational speed ω_{eng} [RPM]

Fuel mass flow rate $w_{fuel} = w_{fuel,out}$

Outputs: Engine torque T_{eng} [Nm]

Exhaust gas temperature T_{ex} [K]

Exhaust mass flow rate w_{ex} [kg/s]

Engine efficiency η_e

Equations:

$$T_{eng} = g(\lambda, \omega_{eng}) \quad (6.83)$$

$$\begin{aligned} \lambda &= \frac{(Air/fuel)_{actual}}{(Air/fuel)_{stoichiometric}} \\ &= \frac{\frac{w_{ie}}{w_{fuel}}}{14.22} \end{aligned} \quad (6.84)$$

$$\frac{dw_{fuel,out}}{dt} = \tau(w_{fuel,in} - w_{fuel,out}) \quad (6.85)$$

$$T_{ex} = f(\lambda, \omega_{eng}) \quad (6.86)$$

$$w_{ex} = w_{ie} + w_{fuel} \quad (6.87)$$

$$\eta_e = \frac{T_e \times \omega_{eng}}{w_{fuel} \times Q_{HV}} \quad (6.88)$$

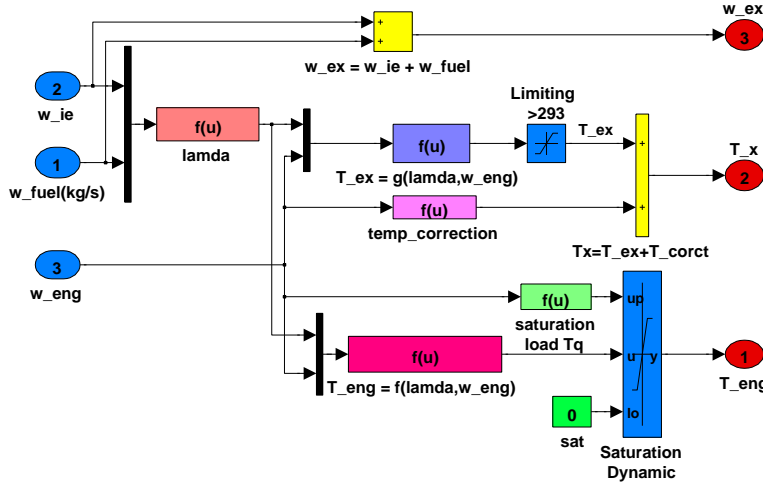


Figure 6.19: Simulink block diagram of the Engine Cylinder

6.6.1.4 Turbocharger

Since the turbocharger model, as described in Section 6.3.4, involves a lot of map fittings and corrections, it is one of the most complicated models. It has three sections namely, the compressor on the inlet side, the turbine on the exhaust side and a common turbo-shaft. Figures 6.20 and 6.21 present the simulink implementation of the compressor at different levels. Figure 6.22 presents the simulink implementation of the turbine.

- Inputs:
- Inlet manifold pressure p_i [kPa]
 - Atmospheric pressure $p_{atm} = 100$ [kPa]
 - Atmospheric temperature $T_{atm} = 293.15$ [K]
 - Exhaust manifold pressure p_x [kPa]
 - Exhaust manifold temperature T_x [K]
 - VGT vane position u_{vgt} [0-1]

Outputs: Compressor mass flow rate w_{ci} [kg/s]

Compressor outlet temperature T_{ci} [K]

Turbine mass flow rate w_{xt} [kg/s]

Equations:

$$\frac{d\omega_{tc}}{dt} = \frac{1}{J_{tc}}(T_t - T_c) \quad (6.89)$$

$$w_{ci} = g_1\left(\frac{p_i}{p_{atm}}, \omega_{tc}\right) \text{Compressor mass flow fitting model} \quad (6.90)$$

$$\eta_c = g_2(\omega_{tc}) \quad \text{Compressor efficiency fitting model} \quad (6.91)$$

$$w_{xt} = w_{xt}^* \cdot \sqrt{\frac{T_{ref}}{T_x}} \cdot \frac{p_x}{p_{ref}} \quad (6.92)$$

$$w_{xt}^* = f_1\left(A_t, \frac{p_{atm}}{p_x}\right) \quad (6.93)$$

$$A_t = f_2\left(\frac{p_{atm}}{p_x}, u_{vgt}\right) \quad (6.94)$$

$$T_c = \frac{w_{ci}c_p T_{atm} \left(\left(\frac{p_i}{p_{atm}}\right)^{\frac{\kappa-1}{\kappa}} - 1 \right)}{\eta_c \omega_{tc}} \quad (6.95)$$

$$T_t = \frac{w_{xt}c_p T_x \left(\left(\frac{p_{atm}}{p_x}\right)^{\frac{\kappa-1}{\kappa}} - 1 \right)}{\eta_t \omega_{tc}} \quad (6.96)$$

$$T_i = T_{ci} - \eta_{ic}(T_{ci} - T_{coolant}) \quad \text{Intercooler} \quad (6.97)$$

6.6.2 Discussion of simulation results

In this section, results only related to the validation of the engine model and its stand alone simulation will be presented and then in the Chapter 9, transient results related to the engine model integrated to the drivetrain of the series HEV will be presented.

Figure 6.23 presents the comparison of the fuel consumption calculated by the Ricardo-Wave model (which has been safely taken as the experimental fuel consumption) and predicted by the proposed mean-value model. In this figure, dotted lines

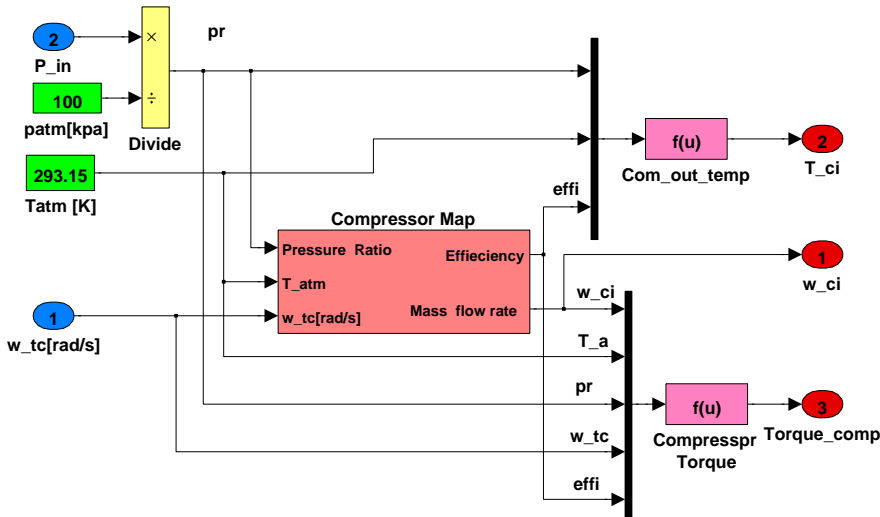


Figure 6.20: Simulink block diagram of the Compressor (level I)

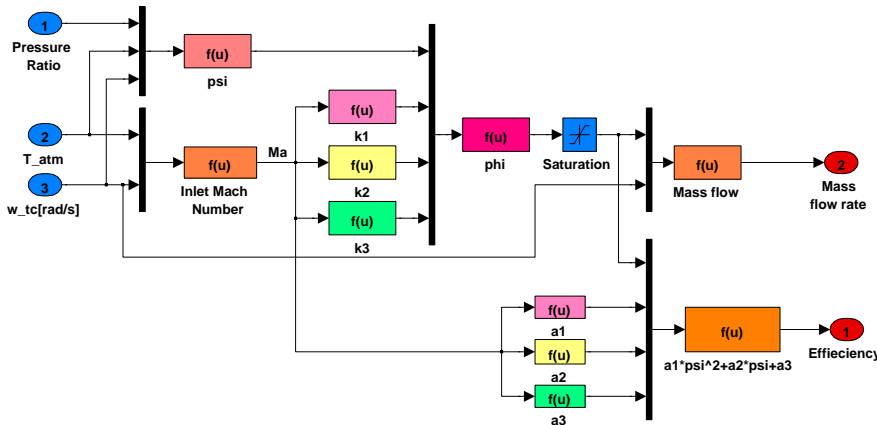


Figure 6.21: Simulink block diagram of the Compressor (level II)

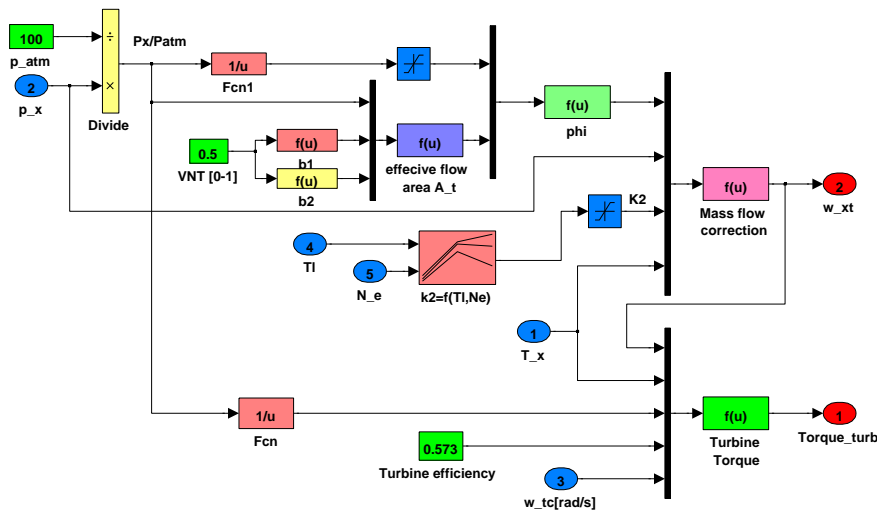


Figure 6.22: Simulink block diagram of the Turbine

Table 6.5: Comparison of the experimental and simulated results for various parameters of the engine such as air-mass flow rate (A_{exp} & A_{sim}), fuel-mass flow rate (F_{exp} & F_{sim}) and exhaust temperature for different combinations of engine speed ω_{eng} and torque T_b

ω_{eng} rpm	T_b Nm	Temp Exp. K	Temp Sim. K	λ	A_{exp} $\times 10^{-2}$ kg/sec	A_{sim} $\times 10^{-2}$ kg/sec	F_{exp} $\times 10^{-3}$ kg/sec	F_{sim} $\times 10^{-3}$ kg/sec	K_{in}	K_x
1000	61.39	645.1	740.2	1.87	1.19	1.16	0.45	0.45	2.40	0.30
1000	84.95	791.3	804.5	1.38	1.20	1.39	0.62	0.62	2.40	0.35
1000	124.5	899	876.9	1.29	1.59	1.67	0.87	0.87	2.40	0.26
1500	44.24	582.7	541.7	2.35	1.69	1.87	0.51	0.58	2.60	0.95
1500	64.04	690.8	666.6	1.95	1.94	1.94	0.70	0.69	2.60	0.93
1500	76.37	704.9	717.5	1.81	2.00	2.04	0.78	0.78	2.60	0.90
1500	86.50	757.8	752.2	1.75	2.24	2.25	0.90	0.90	2.60	0.65
1500	107.9	805	812.6	1.74	2.72	2.54	1.10	1.11	2.60	0.56
1500	129.8	863.2	863	1.59	2.94	2.71	1.30	1.29	2.60	0.55
1500	151.6	919.4	905.8	1.51	3.23	2.87	1.50	1.47	2.60	0.55
1500	185.5	1188	962.6	1.14	3.09	3.15	1.90	1.81	2.60	0.56
2000	29.90	572.7	365	3.97	3.44	2.31	0.61	0.59	2.25	0.56
2000	42.23	636.7	489	2.21	2.14	2.46	0.68	0.70	2.25	0.56
2000	75.03	769.2	702.9	1.69	2.54	3.00	1.06	1.05	2.25	0.54
2000	108.7	836.8	832.2	1.68	3.40	3.48	1.42	1.42	2.25	0.58
2000	121.7	890	871.1	1.60	3.63	3.68	1.60	1.58	2.25	0.59
2000	144.3	951.2	929.9	1.52	4.03	4.00	1.87	1.86	2.25	0.61
2000	167	1010	980.9	1.49	4.53	4.30	2.13	2.16	2.25	0.63
2000	188.4	1054	1023	1.43	4.89	4.56	2.40	2.46	2.25	0.65
2000	214.5	1071	1070	1.36	5.16	4.84	2.67	2.82	2.25	0.68
2500	36.93	587.7	458.6	3.75	4.30	3.43	0.81	0.89	1.88	0.26
2500	42.84	655.2	509.4	2.45	3.13	3.59	0.90	0.96	1.88	0.29
2500	76.60	776.2	750.7	1.90	3.70	4.37	1.37	1.45	1.88	0.43
2500	110.8	876.4	905.8	1.70	4.48	5.05	1.86	1.98	1.88	0.53
2500	142.3	979.4	1008	1.57	5.22	5.50	2.33	2.44	1.88	0.60
2500	163.3	1043	1064	1.50	5.68	5.70	2.67	2.72	1.88	0.65
2500	182.2	1109	1109	1.40	5.99	5.82	3.00	2.96	1.88	0.69
2500	192.8	1190	1132	1.34	6.35	5.87	3.33	3.10	1.88	0.72
3000	36.65	610.6	437.6	4.06	6.06	3.90	1.05	0.94	1.70	0.24
3000	66.91	706.6	688.8	2.76	6.02	5.21	1.53	1.53	1.70	0.37
3000	101.1	817.5	907.5	2.13	6.38	5.81	2.10	2.10	1.70	0.58
3000	174.7	1218	1162	1.29	6.84	7.30	3.73	3.62	1.70	0.71
3500	62.62	743	562	2.75	7.17	7.15	1.83	1.82	1.75	0.24
3500	97.36	855.7	894.3	2.13	7.65	7.30	2.53	2.54	1.75	0.77
3500	176.6	1399	1205	1.10	7.73	9.20	4.94	4.87	1.75	0.92

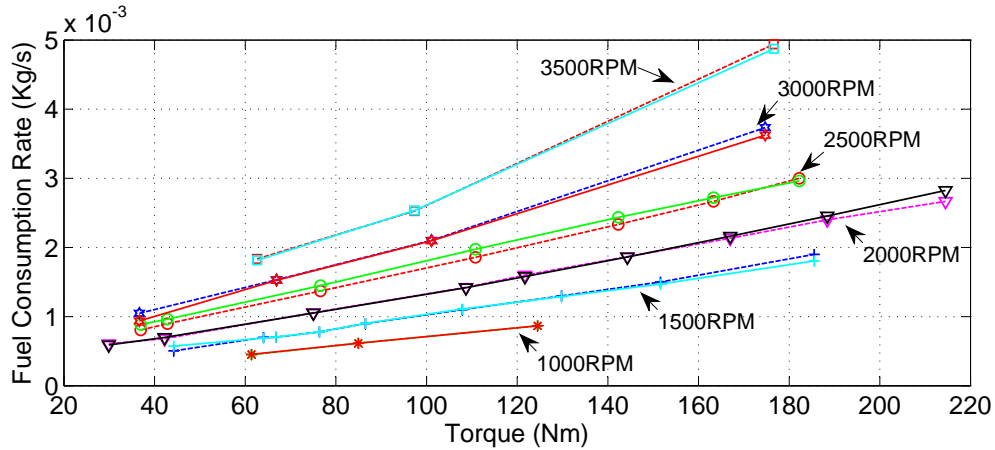


Figure 6.23: Verification of the fuel consumption between the Ricardo-Wave (EXP) model versus the Simulation (SIM) model. For every speed, there are two lines with the same kind of marker but with different kinds of line types. Dashed lines represent the experimental fuel consumption data and continuous lines represent the predicted fuel consumption.

represent the experimental fuel consumption and the continuous lines represent the predicted fuel consumption by the mean-value model. It can be observed in Figure 6.23 and also from Table 6.5 that the predicted values for the fuel consumption and inlet air are very close to the experimental values. The maximum error for the fuel consumption rate prediction, over the complete range of available data, is 6.54% (this error is calculated on the flow rate of kg/sec). This is a very good achievement considering the simplicity of the 0D model in comparison to the detailed 1D Ricardo-Wave model.

From Figures 6.24, 6.25, 6.26 and Table 6.5, it can be observed that predictions of the exhaust temperature by the present model are in reasonable accuracy with the Ricardo-Wave model. If the operating region of the engine is chosen in the range of 75Nm to 215Nm (which is most likely the normal operating range for an engine of an HEV powertrain), then the predictions results related to the exhaust temperature, fuel consumption and inlet air are very good.

There are overall six differential equations among many other empirical equations, involved in the mean-value modelling of the engine to capture the realistic transient behavior of the PUMA engine. Out of those six, two dynamic equations come from the engine-shaft and turbo-shaft inertia, two dynamic equations come from the

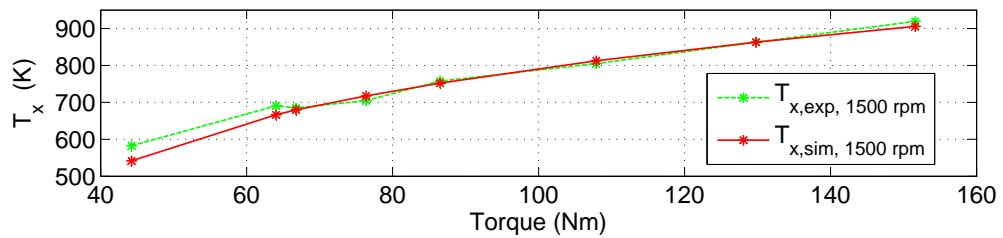


Figure 6.24: Exhaust temperature (T_x) at 1500 rpm. The dashed line represents the experimental exhaust temperature and the continuous line represents the predicted exhaust temperature.

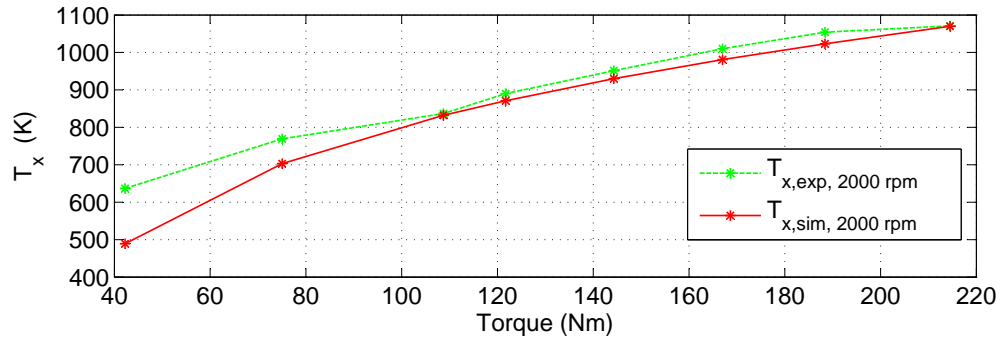


Figure 6.25: Exhaust temperature (T_x) at 2000 rpm. The dashed line represents the experimental exhaust temperature and the continuous line represents the predicted exhaust temperature.

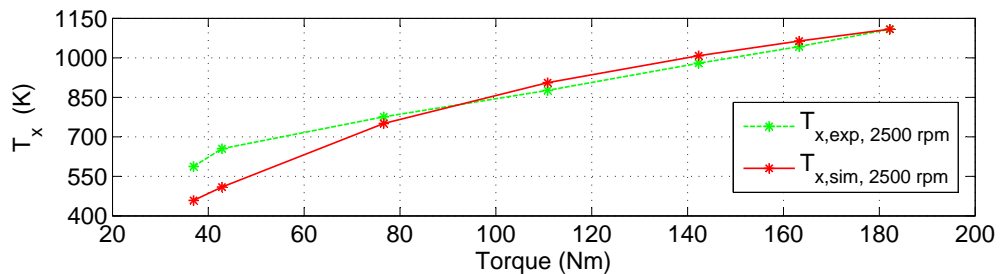


Figure 6.26: Exhaust temperature (T_x) at 2500 rpm. The dashed line represents the experimental exhaust temperature and the continuous line represents the predicted exhaust temperature.

isothermal filling and emptying model of the inlet and exhaust manifolds, while the last two come from the fuel amount control unit and fuel injection modelling. These six dynamic equations are coupled with each other in a very complex way, as depicted in Figure 6.13. Steady state conditions can be reached upon when $w_{ci} = w_{ie}$, $w_{ex} = w_{xt}$, $T_c = T_t$ and $T_{eng} = T_{load} + T_{fric}$. This chapter presents the steady state simulation results and validation for the same against Ricardo-Wave simulation results for Puma 2.0L. After integrating the present mean-value model of the engine, with the rest of the powertrain according to the integration principles mentioned in Chapter 8, transient simulation results will be presented in Chapter 9.

6.7 Summary

- A control-oriented 0D dynamic mean-value model is presented in this work and is validated against the steady state data of the 1D Ricardo-Wave model of the Puma 2L engine.
- For controlled operation of the engine, PID controller based continuous fuel injection amount control strategy has been successfully implemented in this work. A anti-windup loop is also designed to negate the saturation effect in the PID controller of the fuel injection unit.
- A feedback control is successfully implemented for regulating the value of relative air-fuel ratio ($\lambda > 1.3$) which otherwise can cause serious emission problems.
- Table 6.5 presents the predicted values for the inlet air and fuel consumption, which are very close to the experimental values presented in same table. The maximum error for the fuel consumption rate prediction, over the complete range of available data, is 6.54% (this error is calculated on the flow rate of kg/sec).
- Again from Table 6.5, it can be observed that predictions of the exhaust temperature by the present model, provided the operating region of the engine is chosen

in the range of 75Nm to 215Nm (which is most likely the normal operating range for an engine of an HEV powertrain), are in reasonable accuracy with the Ricardo-Wave model.

- Overall, it can be said that while the present model may not be a fully transient, it is definitely not a completely stationary model as well. Rather, this model fills the gap between the map based fully stationary model, generally used for HEV simulation, and the complex transient models such as Ricardo-Wave, which can not be directly used in the HEV powertrain simulation. Precisely, that was the aim of the overall engine modelling in the context of the present work.

CHAPTER
SEVEN

BATTERY MODELLING

7.1 Introduction

A hybrid powertrain, as the name suggests, requires involvement of multiple energy sources. Seeing critical threats to the environment, rechargeable energy sources is one of the foremost catalysts in the development of future transportation vehicles. Rechargeable energy sources have the capacity to produce energy on demand (discharge) and also to accept energy (recharge) on availability. Electrochemical devices such as the fuel cell (FC) and the batteries are the most suitable options in this category. Electrical devices such as ultra capacitors are also rechargeable sources of energy. A desired rechargeable energy source can be described as having qualities such as high energy density, high power density and longer life cycles. But unfortunately, the development of the modern EVs and HEVs is seriously restricted by the unavailability of any such device which can have all the desired qualities simultaneously. Devices such as ultra capacitors have high power density but suffer from lower energy density, while batteries and FC are characterized by high specific energy density but suffer from low specific power density [2]. Even this highest available energy density in the batteries is very small in comparison to the gasoline engine. Therefore, overall, there are many challenges in the field of development of EVs and HEVs having the need for desired rechargeable energy sources.

7.2 Battery

A battery is an electrochemical device that can store energy in the form of chemicals and, on requirement, give it out in the form of electrical energy. Among all the renewable energy sources, batteries are most suitable for furthering the development of HEVs. Basically, a battery has two electrodes namely anode and cathode and these two electrodes are connected to each other by an electrolyte solution (can be liquid or solid) in-between. While discharging the cell, charge flows from anode to cathode in the outer circuit and while charging, the flow of the charge is exactly opposite in direction.

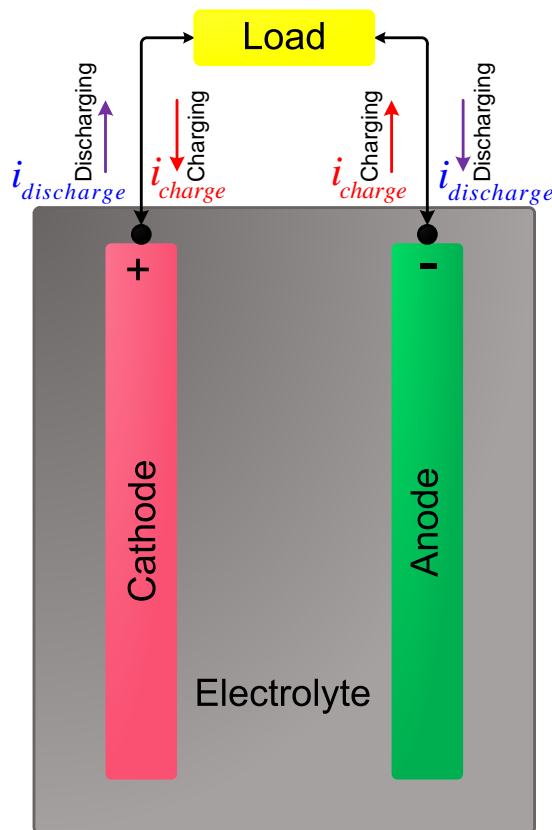


Figure 7.1: Electrochemical cell of a battery

From the time of invention of rechargeable Lead-Acid battery, many combinations of different materials have been tried for better performance, such as Nickel based batteries and Lithium based batteries. Out of many such combinations, Lithium

based batteries have outperformed all other batteries because of having very high power and energy density with very low internal resistance. Although Lead-Acid battery has many advantageous features such as low cost, mature technology and good life cycle, it suffers heavily from low energy density, high internal resistance leading to high self discharging rate, and, very deteriorated performance at low temperatures [2, 23].

Due to very high thermodynamic voltage, the Li-ion based batteries are very promising alternatives to all other forms of renewable energy sources. With ongoing research on the intercalated Li-ion, more powerful and safer Li-ion cells than ever are produced nowadays. Considering all these exciting features of Li-ion cells, the Li-ion based battery is used in the present work. Battery can be used as a range extender or prime power source, depending on the power and energy capacity of the employed battery and supervisory control priorities.

Before going into the analysis of battery dynamics, certain important terms, on which the whole mechanism will be analyzed, need to be defined. These terms specifically are total energy, specific energy, energy density, power density, charge capacity, Amphour efficiency, state of charge (SOC) and self discharge rate.

1. **Total Energy** - Total energy stored in a battery is calculated by the product of voltage and charge stored in the battery.
2. **Specific Energy** - Since both volume and weight are very important constraints, energy and specific energy are very important quantities to analyze battery performance. Specific energy is the energy storing capacity of a particular battery per kg mass of the battery.
3. **Energy Density and Power Density** - Energy density and power density are the energy capacity and power capacity of a battery per unit of battery volume, respectively.
4. **Charge Capacity** - Capacity of a battery is quantified by its ability to supply and accept the amount of electrical charge. The unit used to define this charge

capacity is Amp-hour.

5. **Amp-hour Efficiency** - Amp-hour efficiency is a kind of charging efficiency of the battery. Ideally, if a battery is discharged with certain amount of power and then recharged with the same amount of power, the state of charge will be the same. Rather, SOC will be lesser while recharging than the SOC at the start of discharge.
6. **State of Charge** - State of charge (SOC) is a measurement of the capacity of the battery to supply charge to an external load. The SOC of a battery very strongly depends on the rate of charge and discharge.
7. **Self Discharge** - Batteries get discharged if left unused for long time due to ongoing internal chemical reactions.

Li-ion batteries benefit by virtues of high power and energy densities along with very low self discharge rate. To use a battery in a modelling tool, a battery model which can predict the battery performance with sufficient accuracy is needed. The next section gives a review of many available battery models and based on that analysis, a suitable battery model is chosen for the current project.

7.2.1 Battery modelling

There is a fundamental need of understanding battery dynamics in relation to its charging and discharging process. To enhance the understanding of real battery performance, many different kinds of models are proposed. Frankly, no model developed so far fully captures the real battery performance and none of these models represent all aspects of the battery. Most of the battery models are proposed to predict certain phenomena under focus and have different level of complexity to achieve that purpose.

All proposed battery models to be used in HEVs are broadly categorized in three categories, namely, electrochemical dynamics based models, experimental data

based models and electrical circuits based models [108]. In electrochemistry based models, 1D mathematical model for Li-ion has been used to predict the battery behavior in a simulated environment. The electrochemical lumped thermal model proposed by Smith in [106] solves six coupled partial differential equations related to concentration of charges and species, over-potential and the terminal voltage. These differential equations are formed using the Butler-Volmer kinetic equation, the basis of many other such electrochemical models. The control volume method is employed to solve simultaneous coupled partial differential equations to capture charging and discharging battery behavior under normal operating conditions [109]. Transient responses are critical to the battery performance because at the time of regeneration, energy comes in the form of short bursts of power pulses [106]. It has already been explained that this model is highly computationally expensive due to the involvement of solving coupled differential equations by control volume methods. Similarly, the experimental data based models are very much specific to a particular type of battery for which the model is calibrated and lack the general prediction of the battery performance in different operational situations. Finally, an electrical circuit based battery model was chosen in this work.

Correct estimation of the battery SOC is one of the most important tasks in modelling the battery. SOC is used in the design of the supervisory controller to govern the performance of the battery. Electrochemical dynamics based equations are not very convenient in the estimation of SOC because the SOC heavily depends on the electrical conditioning of the circuitry involved around the battery. For example, the SOC of the battery depletes very fast with depleting voltage if the rate of discharge is high; whereas the SOC does not reduce so drastically for the same voltage levels if the rate of discharge is mild in nature. Overall, SOC is a very important descriptor for a battery and is highly dependent on the rate of current drawn and voltage during that process. Since electrical circuitry based battery models are very good in estimating SOC, the present work has adopted the battery model proposed in [112].

There are mainly four kinds of electrical circuit based battery models included in the ADVISOR library [110]. They are Matlab/Simulink dependent programs as summarized in [110]. These models, such as the RC model and the internal resistance model [111], are based on the different arrangement of resistive and parasitic elements in series or in parallel with a constant DC voltage source. There are two more models, known as the fundamental lead acid model and the neural network model. Most of these models work fine as long as the operation of the battery lies in the steady state. But when the current is subjected to dynamic changes, results are not very accurate and sometime unacceptable. Therefore a generic dynamic Li-ion model described in [112] has been chosen and integrated with the HEV powertrain. This model is now included in the Simulink library as well [113].

7.2.2 Description of the battery model

Originally, Shepherd proposed a battery model in [214], expressing the electrochemical parameters of the battery directly in terms of electrical parameters of the circuit. The main strength of this battery model is that it can be used to establish a relationship between the SOC of the battery, internal resistance, open circuit voltage and current demand. This fundamental model was later improved with some minor corrections to reflect battery dynamics with more accuracy such as in [215]. The same model is further developed in [112] to capture the generic dynamic response of the Li-ion battery. In the present model, open circuit voltage is presented as a non linear expression of the SOC and internal resistance. A polarization voltage term is added to accurately capture dynamics of the real battery. An exponential term $A \exp(-B \cdot it)$ is added in the voltage expression as a correction term to correctly map the real charging and discharging curve obtained in the experiments. One more new term $K \frac{Q}{it - 0.1 \cdot Q} \cdot i^*$ related to the product of polarization resistance and filtered current i^* is added in this model, not present in Shepherd's original battery model [214].

Equations for the Li-Ion Battery

Discharging:

$$V_{bat} = E_0 - R \cdot i - K \frac{Q}{Q - it} \cdot it + A \exp(-B \cdot it) - K \frac{Q}{Q - it} \cdot i^* \quad (7.1)$$

Charging:

$$V_{bat} = E_0 - R \cdot i - K \frac{Q}{Q - it} \cdot it + A \exp(-B \cdot it) - K \frac{Q}{it - 0.1 \cdot Q} \cdot i^* \quad (7.2)$$

Where:

- V_{bat} is the battery voltage (V)
- E_0 is the battery constant voltage (V)
- K is the polarisation constant ($\frac{V}{(Ah)}$) or polarization resistance (Ω)
- Q is the battery capacity (Ah)
- it is the $\int idt$ = actual battery charge (Ah)
- R is the internal resistance (Ω)
- i is the battery current (A)
- i^* is the filtered current (A)
- A is the exponential zone amplitude (V)
- B is the inverse of exponential zone time constant (Ah) $^{-1}$

The term polarization resistance is defined as the ratio of the applied voltage and the resulting current response. This “resistance” is inversely related to the uniform corrosion rate. Polarization resistance and voltage are defined to quantify the effect of internal chemical reactions happening at the electrodes on the internal resistance, output voltage and current. Introduction of these terms allows a simple model to capture the real battery dynamics by establishing the relation between three different aspects of the battery operation, namely, electrochemical, electrical and experimental. The present battery model has some inherent assumptions, which can be described as follows:

- Temperature is constant during operation.
- It has been assumed that either self-discharge of the battery does not take place or it is negligibly small.
- Internal resistance of the battery is constant during charging and discharging of the battery and does not change with current variations.
- Parameters of the battery model are extracted from the discharge characteristics of the battery from data produced by the manufacturer. Although parameters are obtained from the discharge curve, these are assumed to be valid for the charging curve as well.
- Capacity of the battery does not change with the amplitude of current.

With the purpose of simplification, it has been assumed that temperature of the battery will remain constant during complete operation although in real life this is not the case. Internal resistance of the battery changes with temperature of the battery and current drawn from it. Not only higher temperature is problem for operation of the battery but the lower temperature as well. At lower temperature kinetics of the battery becomes extremely slow adversely affecting its performance. The overall assumption of constant temperature for the battery is a strong assumption and in future it will be a good idea to include a temperature model in this battery model.

To extract battery parameters, three points are considered on the discharge characteristics curve of the battery and then those equations (obtained by using Equation (7.1) for three points on the discharge curve) are solved to get the values of constant parameters. In the present case, those values are directly taken from the simulink block for the generic battery model provided in SimPowerSystems (SPS). During the usage of the HEVs, many cells are stacked together in series and in parallel in order to get the required ratings for the desired performances. In the current work, a battery is chosen with maximum rated capacity of 20Ah and maximum rated voltage of 250V. By

Table 7.1: Parameter values of the Li-Ion cell

Parameter	Symbols	Li-Ion Cell
Rated capacity	Q_{max}	20Ah
Capacity at nominal voltage	Q_{nom}	18.09Ah
Initial state of charge	SOC	65%
Fully charged voltage	V_{Full}	250.25V
Nominal Voltage	V_{nom}	215V
Battery constant voltage	E_0	232.92V
Polarization constant	K	0.061Ω
Internal resistance	R	0.1075Ω
Time constant for filtered current (i^*)	T_r	30s
Nominal discharge current	i_{nom}	8.69A
Exponential zone amplitude	A	18.26(V)
Exponential zone time constant inverse	B	$3.05(Ah)^{-1}$

knowing these requirements, a certain number of Li-ion cells are stacked together and the parameters shown in Table 7.1 are calculated for the battery.

7.3 DC/DC Converter

A Hybrid Electric Vehicle requires a high power isolated bidirectional DC/DC converter to power the vehicle from a battery because there is a big difference in voltage levels between the high voltage side (HVS) and lower voltage side (LVS). As the DC bus of the HEV powertrain is 700V, the isolation of the battery staying around 200V to 300V from high voltage, is desirable. Thus an isolated DC/DC converter is required. Regenerating capability is one of the most excellent features of the series HEV. Therefore, to support the regenerating braking, the DC/DC converter has to be bidirectional as well. Unidirectional converters are used to supply power to sensors and other auxiliary power consuming components of the vehicle such as air condition, lights, etc.

When switches are operated in normal operating conditions, they are forced to switch on and off at very high voltage or current or both at the same time. These

kinds of switchings are called hard switching and these have many problems. For instance, high voltage derivative at the switch-off time creates an electromagnetic compatibility problem. High frequency switchings are employed to reduce the humming noise but these increase the switching losses due to constraints of finite time for switching transients. To avoid all these problems, soft switched zero voltage switching (ZVS) is achieved by various means leading to negligible switching losses in switching circuits [216].

A dual Half-bridge topology with zero-voltage-switching (ZVS) in either direction of the power flow without using any extra switching or control devices is implemented for the minimum loss and reduced cost. Isolated bidirectional DC/DC converter involves transformer current as an AC variable, however conventional state-space averaging techniques cannot remove it from the average DC model. A switching frequency-dependent-average model with a linearized small signal model has been derived to predict large and small-signal characteristics of the converter in both directions of the power flow [114]. In this switching frequency-dependent-average model, the duty cycle D , the phase angle shift between LVS and HVS voltages ϕ and switching frequency $f_s = \frac{1}{T_s}$ are the control variables. By controlling any of these three or all of them together, power flow can be controlled in either direction.

In Figure 7.2, the battery is connected to the low voltage side with inductor L_{dc} to provide smooth current to the primary of the transformer. Each switch (MOSFET) is connected with a capacitor in parallel and a diode in anti-parallel for soft switching operation. A switching frequency dependent averaged model is derived in [217], which can be further simplified if the duty cycle is taken as $D = 50\%$. The simplified average model for bidirectional power flow is presented as follows [114]:

$$\frac{di_{bat}}{dt} = -\frac{R_{bat}}{L_{dc}}i_{bat} - \frac{1}{2L_{dc}}v_{12} + \frac{1}{L_{dc}}v_{bat} \quad (7.3)$$

$$\frac{dv_{12}}{dt} = \frac{1}{C_p}i_{bat} - \frac{2\phi(\pi - \phi)}{C_p T_s \omega \cdot 2\omega L_s} v_{34} \quad (7.4)$$

$$\frac{dv_{34}}{dt} = \frac{2\phi(\pi - \phi)}{C_t T_s \omega \cdot 2\omega L_s} v_{12} - \frac{2}{C_t R_s} v_{34} + \frac{2}{C_t R_s} v_s \quad (7.5)$$

With the assumption of duty cycle $D = 50\%$, $v_1 = v_2$ and $v_3 = v_4$, circuits

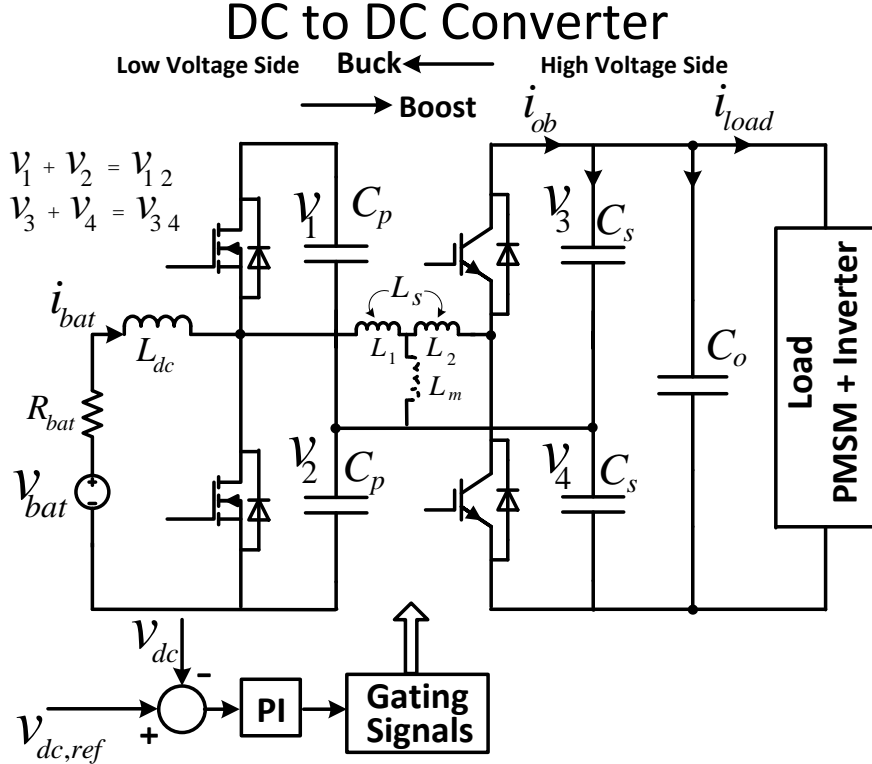


Figure 7.2: Primary referenced equivalent circuit for the DC-DC converter

analysis becomes extremely simple which leads to a set of simple Equations (7.3)-(7.5).

The high voltage side of the DC/DC converter is attached to the common DC-bus of the HEV. The high voltage side of the converter does not have any battery, so $v_s = 0$. When the DC-bus is fed by the high voltage side of the DC-DC converter, a DC current i_{load} is drawn from the high voltage side of the DC-DC converter to drive the HEV. R_s is the total load for the high voltage side of the DC-DC converter. In the present case of the HEV powertrain clearly, the PMSM along-with the inverter is the electrical load for the DC/DC converter. In addition to this, it can also be observed from Figure 7.2 that $v_{dc-link} = v_{34}$, so in such case $\frac{v_{34}}{R_s}$ can be replaced by the DC load current i_{load} and then, Equation (7.5) is transformed into Equation (7.6).

$$\frac{dv_{34}}{dt} = \frac{2\phi(\pi - \phi)}{C_t T_s \omega \cdot 2\omega L_s} v_{12} - \frac{2}{C_t} i_{load} \quad (7.6)$$

- Where $C_t = C_s + 2C_o$
- i_{bat} is the average current drawn from the battery
- v_{12} is the combined average voltage across the two capacitors (C_p) on the lower voltage side
- v_{34} is the combined average voltage across two capacitors (C_s) on the higher voltage side
- The parameters for this converter are as follows: $C_s = 10\text{mF}$, $L_{dc} = 5 \times 10^{-5}\text{H}$, $L_s = 8 \times 10^{-7}\text{H}$, $C_p = 10\text{mF}$, $C_o = 1\text{mF}$, $T_s = 5 \times 10^{-5}\text{sec}$ and $R_{bat} = 0.1075\Omega$.

By doing some rearrangements in Equation (7.6), the resultant form of the DC-link equation is:

$$\begin{aligned}\frac{C_t}{2} \frac{dv_{34}}{dt} &= \frac{\phi(\pi - \phi)}{T_s \omega \cdot 2\omega L_s} v_{12} - i_{load} \\ \frac{C_t}{2} \frac{dv_{34}}{dt} &= i_{ob} - i_{load}\end{aligned}\quad (7.7)$$

Where $i_{ob} = \frac{\phi(\pi - \phi)}{T_s \omega \cdot 2\omega L_s} v_{12}$ is the DC-current produced by the converter on the HVS.

7.4 Control Mechanism

When power flows from LVS to HVS, the DC/DC converter works as a boost converter but during the charging of the battery and regeneration, power flows from HVS to LVS and then, it is known as a buck converter. It has been described earlier that the magnitude and direction of the power flow can be controlled by controlling any of the three variables, D , ϕ and f_s . For the simplification of the control mechanism, however, both the duty cycle and the switching frequency, are taken as constant where $D = 50\%$ and $T_s = \frac{1}{f_s} = 5 \times 10^{-5}\text{sec}$. Now only by controlling a single variable ϕ , both the magnitude and the direction of the power flow can be controlled. When the phase

shift angle ϕ is positive, power flows from LVS to HVS and when ϕ is negative, power flows in the opposite direction (from HVS to LVS). The magnitude of the power flow is proportional to the amplitude of phase shift angle ϕ .

As a part of the control objectives, the DC-link voltage $v_{dc-link}$ also has to be maintained constant at 700V. First of all, a difference between the desired DC-link voltage $v_{dc,ref} = 700V$ and the actual DC-link voltage v_{dc} is calculated. This voltage difference is then passed through a PI controller to generate a reference for the phase shift angle ϕ_{ref} .

$$\phi_{ref} = (K_p + K_i \int dt) \{v_{dc,ref} - v_{dc}\} \quad (7.8)$$

Since the switching frequency is very high and an average model for the DC/DC converter is considered, it has been assumed that the desired phase shift angle ϕ_{ref} can be generated instantaneously by a specific switching pattern. In such conditions, it can safely be assumed that $\phi = \phi_{ref}$ and this ϕ will be directly supplied to the average model of the converters in Equations (7.4)-(7.6). Since there is a maximum and minimum limit for the phase shift angle, a saturation is used to describe this range $-\frac{\pi}{30} < \phi < \frac{\pi}{30}$. Figures 7.3 and 7.4 present simulink block diagrams of the DC/DC converter along with its control mechanism. In Figure 7.4, terms a_{33} and a_{23} are multiplicative constants for voltages v_{34} and v_{12} respectively, given in Equations (7.4)-(7.6).

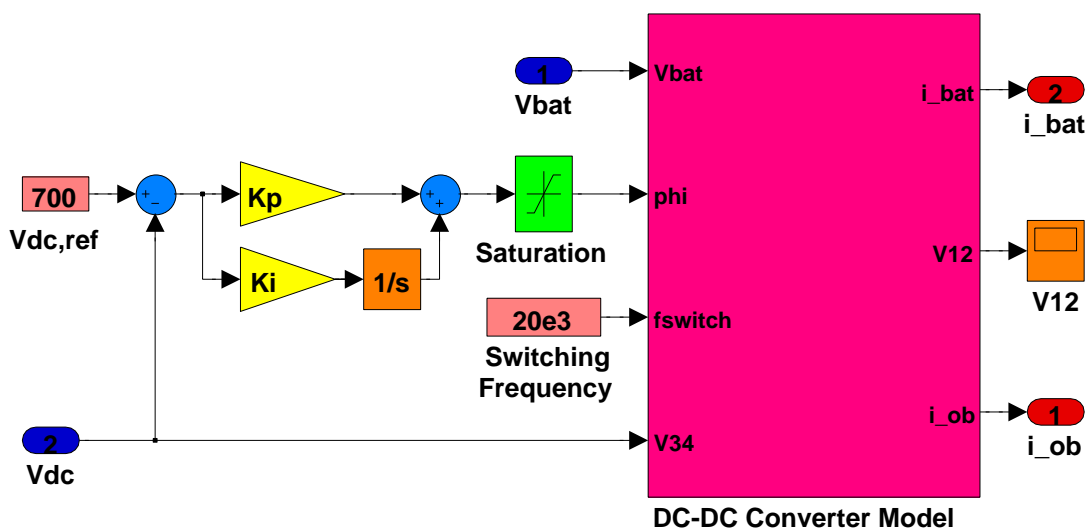


Figure 7.3: Matlab/Simulink block diagram for control of the DC-DC converter, level-I

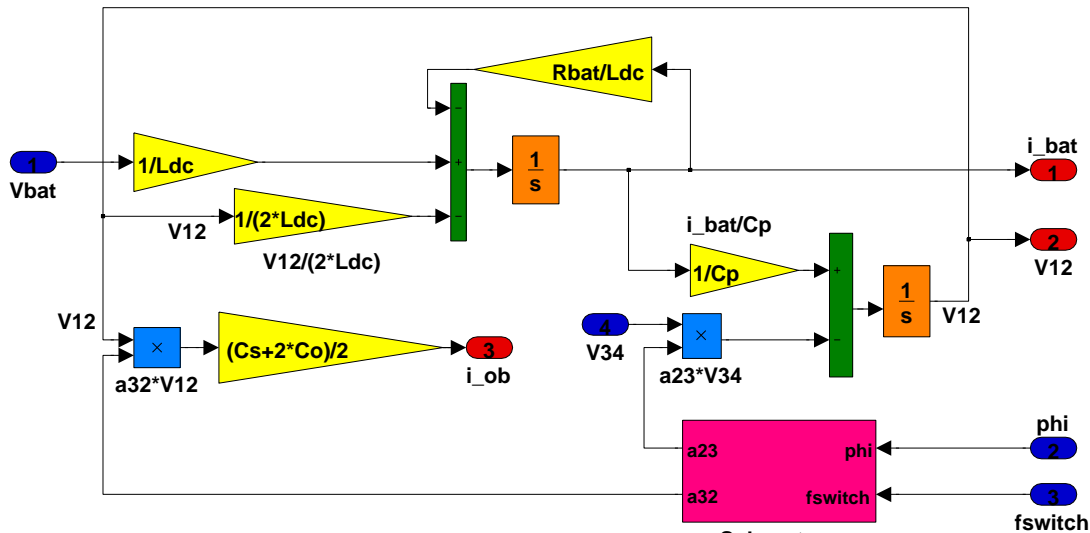


Figure 7.4: Matlab/Simulink block diagram for control of the DC-DC converter, level-II

7.5 Simulink Implementation of Battery Model with DC/DC Converter

In this section, the simulink implementation of the battery model along-with the DC/DC converter will be presented. Figure 7.5 gives the simulink diagram of a battery with DC/DC converter and DC-link. Figure (7.6) presents the simulink

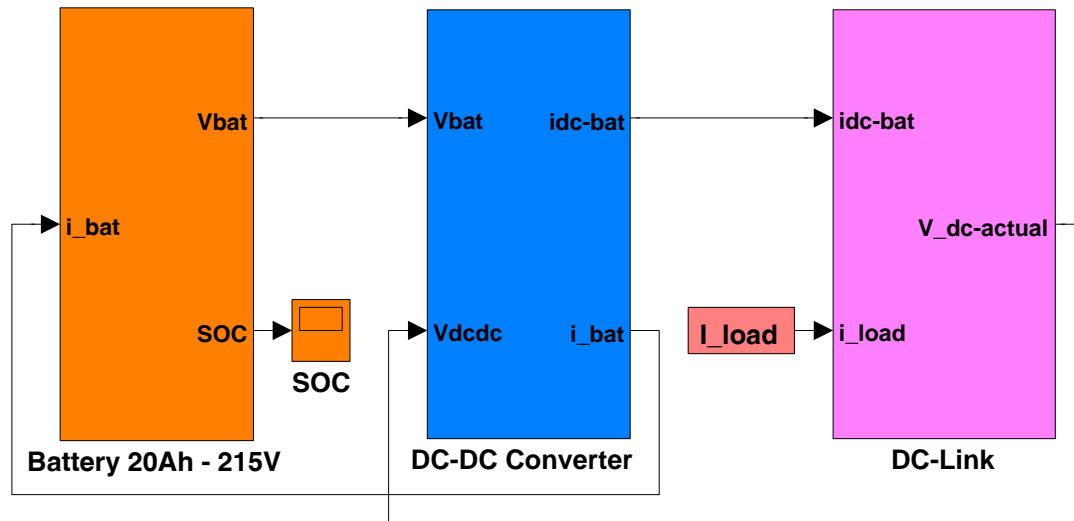


Figure 7.5: Matlab/Simulink block diagram of the battery model along with DC-DC converter and DC-link

implementation of the battery model, described in the form of mathematical Equations

(7.1)-(7.2). Figure 7.7 presents the simulink implementation of the DC-link in the form of mathematical Equation (7.7) and from this figure, it can be understood that $v_{dc} = v_{34}$.

7.6 Simulation Results

In the present section, simulation results related to the battery and DC/DC converter are presented. Since this model is not yet integrated with the PMSM as load, a step load current is designed to test the efficacy of the battery model along with the DC/DC converter.

According to the load current profile as shown in Figure 7.8, for the first 100 sec, the battery will be discharged with demand of constant load current $i_{load} = 20A$ and then for the next 100 sec, the battery will be charged with supply of constant load current $i_{load} = -20A$ (negative sign just signify the charging of the battery). Figure 7.8 presents the battery current i_{ob} profile according to the demand of load current i_{load} at HVS. From Figure 7.9, it can be observed that at first the DC-link voltage decreases during the discharge period of the battery and then at the 100th sec, there is a peak in the DC-link voltage due to a sudden change from the discharging mode to the charging mode. At this instant of time, the DC-link voltage deviates positively from the reference 700V and then the DC-link voltage decreases to settle around 700V as per expectations. Overall, the DC-link voltage is maintained in a very close range around 700V during both the charging and discharging cycles signifying the success of the control mechanism.

The battery is first subjected to discharging and then charging for equal periods of time and with equal amount of load current. Although +ve sign has been used for the discharge current and -ve sign for the charging, the SOC of battery decreases linearly during the discharging mode and increases linearly during the charging mode. If Figure 7.11 is observed carefully, an interesting fact is noted. When the battery is discharged

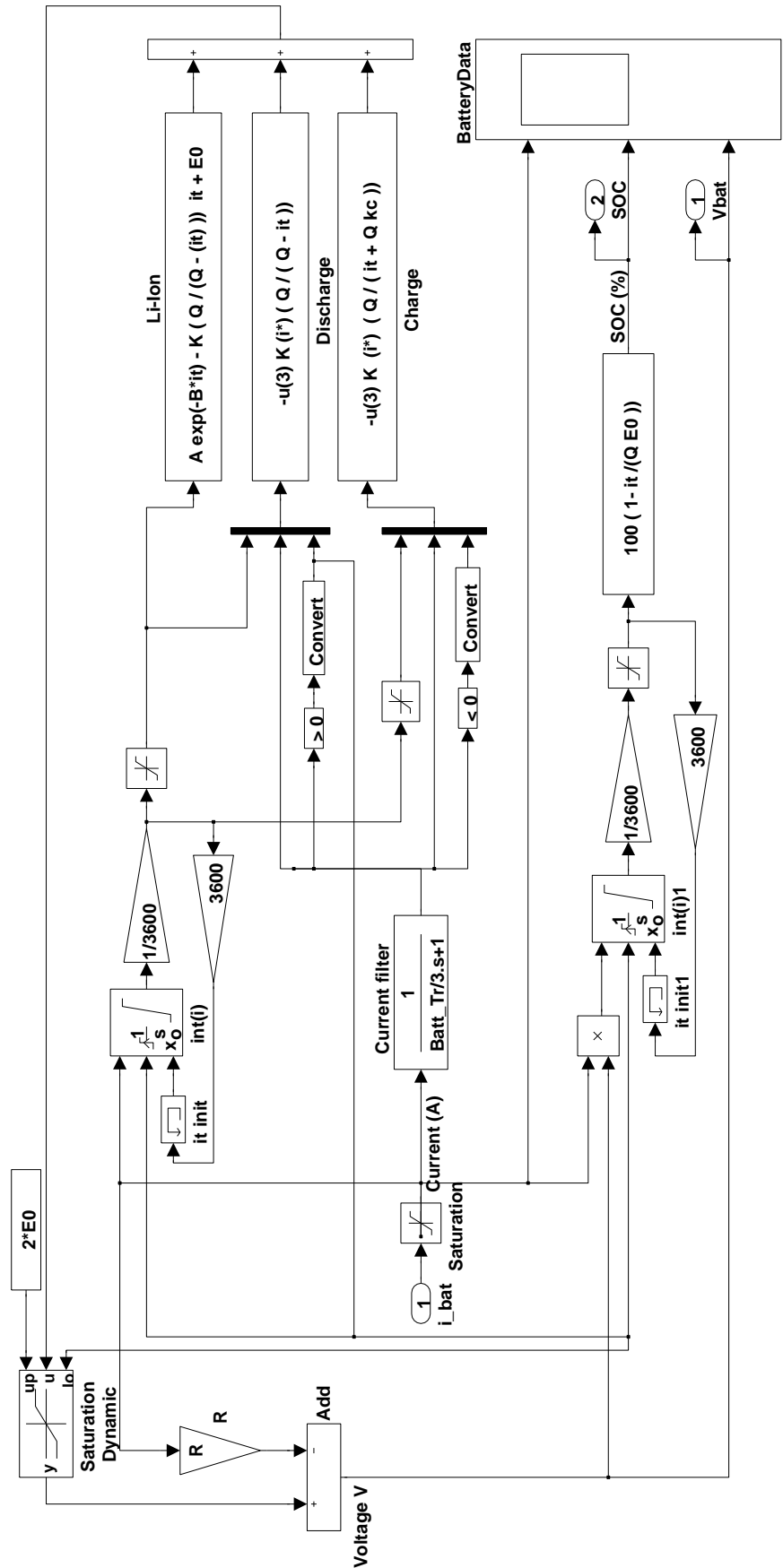


Figure 7.6: Matlab/Simulink block diagram of the battery model

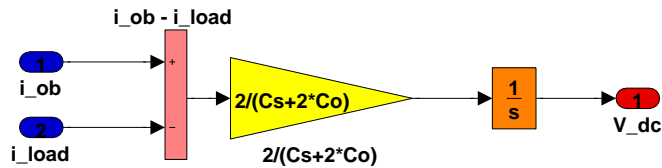


Figure 7.7: Matlab/Simulink block diagram of the DC-link

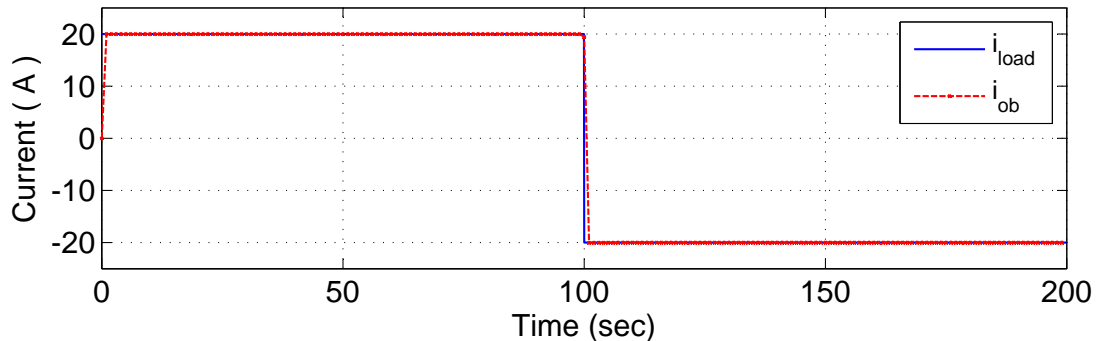


Figure 7.8: Load current i_{load} and dc current i_{ob}

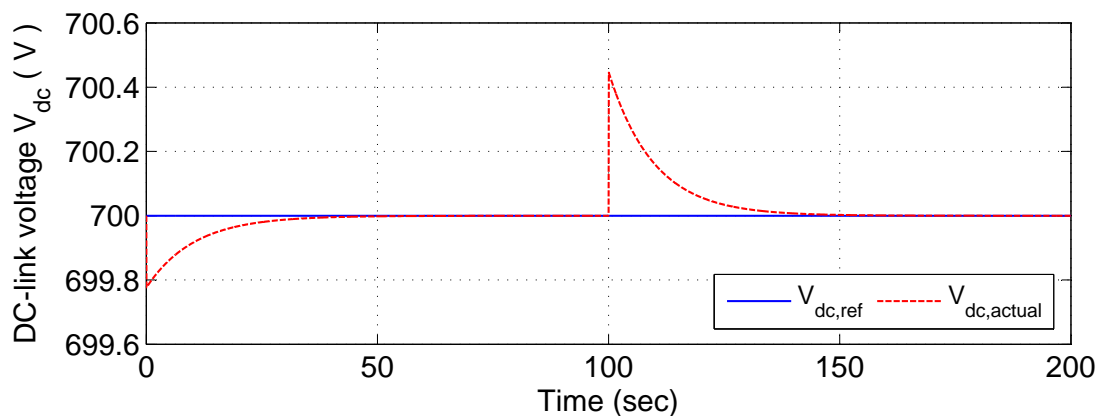


Figure 7.9: Reference DC-link voltage $V_{dc,ref}$ and actual DC-link voltage $V_{dc} = v_{34}$

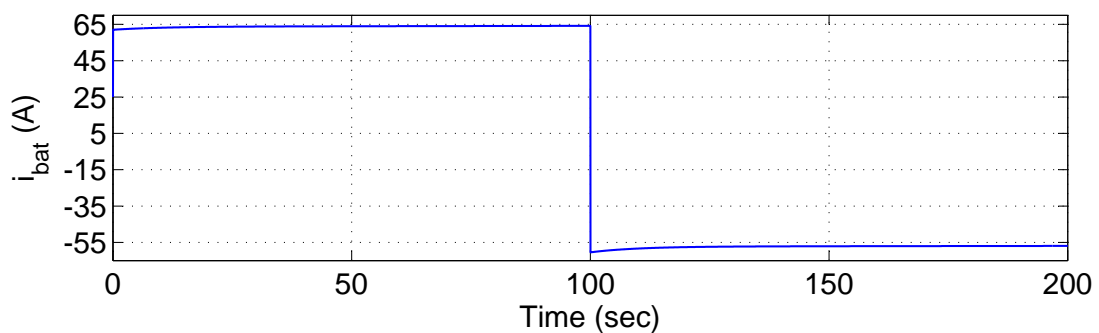


Figure 7.10: Battery current i_{bat}

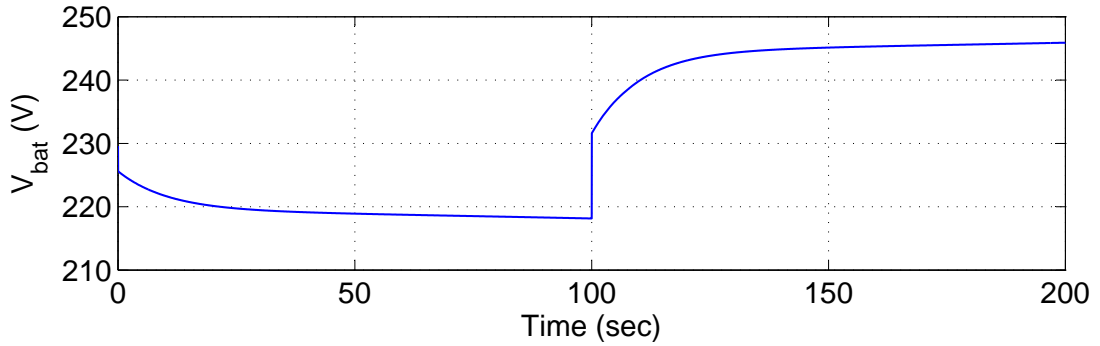


Figure 7.11: Variation of the terminal battery voltage v_{bat} during the charge and discharge cycle of the battery

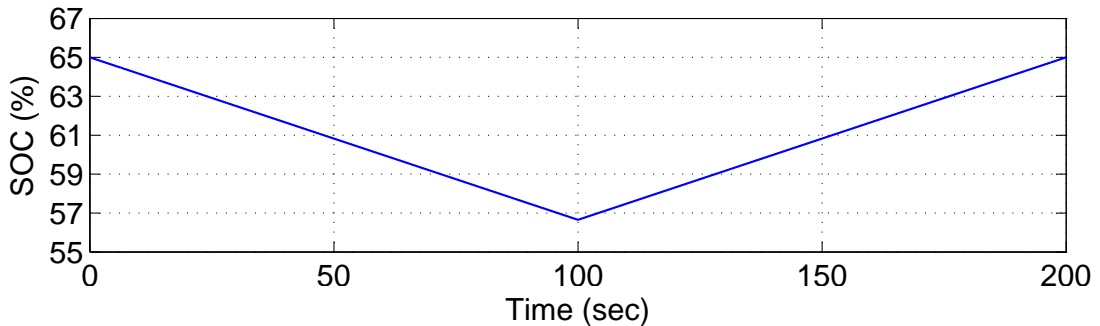


Figure 7.12: State of charge profile of the battery during discharging and charging SOC

under constant load current $i_{load} = 20A$, the terminal voltage of the battery decreases non-linearly from 229.6V to 218.15V with battery current $i_{bat} \simeq 60A$ (in Figure 7.10), while the variation in the SOC is linear (Figure 7.12); and after 100 sec, when the battery is charged under constant load current $i_{load} = -20A$, the battery voltage increases non-linearly from 218.15V to 245.9V, resulting in lower battery current value than in the charging mode ($i_{bat} \simeq -57A$, in Figure 7.10) at the end of 200 sec. This observation confirms the experimental behavior of the battery that the battery voltage does not remain constant, rather it decreases and increases in the charging and discharging modes respectively as shown in Figures 7.11 and 7.12. Here in the present simulation, battery is dealing with a normal constant loading current but such behaviors in the battery current i_{bat} and battery voltage v_{bat} become more critical when the simulations are run for heavy transients during the NEDC tracking operations.

Figures 7.14 and 7.15 show that when the direction of the power flow changes, ϕ also changes its sign accordingly. It has been mentioned that when the working of

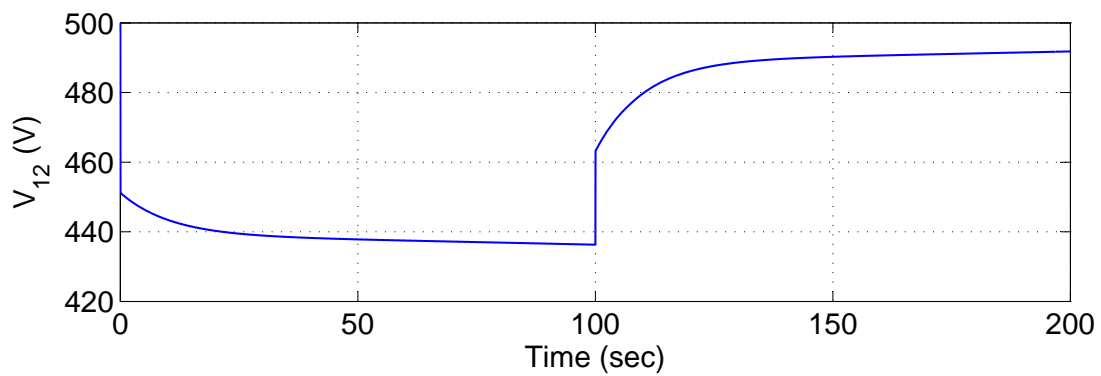


Figure 7.13: v_{12} average voltage

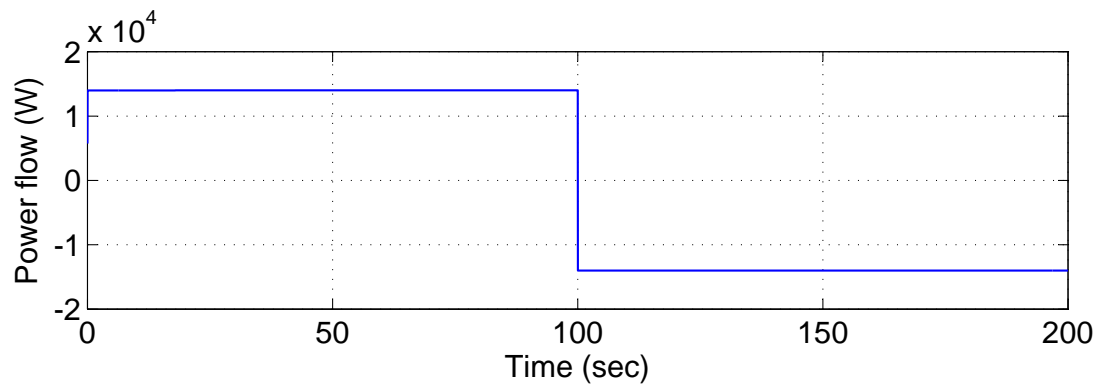


Figure 7.14: Flow of power from the battery

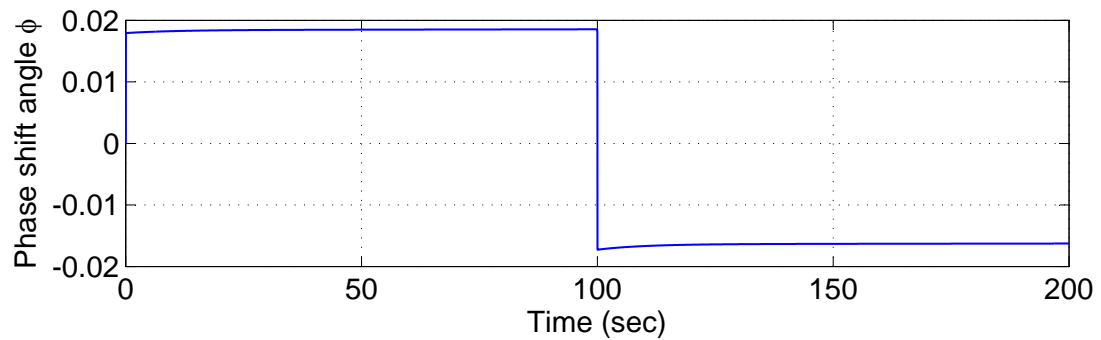


Figure 7.15: Variation of the phase shift angle (in magnitude and sign) corresponding to the power flow during charge and discharge cycle of the battery

the DC/DC converter changes from boost mode to buck mode, the phase shift angle also changes from $\phi > 0$ to $\phi < 0$. Not only does the direction of the power flow, the magnitude of power flow is also proportional to the phase shift angle ϕ .

7.7 Summary

- A generic dynamic model of the Li-ion based battery model is presented in this chapter. Parameters for this model can be easily extracted from the experimental discharge curve provided by the manufacturer.
- This model describes the chemical parameters of the battery purely in the terms of parameters of the electrical circuit ($SOC = f(v_{bat}, i_{bat})$).
- A frequency dependent state space averaged model of the bi-directional DC/DC converter, which connects the battery to the DC-link, is also presented in this chapter.
- Phase shift angle ϕ based control strategy is proposed in this chapter for the bidirectional flow of the power and DC-link voltage control.
- Simulation results are presented and validated against expected standard performance.

CHAPTER
EIGHT

INTEGRATION OF COMPONENT MODELS AND SUPERVISORY CONTROL

8.1 Introduction

Any hybrid system is a collection of many discrete and continuous variables in the same system. Supervisory controllers designed for hybrid systems work on the principles of interaction of discrete control signals (like switch on switch off) with continuous system variables (such as voltage and current of PM machines). Controllers can be mainly of two types - continuous or discrete. Continuous controllers are generally situated in individual components and are described by differential equations which can be easily integrated with the component model (system to be controlled). Discrete controllers are mainly outside the component and generate event based decisions. There is interface circuitry between external discrete controllers and continuous system variables. Due to this interface circuitry, the two different kind of systems communicate with each other. The discrete controller architecture is implemented on a computer based network. Supervisory controller falls in the category of external discrete controllers generating discrete control signals for controlling the individual components of the HEV powertrain.

Supervisory control provides logic for the implementation of power flow management. Its main duty is to switch ON or OFF the different components as per

requirement for optimized utilization of the energy sources. Most of the state of art supervisory controllers used in mass production vehicles are heuristic in nature [120]. Such supervisory controllers highly depend on the knowledge of expected behavior of the vehicle. It is a commonly observed fact that at lower speed, power transmission from the battery to the wheels has higher efficiency in comparison to the power transmission from engine to the wheels. At higher speed, power transmission from the engine to the wheels has overall higher efficiency. In addition to this efficiency considerations, the maximum torque produced by the IC engine at lower speed is very low, whereas due to fast dynamics, the motor produces very high torque even at lower speed. So, an unexceptional general rule for the supervisory control is that at lower power demand, the vehicle is powered by the battery and at higher power demand, the engine is turned-on. The engine powers the vehicle until there is a substantial decline in the power demand or regeneration takes place. Considering these heuristic laws, many such Boolean or Fuzzy rule based supervisory controllers are designed. Figure 8.1 presents a general overview of the different categories of supervisory control strategies.

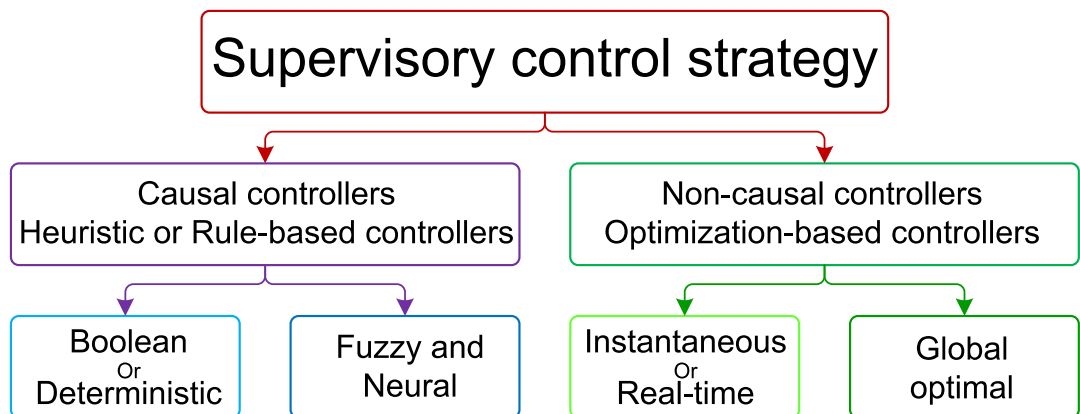


Figure 8.1: Categorization of different supervisory control strategies

There are mainly two categories of supervisory controllers, rule-based [10, 137, 137–148] and optimization based [5, 111, 123, 124]. These controllers can also be categorized as causal and non-causal controllers. Non-causal controllers are required to have “a priori” information of the driving cycle or in a sense, future driving conditions have to be known beforehand. However, there is no such requirement for the causal

controllers. Rule-based supervisory controllers fall in the category of causal controllers whereas optimization based controllers generally fall in the category of non-causal controllers.

Gao has categorized supervisory control strategies in three main categories, thermostat control strategy, power follower control strategy and power split control strategy [218]. But by careful observation, it can be understood that both the thermostat and power follower control strategies belong to the category of rule based supervisory control strategy in many ways. So, in a broad sense, any control strategy not involving any kind of optimization but dependent on fixed sets of rules for operation of the powertrain components can be put into the category of rule based supervisory control strategy.

In most cases, the rule based control strategy is used as an online supervisory controller because it mainly considers the power ratings and higher efficiency regions for operation of the power components. These heuristics or rule based control strategies are found to be more robust and computationally efficient than optimization based power split control strategies [150]. The main drawback of the rule-based control strategies is that they often lead to suboptimal solutions.

To get over the problem of sub-optimal solution, optimization based control strategies are devised by which optimal solutions are guaranteed. Optimization based strategies are also further categorized into instantaneous power split optimization and global power split optimization. Instantaneous optimization based strategies are based on minimizing an objective cost function which optimizes power split at every instant of time, finally giving a solution closer to the global optimum [5, 151–153]. Global optimization based strategies requires “*a priori*” information of the drive cycle leading to global optimal solutions [128, 154, 155]. Some controllers are combinations of the optimization based control and neural network techniques [159]. Optimization based control strategies require complicated optimization techniques such as dynamic programming and genetic algorithm. Therefore, generally, they cannot be used for real time implementation but only for offline analysis. Moreover, resulting solutions are also

very particular to that drive cycle, unrobust and unsuitable for unknown speed profiles.

8.2 Heuristic Supervisory Control

Heuristic or Rule based supervisory controllers are also further categorized in many subcategories depending on the state variables used for determining control rules. These state variables are also called decision variables, because, only on the basis of these variables does the supervisory control generate operational logic to control individual components of the powertrain. Some general properties of the heuristic supervisory control can be described as follows:

- From standstill to certain speed (u_{crit}) of the vehicle, only the battery will power the vehicle.
- Above this certain speed (u_{crit}), the engine will be turned-on to support the drive.
- During the process of discharge, the SOC of the battery should not deplete below a certain threshold value.
- If SOC of the battery depletes below a certain threshold level SOC_{min} , the engine will not only power the motor but recharge the battery as well.
- At the time of regeneration, all power must come back to the battery for the purpose of charging it back till certain maximum threshold value of the SOC (SOC_{max}).
- Even at higher speed, if SOC is very high, then the battery should supply all the required power.
- When the power demand goes extremely high during extra urban drive, the battery should assist the engine in meeting the required power demand.

There are many ways in which control rules can be designed depending on the various state variables or parameters of the powertrain components such as the speed of the vehicle [10, 140], maximum allowed motor and engine torque [141], demanded DC-link current, variations in the value of the SOC, various other component ratings such as power limit of the prime movers [137, 143–148] and temperature of the components, etc. Some controllers are designed on the basis of fuzzy logic [27, 149] and neural networks [159].

$$SOC_{min} < SOC(t) < SOC_{max}$$

$$T_{eng,min} < T_{eng}(t) < T_{eng,max}$$

$$T_{mot,min} < T_{mot}(t) < T_{mot,max}$$

$$T_{gen,min} < T_{gen}(t) < T_{gen,max}$$

$$\omega_{eng,min} < \omega_{eng}(t) < \omega_{eng,max}$$

$$\omega_{mot,min} < \omega_{mot}(t) < \omega_{mot,max}$$

$$\omega_{gen,min} < \omega_{gen}(t) < \omega_{gen,max}$$

$$P_{eng,min} < P_{eng}(t) < P_{eng,max}$$

$$P_{mot,min} < P_{mot}(t) < P_{mot,max}$$

$$P_{gen,min} < P_{gen}(t) < P_{gen,max} \quad (8.1)$$

Where *min* and *max* terms in subscript refer to minimum and maximum ratings of that particular variable, respectively.

All rule based controllers share a few common principles among them such as the lack of involvement of any kind of direct optimization routine and all the control instructions depend on efficient operating zones of the powertrain components. This control is implemented with the logic of an if-else loop. The logical flow chart is designed in such a way that no constraints are violated at any point of time.

Due to the non-involvement of any kind of optimization routine, rule based controllers are computationally very fast, efficient and robust in all the driving conditions. The biggest limitation of this technique is that many times this controller leads to suboptimal solutions. Combination of the optimization based control strategy ECMS and rule based control is also proposed in [219] to get the benefit of robustness and optimality of solution.

8.3 Optimization Based Supervisory Control

Optimization based supervisory controllers are designed to achieve optimal solutions for the power flow management problem. There can be two ways in which this control task can be performed; in one case, energy consumption can be optimized at every instant of time and in another case, energy consumption can be minimized for the overall drive cycle. The first case of optimization approach is known as instantaneous optimization, where splitting of the power flow is done in such a way that the fuel consumption is minimized at every instant of time. Second case of optimization is called global optimization, where it is not necessary to minimize the fuel consumption at every instant of time but it must be minimized for the overall duration of the drive cycle. Normally, global optimization leads to the optimal solution and instantaneous optimization leads to near optimal solutions.

In general, every optimization based supervisory control minimizes some sort of cost function to achieve the desired control objectives [5, 121, 122, 125–127, 147]. A general cost function can be expressed in the following way:

$$J = \int_{t_0}^{t_f} \psi(x(t), u(t), t) dt \quad (8.2)$$

where J is performance index, ψ is cost function variable (can be the rate of fuel consumption), $x(t)$ is state variable vector of the system and $u(t)$ is the sequence of

the control vector input generated by the supervisory control strategies. By adding weighted terms for pollutant emissions in the performance index, this optimization can be made multi-objective.

$$J = \int_{t_0}^{t_f} \psi(x(t), u(t), t) dt + \int_{t_0}^{t_f} \alpha \cdot \dot{\phi}(x(t), u(t), t) dt \quad (8.3)$$

where $\dot{\phi}$ is presented as the rate of pollutant emissions at every instant of time. Similarly, many other terms related to some particular objective can be added together with different weighting factors (i.e. α in Equation (8.3)) respectively to achieve a simultaneous solution for all of them.

This cost function should be minimized along with many soft and hard constraints such as maximum and minimum allowable limits for the SOC, various ratings for power sources, different drivability conditions, etc. Constraints on the different state variables, described in Section (8.2), are also included in the optimization based control. Some of these constraints are included in the cost function itself with varying penalty factors according to their effect on the objective undertaken. For example, to present the constraint on the final state of charge (SOC_f), a function $\phi(x(t_0, t_f))$ can be added to the overall objective function.

$$J = \int_{t_0}^{t_f} \psi(x(t), u(t), t) dt + \int_{t_0}^{t_f} \alpha \cdot \dot{\phi}(x(t), u(t), t) dt + \phi(x(t_0, t_f)) \quad (8.4)$$

There can be various ways in which $\phi(x(t_0, t_f))$ can be defined to ensure that the deviation in the SOC value from the start of the drive mission till the end is confined in the acceptable domain.

In [129], Serrao has defined three broad categories of the optimization methods used for obtaining the optimal solution; firstly numerical methods for global optimization, secondly numerical methods for local optimization and thirdly analytical optimization methods. In the first case, optimization of the cost function is achieved by using numerical methods such as dynamic programming [5, 154, 156–158, 162] and

genetic algorithm [128, 134–136, 155, 164]. Dynamic programming needs the discretized space of state variables and time to search for the optimal solution. Introduction of discretized state space makes the solution suboptimal for the continuous problem. Dynamic programming requires back iterations for calculating the most efficient solution, therefore, in a way forcing itself to be impossible to use in an online analysis [129]. Although, in dynamic programming, the computational burden increases linearly with respect to time, it increases exponentially with increasing number of dimensions in the problem [120, 220]. This increased computational burden makes it practically impossible for any real-time application with a multi objective function. In addition to this, “*a priori*” knowledge of the complete driving cycle is also compulsory [156]. There are some efforts to combine dynamic programming techniques with neural networks to develop some method by which optimization can be done online [221]. But still predominantly, these methods are computationally expensive and can mostly be used only for an offline analysis.

In the second case of numerical methods for local optimization, techniques similar to the dynamic programming are used. Rather than using the full information for future driving conditions, only predictions of the future driving conditions are used. Since emphasis is on the local optimization of the objective function, exact global information is not necessary. For local optimization, global constraints are transformed into local ones. So these methods are capable of use in online optimization but the need for computational ability is enormous [120, 129]. Model predictive control and stochastic dynamic programming are examples of such methods.

The computational complexity of the numerical optimization can be further reduced if somehow a closed analytical solution of the optimization problem can be derived with reasonable simplifications. A Hamiltonian function is defined, where minimization at every instant of time leads to the solution of the optimization problem.

$$H(x(t), u(t), \mu(t)) = \psi(x(t), u(t), t) + \mu(t) \cdot \phi(x(t_0, t_f)) \quad (8.5)$$

To minimize this Hamiltonian at every instant of time $\mu(t)$ must satisfy following condition:

$$\dot{\mu} = \frac{\partial H(x(t), u(t), \mu(t))}{\partial x} \quad (8.6)$$

where $\psi(x(t), u(t), t)$ is an instantaneous cost function, $\phi(x(t_0, t_f))$ is a function representing the dynamics of the overall system and $\mu(t)$ is a vector called adjoint state of the system.

If the objective function can be explicitly presented in terms of control variables, the optimization problem will be more straightforward and simple. For the supervisory control of energy flow, the objective function can be presented as:

$$H(x(t), u(t), \mu(t), t) = P_{ice}(u(t), t) + s(t) \cdot P_{elec}(x(t), u(t), t) \quad (8.7)$$

where P_{ice} is energy generated due to fuel consumption and $P_{elec} = P_{bat}$ is energy generated by operation of the battery, $x(t)$ is SOC of the battery, $u(t)$ is control variable generated due to the supervisory control and $s(t)$ is an equivalence factor. Now, the overall optimization is based on the search for a suitable equivalence $s(t)$ factor which can minimize the overall energy consumption. This control technique is called equivalent consumption minimization strategy (ECMS) [129–133].

Before going into the details of the implementation of our proposed supervisory control strategy, a description of the integration of the powertrain components is necessary. The general principle for the integration of individual components in the powertrain is described in the next section.

8.4 Integration of Component Models

The HEV system is fairly complex in the architecture due to the involvement of the multidisciplinary technologies. Since the whole HEV consists of many subsystems integrated together by mechanical, electrical and control links, the overall performance

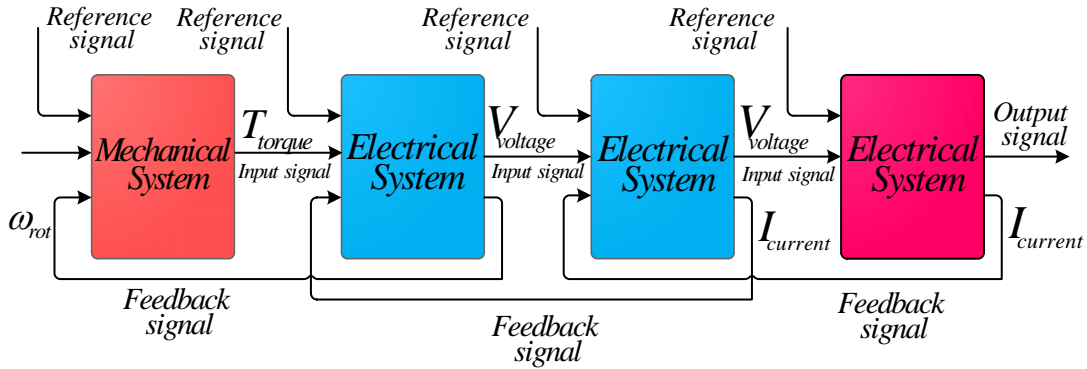


Figure 8.2: Interconnection concept among different kinds of mechanical and electrical subsystems

highly depends on the interactions of these subsystems. Rather than putting all the dynamic equations of different subsystems together as a one system, a modular approach has been adopted where the individual components are first modelled with their specific controller. Subsequently, these subsystems are integrated together in a certain configuration to be operated as a complete powertrain. Different components are modelled with different levels of complexities. For example, electrical machines are modelled in a very detailed way, whereas, converters are modelled with average modelling techniques and non-electrical subsystems such as engine and battery are modelled with a mixed level of complexity. Every component has some inputs and outputs as a result of modelling. These inputs and outputs can be classified as potential or kinetic variables. For an electrical system, voltage is a potential variable and current is a kinetic variable, whereas for a mechanical system, torque is a kinetic variable and speed (rotational or translational) is a potential variable. Two neighboring components are integrated together with an exchange of the input and output variables. As a general rule, the potential variable works as an input for the later component and the kinetic variable works as a feedback signal for the former components. However, in some cases they are interchangeable with one other or a combination of both. Figure 8.2 is again presented here to graphically explain the concept of integration of the different components.

In the series architecture, there are two series path of power flow from power

sources to wheels of the vehicle. In both the cases, ultimately the DC-link feeds the PMSM and inverter which finally drives the vehicle with the help of the driver and transmission. In the first case, power flows from the IC engine to the PMSG and rectifier to the DC-link and in the second case, power flows from the battery and DC-DC converter to the DC-link. The DC-DC converter is chosen bidirectional because during regeneration, all the regenerated power has to flow backward to charge the battery.

8.4.1 Power flow from the IC engine to the wheels

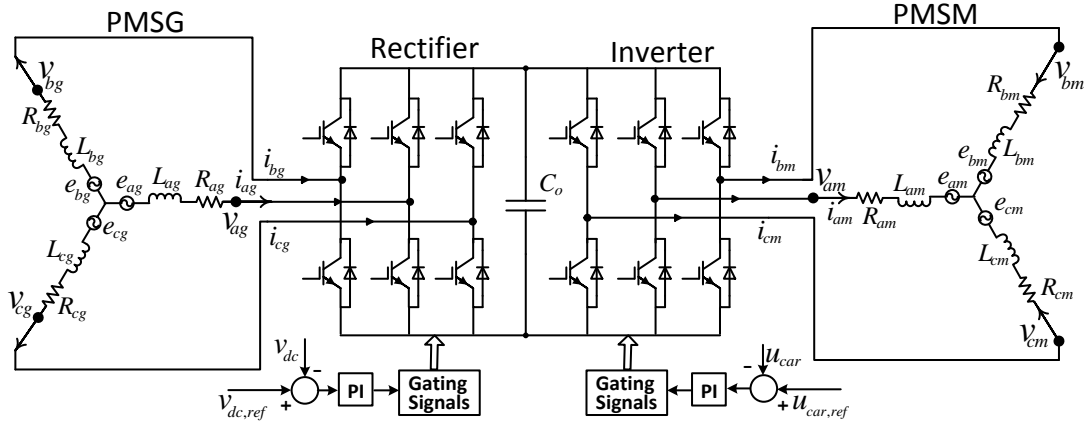


Figure 8.3: Circuit diagram showing the electrical connection of the generator (PMSG), AC/DC rectifier, DC/AC inverter and motor (PMSM). Symbols v , i , R , L and e represent phase voltages, currents, resistances, inductances and induced e.m.f.'s, respectively. Subscripts a , b and c correspond to the individual phases and subscripts g and m correspond to 'generator' and 'motor', respectively. C_0 is the DC-link capacitor, v_{dc} is the DC-link voltage and u_{car} is the forward speed of the car. The signals related to the control of v_{dc} and u_{car} are also shown.

Figures 8.3 and 8.4 present the circuit diagram and block diagram of the powertrain, when the IC engine alone is used as the power source to the powertrain. The longitudinal car takes T_L as input giving back translational speed of the car u_{car} as output. This u_{car} goes back to the driver model as a feedback input. The three phase DC/AC converter (inverter) which feeds the PMSM, takes v_{dc} (potential variable) as the main input from the DC-link along with other inputs (v_{dm} , i_{dm} , v_{qm} and i_{qm}) and gives the DC-link current i_{dc} (kinetic variable) as a output. The DC-link current i_{dc} becomes feedback input for the DC-link. The three phase AC/DC converter (rectifier) takes v_{dc}

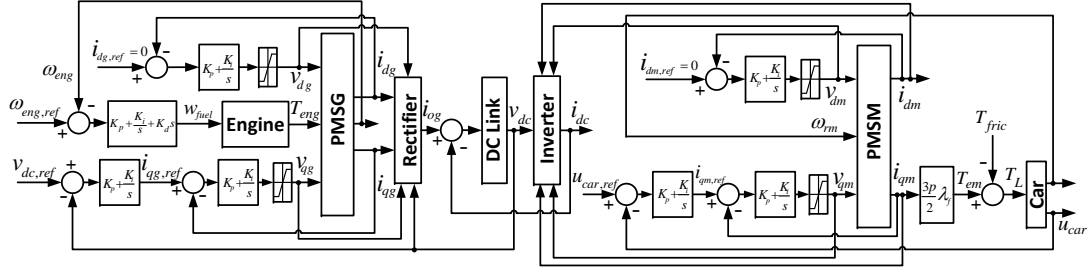


Figure 8.4: Block diagram showing the interconnection of the engine, PMSG, rectifier, inverter, PMSM and car and the related control loops. Symbols v_d , i_d , v_q and i_q represent $d-q$ voltages and currents respectively, while the subscripts g , m and ref correspond to ‘generator’, ‘motor’ and ‘reference’ respectively. ω_{eng} is rotational speed of the engine, w_{fuel} is engine fuel mass rate demand, T_{eng} is engine torque, i_{og} is DC current produced by the rectifier, v_{dc} and i_{dc} are DC-link voltage and current respectively, ω_{rm} is speed of the PMSM rotor, T_{em} is PMSM electromagnetic torque and u_{car} is forward speed of the car.

(potential variable) as a main input from the DC-link along with other inputs v_{dg} , i_{dg} , v_{qg} and i_{qg} and gives i_{og} as an output, which becomes another input for the DC-link model.

Due to the series architecture of the power train, the PMSG gets input power from the diesel engine. The generator rotor-shaft is mechanically coupled to the engine inertia via a fixed gear ratio G . Therefore, the mechanical dynamics of the generator are governed by the following equation:

$$T_{eng} - T_{f,eng} - G(T_e + T_{f,gen}) = (J_e + G^2 J_g) \frac{d\omega_{eng}}{dt}, \quad (8.8)$$

where T_{eng} (indicative torque) is the mechanical torque applied by the IC engine, $T_{f,eng}$ is the friction torque in the engine, $T_{f,gen}$ is the friction torque in the generator, ω_r is the generator rotor speed and J_e and J_g are the moments of inertia of the engine and generator respectively. Here, PMSG takes input mechanical torque T_{eng} from the engine and produces rotational speeds of the generator and engine, ω_r and ω_{eng} , respectively, as outputs. The generator rotor speed and the engine rotor speed are related as:

$$\omega_r = G\omega_{eng}, \quad (8.9)$$

ω_{eng} works as a feedback input signal to the IC engine fuel amount controller. Every component involved in this series integration of the diesel engine to PMSG to rectifier to DC-link to inverter to PMSM and then finally to the longitudinal car has many other input-output state variables at various levels. Since most of them are involved in either internal dynamic or control loops of the components, they are not deliberately discussed in this process of integration. Internal dynamics and control of the particular component have already been discussed in the previous chapters related to the respective components.

8.4.2 Power flow from the battery to the wheels

When the battery with the DC/DC converter feeds the DC-link voltage, it replaces the combination of the IC engine, PMSG and rectifier. Figures 8.5 and 8.6 present the circuit diagram and block diagram of the powertrain, when the battery alone is integrated as the power source to the powertrain. The DC/DC converter takes battery voltage v_{bat} as the main input alongwith phase shift angle ϕ as a control input and produces i_{bat} and i_{ob} (DC current delivered by the DC/DC converter to the DC-link) as output. The current drawn from the battery i_{bat} by the DC-DC converter, in order to deliver the requested power demand by the DC-link, becomes feedback input for the battery model. The control dynamics of the battery with the DC-DC converter have already been explained in the previous chapter.

In a series hybrid vehicle, sometimes the engine supplies the required power to drive the wheels and sometimes the battery. Both paths of power flow (engine to wheels and battery to wheels) are combined together in one powertrain by the implementation of a competent supervisory control. Switching between the two power sources is done with the objectives of attaining maximum fuel efficiency, efficient operation of the power sources and achieving the desired drive performance etc. Details about the supervisory control will be described in the coming sections.

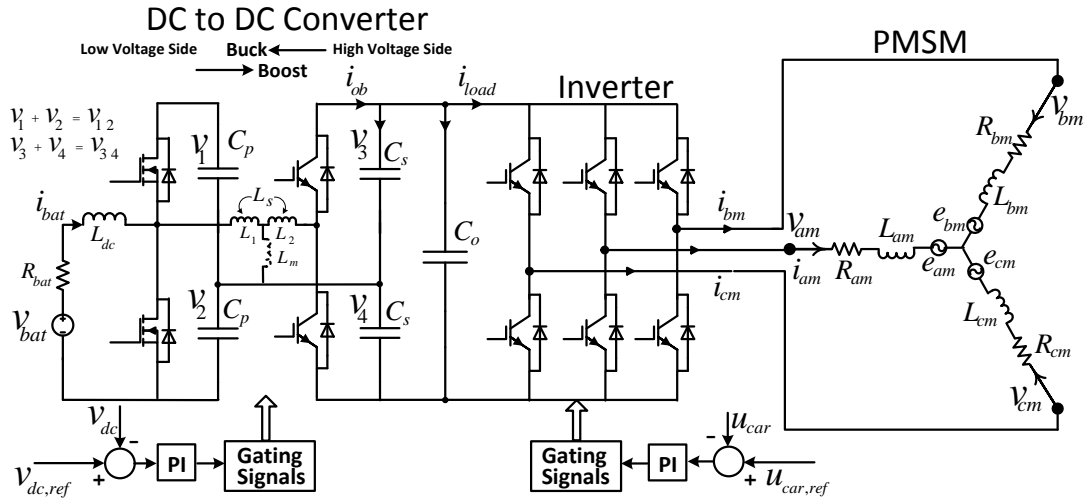


Figure 8.5: Circuit diagram showing the electrical interconnection of the battery, DC/DC converter, inverter, and PMSM. Symbols v , i , R , L and e represent phase voltages, currents, resistances, inductances and induced e.m.f's respectively. Subscripts a , b and c correspond to the individual phases and subscripts g and m correspond to 'generator' and 'motor'. C_0 is DC-link capacitor, v_{dc} is DC-link voltage, v_{bat} and i_{bat} are battery voltage and current respectively, i_{ob} is DC current drawn by the DC/DC converter on the DC-link side and u_{car} is forward speed of the car. The signals related to the control of v_{dc} and u_{car} are also shown.

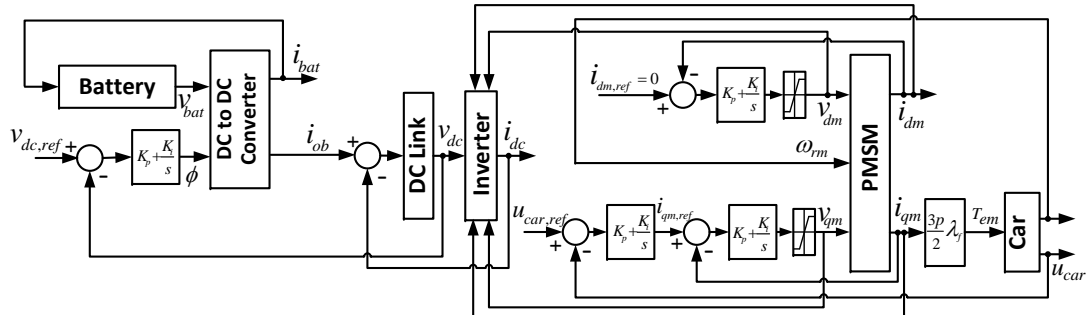


Figure 8.6: Block diagram showing the interconnection of the battery, DC/DC converter, inverter, PMSM and car and the related control loops. Symbols v_d , i_d , v_q and i_q represent d - q voltages and currents respectively, while subscripts m and ref correspond to 'motor' and 'reference' respectively. ϕ is phase shift variable of the DC/DC converter, v_{bat} and i_{bat} are battery voltage and current respectively, i_{ob} is DC current drawn by the DC/DC converter on the DC-link side.

8.4.3 Hybrid mode operation

In the initial stage of design, there were only two modes of operation where either the engine or the battery alone was powering the vehicle. In both these modes of operation, the two power sources are operating alone without any mutual assistance. In this situation, both the power flow paths have their own DC-link capacitor and control loop to maintain the DC-link voltage constant throughout the drive operation. Since the variation of the DC-link voltage was very small, this method of operation was fine and produced correct results with accurate dynamics. But this situation is no longer helpful for hybrid mode of operation where both the power sources, engine-generator and battery, are operating simultaneously. Basically two new modes of operations are introduced with the inclusion of the hybrid mode of operation of the powertrain. The first case of hybrid mode of operation comes during the tracking of the NEDC drive cycle, when SOC goes below the minimum threshold value and the speed of the vehicle is high. In such a situation, the engine has two tasks to perform simultaneously, powering the vehicle and charging the battery. The second case of the hybrid mode of operation arises when the demanded load current goes very high and the engine alone can not support that demand. In such a situation, the battery comes to the assistance of the engine.

Figures 8.7 and 8.8 present the circuit diagram and block diagram of the powertrain, when the IC engine and the battery both are involved in hybrid modes of operation of the HEV powertrain. Details regarding different possible operating modes are described in the next section 8.9. In both these hybrid modes of operation, control strategies used for the single power flow path cannot be used any more. A new control strategy and new structure for the DC-link, very close to the physical reality, has been designed to achieve the purpose.

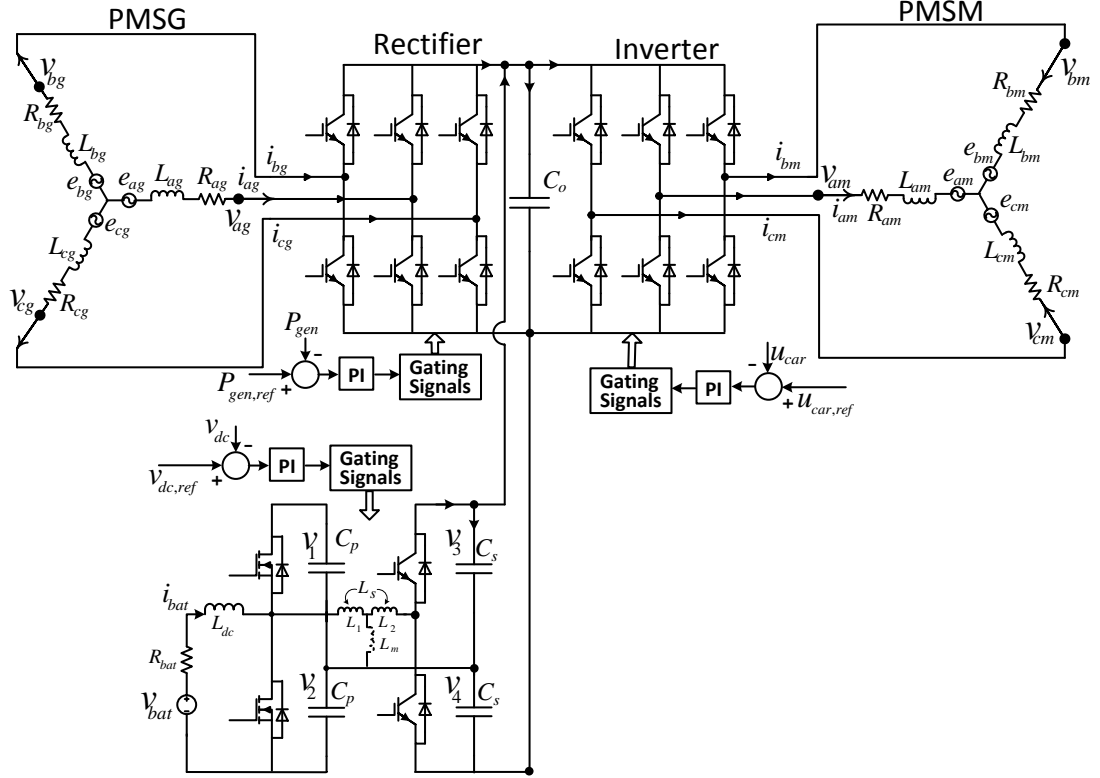


Figure 8.7: Circuit diagram showing the electrical connection of the interconnection of the engine, generator, AC/DC converter, battery, DC/DC converter, DC-link, inverter, PMSM and car in one powertrain. Symbols used in this figure are the same as described in previous figures 8.3, 8.5. This diagram also shows the DC-link control strategy which have two loops - powersplit and DC-link voltage control. P_{gen} and $P_{gen,ref}$ depict actual generator power and reference generator power.

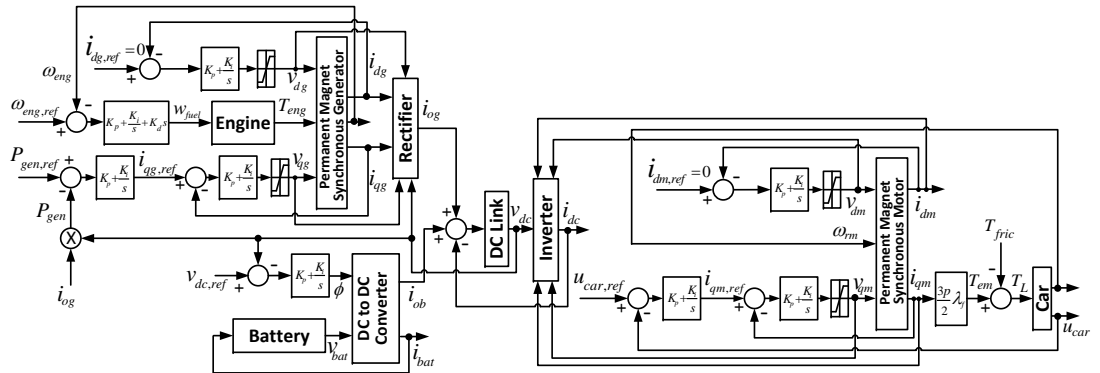


Figure 8.8: Block diagram showing the interconnection of the engine, PMSG, AC/DC converter, battery, DC/DC converter, DC-link, inverter, PMSM, and, car and related control loops. Symbols used in this figure are the same as described in previous figures 8.4, 8.6. This diagram also shows the implementation of the DC-link control strategy which have two different control loops - powersplit and DC-link voltage control. P_{gen} and $P_{gen,ref}$ depict actual generator power and reference generator power as described in Equations (8.13)-(8.13).

8.5 A novel DC-link control strategy

There are two control objectives which must be fulfilled for proper operation of the HEV powertrain. The first control objective is to deliver the required power to the PMSM and the second is to maintain the constant DC-link voltage throughout the operation. When only one power source is active at a given time, both control objectives are fulfilled by a single control loop in every case. For example, when the generator or battery alone is active, maintenance of the constant DC-link voltage and the PMSM power demand both are satisfied by the single outer DC-link voltage control loop. Now when these two power sources are active simultaneously, there cannot be two separate loops to control the same DC-link voltage, which will otherwise lead to destabilization of the HEV system. So the two control objective are now distributed in two different control loops. One control loop is used to maintain the constant DC-link voltage and the other control loop is used to properly split the PMSM power demand between two simultaneously active power sources (i.e., engine-generator and battery) during the complete operation of the HEV. Figure 8.7 and Figure 8.8 describe two control loops responsible for switching of the converters in such a way that the DC-link voltage is maintained constant and power demand by PMSM is achieved.

In hybrid mode of operation, the battery is used as a power buffer which supplies or absorbs the extra power when the DC-link voltage (v_{dc}) is deviating from its reference value ($v_{dc,ref}$), due to lack or excess of the total power at the terminals of the DC-link capacitor. In Figures 8.7 and 8.8, it can be observed that the battery and DC/DC converter are associated with the DC-link voltage control loop whereas PMSG is now associated with the power split control loop.

By applying Kirchhoff's current law at DC-link terminal, the DC-link equation can be expressed as:

$$C_o \frac{dv_{dc}}{dt} = i_{og} + i_{ob} - i_{dc} \quad (8.10)$$

where v_{dc} is actual DC-link voltage, i_{og} is load current contribution from the generator,

i_{ob} is load current contribution from the battery and $i_{dc} = i_{load}$ is the total load current drawn from the DC-link by the PMSM and inverter. In this equation the effect of the two C_s capacitors at the output of the DC/DC converter has been adjusted in the total value of the DC-link capacitor C_o .

Since the DC-link voltage control is associated with the battery and DC/DC converter, in terms of equation, the DC-link voltage control can be expressed as follows:

$$\phi_{ref} = (K_p + K_i \int dt) \{v_{dc,ref} - v_{dc}\} \quad (8.11)$$

First of all, a difference between the desired DC-link voltage $v_{dc,ref} = 700V$ and actual DC-link voltage v_{dc} is calculated. This voltage difference is then passed through a PI controller to generate a reference for the phase shift angle ϕ_{ref} . The appropriate phase shift angle ϕ ensures power flow from the battery in such a way that the DC-link voltage is maintained constant all the time during a drive cycle. This control loop also ensures the contribution of the power fraction from the battery alone to the total power demand by the PMSM.

According to simple power balance, the following equation must be satisfied at all the times during the operation of the HEV powertrain:

$$\begin{aligned} P_{PMSM} &= P_{gen} + P_{bat} \\ 1 &= \frac{P_{gen}}{P_{PMSM}} + \frac{P_{bat}}{P_{PMSM}} \end{aligned} \quad (8.12)$$

At present, losses of the converters are not included in Equation 8.12 but in coming Section 8.6 when efficiency of the converters and transmission will be included in power calculations, all the losses will be accounted accurately.

A new control loop is designed which forces the PMSG and AC/DC converter to track the contribution of the power from the generator P_{gen} to the total power demanded by the PMSM P_{PMSM} . Once the contribution of the power fraction ($s_g = \frac{P_{gen}}{P_{PMSM}}$) from

the generator is ensured, the rest of the power fraction ($s_b = \frac{P_{bat}}{P_{PMSM}}$) automatically comes-from/goes-to the battery. The old voltage controller loop is now replaced with a power split controller loop with new values of k_p and k_i .

$$i_{dq-ref} = (k_p + k_i \int dt) \{P_{gen,ref} - P_{gen}\} \quad (8.13)$$

$$P_{gen,ref} = v_{dc,ref} i_{gen-load} \quad (8.14)$$

$$P_{gen} = v_{dc} i_{og} \quad (8.15)$$

- i_{dq-ref} represents reference phase currents in the $d - q$ frame
- $P_{gen,ref}$ is the reference power from the generator
- P_{gen} is the actual power contribution from the generator
- $v_{dc,ref} = 700V$ is the reference DC-link voltage
- $i_{gen-load}$ is the desired load current contribution from the generator
- v_{dc} is the actual DC-link voltage
- i_{og} is the actual dc current supplied by the generator along with the AC/DC converter

This new power split controller gives the current reference in the $d - q$ frame, which gets multiplied with the required power factor and corresponds to the amplitude of the phase current. All other system dynamic and control equations will be exactly the same as described in section 5.4.2. In simulations, it has been found that after implementation of these control loops, the power distribution among both the power sources is accurate and the maximum deviation in the DC-link voltage is 0.046%. This way of DC-link control is found to be very robust and accurate in all the cases of simulation. Clear allocation of the control objectives to different loops and correspondingly different components is one more salient feature of this control.

8.6 Inclusion of the Various Efficiency Factors

The main aim of the present work is the dynamic modelling of all the components involved in the powertrain. All the electrical and mechanical components have some losses during their operation due to various unavoidable reasons. For example, electrical machines such as PMSM and PMSG have losses in the form of copper losses ($P_{l,c}$), eddy current losses ($P_{l,e}$), hysteresis losses ($P_{l,h}$) and mechanical losses comprising bearing losses ($P_{l,b}$) and windage losses ($P_{l,w}$) [202]. Generally, in most of the modelling mechanisms, these losses are accounted just by inclusion of efficiency, but in the present work, a novel frictional torque is proposed which accounts for all kinds of losses in the PM machines. Switching converters such as AC/DC converter (rectifier), DC/AC converter (inverter) and DC/DC converter also have two major kinds of losses, switching losses and conduction losses. Switches offer resistance in the path of flow of currents which generates the conduction losses. High frequency switching of the current and voltage in the IGBT/MOSFET switches creates stress on the p-n junction, which leads to heat and other kinds of losses, together known as the switching losses. To exactly calculate all these losses one has to have detailed model of the switches. To save the complete model from extreme complexity and lengthy simulation period, average models for the converters are used. In the average model of the converters an average efficiency factor has been utilized to include the conduction and switching losses.

8.6.1 Power balance for the various components of the powertrain

As it has already been discussed, there are mainly five operating modes. Power balance in each mode can be calculated with the inclusion of efficiencies.

Engine alone is powering the HEV

The power balance for the various components of the powertrain is given in the following equations, in which the η terms are average efficiency:

$$\begin{aligned}
Car_{in} &= \eta_{tr} Mot_{out} \\
Mot_{out} + Mot_{loss} &= Mot_{in} \\
Mot_{in} &= Inv_{out} \\
Inv_{out} &= \eta_{inv} Inv_{in} \\
Inv_{in} &= Rect_{out} \\
Rect_{out} &= \eta_{rec} Rect_{in} \\
Rect_{in} &= Gen_{out} \\
Gen_{out} + Gen_{loss} &= Gen_{in} \\
Gen_{in} &= Eng_{out} \\
Eng_{out} + Eng_{loss} &= Eng_{in}
\end{aligned}$$

If all the equations are added together in such a way that common terms at LHS and RHS are canceled, the overall power balance equation can be summarized as follows:

$$\eta_{tr} \eta_{inv} \eta_{rec} Eng_{in} = \eta_{tr} \eta_{inv} \eta_{rec} Eng_{loss} + \eta_{tr} \eta_{inv} \eta_{rec} Gen_{loss} + \eta_{tr} Mot_{loss} + Car_{in} \quad (8.16)$$

Similarly the overall power balance equations can be derived for all other modes of operation.

Battery alone is powering the HEV

$$\eta_{tr} \eta_{inv} \eta_{dcdc} Bat_{in} = \eta_{tr} \eta_{inv} \eta_{dcdc} Bat_{loss} + \eta_{tr} Mot_{loss} + Car_{in} \quad (8.17)$$

Regeneration mode

$$\eta_{tr} \eta_{inv} \eta_{dcdc} Car_{in} + \eta_{inv} \eta_{dcdc} Mot_{loss} = Bat_{in} + Bat_{loss} \quad (8.18)$$

Engine is powering the HEV and charging the battery

$$\eta_{tr}\eta_{inv}\eta_{rec}Eng_{in} = \left[\frac{\eta_{tr}\eta_{inv}}{\eta_{dcdc}}(Bat_{in} + Bat_{loss}) + \eta_{tr}\eta_{inv}\eta_{rec}Eng_{loss} + \eta_{tr}\eta_{inv}\eta_{rec}Gen_{loss} + \eta_{tr}Mot_{loss} + Car_{in} \right] \quad (8.19)$$

Engine and Battery both are powering the HEV

$$\eta_{tr}\eta_{inv}\eta_{rec}Eng_{in} + \frac{\eta_{tr}\eta_{inv}}{\eta_{dcdc}}Bat_{in} = \left[\frac{\eta_{tr}\eta_{inv}}{\eta_{dcdc}}Bat_{loss} + \eta_{tr}\eta_{inv}\eta_{rec}Eng_{loss} + \eta_{tr}\eta_{inv}\eta_{rec}Gen_{loss} + \eta_{tr}Mot_{loss} + Car_{in} \right] \quad (8.20)$$

where Car, Mot, Inv, Rect, Gen, Bat and Eng represent the power corresponding to car, motor, inverter, rectifier, generator, battery and engine components, respectively, in their short forms. Subscripts ‘in’, ‘out’ and ‘loss’ represent the amount of input, output and loss of the power of a particular component. η_{tr} , η_{inv} , η_{rec} and η_{dcdc} denote the transmission, DC/AC converter (inverter), AC/DC converter (rectifier) and DC/DC converter efficiency respectively. The average efficiency factor $\eta_{inv} = \eta_{rec} = 94.61\%$ [222–224] and $\eta_{dcdc} = 96\%$ [225–228] are used to scale the DC current in Equation (4.27) to account for power losses in the converter. Two kinds of transmissions are used in the present modelling of the HEV powertrain, the CVT transmission and the fixed gear ratio transmission. The overall average power efficiency of the CVT typically ranges from 89% to 94% [25]. In this work, the value of average efficiency of the toroidal CVT, $\eta_{tr} = 93\%$, is used [184] by scaling the load torque on the transmission shaft appropriately. In the case of fixed gear ratio transmission, it has been assumed an efficiency of 96% [183, 184]. The main purpose of this work is to present a general methodology for modelling of the HEV powertrain. Magnitude of various parameters in any model only signify their relative impact on the numerical values predicted by the model, and do not affect the modelling methodology in any manner. Therefore different efficiency factors used in this work will affect the outcome of the simulations only in terms of numbers, and will not affect the generality of the modelling methodology.

presented in this work.

8.6.2 Dynamic DC-link equations for various modes of operation

Input and output power of the inverter and rectifier can be written in the following way:

Inverter:

$$\eta_{inv} Inv_{in} = Inv_{out} \quad (8.21)$$

$$Inv_{out} = \frac{3}{2}(v_{qm}i_{qm} + d_{dm}i_{dm}) \quad (8.22)$$

Rectifier:

$$\eta_{rec} Rect_{in} = Rect_{out} \quad (8.23)$$

$$\frac{3}{2}(v_{qg}i_{qg} + v_{dg}i_{dg}) = Rect_{in} \quad (8.24)$$

Engine alone is powering the HEV

When the engine (engine-generator) alone is powering the vehicle, power balance equation at the DC-link can be written in the following way:

$$Rect_{out} - Inv_{in} = C_o v_{dc} \frac{dv_{dc}}{dt} \quad (8.25)$$

By substituting the Equations (8.21)-(8.24) in to Equation (8.25), the dynamic equation of the DC-link with efficiency factors of the inverter and rectifier can be described as follows:

$$\begin{aligned} \eta_{rec} \frac{3}{2}(v_{qg}i_{qg} + v_{dg}i_{dg}) - \frac{3}{2\eta_{inv}}(v_{qm}i_{qm} + v_{dm}i_{dm}) &= C_o v_{dc} \frac{dv_{dc}}{dt} \\ \eta_{rec} \frac{3}{2} \left(\frac{v_{qg}}{v_{dc}} i_{qg} + \frac{v_{dg}}{v_{dc}} i_{dg} \right) - \frac{3}{2\eta_{inv}} \left(\frac{v_{qm}}{v_{dc}} i_{qm} + \frac{v_{dm}}{v_{dc}} i_{dm} \right) &= C_o \frac{dv_{dc}}{dt} \end{aligned}$$

$$\begin{aligned}\eta_{rec} \frac{3}{2}(d_{qg}i_{qg} + d_{dg}i_{dg}) - \frac{3}{2\eta_{inv}}(d_{qm}i_{qm} + d_{dm}i_{dm}) &= C_o \frac{dv_{dc}}{dt} \\ \eta_{rec}i_{og} - \frac{i_{dc}}{\eta_{inv}} &= C_o \frac{dv_{dc}}{dt}\end{aligned}\quad (8.26)$$

Similarly, the DC-link equations for the other modes of operation can be described by using the energy balance equation of that operation mode.

Battery alone is powering the HEV

$$\eta_{dcdc}i_{ob} - \frac{i_{dc}}{\eta_{inv}} = C_o \frac{dv_{dc}}{dt}\quad (8.27)$$

Regeneration mode

$$\frac{i_{ob}}{\eta_{dcdc}} - \eta_{inv}i_{dc} = C_o \frac{dv_{dc}}{dt}\quad (8.28)$$

Engine is powering the HEV and charging the battery

$$\eta_{rec}i_{og} + \frac{i_{ob}}{\eta_{dcdc}} - \frac{i_{dc}}{\eta_{inv}} = C_o \frac{dv_{dc}}{dt}\quad (8.29)$$

Engine and Battery both are powering the HEV

$$\eta_{rec}i_{og} + \eta_{dcdc}i_{ob} - \frac{i_{dc}}{\eta_{inv}} = C_o \frac{dv_{dc}}{dt}\quad (8.30)$$

Figure 8.9 presents the implementation of the DC-link equation for all modes of operation. While tracking the NEDC cycle when PMSM has to track constant speed part just after acceleration there is always regeneration for fraction of seconds and if the engine is supplying all the power at this moment we don't want to switch from the engine to the battery for such a small time. Therefore, to avoid such unwanted switchings between the power sources i_{load} is compared with $-0.5A$ rather than 0 .

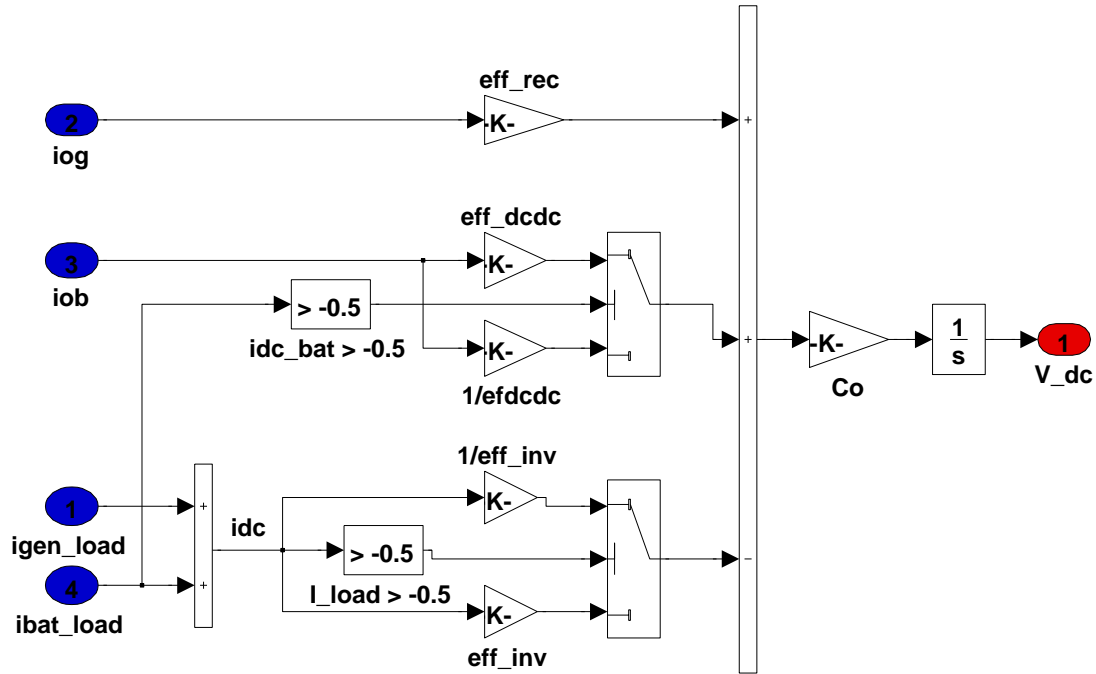


Figure 8.9: Simulink block diagram showing the implementation of DC-link voltage with various efficiency factors for the converters. i_{gen_load} and i_{bat_load} are desired or reference load currents for the generator and battery, respectively. i_{og} and i_{ob} are actually supplied currents from/to the generator and battery, respectively. $i_{dc} = I_{load}$ is DC-link current drawn by the PMSM and inverter. v_{dc} is the actual DC-link voltage

8.7 Supervisory Control Rule

Optimization based supervisory controls are typically implemented on approximation based models, i.e., where the model of the powertrain is just a collection of steady state maps and charts. In such models there is no real time control and all the power demands of the power sink are immediately supplied by the power sources. Due to the simplicity of the powertrain model, complex optimization based control strategies can be implemented. In one sense, it is like implementing complex supervisory control on a simple approximated model. However, in the present work, since the powertrain model is complex, first a simple supervisory control scheme is implemented. Due to the presence of a real time controller for every component, implementing optimization based complex supervisory control will be very difficult. Since the complete HEV powertrain model in itself is very detailed and complex in terms of dynamics, the first attempt should be to develop a robust supervisory control to drive the HEV powertrain.

It has already been established that the biggest advantage of the heuristic controller is its intuitive design and easy implementation. If the controller is properly tuned-up, very good results in terms of reduced fuel consumption and online implementation can be achieved [120]. Considering the modelling complexity the implementation of a rule-based supervisory control is the most robust way to simulate such a dynamic hybrid electric vehicle model.

Two main control strategies, thermostat and power follower (load-current follower), are explained in the following sections.

8.8 Thermostat supervisory control strategy

The most fundamental of all supervisory controllers is the thermostat supervisory controller. This controller works on the principle of a normal thermostat for temperature control in homes. In this controller switching on and off of the heater is dictated according to the continuous temperature level of the room. Overall control signals are discrete (either on or off) and the variable to be controlled (temperature) is continuous. Similarly in a hybrid electric vehicle, the engine-generator can be switched on and off depending on the SOC of the battery.

The thermostat supervisory control strategy (TSCS) is also known as an on-off control strategy because in this control strategy, the IC engine operates with fixed power in its most efficient zone all the time, depending on the state of charge of the battery. When the engine is powering the vehicle and the power demand is less, the excess power goes to charge the battery till the upper limit of the SOC (SOC_{max}) is reached. After this, the engine is turned-off completely and the battery operates till SOC reaches its minimum allowable level (SOC_{min}). As soon as the battery reaches to its SOC_{min} , the engine is again turned-on to power the vehicle and to charge the battery with the available excess power. Regeneration also puts extra energy in the battery while braking the vehicle.

For a series hybrid electric vehicle, power demands must be balanced in the following way:

$$P_{req} = S(t) \cdot P_{gen} + \bar{S}(t)P_{bat} \quad (8.31)$$

where P_{req} is the required power to drive the vehicle, P_{gen} is the power produced by the generator and P_{bat} is the power produced by the battery. $S(t)$ and $\bar{S}(t)$ are control signals to switch on and off the power source component and they must satisfy the constraint $S + \bar{S} = 1$, where the control signal $S(t)$ can be defined as:

$$S(t) = \begin{cases} 1, & \text{Engine-generator set is ON} \\ 0, & \text{Engine-generator set is OFF} \end{cases} \quad (8.32)$$

The logic on which basis $S(t)$ takes values 1 or 0 can be described as follows [111]:

$$S(t) = \begin{cases} 0 & \begin{array}{l} \text{if } SOC(t^-) \geq SOC_{max} \\ \text{or } SOC(t^-) > SOC_{min} \text{ & } S(t^-) = 0 \end{array} \\ 1 & \begin{array}{l} \text{if } SOC(t^-) \leq SOC_{min} \\ \text{or } SOC(t^-) < SOC_{max} \text{ & } S(t^-) = 1 \end{array} \end{cases} \quad (8.33)$$

8.9 Power follower supervisory control strategy

The power follower supervisory control strategy (PFSCS) is implemented in various ways in [137, 143–148]. The fundamental principle of the PFSCS is that the prime power source of the HEV tries to follow the maximum power demand of the vehicle in an optimum way. It is a well known fact that an engine performs with higher efficiency at higher loads and with poor efficiency at lower loads. Battery has complementary performance behavior in terms of efficiency. So it is very natural that the battery should power the vehicle at lower power demand and the engine should power the vehicle at higher power demand. Along with this general rule, if SOC of the battery goes beyond the maximum upper limit (SOC_{max}), the battery should power

the vehicle with certain load conditions. Similarly when the SOC of the battery goes below the minimum threshold level of the (SOC_{min}), the battery should be charged by the engine.

Gao, in [111], has proposed a general form of power follower supervisory control strategy with detailed conditions for switching between battery and engine. In this strategy, it has been assumed that the engine-generator, as a prime power source for the HEV powertrain, will be active most of the time except when lower power is required for driving the vehicle and $SOC(t)$ of the battery is greater than SOC_{max} . Gao has presented the control logic for the PFSCS in the following form:

$$P_{req} = S(t) \cdot P_{gen} + \bar{S}(t)P_{bat} \quad (8.34)$$

$$P_{gen} = \begin{cases} 0, & \text{if } S(t)=0 \\ P_{gen,min}, & \left\{ \begin{array}{l} \text{if } S(t) = 1, \text{and} \\ SOC(t) > SOC_{max} \quad \& \quad P_{req} > P_{gen,min} \end{array} \right. \\ P_{gen,ch}, & \left\{ \begin{array}{l} \text{if } S(t) = 1, \text{and} \\ SOC_{min} \leq SOC(t) \leq SOC_{max} \end{array} \right. \\ P_{gen,max}, & \left\{ \begin{array}{l} \text{if } S(t) = 1, \text{and} \\ SOC(t) \leq SOC_{min} \end{array} \right. \end{cases} \quad (8.35)$$

Where,

$$P_{gen,ch} = P_{req} + P_{ch} \cdot \left(\frac{SOC_{max} + SOC_{min}}{2} - SOC(t) \right) \quad (8.36)$$

Where P_{ch} is a constant decided charge power magnitude, $P_{gen,min}$ and $P_{gen,max}$ are maximum and minimum power delivered by the generator, respectively.

8.10 Load follower supervisory control strategy

A load follower supervisory control strategy (LFSCS) based on the power follower supervisory control strategy (PFSCS) is proposed in the present work. Although LFSCS follows similar pattern to the PFSCS, it has very important changes in the decision variables. Contrary to the PFSCS proposed in [111] assuming that the engine-generator will be the prime power source, the engine battery will be the default prime power source in the LFSCS. But unlike the TSCS, where $SOC(t)$ is the only decision variable, the DC-link current $i_{dc-link}$ will also be a important decision variable in the LFSCS.

In a series hybrid electric vehicle, the traction motor drives the wheels of the vehicle and the power demand is always equal to $P_{req} = v_{dc-link}i_{dc-link}$. Since the DC-link voltage $v_{dc-link}$ is maintained constant at all times, the overall power fluctuations are mainly due to transients in the drawn DC-link current $i_{dc-link}$. When the engine is supplying the power, the demanded DC-link current gets directly translated into the demanded mechanical torque of the PMSG. Since the rotational speed of the engine-generator coupled rotor is maintained at constant speed, all the transients in the DC-link current $i_{dc-link} = i_{load}$ (load current) get reflected in T_L (load torque for the engine-generator set). In the present model, there is an involvement of the DC-link equation with all its dynamics, where constancy of the DC-link voltage and deliverance of the demanded power highly depend on the DC-link current. Also the value of the DC-link current is found to be very critical to the performance of the power supplying components. Switching and splitting of the power between different power sources such as the engine and battery is more straightforward in terms of the DC-link current than power in the present architecture of the powertrain. Tracking the DC-link current demand indirectly tracks the requested power demand also in the series configuration. So after overall analysis, it has been found that the LFSCS will be more logical and straightforward in implementation than the PFSCS. When both the engine and battery are active, power splitting is done by splitting the current contributions by the PMSG

and battery to the total DC-link current, $i_{dc-link}$, according to Equation (8.10).

Control logic for the implementation of LFSCS can be summarized as follows:

$$P_{req} = S(t) \cdot P_{gen} + \bar{S}(t)P_{bat} \quad (8.37)$$

$$P_{req} = \begin{cases} P_{bat}, & \left\{ \begin{array}{l} \text{if } SOC(t) \geq SOC_{max} \text{ Battery is fully charged;} \\ \text{or } SOC(t) \geq SOC_{min} \text{ \& } i_{dc-link} < i_{(crit,1)} \text{ Pure electric mode;} \\ \text{or } i_{dc-link} < 0 \text{ Regeneration;} \end{array} \right. \\ P_{gen,ch} - P_{bat,ch}, & \left\{ \begin{array}{l} \text{if } SOC_{max} \leq SOC(t) \leq SOC_{min} \text{ \& } i_{dc-link} < i_{crit,1} \\ \text{Battery is getting charged till } SOC_{max}; \end{array} \right. \\ P_{gen}, & \left\{ \begin{array}{l} \text{if } SOC(t) \leq SOC_{max} \text{ \& } i_{dc-link} < i_{(crit,2)} \\ \text{Engine alone is powering;} \end{array} \right. \\ P_{gen,max} + P_{bat}, & \left\{ \begin{array}{l} \text{if } i_{dc-link} > i_{crit,2} \\ \text{engine and battery both are powering;} \end{array} \right. \end{cases} \quad (8.38)$$

Where $P_{gen,ch}$ and $P_{bat,ch}$ are power produced by the generator and absorbed by the battery while the generator is driving the powertrain and charging the battery simultaneously. P_{gen} is power produced by the generator when it is alone driving the powertrain and not charging the battery. $P_{gen,max}$ is the maximum power produced by the generator, when power demand is very high and battery is also assisting the engine to drive the powertrain. $i_{(crit,1)}$ and $i_{(crit,2)}$ are the critical values of the DC-link current on the basis of which switching of the power sources are done. Here a simplified control logic for the LFSCS has been presented but its detailed implementation is given in the next Chapter 9.

8.11 Simulink block diagram of the series HEV powertrain

Figure 8.10 presents the Simulink implementation of the complete powertrain of the series HEV, which contains the individual components such as longitudinal car, PMSM, DC/AC converter, DC/DC converter, battery, AC/DC converter, PMSG and the turbocharged diesel engine. These simulink blocks are connected to each other by the compatible input-output links. The diesel engine and the battery are the power sources of the overall powertrain. Every component of the powertrain has their own individual controllers inside the component block itself. A supervisory controller is also designed to run the HEV in the normal operating conditions. Since detailed description of the other parts of the powertrain, such as PMSM, Car, converters and PMSG, has already been given in the previous chapters, mathematical equations for them are not presented here.

8.12 Summary

- Theoretical analysis of the various supervisory control strategies have been described in this chapter.
- Different types of the electrical and mechanical components are integrated together in one powertrain by exchanging the input and output in the form of potential and kinetic variables.
- To account for the losses, in the different components of the powertrain, various efficiency factors are included in the model. Energy balance for the different operating modes of the HEV powertrain with efficiency factors are described.
- A novel DC-link control strategy has been proposed by integrating the power-splitting control loop to the PMSG drive and the DC-link voltage control to the

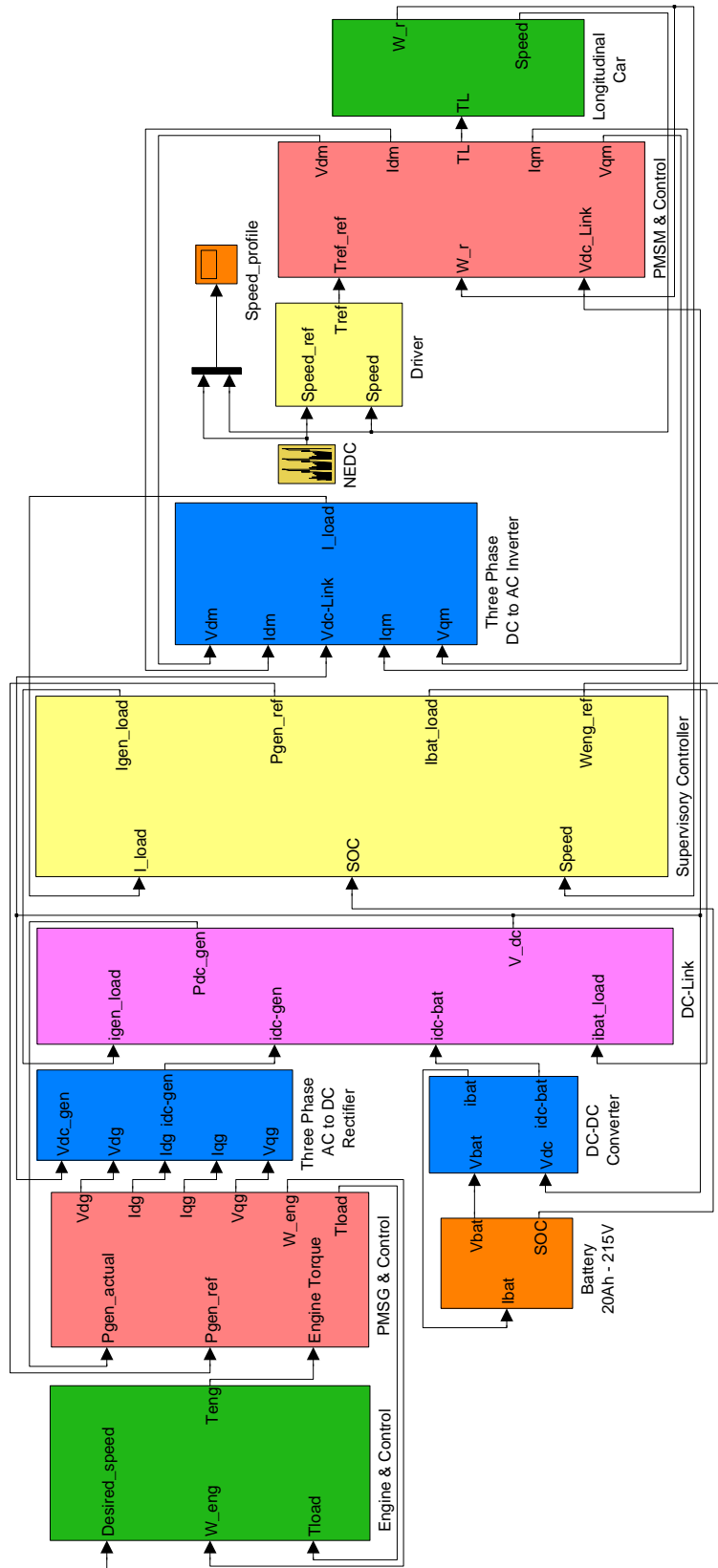


Figure 8.10: Simulink block diagram of the HEV powertrain containing longitudinal car, PMSM, DC/AC converter, DC/DC converter, battery, AC/DC converter, PMSG and turbocharged diesel engine

battery and DC/DC converter.

- Dynamic equations for the DC-link under the various operating modes are also presented to test the efficacy of its real time control.
- Finally on the basis of two most prominent supervisory control strategies namely thermostat control and power follower, a “load follower” supervisory control strategy is proposed in this chapter.

CHAPTER**NINE**

SIMULATION RESULTS AND DISCUSSIONS

9.1 Introduction

Supervisory control is an overall controller of the system that decides how to operate the HEV powertrain in the most efficient way so that all the desired objectives can be achieved successfully. The previous chapter discusses the method of integration of all the components in the series hybrid powertrain and reviews various supervisory control strategies. This chapter presents the simulation results of two particular supervisory control strategies. The hybrid powertrain is a collection of many electrical and mechanical subsystems containing state variables (decision variables) of many kinds such as voltage (v_{qm} , v_{dm} , v_{qg} , v_{dg} , $v_{dc-link}$ and v_{bat}), current (i_{qm} , i_{dm} , i_{qg} , i_{dg} , $i_{dc-link} = i_{load}$, i_{dc-gen} and i_{bat}), torque (T_L , T_{em} , $T_{fric,m}$, T_{eg} , $T_{fric,g}$, T_{eng} and $T_{fric,eng}$) and speed (ω_{rm} , ω_{em} , ω_{rg} , ω_{eg} , ω_{wheel} and $u_{car,actual}$). These decision variables are the important parameters of the powertrain, on the basis of which supervisory control generates the operational logic. Due to the availability of the detailed dynamic model of the powertrain components, we have realtime access to all these variables. By properly controlling these variables, losses in the components of the powertrain can be minimized. Minimization of losses in the powertrain components leads to lower energy demand from energy sources which in turn minimizes the overall required energy, fuel consumption, emissions and improves battery life. It has been found that supervisory

control strategy has very non-linear kind of interaction with system variables of the HEV powertrain. Not only that, the performance of the supervisory control also depends on the drive cycle used for testing. A particular type of supervisory control may not be optimum for one drive cycle but often produces suboptimal solution for another kind of drive cycle. The high fidelity model presented in this work creates an advanced platform to visualize and control all the important variables of the HEV powertrain analyzing their roles in the overall performance of the vehicle. This work explores the opportunity to optimize the performance of the HEV powertrain at component level itself rather than solely depending on supervisory controllers. Most of the models (available in current literature as summarized in Chapter 2) apply supervisory control strategy at low fidelity averaged model which may not be the best in all cases.

9.2 Simulation results

Two sets of supervisory control strategies, namely, thermostat and load-follower have been implemented and the generated results are analyzed. Both of these supervisory control strategies are tested on the standard NEDC drive cycle. The NEDC cycle is made-up of four repeated ECE-15 driving cycles and one high speed extra urban drive cycle named EUDC [6]. This drive cycle is used by various test laboratories for independent testing of vehicle performance and emissions [25]. The complete drive cycle lasts for almost 1200 sec of which the first 800 sec belong to repeated ECE-15 cycles, measuring vehicle performance and fuel economy for urban driving and the rest of the 400 sec, from 800 sec to 1200 sec, measuring vehicle performance and fuel economy in the extra urban driving. Figure 9.1 graphically describes the standard NEDC drive used in this work to test the efficacy of the supervisory control strategies.

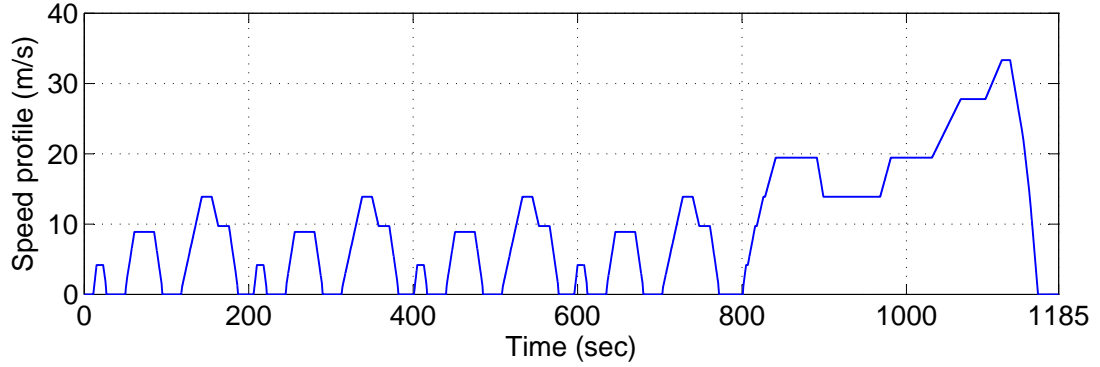


Figure 9.1: NEDC drive cycle for testing the supervisory controller of the HEV power-train

9.2.1 Thermostat supervisory control strategy

In this strategy, at first when the vehicle starts from standstill, the battery supplies all the required power, which leads to decreasing SOC of the battery with time. Till the current $SOC(t)$ is greater than SOC_{min} , the battery will keep on powering the vehicle and when $SOC(t)$ goes below SOC_{min} , the engine will be switched on to charge the battery and drive the vehicle simultaneously, till $SOC(t) = SOC_{max}$ is reached. In the mean time all the energy recaptured due to regeneration will be used to recharge the battery even while the engine is engaged to power the vehicle. Since in this control strategy the only decision variable is the SOC , its implementation is very simple and straight forward. Figure 9.2 shows the state flow chart for the implementation of TSCS.

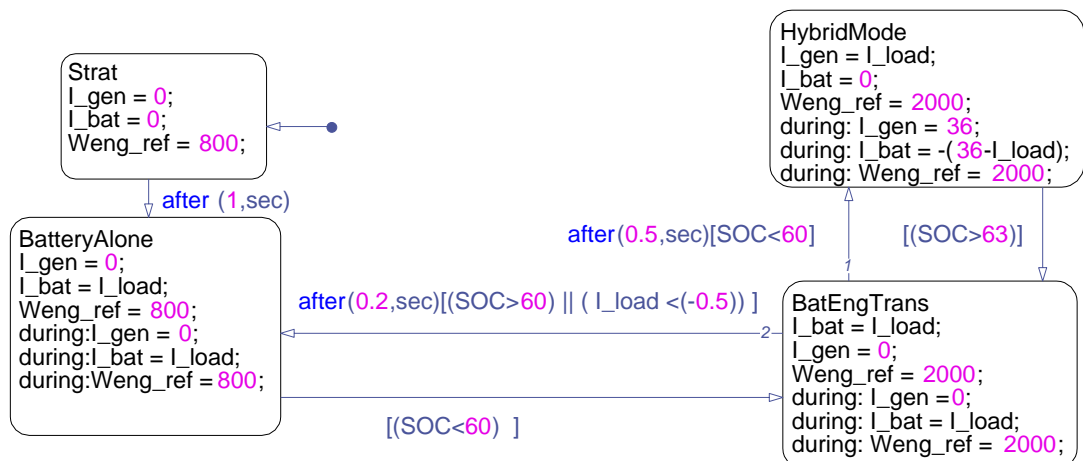


Figure 9.2: Stateflow chart for the thermostat supervisory control

Six different simulations are performed, in five of which, the car has fixed final

drive ratios of 2, 3, 4, 5 and 6, and in one, it has variable transmission ratio provided by the CVT. The NEDC drive cycle is supplied for testing the supervisory control strategy in all cases. The speed tracking in all cases is accurate and error involved in the tracking is shown in Figure 9.3. The energy provided by the sources in each simulation is shown in Figure 9.5. Coming sections will analyze the energy generation by the various power

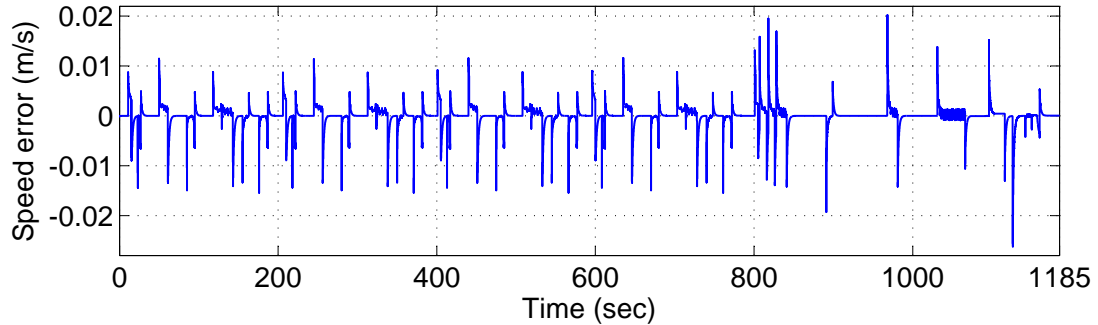


Figure 9.3: Error between desired speed profile and actual forward speed of the CVT installed longitudinal vehicle with the TSCS. Almost same results are obtained for the powertrains having fixed gear ratios $f_{drat} = 2, 3, 4, 5$ and 6

sources and energy consumed by different components of the powertrain. But before this analysis calculation of SOC equivalent energy will be given in the next section.

9.2.1.1 Calculation of the SOC equivalent energy

The Recharging energy shown in Figure 9.5 contains both regeneration and charging by the engine. Although the engine charges the battery only when $SOC(t) < SOC_{min}$, the regenerated energy is always sent to recharge the battery. The initial SOC of the battery is 65% and when SOC goes below 60%, the engine is used to charge the battery. For an ideal charge sustaining HEV, SOC_f (SOC at the end of the drive cycle) must remain in close range of SOC_i (SOC at the start of the drive cycle). Any positive deviation in the SOC ($\Delta SOC = SOC_f - SOC_i$) indicates some amount of energy has been taken out of the stored energy of the battery and not returned back to the battery. Ideally, this energy must be recharged back to the battery by the engine or regeneration. Since regeneration is treated as free energy for the battery, any deviation in the stored energy of the battery will be compensated with engine energy.

Sometime hard constraints are imposed on the SOC with the help of the supervisory control to make sure that ($\Delta SOC = 0$). Since in the present supervisory control there is no such arrangement provided, final SOC has deviated from initial SOC in almost all the five cases of simulations. However, the deviations are limited to a very narrow domain. If at the end of the NEDC cycle final $SOC_f < SOC_i$ (negative deviation of the SOC ($\Delta SOC < 0$)), it is clear that the powertrain has consumed the stored energy and this energy must come from the engine as a penalty. So, an equivalent energy (SOC equivalent) calculation is performed to account for this deviation of the SOC_f from SOC_i . But when there is positive deviation of the SOC ($\Delta SOC > 0$), it is assumed that engine has worked more and excess energy will be negatively sent penalized from the engine. Although in another sense, this excess charging of the battery can be utilized for further drive range when during next tracking battery will start higher initial SOC($SOC_i > 65\%$) than the normal value of 65%. For example, in the case of $f_{drat} = 5$, there is a small positive deviation of the SOC ($\Delta SOC > 0$).

To calculate equivalent energy a relation between SOC of the battery and engine energy has to be calculated. For this purpose, how much engine has to work to increase the SOC of the battery by 1%, has been calculated. When engine is used only to charge the battery from $SOC_i = 65\%$ to $SOC_f = 66\%$ at the constant current of $i_{gen} = 36A$, energy spent and fuel consumed by the engine are 220799 J and 0.0136 Kg respectively. By assuming the linear relationship between SOC of the battery and related engine energy and fuel consumption, any deviation in the SOC (ΔSOC) corresponds to equivalent energy engine of $E_{eq,SOC} = 220799 \cdot \Delta SOC$ J and fuel consumption of $Fuel_{eq,SOC} = 0.0136 \cdot \Delta SOC$ Kg.

Figure 9.4 presents SOC profile during the NEDC drive cycle for all simulation cases.

9.2.1.2 Energy consumption and loss analysis

The total energy used and time history of the fuel consumption, to complete the drive cycle in each case is shown in Figures 9.5 and 9.6 respectively. It is clear that the

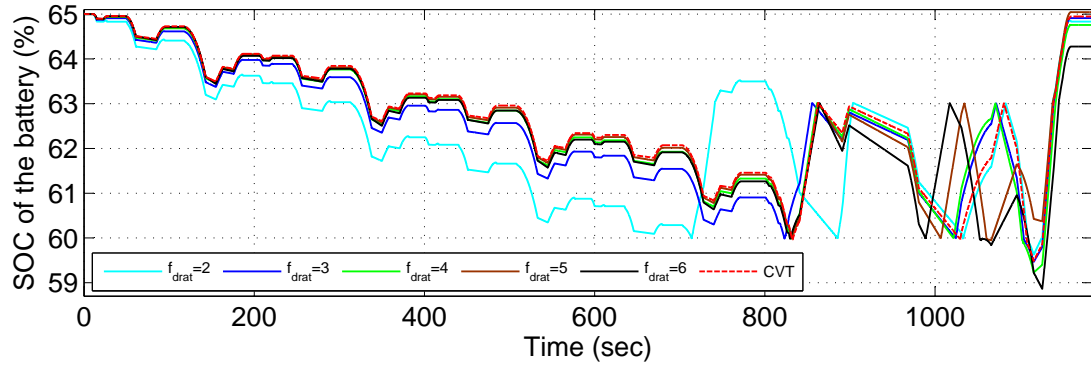


Figure 9.4: Time history of the *SOC* of the battery while tracking the NEDC drive cycle for fixed gear ratios $f_{drat} = 2, 3, 4, 5, 6$ and CVT with the TSCS

car with the CVT installed outperforms all other cases, giving reduction of 1.42% and 1.12% in the total energy and total fuel consumption respectively, as compared to the best case of fixed final drive ratio, $f_{drat} = 3$.

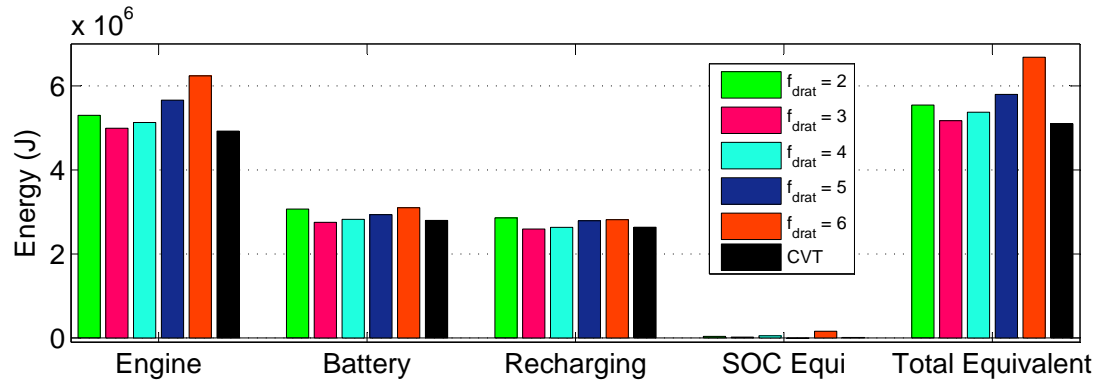


Figure 9.5: Energy provided by the engine, battery, battery recharging, SOC equivalent and total energy spent, in the powertrains having fixed gear ratios ($f_{drat} = 2, 3, 4, 5, 6$) and CVT, in tracking the NEDC drive cycle with the TSCS

Figure 9.7 describes the major losses in the different components of the powertrain for the six different simulations. From this figure it can be observed that although CVT losses highest energy in the for transmission losses but it saves more energy by minimizing overall losses in the PMSM (both PMSM friction and resistance losses). In all other form of losses also although CVT is minimum but major benefit of energy saving comes from optimizing PMSM performance. This analysis will be done in more detail on coming sections where losses in the individual components will be discussed in more detail.

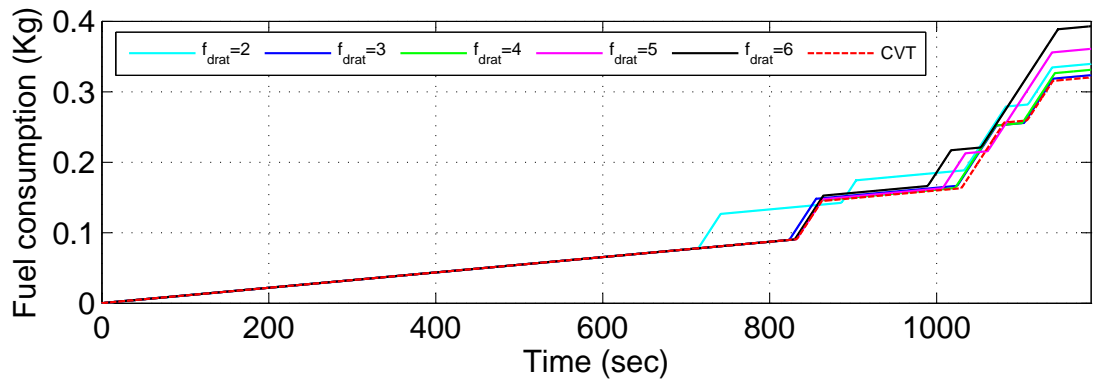


Figure 9.6: Time history of the total fuel consumption during NEDC cycle tracking in the cases of fixed gear ratios $f_{drat} = 2, 3, 4, 5, 6$ and CVT with the TSCS

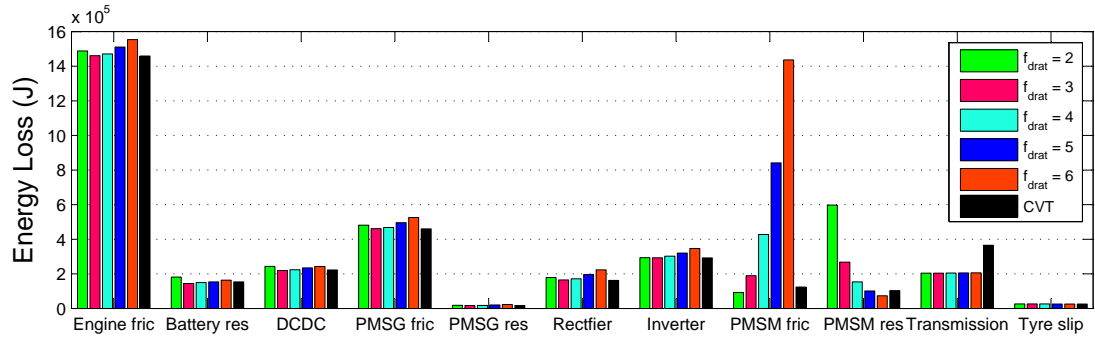


Figure 9.7: Energy dissipated by the engine, battery, DC/DC converter, PMSG and PMSM friction, PMSG and PMSM copper resistance, Rectifier, Inverter, Transmission and tyres, in the powertrains having fixed gear ratios ($f_{drat} = 2, 3, 4, 5, 6$) and CVT, while tracking the NEDC drive cycle with the TSCS.

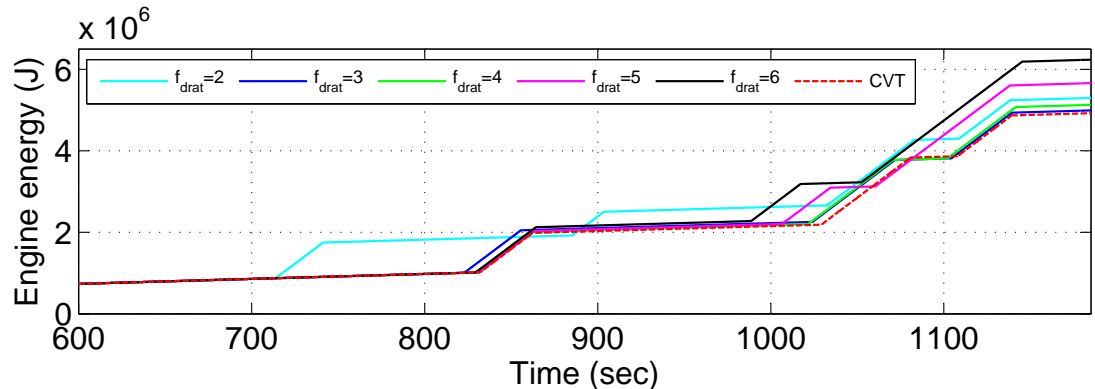


Figure 9.8: Time history of the energy generated in the engine for the powertrains having fixed gear ratios ($f_{drat} = 2, 3, 4, 5, 6$) and CVT, while tracking the NEDC drive cycle with the TSCS.

From Figures 9.5 and 9.8, it can be observed that in the case of CVT installed powertrain, the HEV requires the minimum energy from the engine in comparison to all other cases. Figures 9.7 and 9.9 demonstrate that there is a substantial energy loss in the engine due to friction; this loss is alleviated by operating the engine at two different speeds as described in Section 6.5. In Figure 9.7, the magnitude of different kinds of losses are compared so they all are shown with positive bars. But, everywhere else all the different kinds of losses are shown negatively just to depict the fact that loss means dissipation and total energy supplied is equal to the total energy loss in the HEV powertrain (which shows a kind of energy balance).

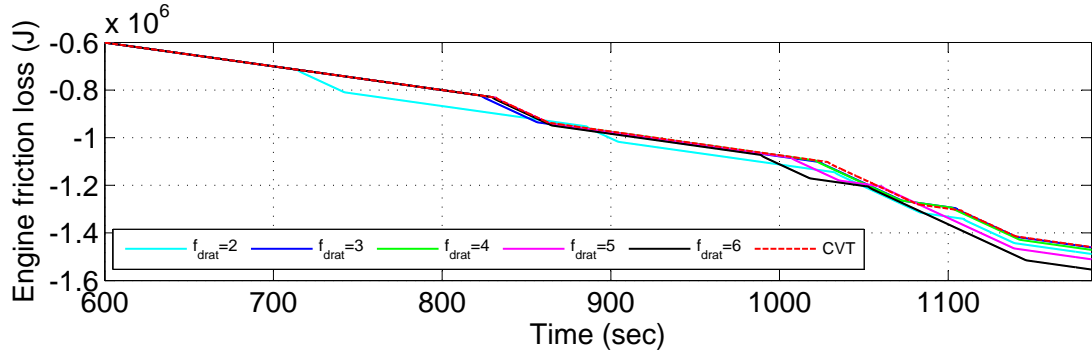


Figure 9.9: Time history of the engine friction loss in the powertrains having fixed gear ratios ($f_{drat} = 2, 3, 4, 5, 6$) and CVT, while tracking the NEDC drive cycle with the TSCS.

9.2.1.3 Losses in the PMSG

In Figures 9.7 and 9.10, there are descriptions of the losses in the PMSG denoted as friction loss and these are calculated by the expression $T_{fric} \cdot \omega_{rg}$. But as already described in Section 5.5, the proposed loss represents not only frictional loss but also includes many other kinds of losses such as eddy current losses ($P_{l,e}$), hysteresis losses ($P_{l,h}$), bearing losses ($P_{l,b}$) and windage losses ($P_{l,w}$) [202]. Figure 9.10 demonstrates that this loss is minimum when a CVT transmission is used than fix gear ration transmission. Usage of the CVT transmission minimizes the copper losses as well in the PMSG as shown in Figure 9.11.

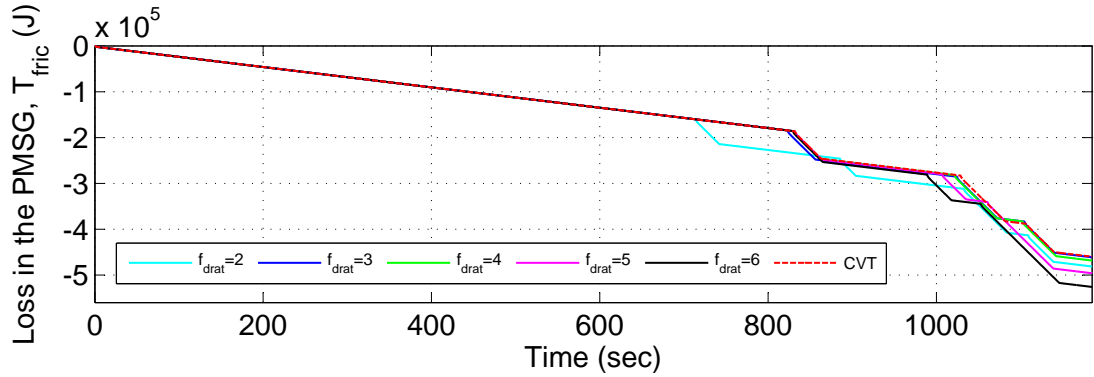


Figure 9.10: Quantification of all the losses except the copper loss in the PMSG, with the powertrains having fixed gear ratios ($f_{drat} = 2, 3, 4, 5, 6$) and CVT, during NEDC cycle with respect to time under the TSCS.

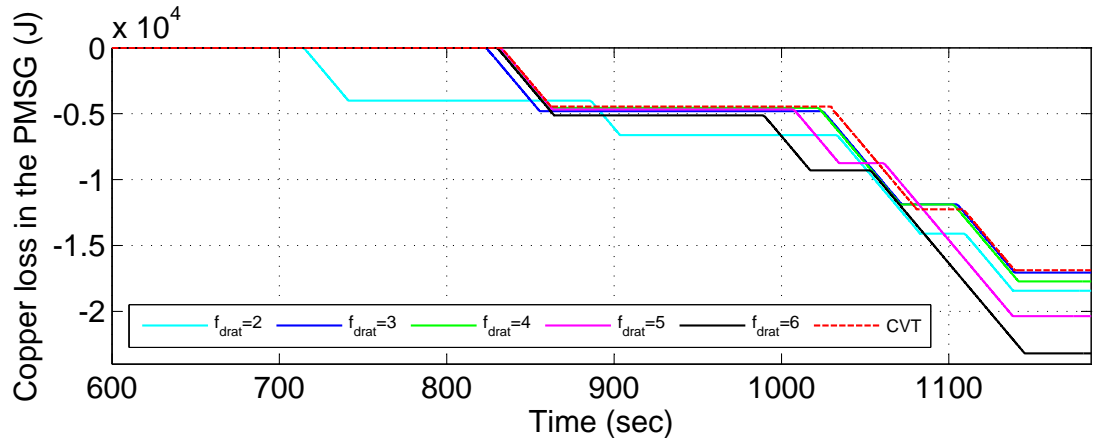


Figure 9.11: Quantification of the copper loss in the PMSG, with the powertrains having fixed gear ratios ($f_{drat} = 2, 3, 4, 5, 6$) and CVT, during NEDC cycle with respect to time under the TSCS.

9.2.1.4 Losses in the PMSM

The relative magnitude of other types of losses, such as tyre slip losses, can also be seen in Figure 9.7. The major benefits of using the CVT are demonstrated by reduction in energy loss in the PMSM, caused both by friction and resistance of the windings as compared to the fixed final drive ratio cases. Figures 9.12 and 9.13 give the time history of the copper loss and friction loss in the PMSM. Although both losses for the CVT are not minimum individually, but definitely their sum as the total loss in the PMSM is minimum among all drive ratios as shown in Figure 9.14. From this figure, it can be easily observed that the difference in the performances of fixed final drive ratios

and CVT become extremely prominent during the EUDC cycle. The case with the final drive ratio $f_{drat} = 3$ is the best among all the fixed final drive ratio cases and the closest one to the CVT installed case, in terms of total loss in the PMSM and in overall energy consumption as well. Losses involved in the vehicle such as aerodynamic, tyre slip and suspension are almost same in all the different cases of transmission on account of using the same NEDC drive cycle and a fixed structure of the vehicle. By the virtue of using different gear ratios, the PMSM has different copper and frictional losses in the different cases of transmission. Minimization of PMSM losses in the CVT case excels the performance of the CVT in comparison to fixed gear transmissions.

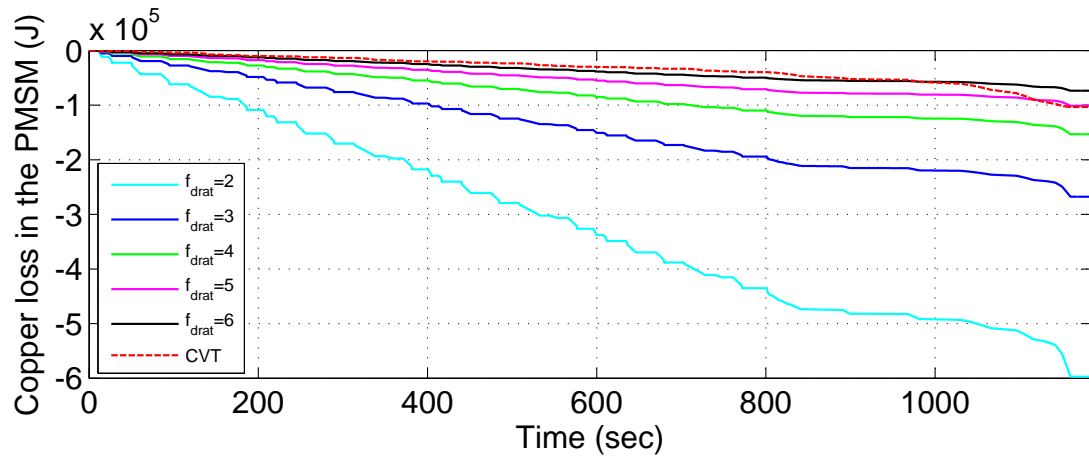


Figure 9.12: Quantification of copper loss in the PMSM, with the powertrains having fixed gear ratios ($f_{drat} = 2, 3, 4, 5, 6$) and CVT, during NEDC cycle with respect to time under the TSCS.

If only losses in the PMSM are compared, the CVT case is almost 100% better than the $f_{drat} = 3$ case as total PMSM losses in the case of the CVT and its closest competing case $f_{drat} = 3$ are around 2.26×10^5 J and 4.56×10^5 J, respectively. But the CVT case suffers through worse losses due to its lower transmission efficiency in comparison to fixed gear ratios. Figure 9.15 presents comparative quantification of all the major losses in the powertrain after the DC-link. In the series hybrid powertrain all the energy reaching the vehicle has to go through the PMSM and transmission. The CVT case excels all fixed gear ratio cases due to its minimum energy losses in the PMSM but this enormous energy gain in the PMSM is up to a large extent compromised

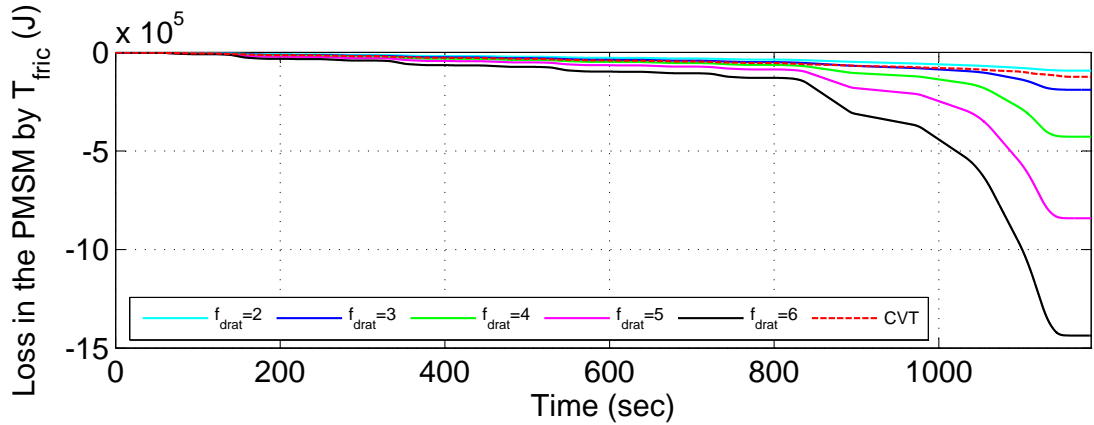


Figure 9.13: Quantification of all losses except copper loss in the PMSM, with the powertrains having fixed gear ratios ($f_{drat} = 2, 3, 4, 5, 6$) and CVT, during NEDC cycle with respect to time under the TSCS.

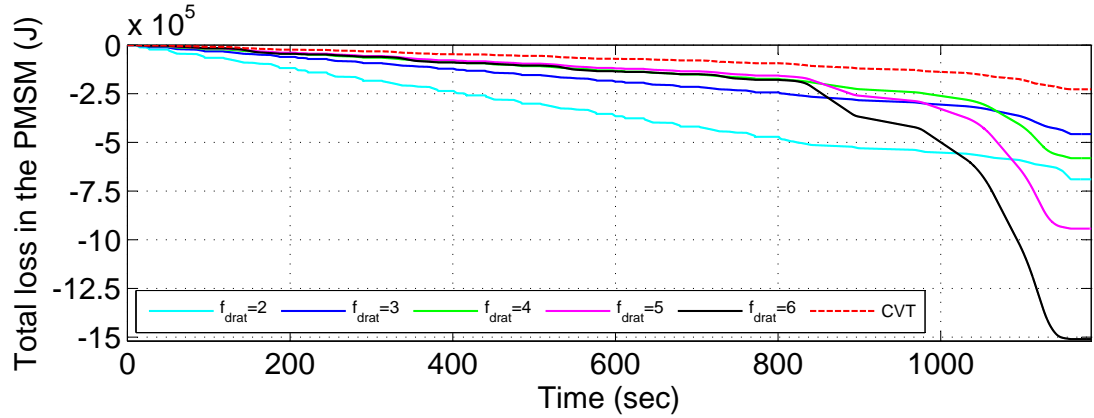


Figure 9.14: Time profile of total energy loss in the PMSM, with the powertrains having fixed gear ratios ($f_{drat} = 2, 3, 4, 5, 6$) and CVT, during NEDC drive cycle under the TSCS

due to high loss in the transmission. If the total energy entering in to the inverter from the DC-link is compared in all the different cases of simulations, the CVT case gives the best performance of 2.56% reduction in comparison to the best energy efficient case of fixed gear $f_{drat} = 3$ as shown in Figure 9.15. If somehow the efficiency of the CVT transmission can be improved, the CVT led transmission will give enormous savings in terms of total energy and fuel consumption.

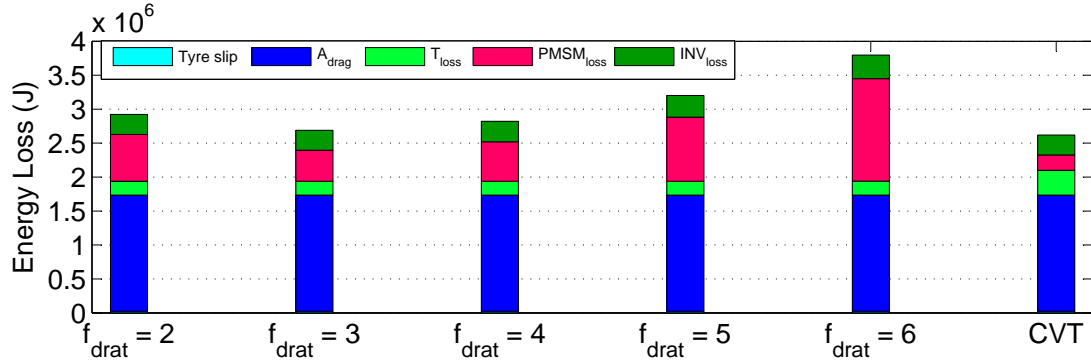


Figure 9.15: Quantification of the total energy supplied from DC-link onwards against different losses in the inverter, PMSM and car while tracking the NEDC drive cycle with the the thermostat control strategy.

9.2.2 Load follower supervisory control strategy

$i_{dc-link}$, SOC and u_{car} are chosen as decision variables for the LFSCS. The performance of power sources and overall powertrain highly depends on these variables. On the basis of these decision variables, switching between the engine and battery as power source can be decided. In the present case of battery model, it has been observed that the battery performance deteriorates when $i_{ob} > 30A$, so $i_{dc-link} = 30A$ can be a threshold value for switching from battery to engine. The expected optimum performance of the battery occurs at $60\% < SOC < 65\%$. The engine utilization at two different speeds, 800 rpm and 2000 rpm, is related to the minimization of the friction losses of the engine and generator when these are not being used. The engine alone cannot provide more than 48A of load current while maintaining the DC-link voltage constant and running at 2000 rpm engine speed, so the battery has to support it by providing the rest of the power. A state flow-map is used to generate the supervisory control signals for different operating modes. Primarily, four operating modes and one transitory operating mode are conceived in the present supervisory control. These operating modes and conditions for transitions from one mode to the other are explained in Figure 9.16 in the form of a state-flow-chart.

The operating modes are described as rectangular blocks and arrows pointing from one operating mode to another to show possible transition ways. The conditions of

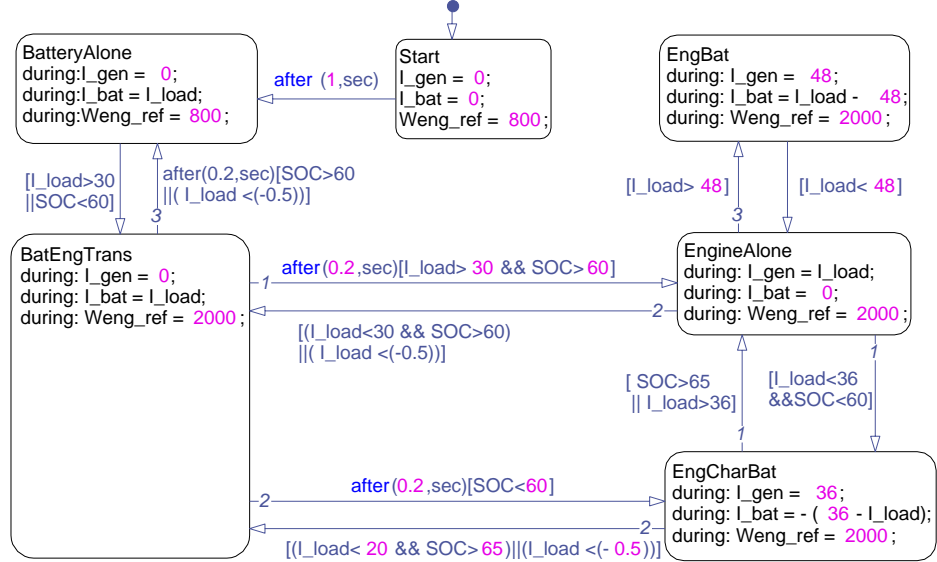


Figure 9.16: Stateflow chart for the proposed load follower supervisory control strategy. i_{gen} and i_{bat} are the desired or reference load currents for the PMSG and battery respectively. i_{load} is the DC-link current drawn by the PMSM and inverter. $\omega_{eng-ref} = \omega_{desired}$ is the desired speed for the engine. BatteryAlone, BatEngTrans, EngineAlone, EngCharBat and EngBat are overall five modes of operation of the powertrain, and their names are self explanatory.

the transitions are written on the arrows and if all the conditions written on the arrows are true, the powertrain will transit from one mode to another. At first, when the vehicle starts from a standstill position, the battery starts powering the HEV. This pure electric mode of operation is called BatteryAlone. While tracking the complete NEDC cycle, when the DC-link load current demand goes beyond 30A ($i_{dc-link} = i_{load} > 30A$) or the *SOC* of the battery goes below 60% ($SOC < 60\%$), the HEV goes in a transitory operating mode named BatEngTrans. In this transitory operating mode, the engine is turned on but the DC-link load current is still supplied by the battery only. This transition is important because the engine need some time to switch its speed from $\omega_{idle} = 800$ rpm to $\omega_{operating} = 2000$ rpm. The HEV remains in this transitory mode (BatEngTrans) for the next 0.2 sec and from this operating mode, there are total three ways in which further transition can happen. Firstly, if SOC remains $SOC > 60\%$ or if there is a regeneration $i_{load} < -0.5A$, the HEV will again come back to the pure battery mode (BatteryAlone) of operation. Secondly, if the DC-link load current demand remains $i_{load} > 30A$ with $SOC > 60\%$, then the HEV will transit to the EngineAlone

mode of operation, where the engine is supplying all the power demanded by the HEV and the battery is simply switched off from the powertrain. Thirdly, if $SOC < 60\%$, the HEV will go into the EngCharBat mode of operation where the engine will be supplying all the power demand of the HEV and charging the battery as well. In EngCharBat mode, a constant current 36A is drawn from the engine-generator and the rest of the current $-(36 - I_{load})$ is used to charge the battery. The HEV can further transit from the EngCharBat mode of operation to either EngineAlone or BatEngTrans depending on the values of the state variables SOC and i_{load} . The HEV will enter from EngCharBat to BatEngTrans if $i_{load} < 20\text{A}$ and $SOC > 65\%$ or regeneration $i_{load} < -0.5\text{A}$ takes place. Depending on the values of SOC and i_{load} , there can be further transitions from the BatEngTrans mode to the other modes. The HEV will enter from EngCharBat to EngineAlone if $SOC > 65\%$ or $i_{load} > 36\text{A}$. From EngineAlone mode, there can be transitions to three other modes BatEngTrans, EngCharBat and EngBat. HEV can enter from EngineAlone to BatEngTrans if $i_{load} < 30\text{A}$ and $SOC > 60\%$ or regeneration $i_{load} < -0.5\text{A}$ takes place. Depending on the values of the SOC and i_{load} there can be further transitions from the BatEngTrans mode to the other modes. HEV can enter from EngineAlone to EngCharBat if $i_{load} < 36\text{A}$ and $SOC < 60\%$. HEV can enter from EngineAlone to EngBat if $i_{load} > 48\text{A}$, where the engine alone cannot support the power demand of the PMSM causing the battery to come for assistance. EngBat is a hybrid mode of operation during high power demand but required only with high drive ratios such as $f_{drat} = 6$ and higher.

9.2.2.1 Energy consumption and loss analysis

Again in this supervisory control case also six different simulations are performed, in five of which, the car has fixed final drive ratios of 2, 3, 4, 5 and 6, and in one, it has variable transmission ratio provided by the CVT. Speed tracking in all the cases is accurate and the error in the tracking is shown in Figure 9.17. The energy provided by the sources in each simulation is shown in Figure 9.18.

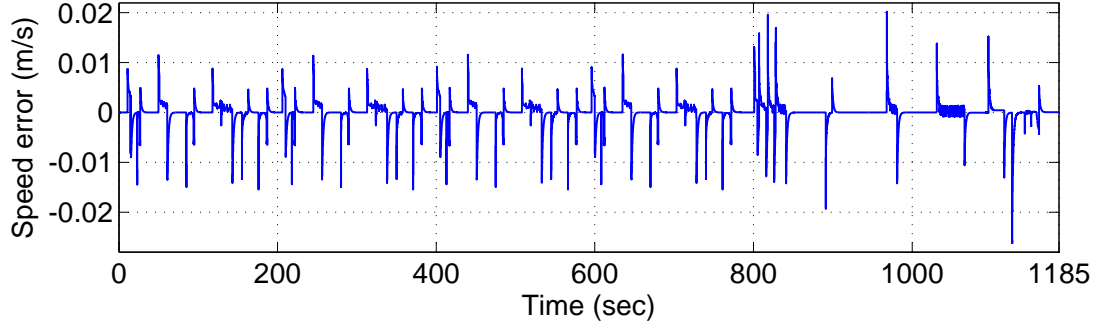


Figure 9.17: Error between desired speed profile and actual forward speed of the longitudinal vehicle with the LFSCS

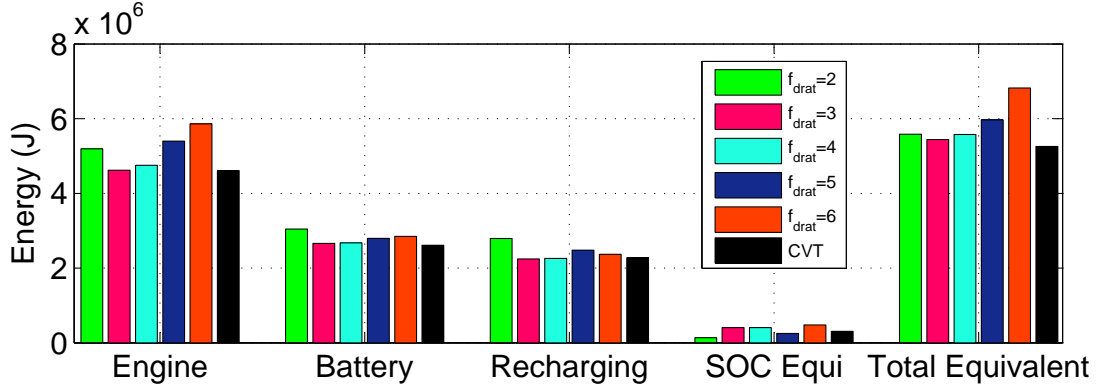


Figure 9.18: Energy provided by the engine, battery, battery recharging, SOC equivalent and total energy spent, in the powertrains having fixed gear ratios ($f_{drat} = 2, 3, 4, 5, 6$) and CVT, in tracking the NEDC drive cycle with the LFSCS

All labels used for quantification of energy are same as used in previous cases such as engine energy, battery energy and SOC equivalent energy. SOC equivalent energy in this also has been calculated in similar manner as done in the TSCS case. Once again with LFSCS also, CVT installed HEV powertrain clearly excels in performance in comparison to all other fixed final drive ratios as shown in Figure 9.18. But under the effect of LFSCS, CVT led HEV powertrain is 3.52% more efficient in terms of total energy than its closest competitor case of fixed final drive ratio, $f_{drat} = 3$. In terms of fuel consumption also CVT led HEV powertrain is 1.72% more efficient, as compared to the best case of fixed final drive ratio, $f_{drat} = 3$. The total energy used and time history of the fuel consumption, to complete the drive cycle in each case are shown in Figures 9.18 and 9.20, respectively. Figure 9.19 describes major losses in the different components of the powertrain for six different simulations. Energy generated and

dissipated by the engine, battery, DC/DC converter, PMSG, PMSM, rectifier, inverter, transmission and tyres, in the powertrains having fixed gear ratios ($f_{drat} = 2, 3, 4, 5, 6$) and CVT, while tracking the NEDC drive cycle with the LFSCS are tabulated in Table 9.1.

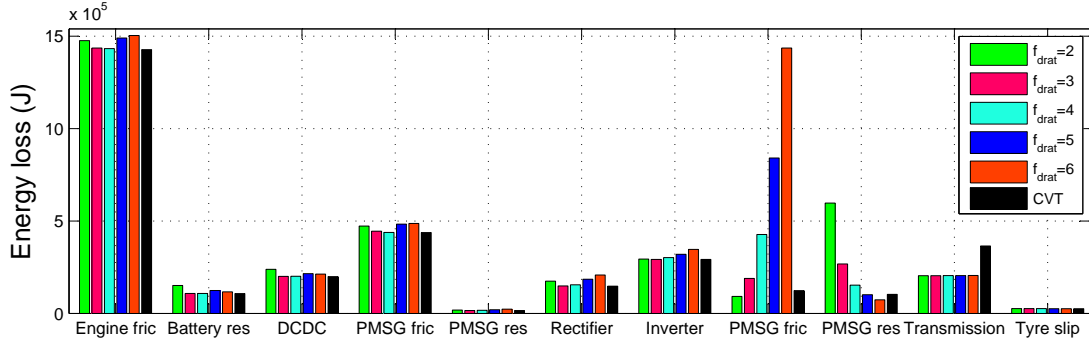


Figure 9.19: Energy dissipated by the engine, battery, DC/DC converter, PMSG and PMSM friction, PMSG and PMSM copper resistance, Rectifier, Inverter, Transmission and tyres, in the powertrains having fixed gear ratios ($f_{drat} = 2, 3, 4, 5, 6$) and CVT, while tracking the NEDC drive cycle with the LFSCS.

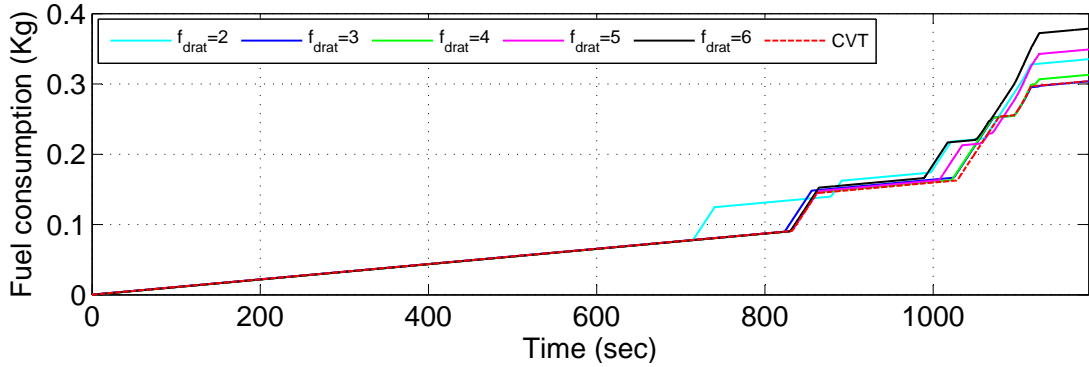


Figure 9.20: Time history of the total fuel consumption during NEDC drive cycle tracking in the cases of fixed gear ratios $f_{drat} = 2, 3, 4, 5, 6$ and CVT with the LFSCS

9.2.2.2 Losses in the Engine

From Figures 9.18 and 9.21, once again, it can be observed that in the case of CVT installed powertrain, the HEV requires the minimum energy from the engine in comparison to all other cases.

Figures 9.19 and 9.22 demonstrate that there is a substantial energy loss in the

Table 9.1: Quantification of all the energy generation and losses involved in different components of the HEV powertrain while operating with the load follower supervisory control strategy.

Parameters	$f_{drat} = 2$	$f_{drat} = 3$	$f_{drat} = 4$	$f_{drat} = 5$	$f_{drat} = 6$	CVT
Fuel Cons.(kg)	0.3352	0.3037	0.3130	0.3491	0.3787	0.3041
Engine Energy (J)	5193788	4620150	4751287	5399722	5862718	4609317
Battery Discharge (J)	3046440	2662086	2676547	2796757	2850473	2613284
Recharging (J)	2791776	2246248	2258569	2481404	2370031	2272905
$SOC_i(\%)$	65.00	65.00	65.00	65.00	65.00	65.00
$SOC_f(\%)$	64.38	63.16	63.15	63.86	62.83	63.61
SOC Equivalent (J)	136330	405391	408151	251623	479139	306671
Total fuel Cons. (kg)	0.3436	0.3287	0.3382	0.3646	0.4082	0.3230
Total equi. energy (J)	5584781	5441379	5577415	5966698	6822299	5256368
Losses in the powertrain components						
Engine fric. loss (J)	1476525	1435966	1433003	1490639	1503817	1427551
Battery loss (J)	151106	107919	107963	124211	116509	107444
DC/DC conv. loss(J)	238746	200373	201419	215455	212741	199454
PMSG fric. loss (J)	472858	445129	438030	483445	487200	437704
PMSG res. loss (J)	18330	15706	16779	20079	23401	15710
Total PMSG loss (J)	491187	460834	454809	503524	510600	453414
AC/DC conv. loss (J)	174352	148793	154786	185267	207817	147491
DC/AC conv. loss (J)	293840	292582	301895	319985	346475	292217
PMSM fric. loss(J)	92195	189310	427333	841332	1436215	123419
PMSM res. loss (J)	597257	267624	153260	101149	73602	103443
Total PMSM loss (J)	689452	456934	580593	942481	1509817	226862
Transmission loss (J)	204033	204262	204630	205120	205726	365111
Tyre slip loss (J)	26060	25954	25875	25823	25791	25774
Suspension loss (J)	257	259	260	260	259	261
Tyre damping loss (J)	1.86	1.90	1.92	1.92	2	1.95
Aerodynamic loss (J)	1708893	1708843	1708820	1708808	1708802	1708809

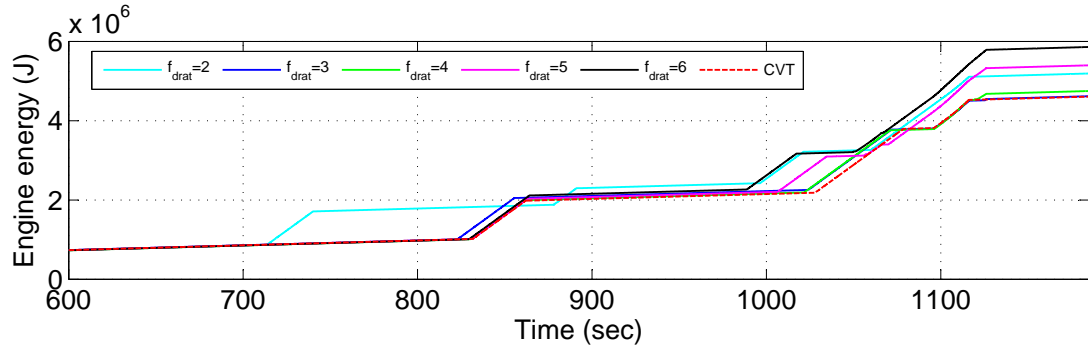


Figure 9.21: Time history of the energy generated in the engine for the powertrains having fixed gear ratios ($f_{drat} = 2, 3, 4, 5, 6$) and CVT, while tracking the NEDC drive cycle with the LFSCS.

engine due to friction; this loss is alleviated by operating the engine at two different speeds as described in section 6.5.

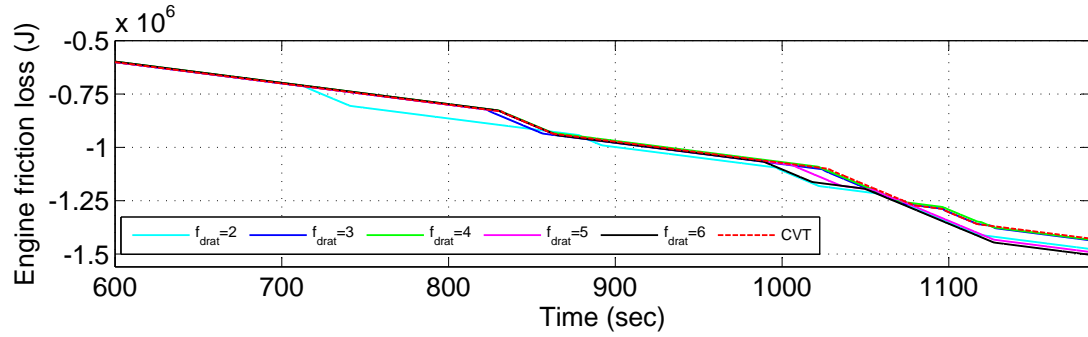


Figure 9.22: Time history of the energy lost due to engine friction in the powertrains having fixed gear ratios ($f_{drat} = 2, 3, 4, 5, 6$) and CVT, while tracking the NEDC drive cycle with the LFSCS.

9.2.2.3 Losses in the PMSG

In Figures 9.19 and 9.23, there are descriptions of the losses in the PMSG denoted as friction loss and is calculated by the expression $T_{fric}\omega_{rg}$. But as already described in section 5.5, proposed loss does not represent only frictional loss but includes many other kinds of losses such as eddy current losses ($P_{l,e}$), hysteresis losses ($P_{l,h}$), bearing losses ($P_{l,b}$) and windage losses ($P_{l,w}$) [202]. Figure 9.23 demonstrates that this loss is minimum when CVT transmission is used. Usage of the CVT transmission minimizes the copper losses as well in the PMSG as shown in Figure 9.24.

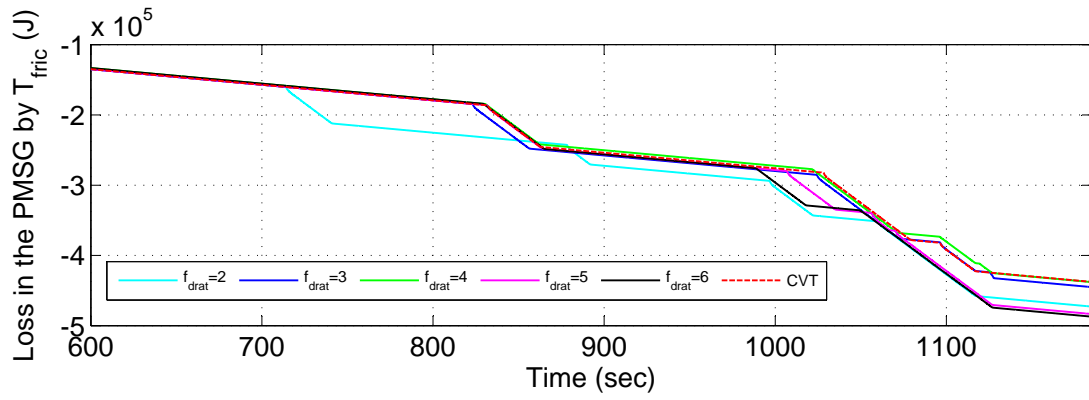


Figure 9.23: Quantification of all the losses except the copper loss in the PMSG, with the powertrains having fixed gear ratios ($f_{drat} = 2, 3, 4, 5, 6$) and CVT, during NEDC cycle with respect to time under the LFSCS.

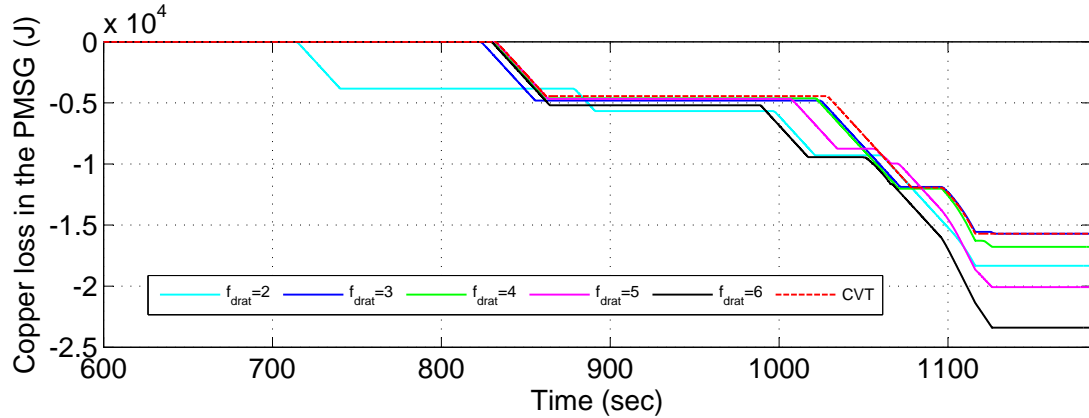


Figure 9.24: Quantification of the copper loss in the PMSG, with the powertrains having fixed gear ratios ($f_{drat} = 2, 3, 4, 5, 6$) and CVT, during NEDC cycle with respect to time under the LFSCS.

9.2.2.4 Losses in the PMSM

The relative magnitude of other types of losses, such as tyre slip losses, can also be seen in Figure 9.19. The benefits of using the CVT are demonstrated by the reduction in energy loss in the PMSM, caused both by friction and resistance of the windings when compared with the fixed final drive ratio cases.

Figures 9.25 and 9.26 give the time history of the copper loss and friction loss in the PMSM. Although both the losses for the CVT are not minimum individually, their sum as the total loss in the PMSM is minimum among all drive ratios as shown in Figure 9.27. From this figure, it can be easily observed that difference in the performances of

constant drive ratios and CVT becomes extremely prominent during the EUDC cycle. Once again, the case with the final drive ratio $f_{drat} = 3$ is the best among all the fixed final drive ratio cases and the closest one to the CVT installed case, in terms of total loss in the PMSM and overall energy consumption.

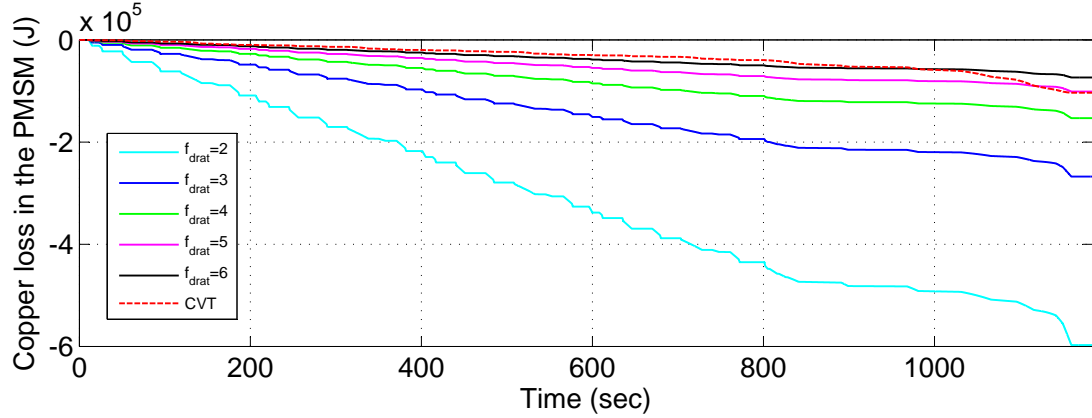


Figure 9.25: Quantification of copper loss in the PMSM, with the powertrains having fixed gear ratios ($f_{drat} = 2, 3, 4, 5, 6$) and CVT, during NEDC cycle with respect to time with the LFSCS.

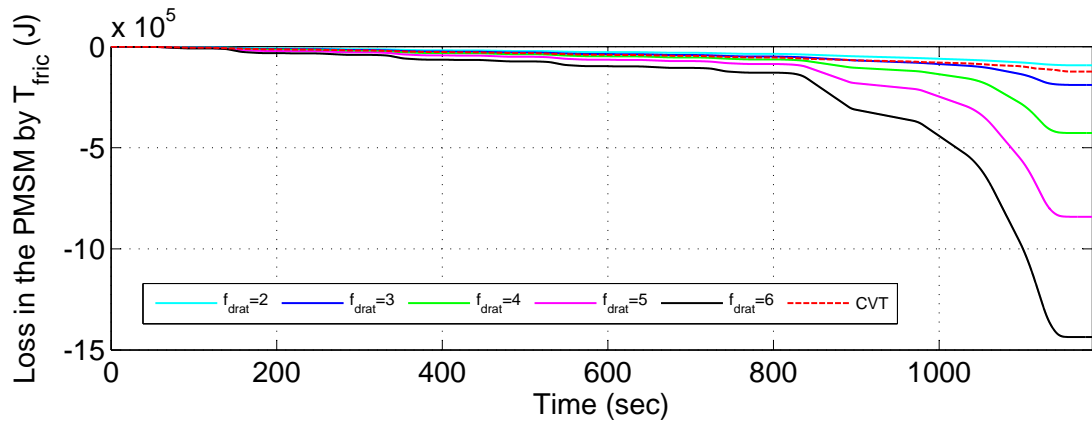


Figure 9.26: Quantification of all losses except the copper loss in the PMSM, with the powertrains having fixed gear ratios ($f_{drat} = 2, 3, 4, 5, 6$) and CVT, during NEDC cycle with respect to time with the LFSCS.

Under LFSCS, if only the losses in the PMSM are compared, the CVT case is almost 100% better than $f_{drat} = 3$ case. If the total energy entering into the inverter from the DC-link is compared in all different cases of simulations, CVT case gives the best performance by reduction of 2.67% in comparison to the best energy efficient case of fixed gear $f_{drat} = 3$ which is again an improvement over the TSCS case. Figure 9.28

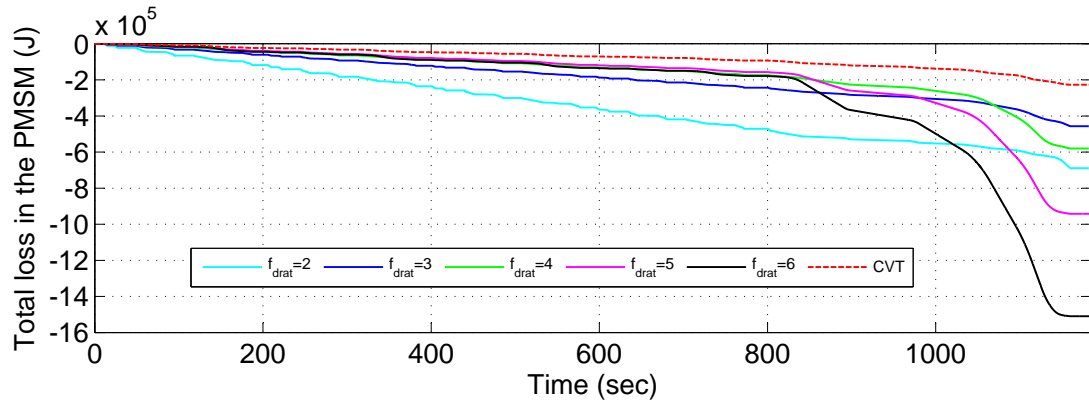


Figure 9.27: Time profile of total energy loss in the PMSM, with the powertrains having fixed gear ratios ($f_{drat} = 2, 3, 4, 5, 6$) and CVT, during NEDC drive cycle with the LFSCS.

shows the quantification of energy allocated to different categories of major losses in the powertrain after the DC-link.

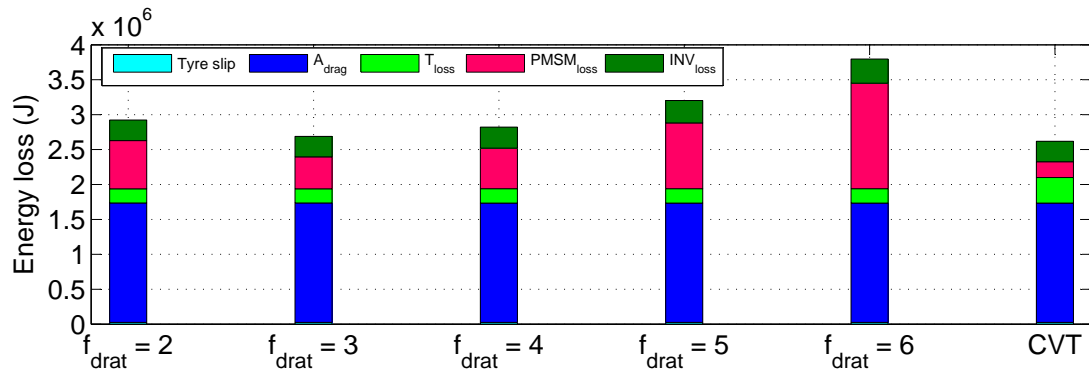


Figure 9.28: Quantification of the total energy supplied from DC-link onwards against different losses in the inverter, PMSM and car while tracking the NEDC drive cycle with the load-follower control strategy

9.2.2.5 Analysis of the efficiency and final drive ratio (f_{drat}) for the PMSM

Figure 9.29 and 9.30 compares the efficiency of the PMSM operation among all the fixed final drive ratios and CVT during one ECE-15 and EUROCARTE drive cycle. From Figure 9.29, it can be deduced that the overall efficiency of the PMSM in the case of CVT remains very close to 90%, which is best during the ECE-15 drive cycle. Although during the ECE-15 drive cycle efficiency of the PMSM with final drive ratio $f_{drat} = 2$ is lowest, during the EUROCARTE cycle efficiency of final drive ratio $f_{drat} = 2$ excels even

the CVT, specially at the ends of higher speed range as shown in Figure 9.30. Both the Figures 9.29 and 9.30 give very interesting insight as to how a particular kind of transmission is not optimum all the time during different phases of operation even if the overall performance is best. This almost best average 90% efficiency in the case of CVT is attained by changing the final drive ratio to track the line of the highest efficiency as described in section 3.4.1. Figures 9.31 and 9.32 describe the variation of the final drive ratio of the CVT during ECE-15 and EUDC cycles respectively.

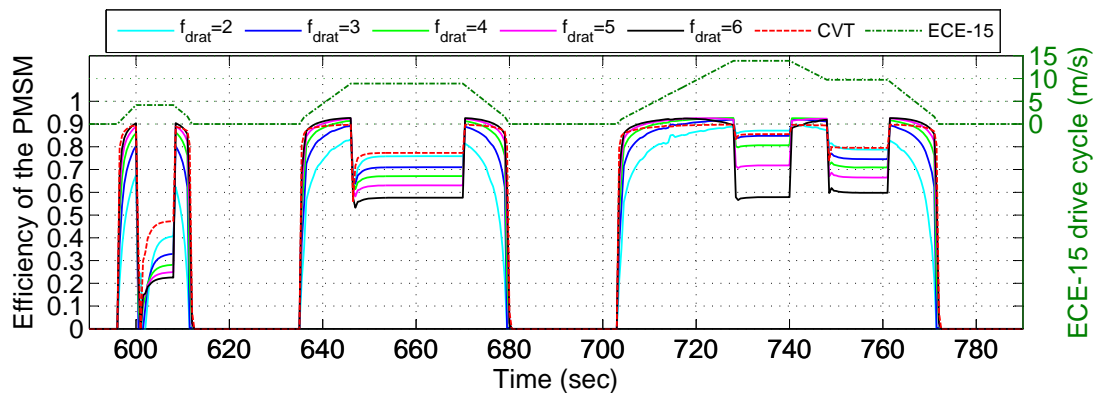


Figure 9.29: Time history of PMSM efficiencies in the cases of $f_{drat} = 2, 3, 4, 5, 6$ and CVT for urban (ECE-15) part of the NEDC drive cycle.

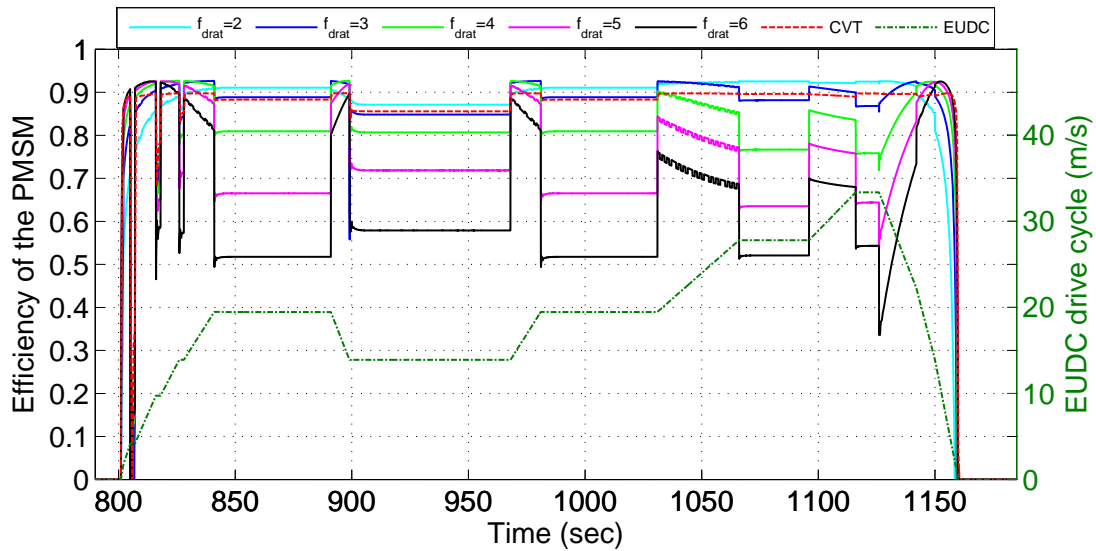


Figure 9.30: Time history of PMSM efficiencies in the cases of $f_{drat} = 2, 3, 4, 5, 6$ and CVT form extra urban (EUDC) part of the NEDC drive cycle.

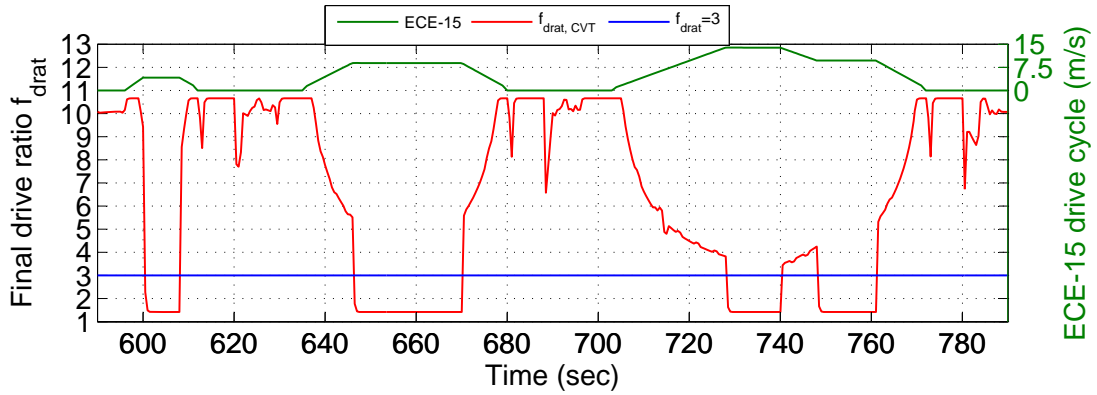


Figure 9.31: Variation of the f_{drat} in the case of CVT for the urban (ECE-15) part of the NEDC drive cycle.

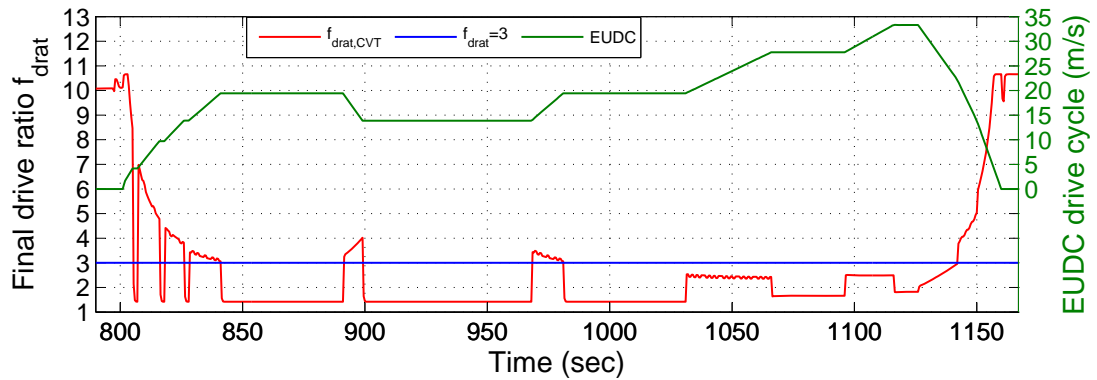


Figure 9.32: Variation of the f_{drat} in the case of CVT for the extra urban (EUDC) part of the NEDC drive cycle.

9.2.2.6 Efficacy of the DC-link voltage control strategy

Figure (9.33) describes the success of the DC-link voltage control scheme by splitting the control objectives between two different control loops. The power splitting control loop is integrated with the PMSG-drive controller and the DC-link voltage control is integrated with the DC/DC converter, where the battery works as a power buffer. The maximum deviation of the DC-link voltage throughout the NEDC cycle is around 0.046%.

9.2.2.7 Analysis of the DC-link current

The magnitudes of all the losses and energy consumption, in the different components of the powertrain before DC-link (such as the engine, PMSG, battery

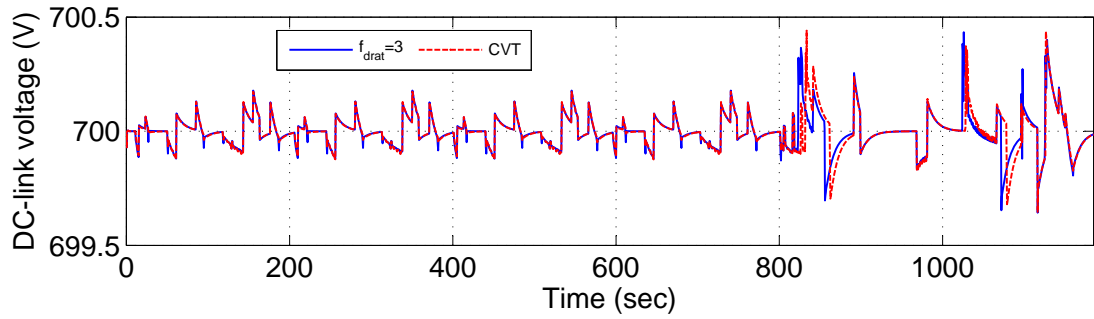


Figure 9.33: DC-link voltage profile during the tracking of the complete NEDC cycle

and converters), highly depend on the demanded DC-link current. The overall power demand by the PMSM and inverter is supplied by the different operating combinations of the engine and battery as described in Equations (8.27)-(8.30). Figures 9.34 and 9.35 show the time histories of the DC-link current for f_{drat} of 2, 4, 5 and 6 and the case when the CVT is installed for two segments of the NEDC cycle, ECE-15 cycles and EUDC cycle, respectively. In Figure 9.34, only the DC-link current for $f_{drat} = 2$ and CVT are shown because the currents in other fixed drive ratios are very closely lying between these two cases.

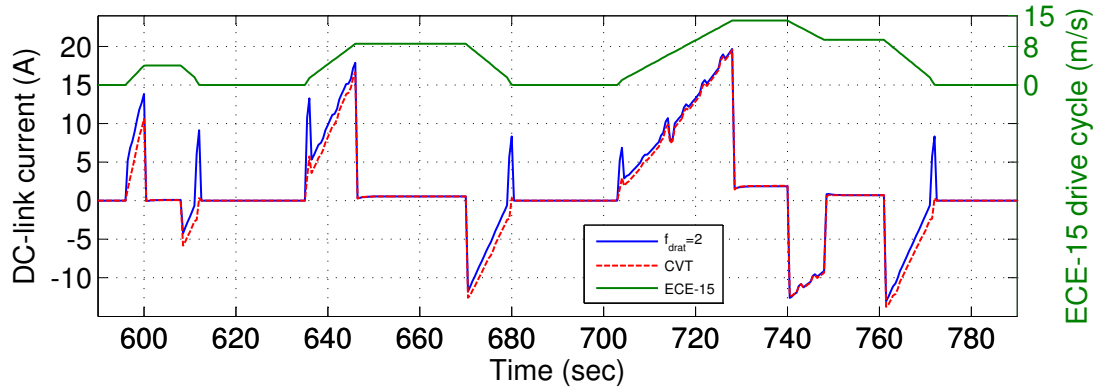


Figure 9.34: DC-link current time history for urban (ECE-15) part of the NEDC drive cycle.

It is evident that when the car accelerates, the current increases positively and conversely while the car is decelerating, regeneration takes place and the current becomes negative. It has also been seen that the car with CVT requires less driving current and produces more regenerative current, as compared to the constant final drive ratio cases, which is consistent with the energy loss reduction brought about by the CVT.

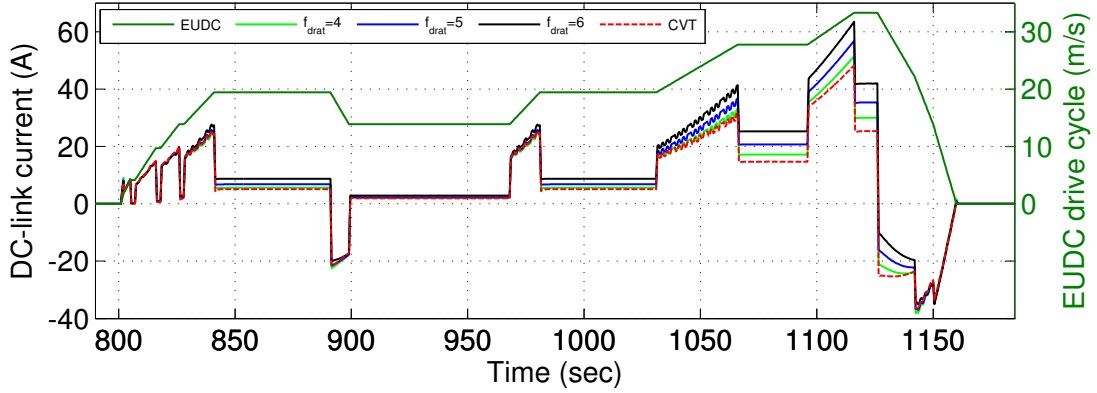


Figure 9.35: DC-link current time history for extra urban (EUDC) part of the NEDC drive cycle.

One more important point can be observed from the simulation, that the regeneration is not possible at every speed level with fixed drive ratio especially at lower values of the speed; for example at 680 sec in Figure 9.34, the DC-link current becomes positive for $f_{drat} = 2$ case. However, in the case of CVT, gear ratios are adjusted in such a way that the maximum regeneration becomes possible at all speeds; for example at 680 sec in same Figure 9.34, the DC-link current remains negative for the CVT case. However, regeneration capability of the PMSM primarily depends on the parasitic elements used in the stator windings.

9.2.2.8 Power splitting at the DC-link

The DC-link current is governed by Equation (8.10), where $i_{og} = i_{dc,gen}$, $i_{ob} = i_{dc,dc}$ and $i_{dc} = i_{dc-link}$, so in steady state, the DC-link current will simply be the sum of the currents fed by the PMSG and the battery $i_{dc-link} = i_{dc,gen} + i_{dc,dc}$ with appropriate multiplication of efficiency factors. Since PMSG gives the power only during the EUDC cycle, for all other time $i_{og} = i_{dc,gen} = 0A$. Figure 9.36 presents the time history of all the three currents during the EUDC cycle. When the $SOC(t)$ of the battery goes below 60% at $t = 831.4$ sec and $t = 1027$ sec, PMSG start supplying all the power demand of the PMSM and charges the battery as well with the rest of the current till $SOC(t)$ of the battery goes above 63%. Now again, from $t = 1096$ sec to $t = 1116.45$ sec,

PMSG alone is providing all the power, but now the battery should not be participating ($SOC > 60\%$) in any kind of power contribution. Still in Figure 9.36, $i_{ob} = i_{dc,dc} \neq 0A$ because during this time the battery along with the DC/DC converter is working as a power buffer, maintaining DC-link voltage constant by supplying and absorbing excess power. Although the battery is doing its task of the power buffer throughout the NEDC cycle, during this time period, this task is clearly visible. This shows that both of the control loops are working perfectly according to the intended jobs assigned to them.

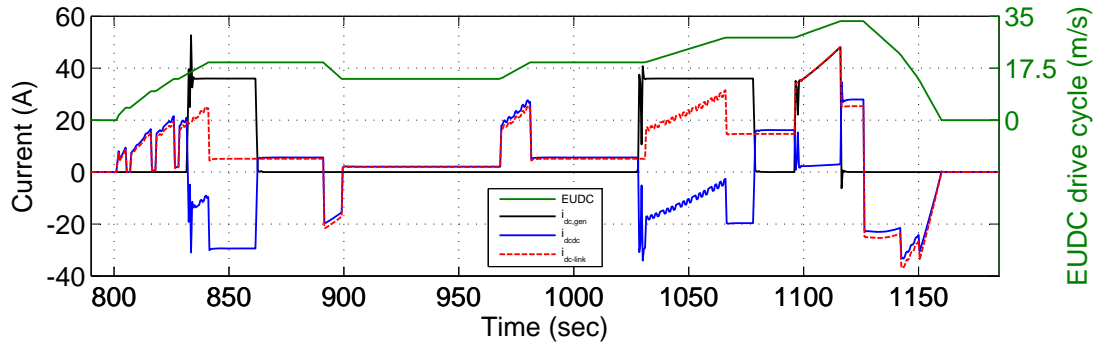


Figure 9.36: Current generated by the PMSG-rectifier($i_{og} = i_{dc,gen}$, by the battery-DC/DC converter $i_{ob} = i_{dc,dc}$ and DC-link load current supplied to the PMSM-inverter combination.

9.2.2.9 Analyzing the dynamic responses of the different variables(v_d ,

v_q , i_d , i_q , T_L and ω_{PMSM}) of the PMSM

Figures 9.37 and 9.38 give the time history of the quadrature current (i_q) in the PMSM during an ECE-15 and EUDC cycle. The quadrature current for the CVT case, during the ECE-15 cycle remains between $-50A$ to $50A$ whereas in the EUDC cycle, between $-100A$ to $100A$. During both the drive cycles, the transient current is small and overall smooth in the case of CVT, whereas in the case of $f_{drat} = 2$, not only the transient but the steady state current are also exceptionally high. During the ECE-15 cycle, the average quadrature current is lowest in the CVT case compared to all other fixed drive ratio cases, but this is not the case during the EUDC cycle. By observing the quadrature current and efficiency of the PMSM during ECE-15 and EUDC cycles it is seen that optimum performance of the HEV powertrain requires separate tuning

for both the drive cycles. Same parameters cannot give the best performance all the time during the two different drive cycles, the ECE-15 (a low speed urban drive) and the EUDC (a high speed extra urban drive). To obtain the best performance of the supervisory controller, decision variables must include speed and acceleration level of the drive cycle as well. Here the need of “a priori” knowledge of the drive cycle to achieve optimum performance is demonstrated which is the most important ingredient of optimization based supervisory control strategies.

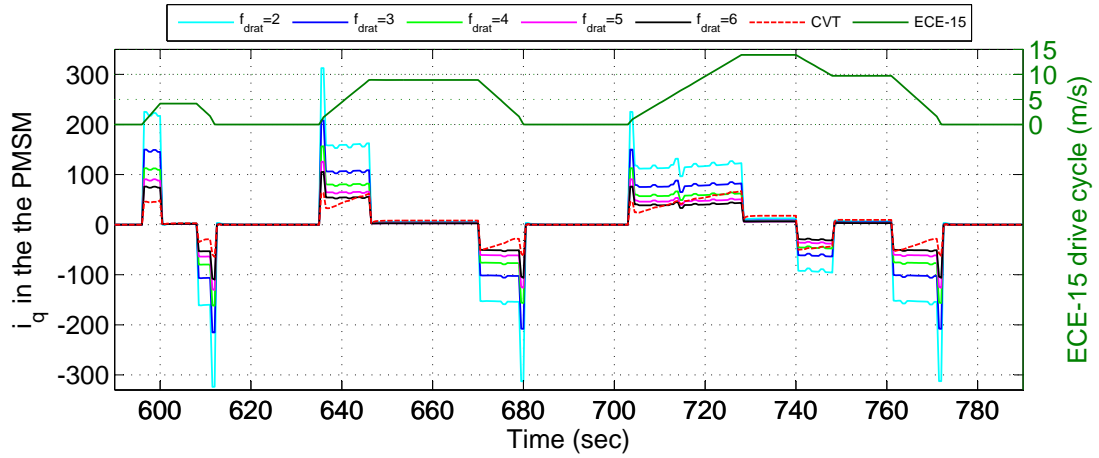


Figure 9.37: Quadrature axis current profile in the PMSM with $f_{drat} = 2, 3, 4, 5, 6$ and CVT implemented car, during the ECE-15 cycle

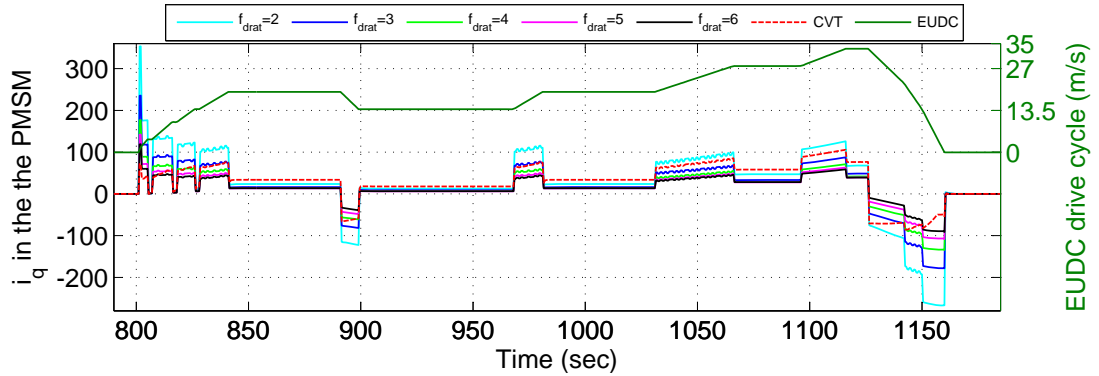


Figure 9.38: Quadrature axis current profile in the PMSM with $f_{drat} = 2, 3, 4, 5, 6$ and CVT implemented car, during the EUDC cycle

Since in the linearized model of the PMSM electromagnetic torque $T_e \propto i_q$, the pattern of the quadrature current is directly translated into load torque applied on the transmission, as shown in Figures 9.39 and 9.40. By further observing Figures 9.41 and

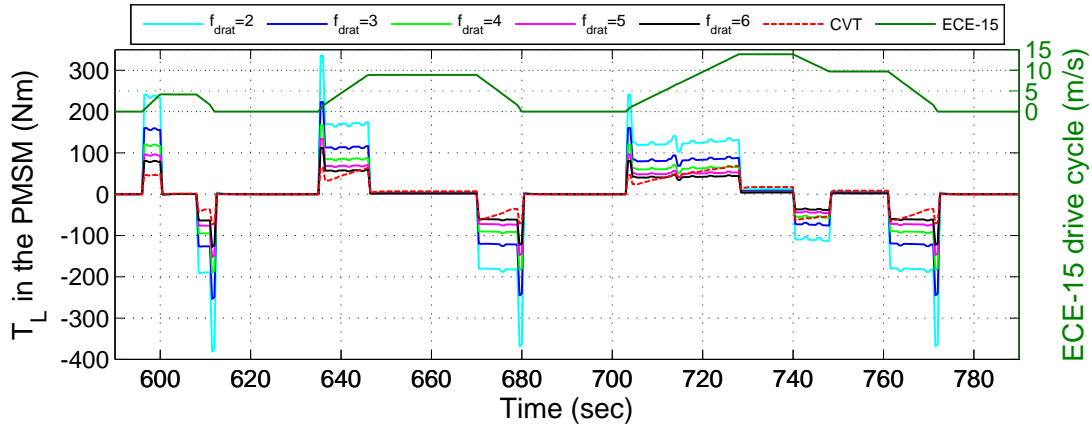


Figure 9.39: Load torque profile of the PMSM with $f_{drat} = 2, 3, 4, 5, 6$ and CVT implemented car, during the ECE-15 cycle

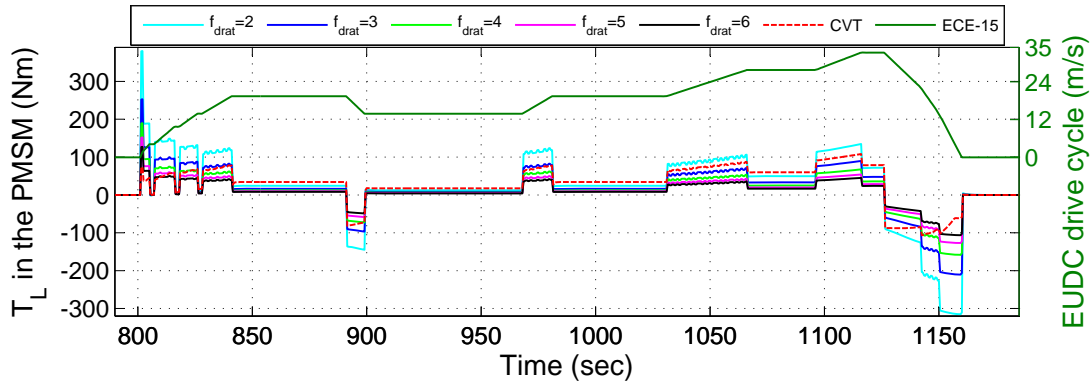


Figure 9.40: Load torque profile of the PMSM with $f_{drat} = 2, 3, 4, 5, 6$ and CVT implemented car, during the EUEDC cycle

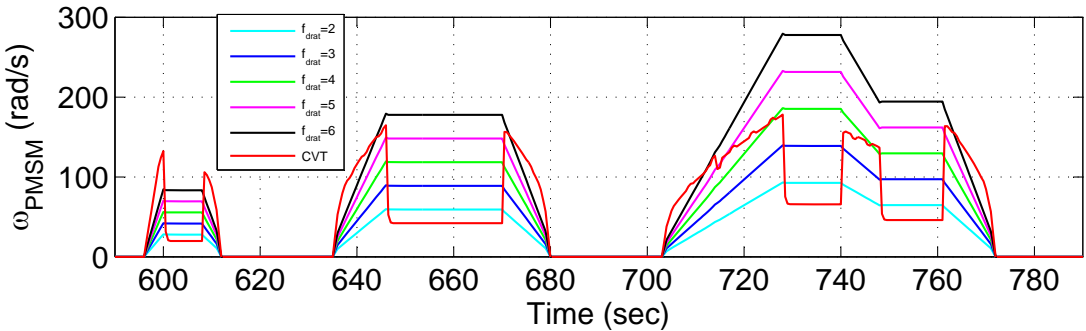


Figure 9.41: Rotational speed profile of the PMSM with $f_{drat} = 2, 3, 4, 5, 6$ and CVT implemented car, during the ECE-15 cycle

9.42, it can be asserted that in the case of CVT, load torque and rotational speed of the PMSM is adjusted in such a way that the efficiency is maximum all the time. At steady state, when power demand is very small in the CVT, the rotational speed is reduced and load torque is increased by changing the drive ratio. The result is that the power can be

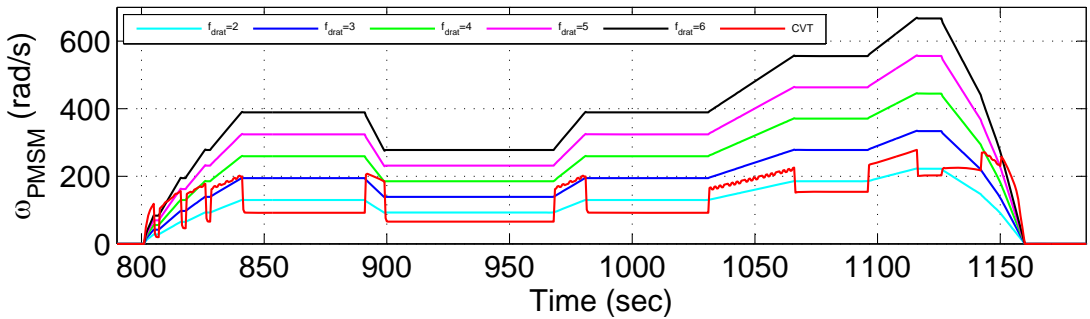


Figure 9.42: Rotational speed profile of the PMSM with $f_{drat} = 2, 3, 4, 5, 6$ and CVT implemented car, during the EUDC cycle

delivered at higher efficiency, as can be seen in Figures 9.30, 9.31 and 9.32. But in the case of fixed drive ratios, this option of adjusting the rotational speed is not available, resulting in efficiency loss.

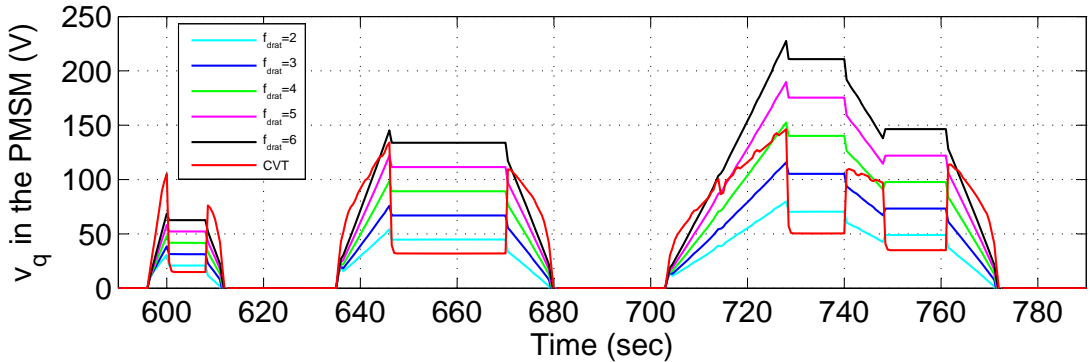


Figure 9.43: Quadrature axis voltage profile of the PMSM with $f_{drat} = 2, 3, 4, 5, 6$ and CVT implemented car, during the ECE-15 cycle

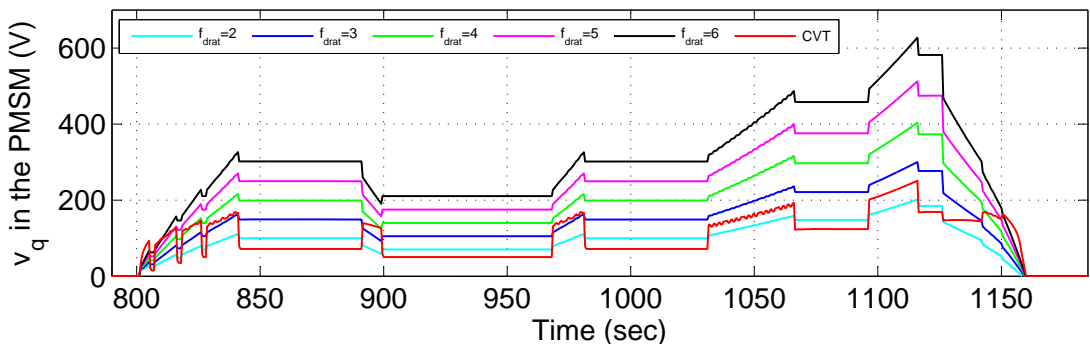


Figure 9.44: Quadrature axis voltage profile of the PMSM with $f_{drat} = 2, 3, 4, 5, 6$ and CVT implemented car, during the EUDC cycle

Figures 9.43 and 9.44 give the time history of the quadrature axis voltage (v_q) in the PMSM during ECE-15 and EUDC cycles. Once again it is evident that in the case

of the CVT, the overall voltage and current transients are minimum and smooth. So, it can be concluded that in the case of CVT, the PMSM used for providing the traction power can be of smaller ratings than used for the fixed drive ratio transmission. Figure 9.45 gives the time history of the direct axis current in the PMSM. According to the desired control point of view, i_d should be zero but due to the dynamic nature of model, there is a deviation during transients. From Figure 9.45, it can be observed that the deviations are there only during transients while at steady state $i_d = 0A$. Even during deviations, the value of the i_d is very small in comparison to i_q , so it is acceptable.

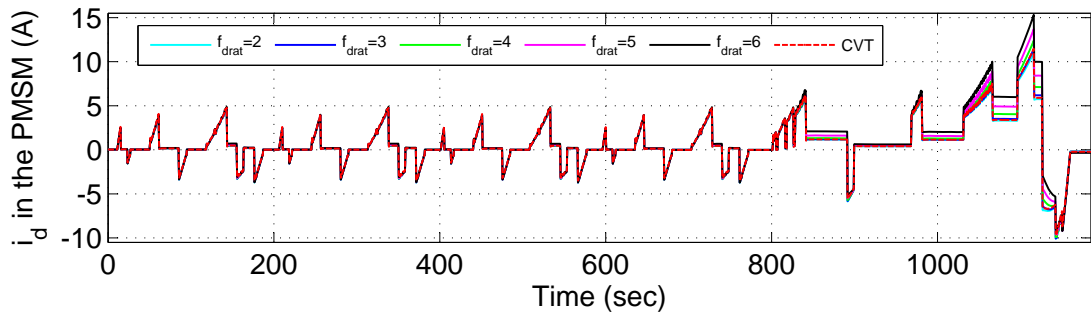


Figure 9.45: Direct axis currents profile in the PMSM with $f_{drat} = 2, 3, 4, 5, 6$ and CVT implemented car during NEDC cycle

9.2.2.10 Analyzing the dynamic responses of the different variables(ϕ ,

v_{bat} , i_{bat} , SOC and energy of the battery

The DC-link current is calculated by the $d - q$ axis voltages and currents as described in Equation (8.10). When the DC-link current is positive, power is flowing from the DC-link to the PMSM and subsequently to the wheels of the car. When there is regeneration, the DC-link current is negative and power flows back from DC-link to the battery to recharge it. This bidirectional flow of the power from the DC-link is made possible by having a bidirectional DC/DC converter. Change in the direction of the power flow is possible by changing the sign of the phase shift angle ϕ in the model of the DC/DC converter, as shown in Figure 9.46. The terminal voltage of the battery in reality is expected to increase with the charging and decrease with the discharging, as seen in Figure 9.47.

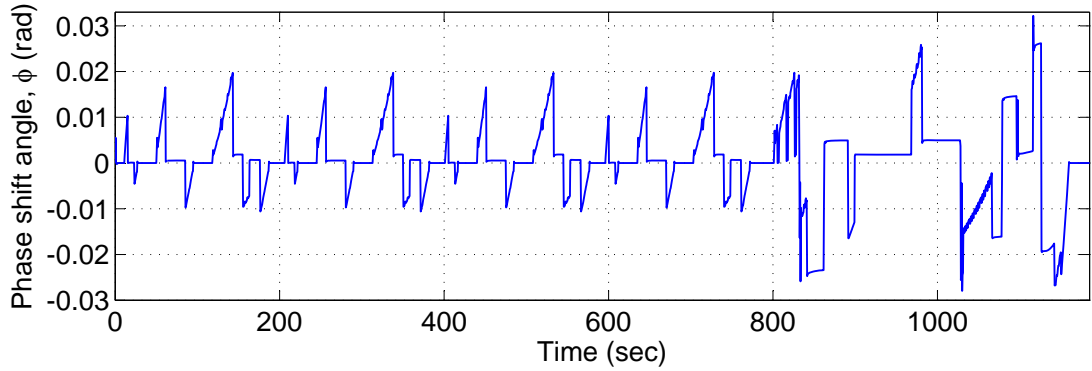


Figure 9.46: Phase shift angle of the DC/DC converter during complete NEDC cycle. Positive phase shift angle stands for discharging of the battery and negative stands for charging by both the regeneration and engine-genset charging.

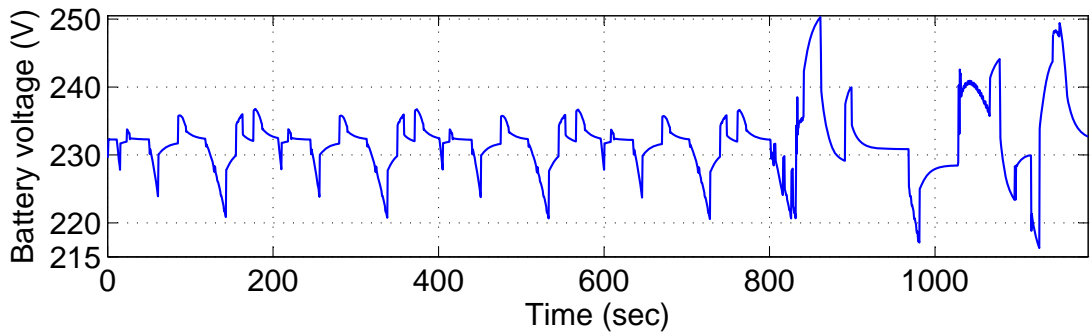


Figure 9.47: Time history of battery voltage during the complete NEDC cycle

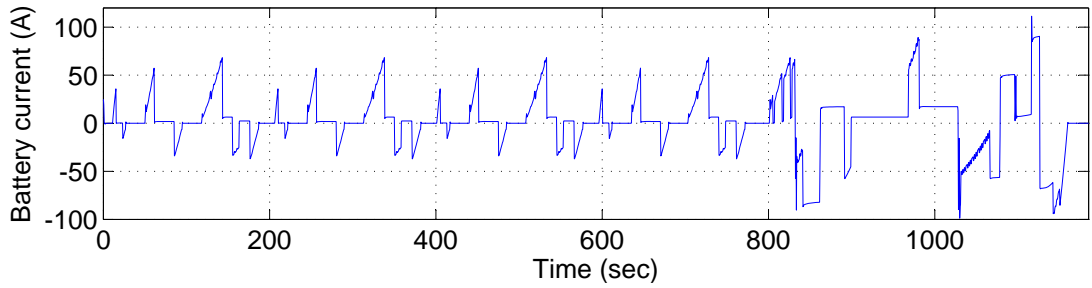


Figure 9.48: Time history of battery current during the complete NEDC cycle

There is one very interesting fact which can be observed in regard to the effect of final drive ratio on the battery performance. From Figures 9.49, 9.50 and 9.53, it can be clearly observed that $f_{drat} = 2$ discharges and charges the battery very heavily in comparison to all the transmission cases. This heavy charging and discharging also leads to high resistance losses in the battery as can be seen in Figure 9.51. However, from the Figure 9.52 it can be asserted that this strategy of fierce charging and discharging finally ends up having lower energy consumption in the case of $f_{drat} = 2$. But it is a

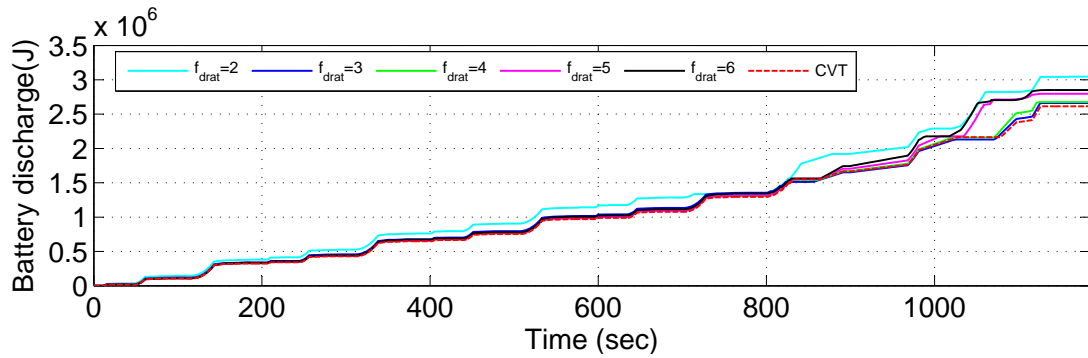


Figure 9.49: Time history of the energy discharged by the battery, in the powertrains having fixed gear ratios ($f_{drat} = 2, 3, 4, 5, 6$) and CVT, during the complete NEDC cycle

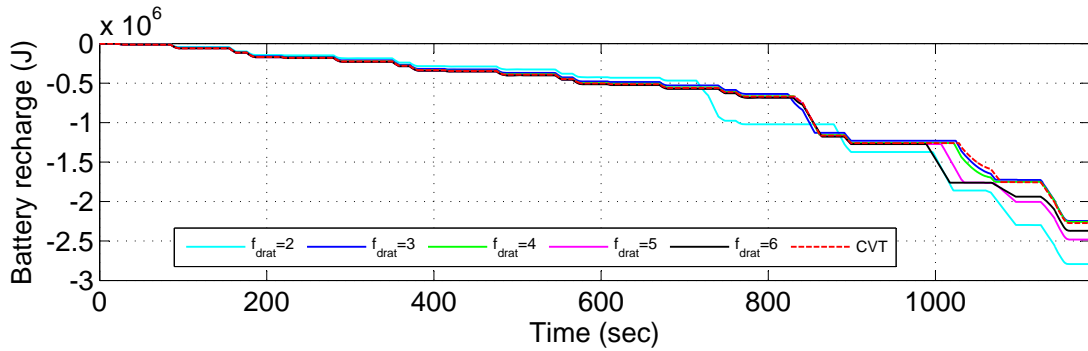


Figure 9.50: Time history of the energy recharged to the battery (contribution comes both from engine recharging and regeneration as well), with the powertrains having fixed gear ratios ($f_{drat} = 2, 3, 4, 5, 6$) and CVT, during the complete NEDC cycle

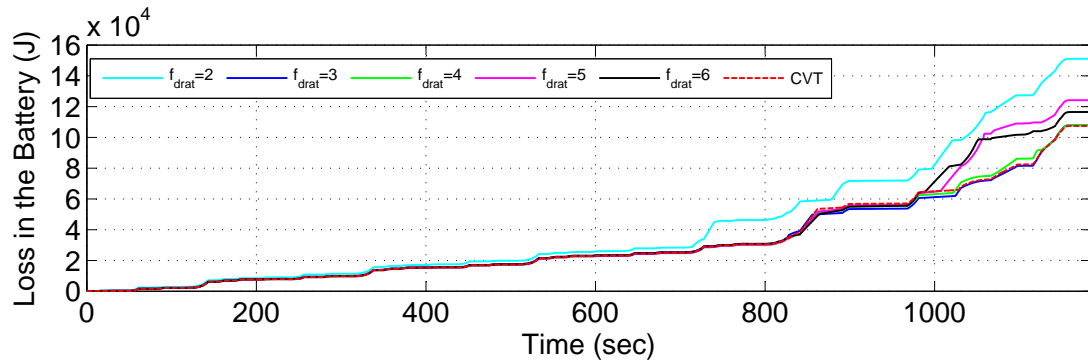


Figure 9.51: Time history of the energy loss due to internal resistance of the battery, with the powertrains having fixed gear ratios ($f_{drat} = 2, 3, 4, 5, 6$) and CVT, during the complete NEDC cycle

well known fact from practical point of view that, steep charging-discharging pattern damages the battery performance in the long run and ultimately reduces the life cycle of the rechargeable battery. However, in present battery model prediction of battery life cycle is ignored but it can be interesting issue for future research. By observing

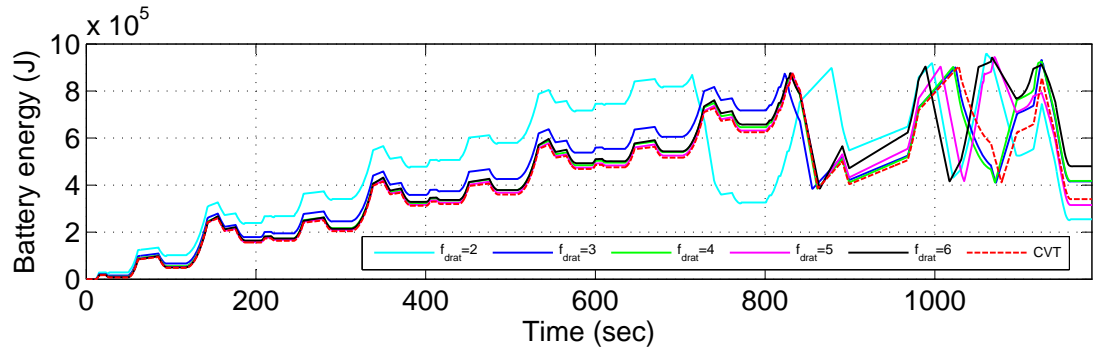


Figure 9.52: Time history of the total battery energy level, with the powertrains having fixed gear ratios ($f_{drat} = 2, 3, 4, 5, 6$) and CVT, during the complete NEDC cycle

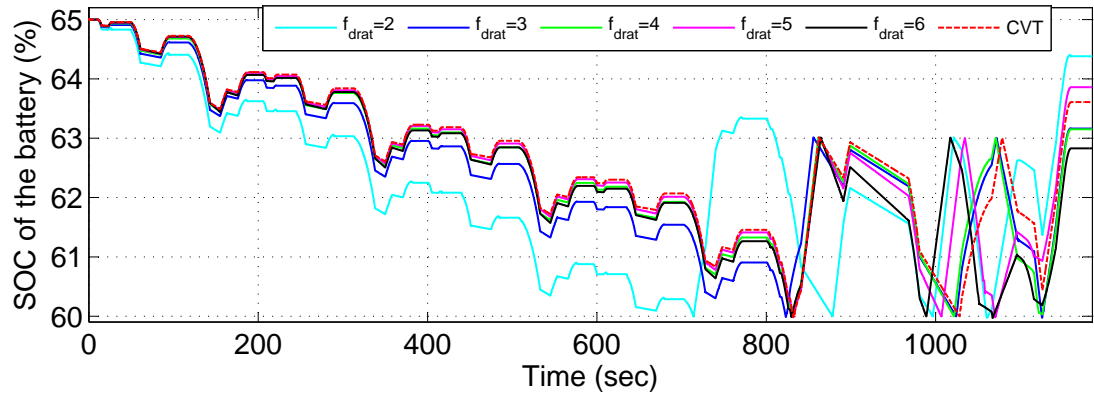


Figure 9.53: Time history of the SOC of the battery, with the powertrains having fixed gear ratios ($f_{drat} = 2, 3, 4, 5, 6$) and CVT, during the complete NEDC cycle

Figures 9.49, 9.50, 9.51, 9.52 and 9.53, it can be concluded that in the case of CVT installed powertrain the battery is charged and discharged with best moderate possible way, leading to higher battery life cycle in the long run.

9.2.2.11 Analyzing the dynamic responses of the different variables(v_d , v_q , i_d and i_q) of the PMSG

According to the supervisory control, when the DC-link current becomes very high or the SOC of the battery goes below 60%, the engine-genset comes to feed the total power demand by the PMSM. According to the present control, engine and generator are coupled together. A standard vector control technique is used to linearize the PMSG in order to design the power split control loop, as in the case of PMSM, the speed control loop was designed. Since the battery alone is able to support the

PMSG power demand for all the four ECE-15 parts, the PMSG comes to support the powertrain only during the final EUDC part of the NEDC cycle. Figures 9.54, 9.55, 9.56 and 9.57 give the time histories of the $d - q$ axis currents and voltages of the PMSG. Since the demand of the DC-link current is minimum in the CVT installed machine, the quadrature current and voltage are also minimum, as can be seen in Figures 9.54 and 9.56.

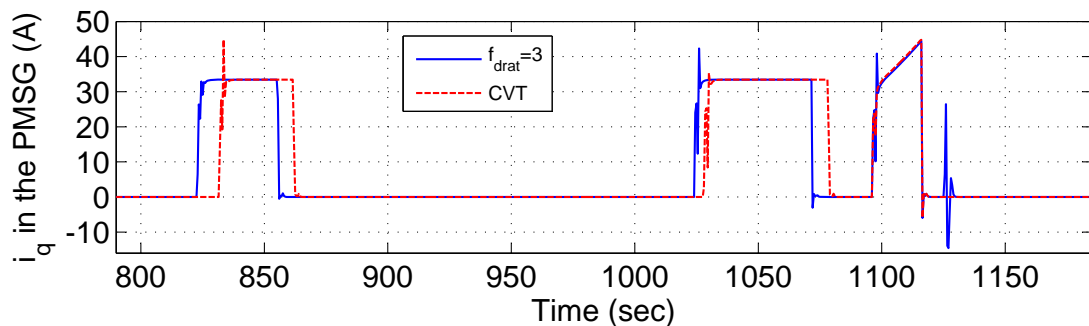


Figure 9.54: Time history of quadrature axis current i_q in the PMSG during the EUDC cycle

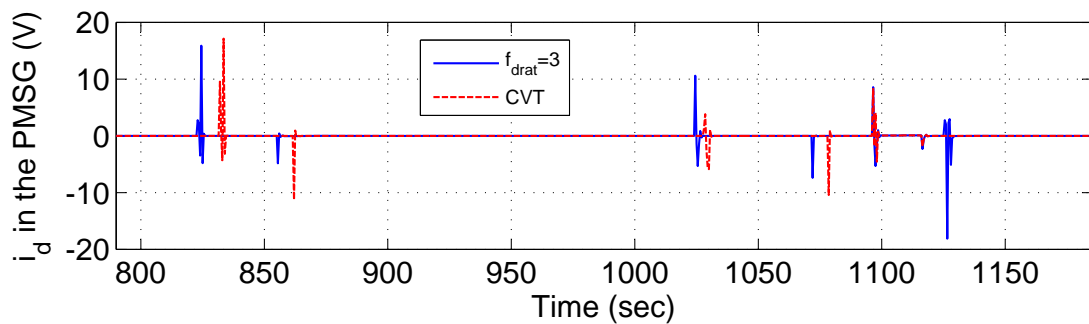


Figure 9.55: Time history of direct axis current i_d in the PMSG during the EUDC cycle

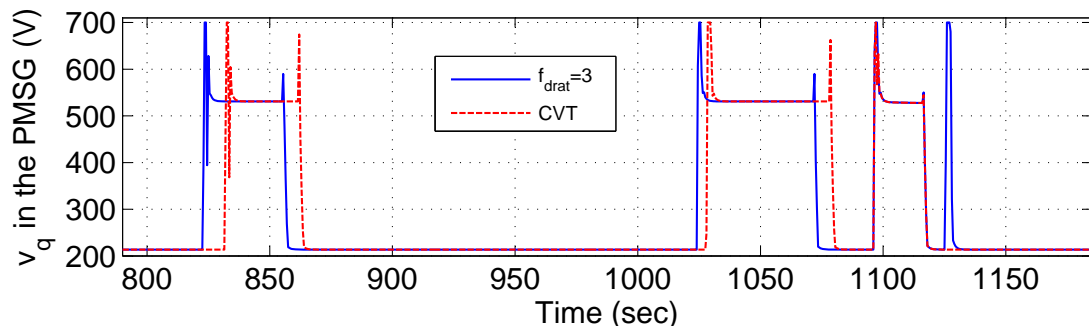


Figure 9.56: Time history of quadrature axis voltage v_q in the PMSG during the EUDC cycle

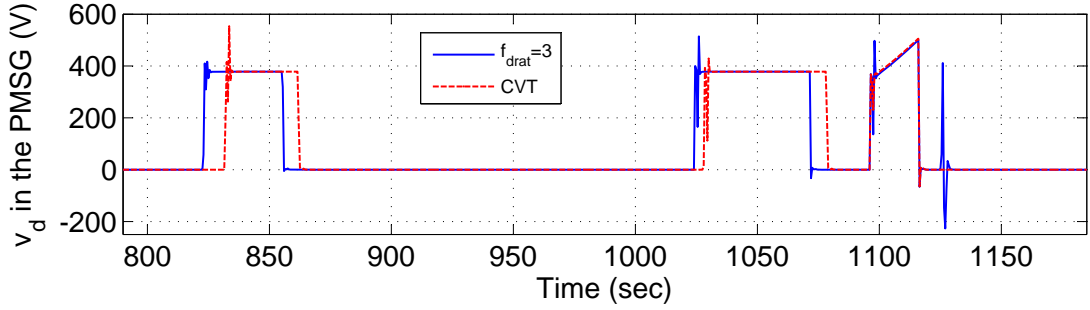


Figure 9.57: Time history of direct axis voltage v_d in the PMSG during the EUDC cycle

9.2.2.12 Analyzing the dynamic responses of the different variables (T_{eng} , $T_{eng,fric}$, T_{load} , ω_{rg} , ω_{eng} , ω_{tc} , $w_{ie,air}$, w_{fuel} and λ) of the turbocharged diesel engine

Mean-value model of the engine described in Chapter 6 is integrated with the rest of the powertrain and detailed analysis of transient simulation results are discussed in this section. When the powertrain is supplied with the NEDC drive cycle for tracking, the driver model calculates the required torque to be generated by the PMSM, and subsequently, the PMSM demands the required power to be supplied by the inverter. The inverter is connected to the DC-link and the DC-link is fed by two power sources, the engine and battery. Supervisory control strategy supplies the required commands to operate the engine and battery, depending on the available states of the power sources and operating conditions known as decision variables.

Since the engine friction is the reason for the prominent energy loss in the overall powertrain, to alleviate this power loss, two speed levels are chosen for engine operation. Whenever the engine supplies power to the DC-link, the engine operates at $\omega_{operating} = 2000$ rpm and when it is not used for the power supply, it keeps on idling at $\omega_{idling} = 800$ rpm. As a general rule for HEV operation, the battery and engine are used for lower and high power demands, respectively. When the battery alone is supplying all the required power to the DC-link, the engine is operated in idling mode. In idling mode, the engine generates indicative torque T_{eng} , just sufficient to sustain the idling speed by overcoming all the frictional torques of the engine and generator

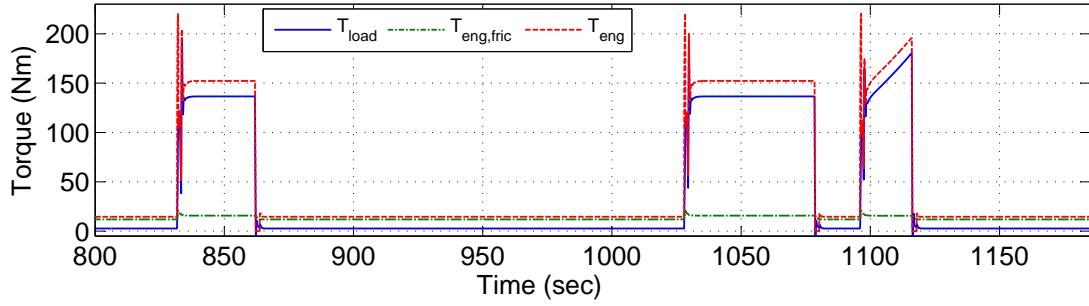


Figure 9.58: Time history of the various torques such as the indicative torque T_{eng} , the engine friction torque T_{fric} and the load torque T_{load} . The load torque T_{load} is a combination of the electromagnetic torque and the friction torque at the generator shaft

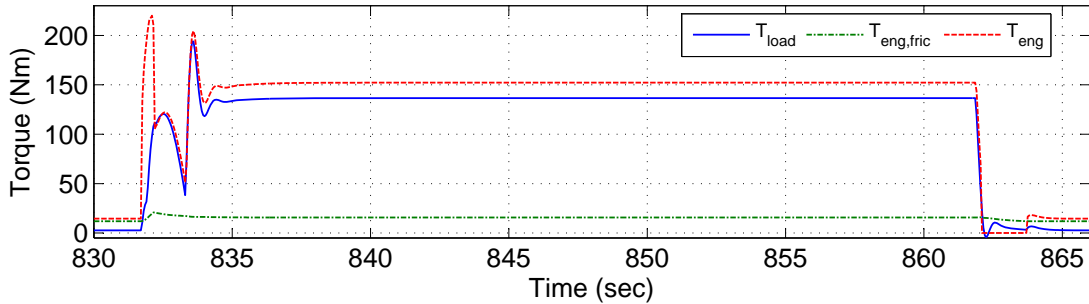


Figure 9.59: A closer look at the first part of the transient dynamics of the various torques such as the indicative torque T_{eng} , the engine friction torque T_{fric} and the load torque T_{load} .

together. There are mainly three different occasions when the engine supplies power to the DC-link; when the engine charges the battery, when the engine alone supplies all the power to the DC-link and when the engine is assisted by the battery to meet extremely high power demands of the HEV powertrain. Demand of the high load current at the DC-link gets translated into high load torque applied on the engine shaft and at the high load torque fuel conversion efficiency of the engine is maximum around 40%. Figure 9.58 gives the time history of the engine friction torque T_{fric} , load torque T_{load} and indicative torque T_{eng} in the IC engine during the EUDC part of NEDC cycle (during all the four ECE-15 cycles engine remains in idling mode). Torque generation in the engine is controlled by the amount of fuel injection inside the engine cylinder.

According to the supervisory control, when the engine is asked to supply the required power, engine speed is switched from 800 rpm to 2000 rpm. This step change in the reference speed demands a heavy transient in T_{eng} , clearly visible in Figure 9.58.

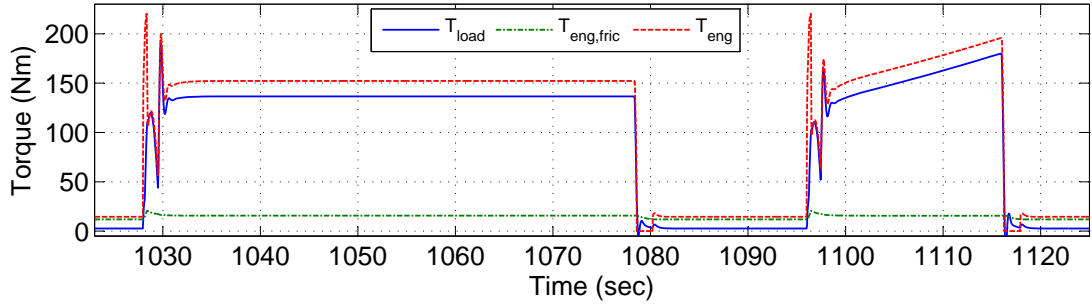


Figure 9.60: A closer look at the second part of the transient dynamics of the various torques such as the indicative torque T_{eng} , the engine friction torque T_{fric} and the load torque T_{load} .

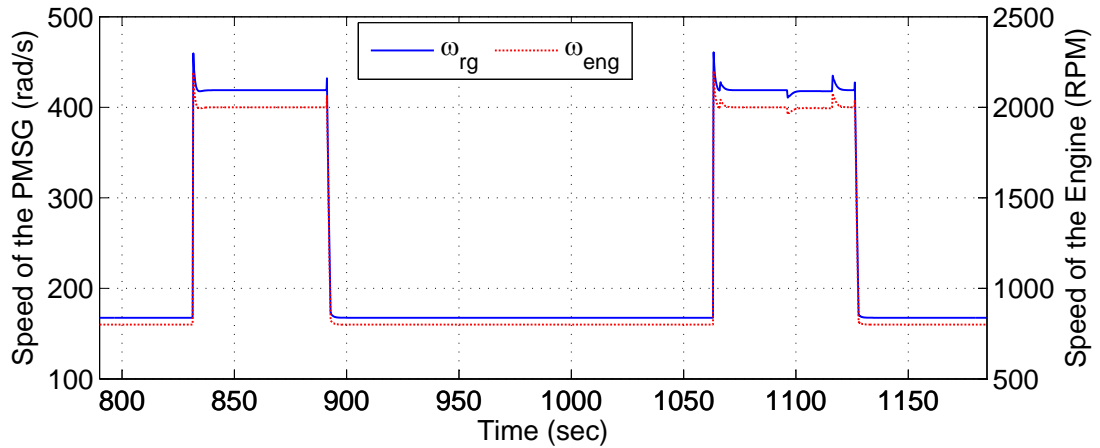


Figure 9.61: Time history of the rotational speed of the PMSG (ω_{rg}) and the engine shaft (ω_{eng}), which are coupled together with a constant gear ratio ($G = 2$) during the EUDC cycle

Figures 9.59 and 9.60 are presented to give closer views of various torques involved in the operation of IC engine for the first and the second part of the transient responses during the EUDC cycle. Figure 9.61 presents the speed profile of the engine-shaft and generator shaft connected through a constant gear ratio ($G = 2$). Speed difference ($\Delta\omega = \omega_{desired} - \omega_{actual}$) is sometimes positive and sometimes negative. For example, when $\omega_{desired} = 2000$ rpm & $\omega_{actual} < 2000$ rpm, it is positive and when $\omega_{desired} = 800$ rpm & $\omega_{actual} > 800$ rpm, it is negative. This speed difference is fed to the PID controller of the fuel amount control unit to calculate the required amount of fuel to be burned to make this speed difference zero. At positive speed difference, the controller tries to push the positive amount of fuel inside the engine cylinder to overcome the load torque while trying to maintain the desired speed level constant. But again, whenever

the speed difference becomes negative, the PID controller tries to put negative amount of fuel to decelerate the engine-shaft. Due to saturation, this is not possible.

Figure 9.62 presents the fuel-mass ($w_{fuel,cal}$) calculated by the PID controller and the actual fuel-mass (w_{fuel}) injected inside the cylinder. Theoretically $w_{fuel,cal}$ can be negative as it is just a mathematical variable calculated by the PID controller but actual fuel injection w_{fuel} can not be negative as shown in figure 9.62. Due to calculation of negative fuel amount, the integrator of the PID controller used to get saturated negatively. An anti-windup loop is designed to overcome this limitation. This fuel amount w_{fuel} is used to calculate λ by which the torque required (T_{eng}) to track the NEDC cycle is generated.

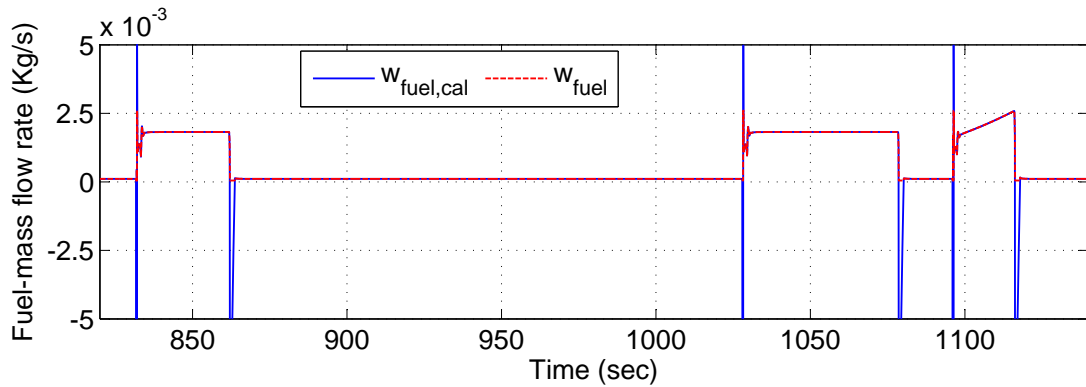


Figure 9.62: Transient time history of the calculated fuel-mass flow rate ($w_{fuel,cal}$) and the actual fuel-mass flow rate (w_{fuel}) during the EUDC cycle

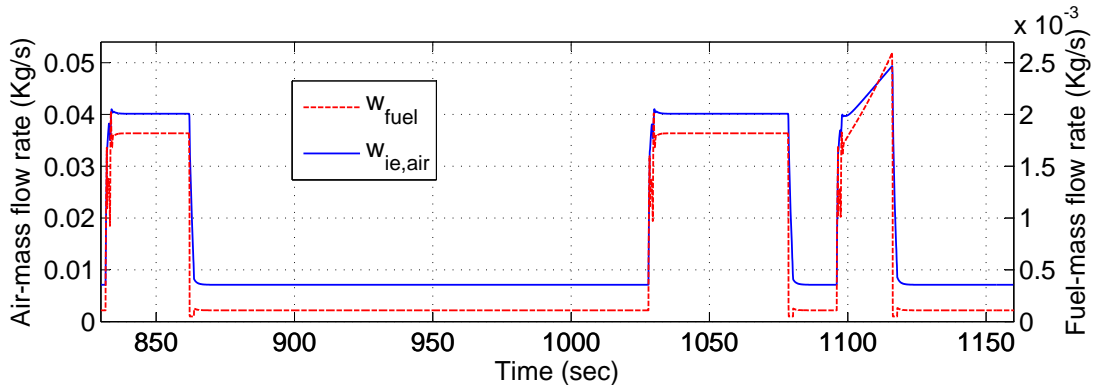


Figure 9.63: Transient time history of the air mass flow rate ($w_{ie,air}$) and the fuel-mass flow rate (w_{fuel}) during the EUDC cycle

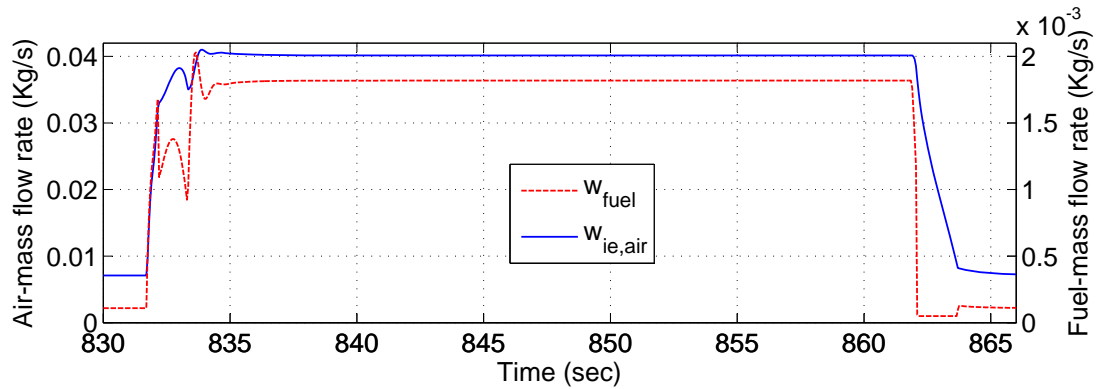


Figure 9.64: A closer look at the first part of the transient dynamics of the air mass flow rate ($w_{ie,air}$) and the fuel-mass flow rate (w_{fuel}) during the EUDC cycle

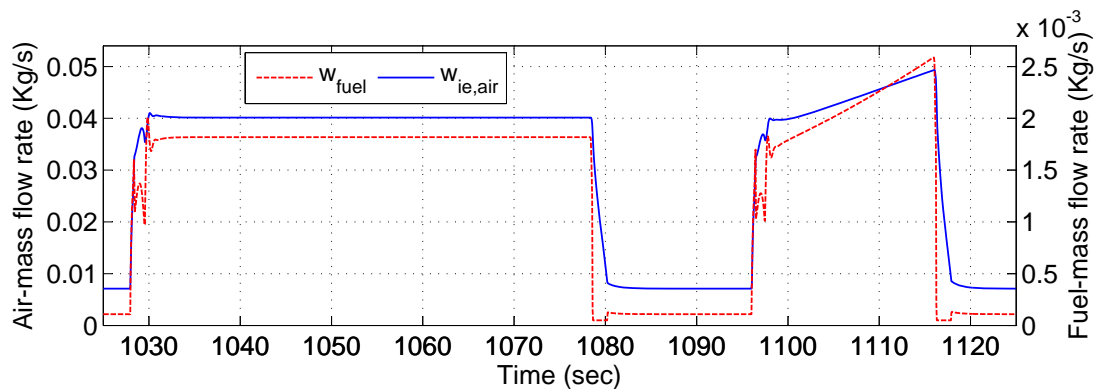


Figure 9.65: A closer look at the second part of the transient dynamics of the air mass flow rate ($w_{ie,air}$) and the fuel-mass flow rate (w_{fuel}) during the EUDC cycle

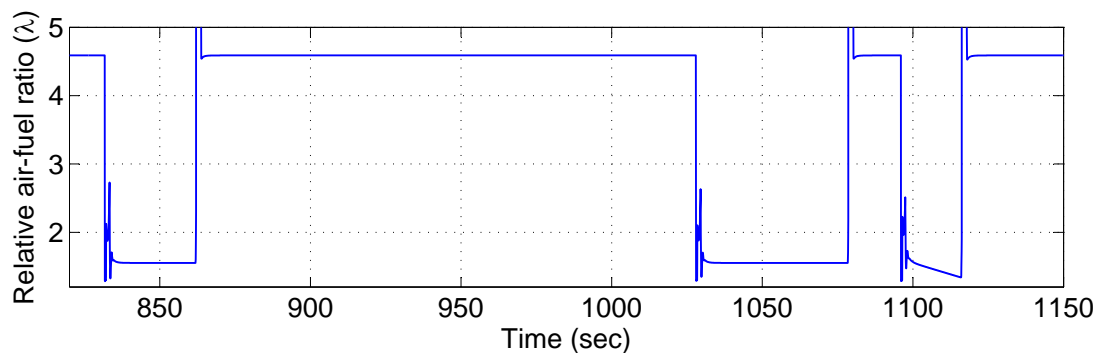


Figure 9.66: Time history of the relative air-fuel ratio (λ) during the EUDC cycle

Figure 9.63 presents the time history of the air-mass flow rate and the fuel mass flow rate through the EUDC cycle. Since time scale for the EUDC cycle is around 400 sec, air-mass flow and fuel-mass flow dynamics look instantaneous. Figures 9.64 and 9.65 are presented to give a closer view of the mass flow rates. When there is a sudden demand of torque, in response to this demand, fuel is injected in the cylinder at

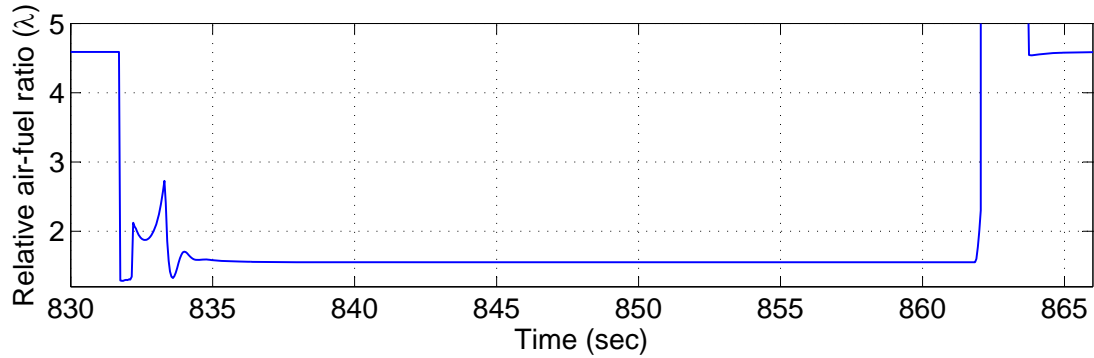


Figure 9.67: A closer look at the first part of the transient dynamics of the relative air-fuel ratio (λ) during the EUDC cycle

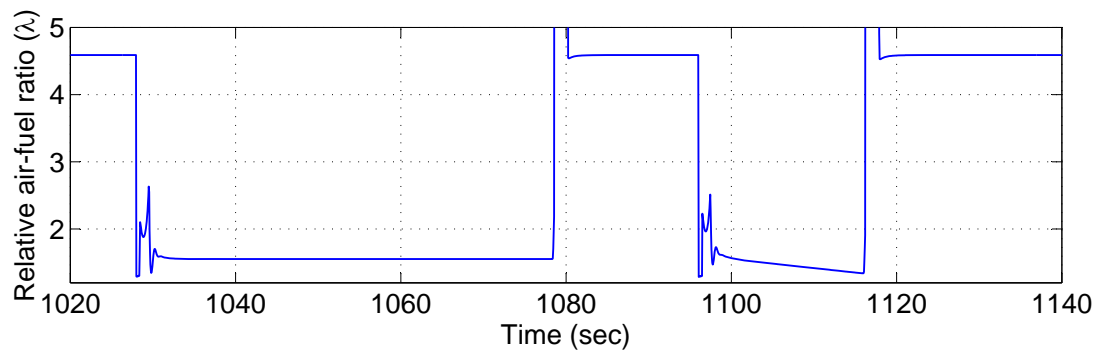


Figure 9.68: A closer look at the second part of the transient dynamics of the relative air-fuel ratio (λ) during the EUDC cycle

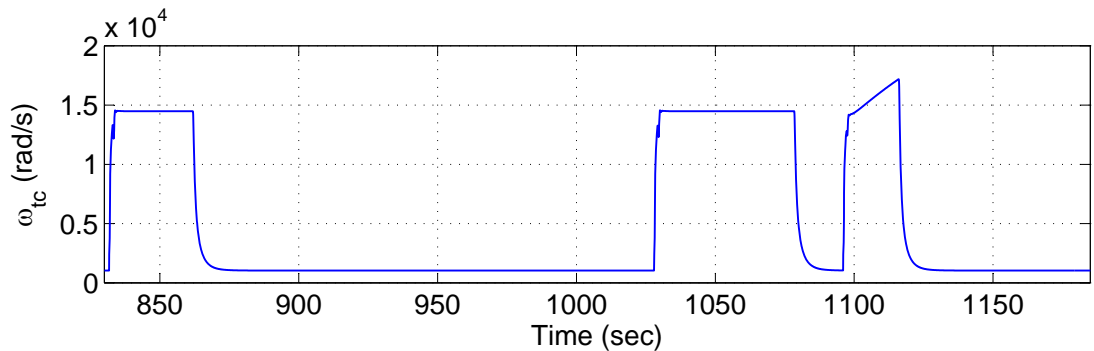


Figure 9.69: Transient time history of the rotational speed of the turbo-shaft (ω_{tc}) during the EUDC cycle

very fast rate. Due to an already existing lean mixture, there is sufficient air to burn the injected fuel. Due to injection of the fuel, relative air-fuel ratio (λ) decreases because the dynamics of the air-mass flow is much slower than the fuel injection. Dynamics of the air-mass flow depends on the turbocharger's speed, which takes some time to increase its speed for supplying sufficient air to keep burning the increased injected

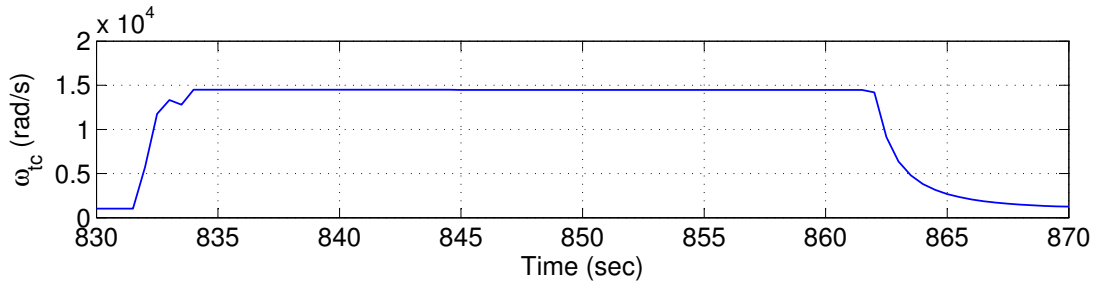


Figure 9.70: A closer look at the first part of the transient dynamics of the rotational speed of the turbo-shaft (ω_{tc}) during the EUDC cycle

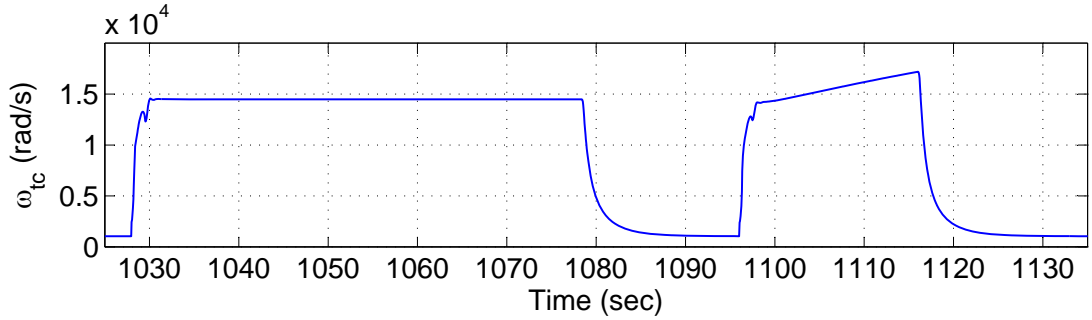


Figure 9.71: A closer look at the second part of the transient dynamics of the rotational speed of the turbo-shaft (ω_{tc}) during the EUDC cycle

fuel amount. Figures 9.66 and 9.69 show the dynamics of the relative air-fuel ratio (λ) and rotational speed of the turbo-shaft (ω_{tc}), respectively, during the EUDC cycle. To limit emissions beyond certain acceptable level a minimum allowable value of air-fuel ratio is set to ($\lambda_{min} = 1.3$). This restriction on the value of air-fuel ratio is complied by successfully implementing a control scheme described in Section 6.5.2. Once again, Figures 9.67, 9.68, 9.70 and 9.71 are presented to give closer views of the relative air-fuel ratio and the turbocharger speed for the first and the second part of the transient response for the EUDC cycle.

9.3 Summary of the results

- Two supervisory control strategies namely ‘thermostat supervisory control strategy’ (TSCS) and ‘load follower supervisory control strategy’ (LFSCS) have been implemented over detailed dynamic model of the series hybrid electric

powertrain.

- With every supervisory control strategy total six different simulations are performed, in five of which, the car has fixed final drive ratios of 2, 3, 4, 5 and 6, and in one, it has variable transmission ratio provided by the CVT. The NEDC drive cycle is supplied for testing the supervisory control strategy in all cases. The speed tracking in all cases is accurate and the average error in the tracking is in the order of 10^{-4} m/s.
- With the usage of the TSCS car with the CVT installed outperforms all other cases, giving reduction of 1.42% and 1.12% in the total energy and total fuel consumption respectively, as compared to the best case of fixed final drive ratio, $f_{drat} = 3$.
- Under the effect of the LFSCS, CVT led HEV powertrain is 3.52% more efficient in terms of total energy than its closest competitor case of fixed final drive ratio, $f_{drat} = 3$. In terms of fuel consumption also CVT led HEV powertrain is 1.72% more efficient, as compared to the best case of fixed final drive ratio, $f_{drat} = 3$.
- If only losses in the PMSM are compared, the CVT case is almost 100% better than the $f_{drat} = 3$. If the total energy entering in to the inverter from the DC-link is compared in all the different cases of simulations, the CVT case gives the best performance of 2.56% reduction in comparison to best energy efficient case of fixed gear $f_{drat} = 3$.
- With the implementation of the novel DC-link control strategy, where power splitting control loop is integrated with the PMSG-drive controller and the DC-link voltage control is integrated with the DC/DC converter, the maximum deviation of the DC-link voltage throughout the NEDC cycle is around 0.046%.
- Performance of the battery and DC/DC converter is observed and found in accordance with the standard performance; For example change in the direction

of the power flow is exhibited by changing the sign of the phase shift angle ϕ in the model of the DC/DC converter and change of the terminal voltage of the battery with the charging and discharging.

- Transient performance of the turbocharged diesel engine is observed and closely resemble the real behavior of the engine; for example fast dynamics of the fuel-mass flow and slow dynamics of the air-mass flow (due to its dependence on the turbocharger dynamics) are very realistic in the nature.
- The overall results presented in this chapter, with high fidelity model of the HEV powertrain, indicates in the direction of ample opportunities to optimize the performance of the HEV powertrain by having access to the dynamics of the system at component level itself.

These kinds of transients are produced due to interactions of the dynamic components. Implementation of the control and ratings of the components highly depend on the understanding of the real dynamic nature of the individual components. Static maps and charts based model do not capture these transient behaviors and detailed dynamics, so the implementation of real control at components is not possible.

CHAPTER

TEN

CONCLUSIONS AND FUTURE WORK

10.1 Conclusions

Hybrid Electric vehicles contain different electrical, mechanical and electrochemical components in one powertrain. These components are modelled mathematically and simulated on the Matlab/Simulink platform. The detailed mathematical modelling is supposed to give more accurate and realistic results than simple steady-state based modelling. Dynamics of a component is very important in understanding its fundamental nature and behavior. Mathematical equations based models are not only close to reality but also give more flexibility in designing novel component level controllers. Maps and charts based models give very little insight and flexibility at the component level. Therefore, dynamic modelling in the present work is not merely an academic exercise but also the satisfaction of a need for ongoing research in the direction of better understanding and modelling the HEV problem.

In the present work, most of the models are designed on the basis of fundamental physics and mathematics; but definitely not for every single process and component involved in the operation of the HEV powertrain, such as, combustion and PWM

switching. Therefore a trade off has been made between the detailed and the average modelling approach. This trade off has been decided on the basis of the very modelling purpose. For example, combustion modelling of fuel is not included in the present engine model because of its fast dynamics and inability to participate in any kind of external control process. The same can be said about the dynamics of the PWM switchings, which generally lies in the order of KHz whereas the longitudinal dynamics of the car is in the order of few Hz. So, a modelling of such fast dynamic processes does not contribute either in the control strategy or in energy calculation, rather only complicating the model from the computational point of view. The present model with the current level of complexity takes almost 3 hours to simulate one full NEDC cycle and inclusion of more details about physical processes will further lengthen the simulation time.

Mathematical models that are believed to provide accurate prediction of hybrid electric vehicle dynamic response are presented in this work. A series powertrain topology is considered by integrating the relevant component models into an overall dynamic model that includes control systems for the individual components, a supervisory controller for the management of the power flow, and a driver model for the execution of drive cycle tracking simulations. Regenerative braking is also accommodated by utilizing bidirectional electronic converters with reverse operation of the permanent magnet synchronous motor that normally drives the car.

Simulation results for different transmission configurations, in which the car follows the standard test drive cycles, are presented. The power losses in the various components are quantified and their relative magnitude and importance is understood. The model is qualified for the overall balance of the energy, entering and leaving the HEV. It is demonstrated that the use of a continuously variable transmission helps to reduce the overall energy required to complete the full drive cycle, thus leading to fuel savings. The CVT control scheme is informed by a novel power loss model of the PMSM in which a speed-dependent frictional torque is included to capture the eddy

current, hysteresis and mechanical losses. Overall, the modelling work has the potential to act as a platform for the development of sophisticated supervisory controllers that bring further fuel savings and enable overall design optimization of the car and its powertrain.

The overall accomplishments of my PhD research work can be summarized in the following points:

1. Using a first-principles approach, the constituent components of a series hybrid electric car are modelled and subsequently integrated to form an overall coupled dynamic model.
2. The powertrain comprises a diesel engine and a common DC-link of 700V, on which a Permanent Magnet Synchronous Generator (PMSG) with the associated AC/DC converter, a Permanent Magnet Synchronous Motor (PMSM) with the associated DC/AC converter and a battery with the associated DC/DC converter are connected.
3. A control oriented 0D dynamic model of the turbocharged diesel engine has been built while preserving the simplicity and accuracy of the predictions. This engine model involves inlet manifold, exhaust manifold, engine cylinder and turbocharger. The maximum error for the fuel consumption rate prediction, over the complete range of available data, is 6.54% (this error is calculated on the flow rate of kg/sec).
4. To predict the accurate dynamic behavior of the battery, a generic dynamic Li-ion model has been chosen which expresses the electrochemical parameters of the battery directly in terms of electrical parameters of the circuit.
5. Controllers for the individual components are constructed, and are combined with a supervisory controller and driver model to enable simulation of the vehicle under general operating conditions.

6. Every component modelled in the current project is first validated standalone against the experimentally available data and the data available in the published literature.
7. Two supervisory control strategies namely ‘thermostat supervisory control strategy’ (TSCS) and ‘load follower supervisory control strategy’ (LFSCS) are implemented. Under the effect of the TSCS, CVT led HEV powertrain gives reduction in the total energy and fuel consumption by 1.42% and 1.12% as compared to the best case of fixed final drive ratio, $f_{drat} = 3$, and with the LFSCS these reductions are 3.52% and 1.72% respectively.
8. Software used during this project are Matlab, Simulink, Sfunction, State-flow charts, AutoSim, C/C++ in Microsoft Visual Studio, TableCurve2D-3D and Ricardo-Wave for engine simulation. Many modelling tools are reviewed during the research such as PSAT, AVL cruise, Simdriveline, Simscape, AMESim, dymola, modelica, least square method and parametric curve and surface fitting tools.

10.2 Novel Contributions

The novelty of the present work is depicted by the dynamic response of all the components involved in the powertrain of HEV. Although detailed mathematical models of many components were already present in the literature for different research purposes in their corresponding fields, it is for the first time that all these components along-with their dynamics are integrated together to realize a single HEV powertrain.

Integration of the mathematically modelled components brings challenges on various issues like complexity of the overall power train, compatibility of different components with each other, suitable control architecture at various levels of the powertrain and feasibility of overall fast simulation in acceptable time domain. DC-link voltage control, CVT control, Dynamic IC engine control and implementation of the

supervisory control (TSCS and LFSCS) to such a detailed dynamic model of the series HEV are some of the outstanding contributions to the present research field of the HEV modelling and simulation. This work also presents the forward facing modelling platform for HEV, which can be improved and extended to other powertrain structures (such as series-parallel hybrid) later on. Application of different optimization techniques and its comparisons will be part of the future research on the basis of the present work.

The contribution in summary are:

- There is a novel attempt to present a general mathematical dynamic model for all the components of a series HEV in a single powertrain.
- Use of static or numerical tables has been avoided where possible to make modelling more general, flexible and dynamic.
- A novel frictional torque model is proposed to quantify various electrical and mechanical losses to its utmost accuracy in the PMSM and PMSG.
- A novel DC-link control model is presented to enable the dynamically controlled hybrid mode operations of the HEV powertrain.
- A novel 0D control oriented dynamic turbocharged diesel engine is modelled to be used in the overall simulation of the HEV powertrain. This engine model is very detailed and dynamic in comparison to the general engine models available in the advisor and Simulink libraries for modelling and simulation of the HEV powertrain. Two calibration factors are proposed to be used in the engine model with the purpose of accurately predicting the torque generation and fuel consumption.
- A novel control mechanism for controlling the fuel amount to be burned and minimum allowable value for relative air-fuel ratio (λ) is proposed in present work. Two calibration factors are chosen to account for major assumptions and uncertainties involved in the engine modelling.

- A novel “load follower” supervisory control strategy is proposed in the present work to utilize the capability of having access to the internal variables of the HEV powertrain system such as (e.g. transient DC-link load current). The modelling methodology developed in present work shapes the pathway for developing more sophisticated supervisory control mechanisms for dynamic models of the HEV powertrain.

10.3 Future Scope of the work

Modelling and control of the HEV is a very vibrant and urgent field of research, both for the industry and academics. Vibrancy comes in this field by the market share competition among automobile companies and it is well reflected by the amount of money and resources poured in this field for research in the last two decades. Urgency comes from the fact that there is an increasing pressure for minimizing the CO_2 emissions from all corners of the society. Governments all around the world are systematically aiming towards the ideal zero emission conditions by raising the bars for emission restrictions.

The present work is a significant contribution in the direction of dynamic modelling and simulation of the HEV. The present model gives ample opportunity to the control engineers to design newer and advanced control schemes for fuel conservative HEVs. Due to the involvement of dynamics of the powertrain components, the model has mixed complexity level. However, every component has room for further improvements in terms of design and control. Additionally, there are good opportunities to implement more advanced supervisory control strategies for saving more fuel.

10.3.1 Vehicle Dynamics

- At present, the car dynamics is generated through VehicleSim® and it can be simulated only for a fixed time step. However, all other models of the HEV powertrain can be simulated with a variable time step, which will be much faster than AutoSim. After analysis, it has been found that a significant amount of energy supplied to the car goes into overcoming drag losses and all other losses (e.g., tyre slip), are insignificant in comparison to drag losses. Since drag losses depend on the speed profile and drag constants, rather than using such a detailed model for vehicle dynamics, a more simplistic car model can be utilized to predict drag losses, and this will reduce simulation time as well.
- At present, to test the performance of dynamic powertrain, only longitudinal car dynamics has been used with longitudinal tyre motion, but in the future, the car model can be equipped with the ability of lateral motion to test other kinds of driving tests such as turning through a corner.
- At present, the CVT is implemented with a combination of the most efficient f_{drat} , a first order time lag (for time response) and constant average efficiency. However a more accurate model of CVT can be used, where efficiency can be modelled as function of torque, speed and rate of change of the drive ratio.
- At present, the driver model is a simple PID controller but this model can be updated with a more advanced preview based driver model, which can be used better in association with a non-causal supervisory controller.
- At present, the final drive ratio of the transmission f_{drat} is chosen in such a way that the PMSM can operate with maximum efficiency, indirectly making all other components perform better in terms of energy savings. However, can f_{drat} itself be chosen from the start in such a way that the overall performance of the HEV improves rather than only the PMSM, is the question that can be investigated further.

- In the present model, there is no mechanical brake and has been found that tracking of NEDC cycle can be done successfully by having only regenerative and dynamic braking. In reality, mechanical brakes are compulsory for an HEV from a security point of view.

10.3.2 Electric Machines

- Dynamic $d - q$ frame equations are used to model and control the PMSM and PMSG drives in the present work but there is no model for measuring the thermal effects of the operation. Due to mechanical friction and eddy currents, the temperature of electric machines is increased affecting the resistance and inductance of the machine, thereby finally affecting the machine performance. So a simple thermal model can be incorporated to capture this important thermal behavior of the machines under different operating conditions.
- Size, weight, volume and power ratings of the electrical machines can be parameterized to evaluate the performances of the powertrain with different available options.
- There is significant amount of energy loss in the PMSG and engine due to friction and other such factors. The possibility of implementing a CVT between the PMSG and engine can be investigated so that both engine and PMSG can operate in their most efficient zone, leading to fuel savings.

10.3.3 Electronic Converters

- The switching models of the converters are ignored in the current work to increase simulation speed. Additionally, average efficiency factors are used to calculate the losses involved. Although the usage of average efficiency factors is well justified, there is still room for inclusion of simple average models for the calculation of

more realistic switching losses and conduction losses depending on the voltage levels and power transfer at input and output ports of the converters.

10.3.4 Battery Model

- The battery is the biggest hurdle in the direction of achieving long range and cost effective electric vehicles. There was an effort to develop an electrochemistry based 1-D mathematical model for the Li-ion battery. The control volume method has been employed to solve the simultaneous coupled partial differential equations to capture the realistic charging and discharging behavior of the battery under normal operation conditions. The code has been developed in C++ and it is general enough to simulate any other lithium battery cell by just changing the electrochemical parameters used in the battery model. But this model was found extremely computationally expensive for Simulink platform based simulation in conjunction with other components, so another model has been used to complete the powertrain. In the future, efforts can be made to solve those equation in a more simplistic way so that computational complexity can be minimized and the detailed model can be used with the rest of the powertrain.
- The present generic model is very good in predicting the battery behaviour in normal operating conditions but is insensitive to the temperature conditions and lacks any kind of thermal modelling. The electrochemistry based 1-D mathematical model has an in-built thermal model and therefore, has a very important advantage over this generic model.
- It will be highly useful and interesting to include a mechanism to predict life cycle of the battery depending on the intensity of the charging and discharging pattern which current model ignores completely.

10.3.5 Engine

A control-oriented dynamic 0D turbocharged diesel engine model is presented in the work and is validated against the steady state data of *1D* Ricardo-Wave model of PUMA2L engine. The engine model with the inclusion of engine-shaft inertia and turbo-shaft inertia has the capacity to capture the real dynamics of the turbocharged diesel engine. At present, this engine model is not yet fully utilized to its full capacity and a few more important developments that can be pursued in the future are:

- Required changes should be done to include completely shutting down the engine when it is not used during the ECE-15 cycle.
- Since this model has a dynamic turbocharger, the effect of downsizing the engine with increasing boost pressure can be analyzed with this model.
- Any real engine has various kinds of losses but the present engine has included only the frictional losses, so the effect of all other kinds of losses can be included in the present model.
- An efficiency map can be built by running the engine model with various speed and torque combinations and then a control scheme should be designed to choose the suitable speed to deliver the required torque at the highest possible efficiency. Since the generator and engine shaft are coupled, the speed must be chosen in such a way that the DC-link voltage can be maintained constant while the generator is delivering the required power to the PMSM.
- The EGR model is proposed in the engine model but due to the lack of EGR data, it has not been activated. In the future, by inclusion of the EGR data, the engine model will be more close to reality.
- A compound turbocharger can be employed to extract more power from the exhaust of the engine. The turbo-machinery group under Dr Ricardo Martinez-

Botas is already investigating this possibility and has shown interest in using the engine model proposed in this work for their purpose.

10.3.6 Supervisory Control Strategy

- The present model is quite complex due to the inclusion of the dynamics, so two online control strategies, ‘thermostat supervisory control strategy’ (TSCS) and ‘load follower supervisory control strategy’ (LFSCS), is implemented. More advanced, optimization based offline non-causal supervisory control strategies, such as ECMS, can be implemented.
- There are complex interactions between the component level controllers and supervisory level controller. This interaction should be studied further in order to design the best control strategy.
- The range of the SOC and the timings to recharge the battery highly depend on the speed profile used for tracking. For example, if the battery is depleting and soon there will be recharging due to regeneration, there is no point in recharging the battery by the engine at that point. Optimized performance of the battery depends on the SOC and requires preview of the future drive cycle. Therefore, the overall constraint on the SOC has to be examined further in association with the driving profile.

In the present work, a series HEV powertrain is presented but due to the modular approach of component modelling, these components can be easily rearranged in parallel and series-parallel combination with proper adjustment to the control architecture.

APPENDIX

A

LONGITUDINAL VEHICLE DYNAMICS

A.1 VehicleSim® code for the longitudinal vehicle

```
;;; Setting up the conditions for AutoSim code ;;
(reset)
(si)
(add-gravity)
(setsym *stiff-integrator* t)
(setsym *multibody-system-name* "Longitudinal car model")
(setsym *safe-divide* t)

;;;;Building longitudinal model by defining all the rigid
bodies which will constitute the longitudinal mode ;;
(setsym ms "tmafa + tmara - maf - mar")
(setsym a "(tmara-mar)*l/@ms")
(setsym f_t_load "0.5*tmafa*g")
(setsym r_t_load "0.5*tmara*g")
(setsym f_s_load "@f_t_load - 0.5*maf*g")
(setsym r_s_load "@r_t_load - 0.5*mar*g")

;; Also defining the points where forces will act on the
vehicle ;;
;; take n0 at mid-wheelbase on ground ;;
(add-point pfhc :body n :coordinates ("1/2" 0 -rcfw)) ;front
hub carrier mass centre
(add-point pfcp :body n :coordinates ("1/2" 0 0)) ;front wheel
contact point

(add-point prhc :body n :coordinates ("-1/2" 0 -rcrw)) ;rear
hub carrier mass centre
(add-point prcp :body n :coordinates ("-1/2" 0 0)) ;rear wheel
contact point
```

```

;;; s is the sprung mass, with all longitudinal freedoms only.
    Its origin coincides with that of n ;;
(add-body s :parent n :name "sprung mass" :mass @ms :translate
  (x z)
  :inertia-matrix (0 isy 0) :joint-coordinates (0 0 0)
  :body-rotation-axes y :parent-rotation-axis y :reference-
  axis z
  :cm-coordinates ("1/2-@a" 0 -h))

(add-point aero_f :body s :coordinates ("1/2" 0 0))
(add-point aero_r :body s :coordinates ("-1/2" 0 0))

;;; Front hub carrier with contact point with the road
    combined from left and right = x2 ;;
(add-body fhc :name "front hub carrier"
  :parent s :translate z :mass "maf"
  :inertia-matrix (0 "ifhcy*2" 0) :joint-coordinates pfhc)
(add-point fcpc :body fhc :coordinates pfcp :name "front
  contact point")

;;; Rear hub carrier with contact point with the road combined
    from left and right = x2 ;;
(add-body rhc :name "rear hub carrier"
  :parent s :translate z :mass "mar"
  :inertia-matrix (0 "irhcy*2" 0) :joint-coordinates prhc)
(add-point rpcp :body rhc :coordinates prcp :name "rear
  contact point")

;;; Add wheels to hub carriers with spin freedom and inertia
    only combined from left and right = x2
(add-body fwhl :name "front wheel" :parent fhc :joint-
  coordinates pfhc
  :mass 0 :body-rotation-axes y :parent-rotation-axis y :
  reference-axis z
  :inertia-matrix (0 "ifwhly*2" 0))
(add-body rwhl :name "rear wheel" :parent rhc :mass 0 :joint-
  coordinates prhc
  :inertia-matrix (0 "irwhly*2" 0) :body-rotation-axes y :
  parent-rotation-axis y :reference-axis z)

;;; Defining motor and transmission system ;;
(add-body motorshaft :name "motorshaft" :parent s :mass 0 :
  body-rotation-axes x
  :parent-rotation-axis x :reference-axis y :inertia-matrix ("
  Js" 0 0))

;;; Defining the final drive ratio "fdrat" parameter to be
    used in the CVT transmission ;;
;(add-input fdrat "L" :name "gear ratio")
(setsym fd_rat "fdrat")

```

```

(add-speed-constraint "ru(motorshaft)- ru(rwhl)*@fd_rat" :u "
    ru(motorshaft)")
(add-position-constraint "rq(motorshaft)- rq(rwhl)*@fd_rat" :q
    "rq(motorshaft)")

(kinematics)
;;; Defining spring and damper suspension systems ;;

;;; linear spring/damper front suspension combined from left
and right = x2 ;;
(add-line-force fsusp :name "front suspension force" :
    direction [sz]
    :point1 fwhl0 :point2 s0
    :magnitude "@f_s_load*2 - ksuspf*(x-x0)*2 - csuspf*v*2" :no-
        forcem t)

;;; linear spring/damper rear suspension combined from left
and right = x2 ;;
(add-line-force rsusp :name "rear suspension force" :direction
    [sz]
    :point1 rwhl0 :point2 s0
    :magnitude "@r_s_load*2 - ksuspr*(x-x0)*2 - csuspr*v*2" :no-
        forcem t)

;;; Defining spring and damper tyre systems - negative tyre
forces= 0, this implies tyres have lost contact with ground
;;
;;; front tyre load that can lose ground contact (always
positive) combined from left and right = x2 ;;
(add-line-force ftload :name "front tyre load" :point1 fcpc :
    point2 n0
    :direction [nz] :magnitude "min(-0.1,-@f_t_load*2 - k_tyr*(x
        -x0)*2 - c_tyr*2*v)" :no-forcem t)

;;; rear tyre load that can lose ground contact (always
positive) combined from left and right = x2 ;;
(add-line-force rtload :name "rear tyre load" :point1 rcpc :
    point2 n0
    :direction [nz] :magnitude "min(-0.1,-@r_t_load*2 - k_tyr
        *2*(x-x0) - c_tyr*2*v)" :no-forcem t)

;;; Compliant tyre radius ;;
;;; distance of tyre contact point to axis of rotation ;;
(setsym rTyF "-dot(pos(fhc0),[nz])")
(setsym rTyR "-dot(pos(rhc0),[nz])")

;;; Magic Formula ;;
;;; Longitudinal slip expressions ;;
(setsym kappafr "z(-(dot(vel(fcpc),[nx])+ru(fwhl)*@rTyF)/max(
    tysl_min, dot(vel(fhc0),[nx]))")
```

```

(setsym kapparr "z(-(dot(vel(rcpc),[nx])+ru(rwhl)*@rTyR)/max(
    tysl_min, dot(vel(rhc0),[nx])))")

;; Wheel loads ;;
(setsym frl "-fm(ftload)/2")
(setsym rrl "-fm(rtload)/2")

;; Front tyre ;;
(setsym C_fkappafr "z(@frl*(b1*@frl+b2)/exp(b3*@frl))")
(setsym C_falphafr "z(b4*sin(2*atan(@frl/b5)))")
(setsym C_malphafr "z(@frl*(b6*@frl+b7)/exp(b8*@frl))")
(setsym C_fgamm afr "z(@frl*(b9*@frl+b10))")

(setsym D_fxfr "z(@frl*(b11*@frl+b12))")
(setsym D_fyfr "z(@frl*(b13*@frl+b14))")
(setsym D_mzfr "z(@frl*(b15*@frl+b16))")
(setsym k_pfr "z(k_p0+k_p1*@frl+k_p2*@frl**2)")
(setsym a_pfr "z(a_p0+a_p1*@frl+a_p2*@frl**2)")
(setsym a_efr "z(gammafr*(@C_fgamm afr+b17*@frl)/@C_falphafr)")

(setsym c_kfr "z(log(l_bar*p*D_fxfr/(@k_pfr*C_fkappafr))/
    @k_pfr)")
(setsym c_afr "z(log(l_bar*p*D_fyfr/(@a_pfr*C_falphafr))/
    @a_pfr)")
(setsym m_kfr "z(@C_fkappafr*exp(@c_kfr*k_pfr)*(1+@c_kfr*
    @k_pfr)/@D_fxfr)")
(setsym m_afr "z(@C_falphafr*exp(@c_afr*a_pfr)*(1+@c_afr*
    @a_pfr)/@D_fyfr)")
(setsym int_kfr "z((@C_fkappafr*exp(@c_kfr*k_pfr)/@D_fxfr-
    @m_kfr)*@k_pfr)")
(setsym int_afr "z((@C_falphafr*exp(@c_afr*a_pfr)/@D_fyfr-
    @m_afr)*@a_pfr)")

(setsym k_barfr "z(ifthen(@k_pfr-abs(@kappafr), @C_fkappafr*
    @kappafr*exp(@c_kfr*abs(@kappafr))/@D_fxfr, ~
    @m_kfr*@kappafr+sign(1.0,@kappafr)*@int_kfr))")
(setsym a_e_barfr "z(ifthen(@a_pfr-abs(@a_efr), @C_falphafr*
    @a_efr*exp(@c_afr*abs(@a_efr))/@D_fyfr, ~
    @m_afr*@a_efr+sign(1.0,@a_efr)*@int_afr))")
(setsym l_barfr "z(sqrt(@a_e_barfr**2+k_barfr**2))")
(setsym l_fnfr "z(0.5*(1+tanh(2.207*log(max(eps,@l_barfr))
    -1.636)))")
(setsym phi_barfr "z((1-E)*@l_barfr+(E/BB)*atan(BB*@l_barfr))"
    )

(setsym Fnfr "z(sin(CC*atan(BB*phi_barfr)))")
(setsym D_mfr "z(sqrt((@D_fxfr*k_barfr/@l_barfr)**2+(@D_fyfr*
    @a_e_barfr/@l_barfr)**2))")
(setsym Fmfr "@D_mfr*Fnfr")

```

```

(setsym Fx1fr "@Fmfr*@k_barfr/@l_barfr")
(setsym lambdafr "sqrt(@kappafr**2+alphafr**2)")
(setsym Fx2fr "@Fmfr*@kappafr/@lambdafr")
(setsym Fxfr "z(@Fx1fr+(@Fx2fr-@Fx1fr)*@l_fnfr)")

;; Rear tyre ;;
(setsym C_fkapparr "z(@rrl*(b1*@rrl+b2)/exp(b3*@rrl))")
(setsym C_falpharr "z(b4*sin(2*atan(@rrl/b5)))")
(setsym C_malpharr "z(@rrl*(b6*@rrl+b7)/exp(b8*@rrl))")
(setsym C_fgammarr "z(@rrl*(b9*@rrl+b10))")

(setsym D_fxrr "z(@rrl*(b11*@rrl+b12))")
(setsym D_fyrr "z(@rrl*(b13*@rrl+b14))")
(setsym D_mzrr "z(@rrl*(b15*@rrl+b16))")
(setsym k_prr "z(k_p0+k_p1*@rrl+k_p2*@rrl**2)")
(setsym a_prr "z(a_p0+a_p1*@rrl+a_p2*@rrl**2)")
(setsym a_err "z(gammarr*(@C_fgammarr+b17*@rrl)/@C_falpharr)")

(setsym c_krr "z(log(l_barpp*D_fxrr/(@k_prr*C_fkapparr))/ @k_prr)")
(setsym c_arr "z(log(l_barpp*D_fyrr/(@a_prr*C_falpharr))/ @a_prr)")
(setsym m_krr "z(@C_fkapparr*exp(@c_krr*k_prr)*(1+@c_krr* @k_prr)/@D_fxrr)")
(setsym m_arr "z(@C_falpharr*exp(@c_arr*a_prr)*(1+@c_arr* @a_prr)/@D_fyrr)")
(setsym int_krr "z((@C_fkapparr*exp(@c_krr*k_prr)/@D_fxrr- @m_krr)*@k_prr))")
(setsym int_arr "z((@C_falpharr*exp(@c_arr*a_prr)/@D_fyrr- @m_arr)*@a_prr))")

(setsym k_barr "z(ifthen(@k_prr-abs(@kapparr), @C_fkapparr* @kapparr*exp(@c_krr*abs(@kapparr))/@D_fxrr, ~ @m_krr*@kapparr+sign(1.0,@kapparr)*@int_krr))")
(setsym a_e_barr "z(ifthen(@a_prr-abs(@a_err), @C_falpharr* @a_err*exp(@c_arr*abs(@a_err))/@D_fyrr, ~ @m_arr*@a_err+sign(1.0,@a_err)*@int_arr))")
(setsym l_barr "z(sqrt(@a_e_barr**2+@k_barr**2))")
(setsym l_fnrr "z(0.5*(1+tanh(2.207*log(max(eps,@l_barr))- -1.636))))")
(setsym phi_barr "z((1-E)*@l_barr+(E/BB)*atan(BB*@l_barr))")

(setsym Fnrr "z(sin(CC*atan(BB*phi_barr)))")
(setsym D_mrr "z(sqrt((@D_fxrr*k_barr/@l_barr)**2+(@D_fyrr* @a_e_barr)**2))")
(setsym Fmrr "@D_mrr*Fnrr")

(setsym Fx1rr "@Fmrr*k_barr/@l_barr")

```

```

(setsym lambdarr "sqrt(@kapparr**2+alpharr**2)")
(setsym Fx2rr "@Fmrr*@kapparr/@lambdarr")
(setsym Fxrr "z(@Fx1rr+(@Fx2rr-@Fx1rr)*@l_fnrr)")

;; Translating Magic Formula to tyre longitudinal forces and
driving moments on wheel center ;;
;; Front tire longitudinal force and driving moment;;
combined from left and right = x2 ;;
(add-line-force ffx :name "front tyre longitudinal force" :
point1 fhc0 :point2 n0
:direction [nx] :magnitude "z(@Fxfr*2*1/p_i*(atan(lf_fact*
*(tu(s,1)-sp_tol))+p_i/2)-c_wheel*mag(rot(fwhl))*2/p_i
*(-atan(lf_fact*(tu(s,1)-sp_tol))+p_i/2))" :no-forcem t
)

(add-moment fmy :name "front tyre driving moment" :body1 fwhl :
body2 n
:direction [fwhly] :magnitude "fm(ffx)*@rTyF" :no-forcem t)

;; rear tire longitudinal force and driving moment, combined
from left and right = x2 ;;
(add-line-force rfx :name "rear right tyre longitudinal force"
:point1 rhc0 :point2 n0
:direction [nx] :magnitude "z(@Fxrr*2*1/p_i*(atan(lf_fact*(
tu(s,1)-sp_tol))+p_i/2)-c_wheel*mag(rot(rwhl))*2/p_i*(-
atan(lf_fact*(tu(s,1)-sp_tol))+p_i/2))" :no-forcem t)

(add-moment rmy :name "rear right tyre driving moment" :body1
rwhl :body2 n
:direction [rwhly] :magnitude "fm(rfx)*@rTyR" :no-forcem t)

;; Aerodynamic forces - drag and lift ;;
(setsym aer "0.6135*Xa*tu(s,1)**2")
(add-line-force drag :name "aero_drag" :direction [sx] :point1
s0
:point2 n0 :magnitude "-cd*@aer" :no-forcem t)
(add-line-force liftf :name "aero_lift_front" :direction [sz] :
point1 aero_f
:point2 n0 :magnitude "-clf*@aer" :no-forcem t)
(add-line-force liftr :name "aero_lift_rear" :direction [sz] :
point1 aero_r
:point2 n0 :magnitude "-clr*@aer" :no-forcem t)

;; Input of the external torque by PMSM ;;
(add-input drv_tq "F*L" :name "Torque generated by the motor")
(add-moment mottq :name "motor drive torque" :body1 motorshaft
:body2 s :direction [sx]
:magnitude "-input_ext(drv_tq)" :no-forcem t)

```

```

;;; Implementation of the CVT, pushing PMSM to operate in most
    efficient zone ;;
(setsym idealw "abs(fm(mottq) / (ratio*ru(rwhl)))")
(setsym fdrr "min(fdrrmax, @idealw)")
(setsym fdr "max(fdrrmin, @fdrr)")
(add-state-variable fdrat dfdrat "1")
(set-aux-state-deriv dfdrat "(@fdr-fdrat)/cvt_lag")

;;; Power Supply/Dissipation Analysis ;;
(setsym DragPow "fm(drag)*dot(vel(s0), [sx])")
(setsym TySlPowF "fm(ffd) * (dot(vel(fhc0), [nx]) + dot(rot(fwhl), [
ny]) * @rTyF )")
(setsym TySlPowR "fm(rfd) * (dot(vel(rhc0), [nx]) + dot(rot(rwhl), [
ny]) * @rTyR )")
(setsym TySlPow "@TySlPowR + @TySlPowF")
(setsym SustPowF "fm(fsusp)*tu(fhc)")
(setsym SustPowR "fm(rsusp)*tu(rhc)")
(setsym SuspPow "@SustPowF + @SustPowR")
(setsym TyrtPowF "fm(ftload)*dot(vel(fcpc), [nz])")
(setsym TyrtPowR "fm(rtload)*dot(vel(rcpc), [nz])")
(setsym TyrPow "@TyrtPowF + @TyrtPowR")
(setsym LiftPowF "fm(liftf)*dot(vel(aero_f), [sz])")
(setsym LiftPowR "fm(liftr)*dot(vel(aero_r), [sz])")
(setsym LiftPow "@LiftPowF + @LiftPowR")
(setsym AeroPow "@DragPow+@LiftPow")

;;; Kinetic Energy of Car ;;
(setsym sprungKE "0.5*ms*dot(vel(scm), vel(scm)) + 0.5*isy*dot(
    rot(s), rot(s))")
(setsym frontHubKE "0.5*maf*dot(vel(fhccm), vel(fhccm)) + 0.5*(
    ifhcy*2*dot(rot(fhc), rot(fhc)))")
(setsym rearHubKE "0.5*mar*dot(vel(rhccm), vel(rhccm)) + 0.5*(
    irhcy*2*dot(rot(rhc), rot(rhc)))")
(setsym wheelsKE "0.5*ifwhly*2*dot(rot(fwhl), rot(fwhl)) + 0.5*(
    irwhly+Icshafty)*2*dot(rot(rwhl), rot(rwhl)))")
(setsym motKE "0.5*(Js)*dot(rot(motorshaft), rot(motorshaft))")
(setsym totalKE "@sprungKE+@frontHubKE+@rearHubKE+@wheelsKE+"
    "@motKE")
(setsym gravPow "(@ms*dot(vel(scm), [nz]) + maf*dot(vel(fhccm), [
nz]) + mar*dot(vel(rhccm), [nz])) * g")
(setsym Power_in "fm(mottq)*ru(motorshaft)")
(setsym KePow "-dxdt(@totalKe)")
(setsym Power_out "@gravPow+@KePow+@TySlPowF+@TySlPowR+
    @SuspPow+@TyrPow+@AeroPow")
(setsym netPower "@Power_in+@Power_out")

;;; (add-standard-output)
;;
~~~~~
```

```

(add-out "tu(s,1)" "speed" :long-name "Forward speed" :body s :
    units "L/T")
(add-out "-ru(rwhl)" "+ve rear wheel speed" :long-name "
    angular speed of motor" :body s :units "a/T")
(add-out "-ru(motorshaft)" "motorshaft speed" :long-name "
    angular speed of motorshaft" :body s :units "a/T")
(add-out "@fd_rat" "fd_rat" :long-name "cvt drive ratio")
(add-out "@Power_in" "Power_in" :long-name "Input Power")
(add-out "@Power_out" "Power_out" :long-name "Output Power")
(add-out "@netPower" "netPower" :long-name "Net Power")
(add-out "-@totalKE" "totalKE" :long-name "total KE")
(add-out "@DragPow" "DragPow" :long-name "Drag Power")
(add-out "@TySlPow" "TySlPow" :long-name "Tyre Slip Power")
(add-out "@SuspPow" "SuspPow" :long-name "Suspension Damping
    Power")
(add-out "@TyrPow" "TyrPow" :long-name "Tyre Damping Power")
(add-out "@LiftPow" "LiftPow" :long-name "Aero Lift kiath
    Power total test")
(add-out "@AeroPow" "AeroPow" :long-name "Total Aero Power")
(add-out "@KePow" "KePow" :long-name "Rate of change of Ke")
(add-out "@gravPow" "gravPow" :long-name "power due to gravity"
    )
;;; ~~~~~
(dynamics)
(finish)
;;; (write-model-code) ;;

;;; Defining default values of all the constants used in the
    programme ;;
;;; set units, defaults, and names of parameters ;;
(set-defaults
    rcfw 0.3 Ki 20 Kp 30 rcrw 0.3 ifhcy 0.1 irhcy 0.1 h 0.576 l
        2.695 icrank 0.16 icrowny 0.08 ifwhly 0.653 irwhly 0.653
    isy 2152.1 kstcol 1500 cstr 10 tmafa 884.3 tmara 591.3 maf 60
        mar 60 k_farb 12000 k_rarb 4000 k_tyr 180000 c_tyr 800
    ksuspf 19480 ksuspr 16800 csuspf 1500 csuspr 1500 dsfdz 0
        dsrdz 0.0087 gammafr 0 gammarr 0 alphafr 0 alpharr 0 cd
        0.35
    clf 0.1 clr 0.16 XA 2.0 eps 1e-14 Ipx 0.01 cpin 16 diffrat 4
        stgr 15.35 wf 0.765 wr 0.7375 "tu(s,1)" 0.5
    "ru(fwhl)" -1.6666666666 "ru(rwhl)" -1.6666666666 step
        0.00002 iprint 1000 stopt 12 sp_tol 0.02 lf_fact 1e4
    p_i 3.141592653589793 js 0.0018 Icshafty 0.01 "iv_inpt(2)" 4
        cvt_fact 10000 cvt_maxm 250 c_wheel 50000 tysl_min 0
        fdrmax 20
    fdrmin 0.39 ratio 0.477555 CVT_LAG 0.3 )

```

```
(set-defaults CC 1.47 BB 0.68027 E -0.462 l_bar_p 2.325 Cm 2.46
   Em -2.04
   b1 3.769e-3 b2 23.73 b3 4.744e-5 b4 63310 b5 5094 b6 2.135e
      -4 b7 -5.1e-3
   b8 1.76e-4 b9 4.861e-5 b10 0.2537 b11 -2.347e-5 b12 1.153
      b13 -2.035e-5
   b14 0.9966 b15 2.804e-6 b16 1.551e-3 b17 0.848 k_p0 0.13
      k_p1 -6.5e-6 k_p2 0
   a_p0 0.0786 a_p1 1.657e-5 a_p2 0)

(set-defaults Bt 1.8 Et -12 Bxe 0.0014 Cxe 1.6 Dxe 100000 Exe
   -8 cdiff 10 kbrf 2000 kbrr 500)
```

BIBLIOGRAPHY

- [1] D. Howey, R. North, and R. Martinez-Botas, “Road transportation technology and climate change mitigation,” *Grantham Institute for Climate Change Briefing Paper*, 2010.
- [2] M. Eshani, Y. Gao, S. E. Gay, and A. Emadi, *Modern Electric, Hybrid Electric, and Fuel Cell Vehicles: Fundamentals, Theory, and Design*. CRC Press, 2004.
- [3] V. Wouk, “Hybrids: then and now,” *Spectrum, IEEE*, vol. 32, pp. 16–21, July 1995.
- [4] C. C. Chan, “The state of the art of electric and hybrid vehicles,” *Proceedings of the IEEE*, vol. 90, pp. 247–275, August 2002.
- [5] C. Musardo, G. Rizzoni, and B. Staccia, “A-ecms: An adaptive algorithm for hybrid electric vehicle energy management,” in *44th IEEE Conference on Decision and Control and European Control Conference. CDC-ECC '05.*, pp. 1816 – 1823, December 2005.
- [6] T. J. Barlow, S. Latham, I. S. McCrae, and P. G. Boulter, *A reference book of driving cycles for use in the measurement of road vehicle emissions*. TRL Limited. Published Project Report PPR354.
- [7] S. A. Evangelou and A. Shukla, “Advances in the modelling and control of series hybrid electric vehicles,” *American Control conference*.
- [8] S. A. Evangelou, A. Shukla, and S. Wassif, “Dynamic model development for the evaluation of powertrain, transmission and control of hybrid electric vehicles,” *IEEE Transactions on Vehicular Technology*. (In preperation).
- [9] A. Shukla, R. Martinez-Botas, and S. A. Evangelou, “Dynamic modelling of turbocharged diesel engines,” *ASME Journal of Dynamic Systems, Measurement, and Control*. (In preperation).
- [10] K. B. Wipke, M. R. Cuddy, and S. D. Burch, “Advisor 2.1: a user-friendly advanced powertrain simulation using a combined backward/forward approach,” *IEEE Transactions on Vehicular Technology*, vol. 48, pp. 1751–1761, November 1999.

- [11] A. Brooker, T. Hendricks, V. Johnson, K. Kelly, T. Markel, M. O. Keefe, S. Sprik, and K. Wipke, *ADVISOR 3.2+ Documentation*. National Renewable Energy Laboratory, National Wind Technology Center, Washington, D.C. Office, 2001. www.ctts.nrel.gov/analysis.
- [12] Anon., *PSAT (Powertrain System Analysis Toolkit)*. Argonne National Laboratory, Transportation Technology R & D Center.
- [13] A. Rousseau, *PSAT Training Part 01, PSAT Overview*. Argonne National Laboratory, Transportation Technology R & D Center, U.S. Department of Energy, UChicago Argonne, LLC.
- [14] Anon., *Simulink*. The Mathworks Inc. <http://www.mathworks.com>.
- [15] Anon., *Modelica - A Unified Object-Oriented Language for Physical Systems Modeling, MODELICA Version 3.2*. Modelica Association, Linköping, Sweden, 24 March 2010. <http://www.Modelica.org/>.
- [16] M. Otter, *Modelica Overview*. Modelica Association, Technical University of Munich, 2009.
- [17] G. Ferretti, G. Magnani, P. Rocco, L. Bonometti, and M. Maraglino, “Electric hybrid drive systems for passenger cars and taxis,” *Second Internation Modelica Conference, Proceedings*, pp. 109–115, March 2002.
- [18] L. Roa and M. Prado, *Simulation Languages*. Wiley Encyclopedia of Biomedical Engineering, University of Seville Sevilla, Spain, April 2006. <http://onlinelibrary.wiley.com/doi/10.1002/9780471740360.ebs1089/references>.
- [19] Anon., *AVL Product Description Cruise*. AVL-Advanced Simulation Technologies, AVL List GmbH Hans-List-Platz 1, A-8020 Graz, Austria, 2009. <http://www.avl.com>.
- [20] A. Kalberlah, “Electric hybrid drive systems for passenger cars and taxis,” *SAE Tech. Rep. 910247*, Feburary 1991.
- [21] T. Prius, *Toyota Hybrid Systems, THS-II: Next-generation hibrid technology by Toyota*, August 2011.
- [22] A. Emadi, K. Rajashekara, S. Williamson, and S. Lukic, “Topological overview of hybrid electric and fuel vehicular power system architectures and configuration,” *IEEE Transactions on Vehicular Technology*, vol. 45, May 2005.
- [23] I. Husain, *Electric and Hybrid Vehicles: Design Fundamentals*. University of Akron, Ohio, USA: CRC Press, 2003. ISBN 9780849314667.
- [24] C. D. Rakopoulos and E. G. Giakoomis, *Diesel Engine Transient Operation - Principles of Operation and Simulation Analysis*. London: Springer-Verlag, first edition ed., 2009.

- [25] J. M. Miller, *Propulsion Systems for Hybrid Vehicles*. Michael Faraday House, Six Hills Way, Stevenage Herts, SG1 2AY, United Kingdom: The Institution of Engineering and Technology, December 2003. ISBN-13 978-0863413360.
- [26] J. Larminie and J. Lovry, *Electric Vehicle Technology Explained*. West Sussex: John Wiley Sons Ltd, 2003.
- [27] B. M. Baumann, G. Washington, B. C. Glenn, and G. Rizzoni, “Mechatronic design and control of hybrid electric vehicles,” *Mechatronics, IEEE/ASME Transactions on*, vol. 5, no. 1, pp. 58–72, 2000.
- [28] L. U. Gökdere, K. Benlyazid, R. A. Dougal, E. Santi, and C. W. Brice, “A virtual prototype for a hybrid electric vehicle,” 2000.
- [29] M. Thommyppillai, S. A. Evangelou, and R. S. Sharp, “Advances in the development of a virtual car driver,” *Vehicle System Dynamics*, vol. 47, pp. 1535–1550, 2009.
- [30] M. Thommyppillai, S. A. Evangelou, and R. S. Sharp, “Car driving at the limit by adaptive linear optimal preview control,” *Multibody System Dynamics*, vol. 22, pp. 245–267, 2009.
- [31] Anon., *Autosim 2.5+ Reference Manual*. Mechanical Simulation Corporation, 709 West Huron, Ann Arbor MI, 1998. <http://www.carsim.com>.
- [32] M. P. Thommyppillai, *Optimal path-tracking of virtual race-cars using gain-scheduled preview control*. PhD thesis, Imperial College of London, London, United Kingdom, May 2010.
- [33] H. B. Pacejka, *Tyre and Vehicle Dynamics*. Oxford: Butterworth Heinemann, 2002. ISBN 0-7506-5141-5.
- [34] T.-J. Fu and W.-F. Xie, “Torque control of induction motors for hybrid electric vehicles,” in *American Control Conference, 2006*, p. 6, June 2006.
- [35] G. A. Hubbard and K. Youcef-Toumi, “Modeling and simulation of a hybrid-electric vehicle drivetrain,” in *American Control Conference, 1997. Proceedings of the 1997*, vol. 1, pp. 636 –640 vol.1, jun 1997.
- [36] B. K. Powell, K. E. Bailey, and S. R. Cikanek, “Dynamic modeling and control of hybrid electric vehicle powertrain systems,” *IEEE Control Systems*, vol. 18, pp. 17–33, October 1998.
- [37] Z. Rahman, K. L. Butler, and M. Ehsani, “A comparison study between two parallel hybrid control concepts,” *Society of Automotive Engineers (SAE) Journal*, pp. 135–138, March 2000.
- [38] J. Kim and K. Nam, “Dual inverter control strategy for high speed operation of ev induction motors,” in *Industrial Electronics Society, IECON 2002, 28th Annual Conference of the IEEE 2002*, vol. 1, pp. 163–168, nov. 2002.

- [39] W. Yi and Z. Kaiqi, "Field-oriented vector control of induction motor for electric vehicles," in *Industrial Electronics Society, IECON 2005. 31st Annual Conference of IEEE*, pp. 1610–1614, November 2005.
- [40] P. Vas, *Vector Control of AC Machines*. Oxford: Clarendon Press, Oxford, 1990. ISBN 0-7506-5141-5.
- [41] P. L. Jansen and R. D. Lorenz, "A physically insightful approach to the design and accuracy assessment of flux observers for field oriented induction machine drives," in *Industry Applications Society Annual Meeting, 1992., Conference Record of the 1992 IEEE*, vol. 1, pp. 570–577, October 1992.
- [42] I. Boldea and S. Nasar, *Vector Control of AC Drives*. Florida: CRC Press, Inc., 1992. ISBN 0-7506-5141-5.
- [43] I. Takahashi and T. Noguchi, "A new quick-response and high-efficiency control strategy of an induction motor," *IEEE Transactions on Industry Applications*, vol. IA-22, pp. 820–827, September 1986.
- [44] M. Depenbrock, "Direct self-control (dsc) of inverter-fed induction machine," *IEEE Transactions on Power Electronics*, vol. 3, pp. 420–429, oct 1988.
- [45] G. S. Buja and M. P. Kazmierkowski, "Direct torque control of pwm inverter-fed ac motors - a survey," *Industrial Electronics, IEEE Transactions on*, vol. 51, pp. 744–757, August 2004.
- [46] F. Chen and M. Dunnigan, "Sliding-mode torque and flux control of an induction machine," *Electric Power Applications, IEE Proceedings -*, vol. 150, pp. 227–236, mar 2003.
- [47] T. L. Skvarenina, *The Power Electronics Handbook, Industrial Electronics Series*. CRC Press LLC, 2000 N.W. Corporate Blvd., Boca Raton, Florida 33431: CRC Press, 2002.
- [48] M. Zeraouila, M. E. H. Benbouzid, and D. Diallo, "Electric motor drive selection issues for hev propulsion systems: a comparative study," in *IEEE Conference on Vehicle Power and Propulsion, 2005*, pp. 280–287, September 2005.
- [49] R. Krishnan, *Permanent Magnet Synchronous and Brushless DC Motors*. Mechanical Engineering Series, CRC Press/Taylor & Francis, 2009.
- [50] W. Hong-xing, L. Li-yi, K. Bao-quan, and Z. Ping, "The research on energy regeneration of permanent magnet synchronous motor used for hybrid electric vehicle," in *Vehicle Power and Propulsion Conference, 2008. VPPC '08. IEEE*, pp. 1–4, September 2008.
- [51] P. Pillay and R. Krishnan, "Modelling, simulation, and analysis of permanent-magnet motor drives, Part I: The permanent-magnet synchronous motor drive," *IEEE Transactions on Industry Application*, vol. 25, pp. 265–273, March-April 1989.

- [52] S. Juming, Z. Ming, and S. Yanmin, “Study of optimal efficient control of permanent magnet synchronous motor,” in *Electrical Machines and Systems, 2003. ICEMS 2003. Sixth International Conference on*, vol. 1, pp. 41–44, November 2003.
- [53] Q. Zhang and X. Liu, “Permanent magnetic synchronous motor and drives applied on a mid-size hybrid electric car,” in *Vehicle Power and Propulsion Conference, 2008. VPPC '08. IEEE*, pp. 1–5, September 2008.
- [54] S. Bai and E. W. Zhang, “Based on the model of the dq axis permanent magnet synchronous motor mpc,” in *Electronics and Optoelectronics (ICEOE), 2011 International Conference on*, vol. 3, pp. V3–224 –V3–226, July 2011.
- [55] Y. Ming, L. Gengyin, Z. Ming, and Z. Chengyong, “Modelling of the wind turbine with a permanent magnet synchronous generator for integration,” *Power Engineering Society General Meeting, IEEE*, pp. 1–6, June 2007.
- [56] I. Boldea, *Electric Generators Handbook: Variable Speed Generators*. CRC Press: Taylor-Francis Group, 2nd edition ed., 2006.
- [57] L. Zhong, M. F. Rahman, W. Y. Hu, and K. W. Lim, “Analysis of direct torque control in permanent magnet synchronous motor drives,” *Power Electronics, IEEE Transactions on*, vol. 12, pp. 528–536, May 1997.
- [58] S. Ozcira, N. Bekiroglu, and E. Aycicek, “Speed control of permanent magnet synchronous motor based on direct torque control method,” in *Power Electronics, Electrical Drives, Automation and Motion, 2008. SPEEDAM 2008. International Symposium on*, pp. 268–272, june 2008.
- [59] X. Ye and T. Zhang, “Direct torque control of permanent magnet synchronous motor using space vector modulation,” in *Control and Decision Conference (CCDC), 2010 Chinese*, pp. 1450–1453, may 2010.
- [60] B. Zhang and M. H. Pong, “Maximum torque control and vector control of permanent magnet synchronous motor,” in *Power Electronics and Drive Systems, 1997. Proceedings., 1997 International Conference on*, vol. 2, pp. 548–552, may 1997.
- [61] M. S. Merzoug and F. Naceri, “Comparison of field-oriented control and direct torque control for permanent magnet synchronous motor (pmsm),” 2008.
- [62] J. Simanek, J. Novak, O. Cerny, and R. Dolecek, “Foc and flux weakening for traction drive with permanent magnet synchronous motor,” in *IEEE International Symposium on Industrial Electronics, ISIE 2008.*, pp. 753–758, 30 July 2008.
- [63] R. K. Sharma, V. Sanadhya, L. Behera, and S. Bhattacharya, “Vector control of a permanent magnet synchronous motor,” in *India Conference, 2008. INDICON 2008. Annual IEEE*, vol. 1, pp. 81–86, December 2008.
- [64] F. Heydari, A. Sheikholeslami, K. G. Firouzjah, and S. Lesan, “A new foc technique based on predictive current control for pmsm drive,” *World Journal of Modelling and Simulation*, vol. 5, pp. 287–294, June 2009.

- [65] P. Pillay and R. Krishnan, “Control characteristics and speed controller design for a high performance permanent magnet synchronous motor drive,” *IEEE Transactions on Power Electronics*, vol. 5, pp. 151–159, apr 1990.
- [66] M. S. Merzoug and F. Naceri, “Field-oriented control and direct torque control for permanent magnet synchronous motor(pmsm),” *World Academy of Science, Engineering and Technology*, vol. 45, pp. 299–304, 2008.
- [67] K. P. Louganski, “Modeling and analysis of a dc power distribution system in 21st century airlifters,” Master’s thesis, Department of Electrical Engineering, Virginia Polytechnic Institute and State University, 118 N. Main St. (0337) Blacksburg, VA 24061, USA, 30 September 1999.
- [68] S. Jiao and D. Patterson, “Mathematical model and control system design for a three-phase ac/dc voltage source converter,” *Journal of Electrical and Electronics Engineering, Australia*, vol. 21, pp. 27–31, 2001.
- [69] R. P. Burgos, P. Kshirsagar, A. Lidozzi, F. Wang, and D. Boroyevich, “Mathematical model and control design for sensorless vector control of permanent magnet synchronous machines,” in *Computers in Power Electronics, 2006. IEEE Workshops on*, pp. 76–82, July 2006.
- [70] R. W. Erickson and D. Maksimovic, *Fundamentals of Power Electronics*. University of Colorado, Bouldar, Colorado: Springer Science, second edition ed., 2001. ISBN 978-0-7923-7270-7.
- [71] K. Jonasson, *Control of Hybrid Electric Vehicle with Diesel Engines*. PhD thesis, Department of Industrial Electrical Engineering and Automation, Lund University, 2005.
- [72] L. Guzzela and A. Amstutz, “Control of diesel engines,” *IEEE Control Systems Magazine*, vol. 8, pp. 55–71, 1998.
- [73] T. Markel, “Advisor: a systems analysis tool for advanced vehicle modeling,” *Journal of Power Sources*, vol. 110, no. 2, pp. 255–266, 2002.
- [74] B. He and M. Ouyang, “Average modeling of diesel auxiliary power unit for series hybrid electric vehicle,” in *Vehicular Technology Conference, 2005. VTC-2005-Fall. 2005 IEEE 62nd*, vol. 4, pp. 2372–2376, September 2005.
- [75] S. Bin, Z. Fan-ming, and C. Yu-tao, “Control oriented real time model of marine powerstation diesel engine based on neural network,” in *Third International Conference on Computer Research and Development (ICCRD)*, vol. 4, pp. 386–390, March 2011.
- [76] L. Brzozowska, K. Brzozowski, and J. Nowakowski, “An application of artificial neural network to diesel engine modelling,” in *Intelligent Data Acquisition and Advanced Computing Systems: Technology and Applications, 2005. IDAACS 2005. IEEE*, pp. 142–146, September 2005.

- [77] Z. Fanming, C. Yutao, W. Jiaming, and C. Guojun, “Dynamic modeling and simulation of marine diesel engine using elman networks,” in *Neural Networks and Signal Processing, 2003. Proceedings of the 2003 International Conference on*, vol. 1, pp. 100–103, December 2003.
- [78] M. A. Rahman, A. M. Osheiba, T. S. Radwan, and E. S. Abdin, “Modelling and controller design of an isolated diesel engine permanent magnet synchronous generator,” *IEEE Transactions on Energy Conversion*, vol. 11, pp. 324–330, June 1996.
- [79] M. Ayadi, N. Langlois, and H. Chafouk, “Polynomial control of nonlinear turbocharged diesel engine model,” in *IEEE International Conference on Industrial Technology, IEEE ICIT 2004.*, vol. 3, pp. 1384–1389, December 2004.
- [80] S. Ling-ge, Z. chang Liu, H. Yong-qiang, Z. Guang-yong, and S. Zhao-jie, “Realization of the simulation platform of turbocharged diesel engine with egr loop under transient conditions,” in *Computer Application and System Modeling (ICCASM), 2010 International Conference on*, vol. 8, pp. 274–279, October 2010.
- [81] V. Medica, *Simulation of turbocharged diesel engine driving electrical generator under dynamic working conditions*. PhD thesis, Technical Faculty Rijeka, University of Rijeka, June 1988.
- [82] P. Strandh, *Combustion Engine Models for Hybrid Vehicle System*. PhD thesis, Department of Heat and Power Engineering, Lund Institute of Technology, 2006.
- [83] F. Payri, J. Benajes, J. Galindo, and J. Serrano, “Modelling of turbocharged diesel engines in transient operation. part 2: wave action models for calculating the transient operation in a high speed direct injectionengine,” *Proceedings of the Institution of Mechanical Engineers, Part D: Journal of Automobile Engineering*, vol. 216, pp. 479–493, Junuary 2002.
- [84] J. B. Heywood, *Internal Combustion Engine Fundamentals*. New York: McGraw-Hill Inc., 1988.
- [85] Z. Bazari, “Diesel exhaust emissions prediction under transient operating conditions,” *SAE Technical Paper 940666*, February 1994.
- [86] C. D. Rakopoulos and E. G. Giakoumis, “Review of thermodynamic diesel engine simulations under transient operating conditions,” *SAE Journal*, April 2006.
- [87] A. Darlington, *Diesel Air-Path Mean-Value Modeling and Charge Properties under Transient Conditions*. PhD thesis, Department of Engineering, University of Cambridge, 2006.
- [88] P. Moraal and I. Kolmanovsky, “Turbocharger modeling for automotive control application,” *SAE paper 1999-01-0908*, 1999.

- [89] J. Jensen, A. F. Kristensen, S. C. Sorenson, and N. Houbak, “Mean value modelling of a small turbocharged diesel engine,” *SAE paper 910070*, 1999.
- [90] L. Guzzella and C. H. Onder, *Introduction to Modeling and Control of Internal Combustion Engine Systems*. Berlin: Springer-Verlag, second edition ed., 2010.
- [91] J. Ritzén, “Modelling and fixed step simulation of a turbo charged diesel engine,” Master’s thesis, Department of Electrical Engineering at Linkopings Universitet, June 2003.
- [92] W. Jun, Z. Y. Tong, X. Q. Hui, and W. H. Rong, “Closed-loop control system in electronic control diesel engine,” in *Vehicle Power and Propulsion Conference, 2008. VPPC ’08. IEEE*, pp. 1–4, September 2008.
- [93] A. Amstutz and L. R. D. Re, “Ego sensor based robust output control of egr in diesel engines,” *Control Systems Technology, IEEE Transactions on*, vol. 3, pp. 39–48, March 1995.
- [94] E. Hendricks, “The analysis of mean value engine models,” *Tech. rept. 890563. SAE International*, 1989.
- [95] M. J. van Nieuwstadt, I. V. Kolmanovsky, P. E. Moraal, A. Stefanopoulou, and M. Jankovic, “Egr-vgt control schemes: experimental comparison for a high-speed diesel engine,” *IEEE Control Systems Magazine*, vol. 20, pp. 63–79, June 2000.
- [96] A. G. Stefanopoulou, I. V. Kolmanovsky, and J. S. Freudenberg, “Control of variable geometry turbocharged diesel engines for reduced emissions,” *IEEE Transactions on Control Systems Technology*, vol. 8, pp. 733–745, July 2000.
- [97] M. Jankovic and I. Kolmanovsky, “Robust nonlinear controller for turbocharged diesel engines,” in *Proceedings of the American Control Conference*, vol. 3, pp. 1389–1394, June 1998.
- [98] M. Ammann, N. P. Fekete, L. Guzzella, and A. H. Glattfelder, “Model-based Control of the VGT and EGR in a Turbocharged Common-Rail Diesel Engine: Theory and Passenger Car Implementation,” *Tech. rept. 2003-01-0357. SAE International*, January 2003.
- [99] Anon., “History of battery invention and development,” March 2012.
- [100] J. R. Bumby, P. H. Clarke, and I. Forster, “Computer modelling of the automotive energy requirements for internal combustion engine and battery electric-powered vehicles,” *Physical Science, Measurement and Instrumentation, Management and Education - Reviews, IEE Proceedings A*, vol. 132, pp. 265–279, september 1985.
- [101] M. Stephen and M. Eshani, “An empirically based electrosource horizon lead-acid battery model,” *SAE Journal*, pp. 135–138, February 1996.

- [102] Z. M. Salameh, M. A. Casacca, and W. A. Lynch, “A mathematical model for lead-acid batteries,” *IEEE Transactions on Energy Conversion*, pp. 93–98, March 1992.
- [103] J. Appelbaum and R. Weiss, “Estimation of battery charge in photovoltaic systems,” *16th IEEE Photovoltaic Specialists Conference*, pp. 513–518, September 1982.
- [104] P. Chapman and M. Aston, “A generic battery model for electric and hybrid vehicle simulation performance prediction,” *International Journal of Vehicle Design*, pp. 82–95, September 1982.
- [105] K. E. Bailey and B. K. Powell, “A hybrid electric vehicle powertrain dynamic model,” in *Proceedings of the American Control Conference, 1995*, vol. 3, pp. 1677–1682, June 1995.
- [106] K. Smith and C.-Y. Wang, “Power and thermal characterization of a lithium-ion battery pack for hybrid-electric vehicles,” *Journal of Power Sources*, vol. 160, no. 1, pp. 662–673, 2006.
- [107] W. B. Gu, C. Y. Wang, and B. Y. Liaw, “The use of computer simulation in the evaluation of electric vehicle batteries,” *Journal of Power Sources*, vol. 75, no. 1, pp. 151–161, 1998.
- [108] O. Tremblay, L. A. Dessaint, and A. I. Dekkiche, “A generic battery model for the dynamic simulation of hybrid electric vehicles,” in *Vehicle Power and Propulsion Conference, 2007. VPPC 2007. IEEE*, pp. 284–289, September 2007.
- [109] B. Aghdaee, “Parametric modelling and control of hybrid vehicle,” Master’s thesis, Department of Mechanical Engineering, Imperial College of London, London, United Kingdom, Spetember 2008.
- [110] V. H. Johnson, “Battery performance models in ADVISOR,” *Journal of Power Sources*, vol. 110, no. 2, pp. 321 – 329, 2002.
- [111] J. P. Gao, G. M. G. Zhu, E. G. Strangas, and F. C. Sun, “Equivalent fuel consumption optimal control of a series hybrid electric vehicle,” *Proceedings of the Institution of Mechanical Engineers, Part D: Journal of Automobile Engineering* 2009, vol. 223, pp. 1003–1018, April 2009.
- [112] O. Tremblay and L. A. Dessaint, “Experimental validation of a battery dynamic model for ev applications,” *World Electric Vehicle Journal*, vol. 3, 2009.
- [113] SimPowerSystems, *Implement generic battery model*, August 2011.
- [114] H. Li, F. Z. Peng, and J. S. Lawler, “A natural ZVS high-power bi-directional dc-dc converter with minimum number of devices,” *Industry Applications Conference, Thirty-Sixth IAS Annual Meeting*, vol. 3, pp. 1874–1881, September 2001.

- [115] H. Li, F. Z. Peng, and J. S. Lawler, “Modeling, simulation, and experimental verification of soft-switched bi-directional dc-dc converters,” *Applied Power Electronics Conference and Exposition, APEC 2001. Sixteenth Annual IEEE*, vol. 2, pp. 736–742, March 2001.
- [116] H. Li, F. Z. Peng, and J. Lawler, “A natural zvs medium-power bidirectional dc-dc converter with minimum number of devices,” *Industry Applications, IEEE Transactions on*, vol. 39, pp. 525 – 535, mar/apr 2003.
- [117] S. R. Cikanek and K. E. Bailey, “Regenerative braking system for a hybrid electric vehicle,” in *American Control Conference, 2002. Proceedings of the 2002*, vol. 4, pp. 3129–3134, 2002.
- [118] A. Y. Ungoren and H. Peng, “An adaptive lateral preview driver model,” *Vehicle System Dynamics*, vol. 43, pp. 1–17, 2005.
- [119] M. Plöchl and J. Edelmann, “Driver models in automobile dynamics application,” *Vehicle System Dynamics*, vol. 45, pp. 699–741, 2007.
- [120] L. Guzzella and A. Sciarretta, *Vehicle Propulsion Systems: Introduction to Modelling and Optimization*. Berlin, Heidelberg, New York: Springer-Verlag, 2007. ISBN 978-3-540-74691-1.
- [121] E. T. Stephen and S. P. Boyd, “Finding ultimate limits of performance for hybrid electric vehicles,” *SAE Paper*, 2000.
- [122] G. Steinmauer and L. del Re, “Optimal control of dual power sources,” in *Control Applications, 2001. (CCA '01). Proceedings of the 2001 IEEE International Conference on*, pp. 422–427, 2001.
- [123] G. Paganelli, S. Delprat, T. M. Guerra, J. Rimaux, and J. J. Santin, “Equivalent consumption minimization strategy for parallel hybrid powertrains,” in *Vehicular Technology Conference, 2002. VTC Spring 2002. IEEE 55th*, vol. 4, pp. 2076–2081, 2002.
- [124] S. Delprat, T. M. Guerra, and J. Rimaux, “Control strategies for hybrid vehicles: synthesis and evaluation,” in *Vehicular Technology Conference, 2003. VTC 2003-Fall. 2003 IEEE 58th*, vol. 5, pp. 3246–3250, October 2003.
- [125] Kleimaier and D. Schroder, “An approach for the online optimized control of a hybrid powertrain,” in *7th International Workshop on Advanced Motion Control, 2002*, pp. 215–220, 2002.
- [126] S. Delprat, J. Lauber, T. M. Guerra, and J. Rimaux, “Control of a parallel hybrid powertrain: optimal control,” *IEEE Transactions on Vehicular Technology*, vol. 53, no. 3, pp. 872–881, 2004.
- [127] M. Koot, J. T. B. A. Kessels, B. de Jager, W. P. M. H. Heemels, P. P. J. van den Bosch, and M. Steinbuch, “Energy management strategies for vehicular electric power systems,” *Vehicular Technology, IEEE Transactions on*, vol. 54, pp. 771–782, May 2005.

- [128] M. Montazeri-Gh, A. Poursamad, and B. Ghalichi, "Application of genetic algorithm for optimization of control strategy in parallel hybrid electric vehicles," *Journal of the Franklin Institute*, vol. 343, no. 4-5, pp. 420–435, 2006. Modeling, Simulation and Applied Optimization.
- [129] L. Serrao, S. Onori, and G. Rizzoni, "Ecms as a realization of pontryagin's minimum principle for hev control," in *American Control Conference, 2009. ACC '09.*, pp. 3964–3969, june 2009.
- [130] D. Wu and S. S. Williamson, "Performance characterization and comparison of power control strategies for fuel cell based hybrid electric vehicles," in *Vehicle Power and Propulsion Conference, 2007. VPPC 2007. IEEE*, pp. 55–61, sept. 2007.
- [131] J. Liu and H. Peng, "Modeling and control of a power-split hybrid vehicle," *Control Systems Technology, IEEE Transactions on*, vol. 16, pp. 1242–1251, November 2008.
- [132] L. Xu, J. Li, J. Hua, X. Li, and M. Ouyang, "Optimal vehicle control strategy of a fuel cell/battery hybrid city bus," *International Journal of Hydrogen Energy*, vol. 34, no. 17, pp. 7323 – 7333, 2009.
- [133] P. Tulpule, V. Marano, and G. Rizzoni, "Effects of different phev control strategies on vehicle performance," in *American Control Conference, 2009. ACC '09.*, pp. 3950–3955, june 2009.
- [134] C. Desai and S. S. Williamson, "Optimal design of a parallel hybrid electric vehicle using multi-objective genetic algorithms," in *Vehicle Power and Propulsion Conference, 2009. VPPC '09. IEEE*, pp. 871–876, sept. 2009.
- [135] F. Lincun, Q. Shiyin, X. Gang, L. Tianli, and Z. Kemin, "Simultaneous optimization for hybrid electric vehicle parameters based on multi-objective genetic algorithms," *Energies*, vol. 4, no. 3, pp. 532–544, 2011.
- [136] L. C. Fang, G. Xu, T. L. Li, and K. M. Zhu, "Concurrent optimization for parameters of hybrid electric vehicle based on non-dominated sorting genetic algorithms," in *Advanced Control of Industrial Processes (ADCONIP), 2011 International Symposium on*, pp. 472–476, May 2011.
- [137] H. Wallentowitz and R. Ludes, "System control application for hybrid vehicles," in *Proceedings of the Third IEEE Conference on Control Applications*, vol. 1, pp. 639–650, August 1994.
- [138] N. Jalil, N. A. Kheir, and M. Salman, "A rule-based energy management strategy for a series hybrid vehicle," in *American Control Conference, 1997. Proceedings of the 1997*, vol. 1, pp. 689–693, June 1997.
- [139] C. Liang, W. Qingnian, L. Youde, M. Zhimin, Z. Z. Z, and L. Di, "Study of the electronic control strategy for the power train of hybrid electric vehicle," in *Proceedings of the IEEE Vehicle Electronics Conference*, vol. 1, (Changchun, China), pp. 383–386, 1999.

- [140] K. Wipke, T. Markel, and D. Nelson, “Optimizing energy management strategy and degree of hybridization for a hydrogen fuel cell suv,” in *Proceedings of the 18th Electric Vehicles Symposium*, (Berlin, Germany), 2001.
- [141] Z. Rahman, K. Butler, and M. Ehsani, “A comparative study between two parallel hybrid control concepts,” in *SAE Paper 2002-01-0102*, 2002.
- [142] H. Banvait, S. Anwar, and Y. Chen, “A rule-based energy management strategy for plug-in hybrid electric vehicle (phev),” in *American Control Conference, 2009*, pp. 3938–3943, June 2009.
- [143] D. L. Buntin and J. W. Howze, “A switching logic controller for a hybrid electric/ice vehicle,” in *American Control Conference, 1995. Proceedings of the*, vol. 2, pp. 1169–1175, June 1995.
- [144] P. Bowles, H. Peng, and X. Zhang, “Energy management in a parallel hybrid electric vehicle with a continuously variable transmission,” in *American Control Conference, Proceedings of the 2000*, vol. 1, pp. 55–59, September 2000.
- [145] C. C. Lin, J. M. Kang, J. W. Grizzle, and H. Peng, “Energy management strategy for a parallel hybrid electric truck,” in *American Control Conference, 2001. Proceedings of the 2001*, vol. 4, pp. 2878–2883, 2001.
- [146] S. Fish, T. Savoie, and H. Vanicek, “Modeling hybrid electric hmmwv power system performance,” *IEEE Transactions on Magnetics*, vol. 37, pp. 480–484, January 2001.
- [147] S. Barsali, C. Miulli, and A. Possenti, “A control strategy to minimize fuel consumption of series hybrid electric vehicles,” *Energy Conversion, IEEE Transactions on*, vol. 19, pp. 187–195, march 2004.
- [148] Z. Wang, L. Weimin, and X. Yangsheng, “A novel power control strategy of series hybrid electric vehicle,” in *Intelligent Robots and Systems, 2007. IROS 2007. IEEE/RSJ International Conference on*, vol. 2, pp. 96–102, 29, November 2007.
- [149] E. Cerruto, A. Consoli, A. Raciti, and A. Testa, “Fuzzy logic based efficiency improvement of an urban electric vehicle,” in *Industrial Electronics, Control and Instrumentation, 1994. IECON '94., 20th International Conference on*, vol. 2, pp. 1304–1309, September 1994.
- [150] S. Lorenzo, S. Onori, and G. Rizzoni, “A comparative analysis of energy management strategies for hybrid electric vehicles,” *Joural of Dynamic Systems, Measurement, and Control*, vol. 133, 25, March 2011.
- [151] G. Paganelli, G. Ercole, A. Brahma, Y. Guezennec, and G. Rizzoni, “General supervisory control policy for the energy optimization of charge-sustaining hybrid electric vehicles,” *JSAE Review*, vol. 22, pp. 511–518, 2001.
- [152] A. Sciarretta, M. Back, and L. Guzzella, “Optimal control of parallel hybrid electric vehicles,” *IEEE Transactions on Control Systems Technology*, vol. 12, pp. 352–363, May 2004.

- [153] P. Pisu and G. Rizzoni, "A comparative study of supervisory control strategies for hybrid electric vehicles," *IEEE transaction on Control System Technology*, vol. 15, pp. 506–518, May 2007.
- [154] A. Brahma, Y. Guezennec, and G. Rizzoni, "Optimal energy management in series hybrid electric vehicles," in *American Control Conference, 2000. Proceedings of the 2000*, vol. 1, pp. 60–64, sep 2000.
- [155] A. Piccolo, L. Ippolito, V. Galdi, and A. Vaccaro, "Optimisation of energy flow management in hybrid electric vehicles via genetic algorithms," in *International Conference on Advanced Intelligent Mechatronics, 2001. IEEE/ASME*, vol. 1, pp. 434–439, 2001.
- [156] Y. Zhu, Y. Chen, G. Tian, H. Wu, and Q. Chen, "A four-step method to design an energy management strategy for hybrid vehicles," in *American Control Conference, 2004. Proceedings of the 2004*, vol. 1, pp. 156–161, July 2004.
- [157] L. V. Perez, G. R. Bossio, D. Moitre, and G. O. Garcia, "Optimization of power management in an hybrid electric vehicle using dynamic programming," *Mathematics and Computers in Simulation*, vol. 73, no. 1-4, pp. 244 – 254, 2006. Applied and Computational Mathematics - Selected Papers of the Fifth PanAmerican Workshop - June 21-25, 2004, Tegucigalpa, Honduras.
- [158] W. Li, G. Xu, Z. Wang, and Y. Xu, "Dynamic energy management for hybrid electric vehicle based on adaptive dynamic programming," in *Industrial Technology, 2008. ICIT 2008. IEEE International Conference on*, pp. 1 –6, april 2008.
- [159] Y. Gurkaynak, A. Khaligh, and A. Emadi, "Neural adaptive control strategy for hybrid electric vehicles with parallel powertrain," in *Vehicle Power and Propulsion Conference (VPPC), 2010 IEEE*, pp. 1–6, September 2010.
- [160] A. Sciarretta and L. Guzzella, "Control of hybrid electric vehicles," *IEEE Control Systems Magazine*, vol. 27, pp. 60–70, April 2007.
- [161] F. R. Salmasi, "Control strategies for hybrid electric vehicles: Evolution, classification, comparison, and future trends," *IEEE Transactions on Vehicular Technology*, vol. 56, pp. 2393–2404, September 2007.
- [162] C. C. Lin, H. Peng, J. W. Grizzle, and J.-M. Kang, "Power management strategy for a parallel hybrid electric truck," *IEEE Transactions on Control Systems Technology*, vol. 11, pp. 839–849, November 2003.
- [163] O. Sundstr, D. Amb, and L. Guzzella, "On implementation of dynamic programming for optimal control problems with final state constraints," *Oil Gas Sci. Technol. - Rev. IFP*, vol. 65, pp. 91–102, September 2009. IFP International Conference Advances in Hybrid Powertrains.
- [164] F. Hu and Z. Zhao, "Optimization of control parameters in parallel hybrid electric vehicles using a hybrid genetic algorithm," in *Vehicle Power and Propulsion Conference (VPPC), 2010 IEEE*, pp. 1 –6, sept. 2010.

- [165] M. J. West, C. M. Bingham, and N. Schofield, “Predictive control for energy management in all/more electric vehicles with multiple energy storage units,” in *Electric Machines and Drives Conference, 2003. IEMDC'03. IEEE International*, vol. 1, pp. 222–228, June 2003.
- [166] H. A. Borhan, A. Vahidi, A. M. Phillips, M. L. Kuang, and I. V. Kolmanovsky, “Predictive energy management of a power-split hybrid electric vehicle,” in *American Control Conference, 2009. ACC '09.*, pp. 3970–3976, June 2009.
- [167] G. Ripaccioli, D. Bernardini, S. D. Cairano, A. Bemporad, and I. V. Kolmanovsky, “A stochastic model predictive control approach for series hybrid electric vehicle power management,” in *American Control Conference (ACC), 2010*, pp. 5844–5849, July 2010.
- [168] I. Kolmanovsky, I. Sivergina, and B. Lygoe, “Optimization of powertrain operating policy for feasibility assessment and calibration: stochastic dynamic programming approach,” in *American Control Conference, 2002. Proceedings of the 2002*, vol. 2, pp. 1425–1430, 2002.
- [169] L. Johannesson, M. Asbogard, and B. Egardt, “Assessing the potential of predictive control for hybrid vehicle powertrains using stochastic dynamic programming,” *IEEE Transactions on Intelligent Transportation Systems*, vol. 8, pp. 71–83, March 2007.
- [170] E. Dean, J. W. Grizzle, and H. Peng, “Shortest path stochastic control for hybrid electric vehicles,” *International Journal of Robust and Nonlinear Control*, December 2007.
- [171] R. Cipollone and A. Sciarretta, “Analysis of the potential performance of a combined hybrid vehicle with optimal supervisory control,” in *Computer Aided Control System Design, 2006 IEEE International Conference on Control Applications, 2006 IEEE International Symposium on Intelligent Control, 2006 IEEE*, pp. 2802–2807, October 2006.
- [172] L. Serrao and G. Rizzoni, “Optimal control of power split for a hybrid electric refuse vehicle,” in *American Control Conference, 2008*, pp. 4498–4503, June 2008.
- [173] B. Gu and G. Rizzoni, “An adaptive algorithm for hybrid electric vehicle energy management based on driving pattern recognition,” in *ASME 2006 International Mechanical Engineering Congress and Exposition (IMECE2006)*, (Dynamic Systems and Control Division, Chicago, Illinois, USA), pp. 249–258, November 2006.
- [174] K. M. B. Goh, “Parametric modelling, control and optimisation of hybrid vehicles,” Master’s thesis, Department of Mechanical Engineering, Imperial College of London, London, United Kingdom, Spetember 2010.
- [175] W. O. Schiehlen, “Multibody system dynamics: Roots and perspectives,” *Multibody System Dynamics*, vol. 1, pp. 149–188, June 1997.

- [176] R. S. Sharp, “Testing and improving a tyre shear force computation algorithm,” *Vehicle System Dynamics*, vol. 41, pp. 223–247, 2004.
- [177] R. S. Sharp and M. Bettella, “On the construction of a general numerical tyre shear force model from limited data,” *Journal of Automobile Engineering, Proc. I. Mech. E. Part D*, vol. 217, pp. 165–172, 2003.
- [178] R. S. Sharp and M. Bettella, “Tyre shear force and moment descriptions by normalisation of parameters and the magic formula,” *Vehicle System Dynamics*, vol. 39, pp. 27–56, 2003.
- [179] J. Reimpell, H. Stoll, and J. W. Betzler, *The Automotive Chassis*. Oxford: Butterworth-Heinemann, 2nd edition ed., 2001.
- [180] E. Erden, “Parametric modelling and control of hybrid vehicle,” Master’s thesis, Department of Mechanical Engineering, Imperial College of London, London, United Kingdom, September 2008.
- [181] Anon., *Automotive Handbook*. Stuttgart: Robert Bosch GMBH, 5th edition ed., 2000.
- [182] M. A. Kluger and D. M. Long, “An overview of current automatic, manual and continuously variable transmission efficiencies and their projected future improvements,” *SAE Journal 1999-01-1259*, March 1999.
- [183] B. G. Vroemen, *Component Control for The Zero Inertia Powertrain*. PhD thesis, Technische Universiteit Eindhoven, Netherlands, November 2001.
- [184] R. P. G. Heath, “Seamless amt offers efficient alternative to cvt,” *JSAE Annual Congress 314-20075013*, 2007.
- [185] Anon., *Next-Generation XTRONIC-CVT*. Nissan Motor (GB) Limited, The Rivers Office Park Denham Way, Maple Cross, Rickmansworth, Hertfordshire, UK, 2011. <http://www.newsroom.nissan-europe.com/uk/>.
- [186] Anon., *XTRONIC CVT-Technology Overview*. Nissan Motor (GB) Limited, The Rivers Office Park Denham Way, Maple Cross, Rickmansworth, Hertfordshire, UK.
- [187] T. Kim and H. Kim, “Performance of integrated engine-cvt control considering powertrain loss and cvt response lag,” *Proceedings of the Institution of Mechanical Engineers, Part D: Journal of Automobile Engineering*, vol. 216, pp. 545–553, 2002.
- [188] T. Prius, *Toyota Hybrid System-II: Construction of Main Components*, August 2011.
- [189] T. D. Batzel and K. Y. Lee, “Sinusoidal commutation of slotless permanent magnet synchronous machines using discrete hall sensor feedback,” in *Power Engineering Society 1999 Winter Meeting, IEEE*, vol. 1, pp. 53–58, January 1999.

- [190] Anon., *What is Field Oriented Control and what good is it.* Copley Corporation-Article, Copley Controls, 20 Dan Road, Canton, MA 02021, USA. <http://www.copleycontrols.com/motion/pdf/Field-Oriented-Control.pdf>.
- [191] P. Pillay and R. Krishnan, “Control characteristics and speed controller design for a high-performance permanent magnet synchronous motor drive,” *Proc. IEEE 1987 Power Electronics Specialists Conf.*, pp. 598–606, 1987.
- [192] N. Kroutikova, C. A. Hernandez-Aramburo, and T. c. Green, “State-space model of grid-connected inverters under current control mode,” *Electric Power Applications, IET*, vol. 1, pp. 329 –338, may 2007.
- [193] G. T. R. Das and V. Subrahmanyam, “On the analysis of current source inverter fed permanent magnet synchronous motor,” in *Proceedings of the 1996 International Conference on Power Electronics, Drives and Energy Systems for Industrial Growth, 1996.*, vol. 1, pp. 286–292, January 1996.
- [194] M. S. J. Asghar, *Power Electronics*. Aligarh Muslim University, Aligarh, India: Prentice-Hall of India Pvt.Ltd, 2004. ISBN 8120323963.
- [195] N. Mohan, T. M. Undeland, and W. P. Robbins, *Power Electronics: Converters, Applications, and Design*. USA: John Wiley & Sons, 2002.
- [196] Z. Mihailovic, H. Prasad, and D. Borojevic, “Computer modeling and analysis of vsi fed permanent magnet synchronous motor drive systems with adjustable levels of complexity,” in *Applied Power Electronics Conference and Exposition, 1997. APEC '97 Conference Proceedings 1997., Twelfth Annual*, vol. 2, pp. 728–735, February 1997.
- [197] J. G. Kassakian, M. F. Schlecht, and G. C. Verghese, *Principles of Power Electronics*. Addison-Wesley, 1991.
- [198] V. Vorperian, “Simplified analysis of pwm converters using model of pwm switch. continuous conduction mode,” *Aerospace and Electronic Systems, IEEE Transactions on*, vol. 26, pp. 490–496, May 1990.
- [199] C. Schauder and H. Mehta, “Vector analysis and control of advanced static var compensators,” *Proc. Inst. Elect. Eng.*, vol. 140, pp. 299–306, july 1993.
- [200] G. Georgiadis, “Parametric modelling and control of hybrid vehicles,” Master’s thesis, Department of Electrical Engineering, Imperial College of London, London, United Kingdom, Spetember 2008.
- [201] Anon., *AFM-140 Axial Flux Motor*. EVO-Electric Ltd., Unit 14, Woking Business Park, Woking Surrey, GU21 5JY, UK, 2010. <http://www.evo-electric.com/inc/files/AFM-140-Spec-Sheet-V1.1.pdf>.
- [202] J. Hey, D. A. Howey, R. Martinez-Botas, and M. Lamperth, “Transient thermal modeling of an axial flux permanent magnet (AFPM) machine using a hybrid thermal model,” *International Conference on Fluids and Thermal Engineering*, 2010.

- [203] D. C. Lee, G. M. Lee, and K. D. Lee, “DC-Bus voltage control of three-phase AC/DC PWM converters using feedback linearization,” *IEEE Transactions on Industry Applications*, vol. 36, no. 3, 2007.
- [204] S. Fukuda, Y. Iwaji, and T. Aoyama, “Modelling and control of sinusoidal pwm rectifiers,” *Power Electronics and Applications, Fifth European Conference*, vol. 4, pp. 115–120, 1993.
- [205] Anon., *AFG-140 Axial Flux Generator*. EVO-Electric Ltd., Unit 14, Woking Business Park, Woking Surrey, GU21 5JY, UK, 2010. <http://www.evo-electric.com/inc/files/AFG-140-Spec-Sheet-V1.1.pdf>.
- [206] W. W. Pulkrabek, *Engineering Fundamentals of the Internal Combustion Engine*. Upper Saddle River, New Jersey 07458: Prentice Hall, 2003.
- [207] N. Watson and M. S. Janota, *Turbocharging of Internal Combustion Engine*. London: The Macmillan Press Ltd., 1982.
- [208] B. Lecointe and G. Monnier, “Downsizing a gasoline engine using turbocharging with direct injection,” *SAE Technical Paper 2003-01-0542*, March 2003.
- [209] U. D. of Energy, “Just the basics-diesel engine,” August 2003.
- [210] L. Bai and M. Yang, “Coordinated control of egr and vnt in turbocharged diesel engine based on intake air mass observer,” *Tech. rept. 2002-01-1292. SAE International.*, 2002.
- [211] “<http://www.ricardo.com/en-gb/software/products/wave/>.”
- [212] J. L. Lumely, *Engines An Introduction*. 40 West 20th Street, New York, NY 10011-4211, USA: Cambridge University Press, 1999.
- [213] A. Chen, “Parametric modelling and control of hybrid vehicle,” Master’s thesis, Department of Mechanical Engineering, Imperial College of London, London, United Kingdom, September 2008.
- [214] C. M. Shepherd, “Design of primary and secondary cells - part 2. an equation describing battery discharge,” *Journal of Electrochemical Society*, vol. 112, pp. 657–664, July 1965.
- [215] P. L. Gregory, “Extended Kalman filtering for battery management systems of LiPB-based HEV battery packs: Part 2. Modeling and identification,” *Journal of Power Sources*, vol. 134, no. 2, pp. 262–276, 2004.
- [216] P. Karlsson, M. Bojrup, M. Alakula, and L. Gertmar, “Zero voltage switching converters,” 2011. www.iea.lth.se/ielper/charger/NORPIE2000-paper.pdf.
- [217] H. Li, F. Z. Peng, and J. Lawler, “Modeling, simulation, and experimental verification of soft-switched bi-directional dc-dc converters,” in *Applied Power Electronics Conference and Exposition, 2001. APEC 2001. Sixteenth Annual IEEE*, vol. 2, pp. 736 –742 vol.2, March 2001.

- [218] J. Gao, F. Sun, H. Hongwen, G. G. Zhu, and E. G. Strangas, “A comparative study of supervisory control strategies for a series hybrid electric vehicle,” in *Power and Energy Engineering Conference, 2009. APPEEC 2009. Asia-Pacific*, pp. 1–7, March 2009.
- [219] T. Hofman, M. Steinbuch, R. van Druten, and A. Serrarens, “Rule-based equivalent fuel consumption minimization strategies for hybrid vehicles,” in *Proceedings of the 17th IFAC World Congress*, 2008.
- [220] B. Aghdaee, “On dynamic programming technique applied to a parallel hybrid electric vehicle,” Master’s thesis, Department of Signals and Systems, Chalmers University of Technology, GÄoteborg, Sweden, September 2009.
- [221] A. Boyali and L. Guvenc, “Real-time controller design for a parallel hybrid electric vehicle using neuro-dynamic programming method,” in *IEEE International Conference on Systems Man and Cybernetics (SMC)*, 2010, pp. 4318–4324, October 2010.
- [222] J. S. Lai, R. W. Young, and J. W. McKeever, “Efficiency consideration of dc link soft-switching inverters for motor drive applications,” in *Power Electronics Specialists Conference, PESC ’94 Record, 25th Annual IEEE*, vol. 2, pp. 1003 –1010, June 1994.
- [223] W. Dong, J.-Y. Choi, Y. Li, H. Yu, J. Lai, D. Boroyevich, and F. C. Lee, “Efficiency considerations of load side soft-switching inverters for electric vehicle applications,” in *Fifteenth Annual Applied Power Electronics Conference and Exposition. APEC 2000.*, vol. 2, pp. 1049–1055, 2000.
- [224] P. Sun, J.-S. Lai, H. Qian, W. Yu, C. Smith, and J. Bates, “High efficiency three-phase soft-switching inverter for electric vehicle drives,” in *Vehicle Power and Propulsion Conference, 2009. VPPC ’09. IEEE*, pp. 761–766, September 2009.
- [225] J.-S. Lai, B. York, A. Koran, C. Younghoon, B. Whitaker, and H. Miwa, “High-efficiency design of multiphase synchronous mode soft-switching converter for wide input and load range,” in *Power Electronics Conference (IPEC), 2010 International*, pp. 1849–1855, June 2010.
- [226] J.-S. Lai, “High-efficiency power conversion for renewable energy and distribution generation,” November 2 2009.
- [227] C. M. C. Duarte and I. Barbi, “An improved family of zvs-pwm active-clamping dc-to-dc converters,” *Power Electronics, IEEE Transactions on*, vol. 17, pp. 1–7, January 2002.
- [228] R. W. Erickson, *DC DC Power Converters*. John Wiley & Sons, Inc., 2001.